1-1-1984

A study of polymer deformation by vibrational spectroscopy/

James E. Lasch
University of Massachusetts Amherst

A STUDY OF POLYMER DEFORMATION BY VIBRATIONAL SPECTROSCOPY

By

James Edward Lasch

Submitted to the Graduate School of the
University of Massachusetts in partial fulfillment
of the requirements for the degree of

DOCTOR OF PHILOSOPHY

September 1984

Department of Polymer Science and Engineering

A STUDY OF POLYMER DEFORMATION
BY VIBRATIONAL SPECTROSCOPY

By

James Edward Lasch

Approved as to style and content by:

Shaw Ling Hsu, Chairperson of Committee

William J. MacKnight, Member

Edwin L. Thomas, Member

Hajime Sakai, Member

William J. MacKnight, Head
Department of Polymer Science
and Engineering

ACKNOWLEDGEMENTS

I would like to acknowledge Professor Shaw Ling Hsu for acting as my thesis advisor and for his constructive criticism and encouragement. I would also like to thank Professors William J. MacKnight, Hajime Sakai, and Edwin L. Thomas for serving on my dissertation committee.

I would like to thank the other professors and the students and post-doctoral fellows of the Polymer Science and Engineering Department who have created an enjoyable and challenging atmosphere for learning.

I offer my sincere appreciation to Norm Page and John Domain for their help in building and maintaining various electronics and to Marilyn Putnam for typing my dissertation and drawing its figures. I wish to thank my friends who have brightened my time here.

Finally, I thank my mother, father, sisters, and brothers for their love and support during my education.

I dedicate this dissertation with love to Katie whose many sacrifices and unending support have enabled me to complete this degree.

ABSTRACT

A Study of Polymer Deformation
by Vibrational Spectroscopy
(September, 1984)
James Edward Lasch, B.S., Case Western Reserve University
M.S., University of Massachusetts, Ph.D., University of Massachusetts
Directed by: Professor Shaw Ling Hsu

In drawn and solid state extruded polyethylene, the distribution of straight chain segment lengths (on the order of 5 - 50 nm) have been inferred from the position and bandshape of the longitudinal acoustic mode (LAM). Because LAM is sensitive to the presence of conformational defects within the crystal lattice, it is an excellent technique for revealing the change in structure with draw ratio. An increase in defect content at higher draw ratios for solid state extruded samples was demonstrated and the results from Raman LAM and other characterization techniques were compared.

A new time resolved Fourier transform infrared spectroscopy technique has been developed. In contrast to the methods developed previously, this one has greater flexibility in time resolution 0.1 msec to seconds) and in the choice of strain functions. Experiments demonstrating the applicability of this technique to the understanding of polymer deformation behavior are given.

Infrared rheo-optics, which uses infrared spectroscopy to observe

the dynamics of polymer deformation, was used to study the mechanical properties of the random block copolymer of tetramethylene terephthalate and poly(tetramethylene oxide), Hytrel®. The existence of the stress induced, reversible crystal-crystal phase transition which occurs in poly(tetramethylene terephthalate) has been demonstrated in the copolymer. In addition, infrared rheo-optical experiments have characterized the segmental orientation and the phase transition in this copolymer. From the time resolved infrared spectra obtained for the homopolymer, no delay was found between the applied strain and the crystal phase transition.

Polarization modulation, a differential method for measuring polymer orientation is an alternative to subtracting the parallel and perpendicular spectra. The relative advantages and disadvantages of modulation and subtraction techniques were evaluated. It was demonstrated that the subtraction measurements were not digitization limited and modulation does not provide signal to noise or sensitivity improvements under these conditions. However, those conditions in which modulation would lead to signal to noise improvements were identified.

TABLE OF CONTENTS

LIST OF TABLES

LIST OF FIGURES

Figure

C H A P T E R I

INTRODUCTION

Survey of Dissertation

The goal of this dissertation is to gain a better understanding of polymer structure-property relationships. Raman and infrared spectroscopy are utilized to follow changes in the morphology caused by small, repeatable harmonic strain, or large, irreversible mechanical deformation. The observed data, combined with a general knowledge of the sample morphology lead to a better understanding of the relationship between the morphological features and the mechanisms of viscoelasticity and the macroscopic mechanical properties in terms of stress-strain behavior.

This chapter provides an overview of the dissertation. Chapter II presents a study of ultra-oriented polyethylene by the Raman longitudinal acoustic mode (LAM) technique. A brief summary of the sample preparation, mechanical properties, and structure of ultra-oriented polyethylene is given. The physical basis of the LAM vibration, the type of structural information it provides, the experimental results and conclusions concerning the structure of ultra-oriented polyethylene are discussed in detail. The Raman spectrometer was interfaced to a microcomputer system in order to perform data collection and the data corrections which are necessary to provide

structurally meaningful quantitative results. Chapter III introduces the infrared rheo-optical technique for the study of polymer deformation. The details of a Fourier transform infrared spectroscopy (FT-IR) system, the hydraulic stretcher used in these studies, and the development of a new method for time-resolved spectroscopy are described in detail. Chapter IV presents an investigation of the stress-induced crystal phase transition in poly(tetramethylene terephthalate) (4GT) and a random block copoly(ether-ester), Hytrel®. Time resolved spectroscopy is utilized to examine the rate of crystal transformation in 4GT and in Hytrel®. The selectivity of the IR method allows the deformation behavior of this multiphase polymer to be monitored. In Chapter V, an alternative method for measuring the dynamic changes of polymer orientation is explored. Normally, a ratio or difference of two perpendicularly polarized spectra is measured. Usually these two spectra are extremely similar. Polarization modulation is a differential technique which directly measures that difference. Its advantages and limitations in terms of accuracy, measurement time, and signal to noise ratio are discussed from theoretical as well as experimental viewpoints. Chapter VI summarizes the conclusions of the individual chapters and discusses future work in these areas.

The following section provides a background discussion of the longitudinal acoustic mode and its usefulness in the study of the morphology of ultra-oriented polyethylene samples.

Ultraoriented Polyethylene and the Longitudinal Acoustic Mode

The drawing or solid state extrusion of polyethylene results in samples with very high tensile strength and modulus. The moduli reported (70-240 GPa) are near the theoretical modulus of a perfect polymethylene chain, which is approximately 300 GPa (1,2). The increases in mechanical properties are accompanied by dramatic changes in the sample morphology. The mechanical properties continue to improve with higher draw ratios (3,4). But, because the resulting fibrillar morphology is not as well understood as the starting spherulitic morphology, the morphological features responsible for the increased strength and modulus have not been clearly determined. A wide range of morphological techniques have been applied to these materials. Differential scanning calorimetry (DSC) and wide angle x-ray scattering (WAXS) have been used to determine the crystallinity and crystalline orientation (3,5). Two other frequently used techniques are WAXS line broadening and small angle x-ray scattering (SAXS) (6,7). WAXS 002 integral breadth measurements yield the average coherence length (thickness) of the crystal in the chain axis direction and the SAXS long period yields the spacing of the alternating crystalline and amorphous regions along the fibrils. During the initial deformation stages, crystallinity increases and crystalline orientation develops. However, little further improvement in these features occurs beyond a draw ratio of 10 (3,4). At higher

draw ratios, further changes in the crystal thickness and long period are seen (3,6,8). Changes in the nature and amount of taut tie molecules and/or intercrystalline bridges have been used to explain the increase in tensile properties (9,10). Since the high moduli are sometimes associated with increasing perfection and/or order in the sample (11,12), it may be helpful to examine those features which weaken the structure. These features include amorphous chains, conformational defects, and folded chains present within the fibrils.

Raman longitudinal acoustic mode (LAM) is a technique complementary to WAXS and SAXS; LAM gives the distribution of straight chain lengths in the crystal (13,14) and is sensitive to intracrystal defects and folds (15,16). LAM is the normal vibration associated with a single, extended, all-trans chain segment commonly called a crystal stem. The frequency of the LAM vibration is inversely proportional to the length of an individual stem. The vibration is cooperative - extending over the entire length of the all-trans segment and is decoupled by the folds at the crystal surfaces. A conformational defect within the crystal will perturb the vibration and the remaining segments on either side of it will vibrate with a frequency characteristic of their shortened length (16). The crystalline regions are composed of many stems of various lengths. The frequency distribution of the observed LAM vibrations (measured in the low frequency region of the Raman spectrum) can be related to this distribution of stem lengths.

The information obtained with the Raman technique from drawn and extruded samples is compared with other measurements of crystal size for these samples and with models describing their fibrillar structure. The information obtained by LAM is unique and adds to the understanding of the fibrillar structure and the solid state extrusion and drawing processes.

In the following section an introduction to the use of infrared rheo-optics to observe polymer viscoelastic behavior is presented.

Infrared Studies of Polymer Deformation

A great deal of experimental and theoretical research has been carried out to bring about a better understanding of polymer structure-property relationships. The field of rheology, which deals with the deformation and flow of matter, has traditionally been limited to the study of the sample stress, strain, and strain rate tensors. A better understanding can be obtained by following the microstructural changes during deformation, since the macroscopic stress-strain behavior is controlled by the deformation mechanisms operating on the microstructural level. The morphological features of semicrystalline polymers that affect deformation include the size, shape, and perfection of the crystalline regions, their connection by amorphous chains, and the details of their organization into superstructures (usually spherulites) (17,18).

Typical changes that occur during deformation include rotation and reorganization of crystallites, elongation and disruption of the spherulites, and extension and slippage of the amorphous chains (19,20). WAXS, light scattering, birefringence, and IR dichroism are among techniques which have been used in the past to follow dynamic polymer deformation (17,18,21-25). The term rheo-optics is used for experiments which combine simultaneous stress and strain measurements with morphological observations of polymer deformation. In a typical rheo-optical experiment, Fujita et al. have combined dynamic birefringence results (Figure 1) with dynamic WAXS to determine the microstructural origins of the α and β dynamic mechanical loss peaks (Figure 1b) (26). From their results they were able to conclude that the β loss peak is associated with rotation of the lamellae and the α loss peak is due to the reorientation of crystals within the lamellae (26). Stein et al. (18) have shown that for a step strain the spherulite deformation is nearly instantaneous (<5 msec), while the crystalline and amorphous segments orient at much slower rates. In this experiment, small angle (laser) light scattering (SALS) was used to follow the spherulitic elongation. WAXS was used to measure the crystal orientation, and then the amorphous orientation was calculated by subtracting the crystalline contribution from the total birefringence change.

In contrast, the selectivity of infrared spectroscopy allows the direct and simultaneous measurement of the changes of each component

Figure 1. Rheo-optical behavior of polybutene-1 (ref. 26).
a. real and imaginary components of the dynamic stress-optical coefficients
b. separation of crystalline and non-crystalline contributions to the dynamic strain-optical coefficient

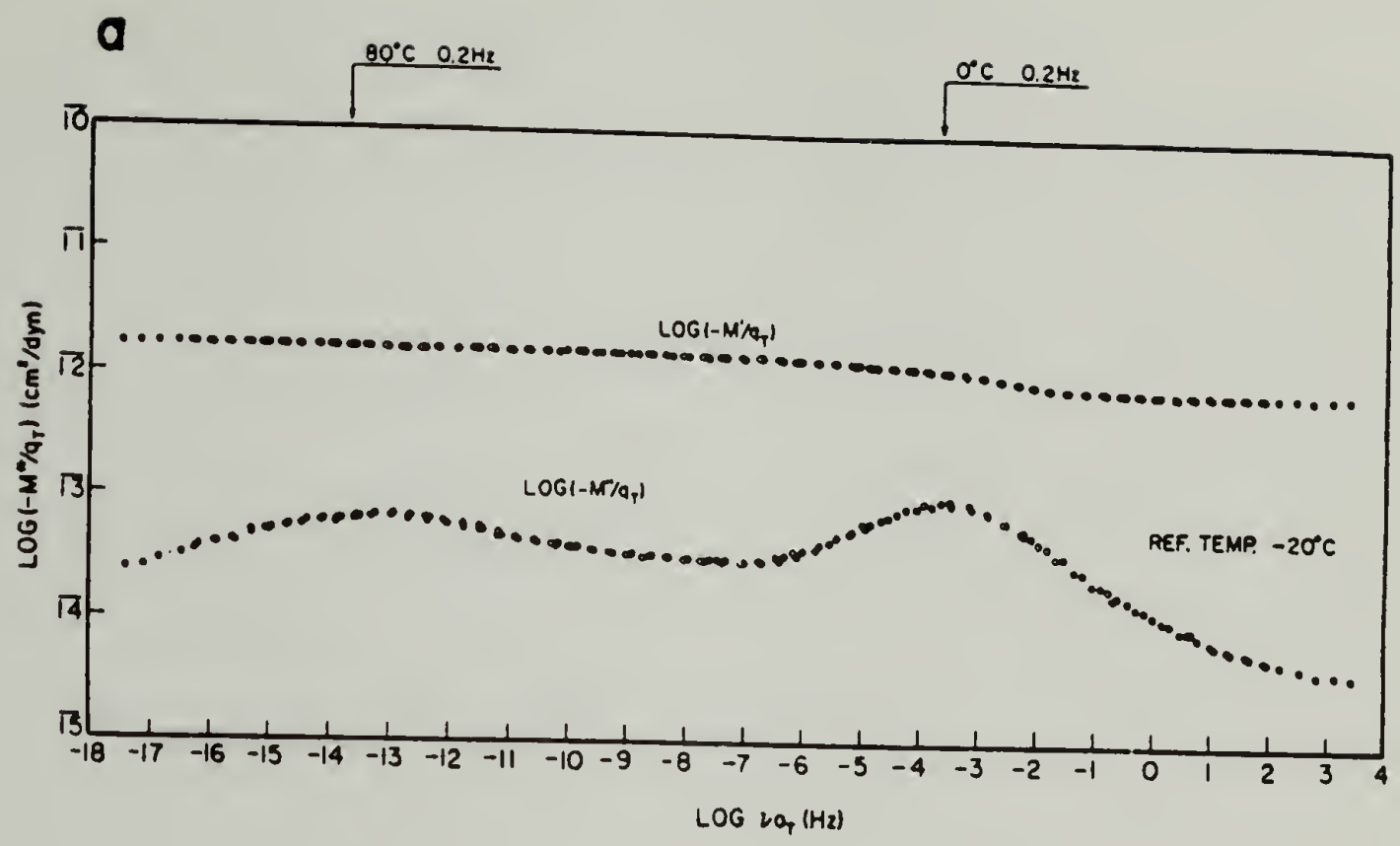
a
80°C 0.2Hz
0°C 0.2Hz
LOG(-M*/a_T) (cm²/dyn)
LOG(-M'/a_T)
LOG(-M''/a_T)
REF. TEMP. -20°C
LOG νa_T (Hz)
b
p_T K' x10²
K'am
K'cry
K''cry
K''am
REF. TEMP -20°C
p_T K'' x10³
LOG νa_T (Hz)

Figure 1

in heterogeneous materials, e.g. copolymers, polymer blends, and semicrystalline polymers by interpreting changes in the IR absorption bands. The IR spectra can distinguish not only chemically distinct chains but different conformations (27), various types of crystalline chain packing (28-30), and the strength of hydrogen bonds (31-34). Furthermore, when the angle of transition dipole moment with respect to the chain axis is known, the orientation of each component can be calculated by determining the infrared dichroism with polarized infrared measurement (35-37). In summary, IR spectroscopy allows deformation induced changes in orientation, conformation, and packing to be followed (38).

Dispersive infrared spectrometers do not allow simultaneous measurement of wide spectral regions and fast time response. Rapid scanning FT-IR spectrometers possessing Felgett's (multiplex) and Jacquinot (throughput) advantages together with sensitive, low-noise, cooled detectors, can scan a complete spectrum quickly and with high signal to noise ratios (39). However, in order to fully characterize the viscoelastic response of the polymer microstructure, even higher time resolution and signal to noise ratios are required than are generally obtainable through rapid scanning techniques (40-42). Time-resolved FT-IR spectroscopy (TRS) is a technique that allows measurement of events occurring in times shorter than a single interferometer scan (41,43-47). TRS also enables the coaddition of scans for improving signal to noise ratios. Several modifications of the technique have been developed previously, but all have in common the

repeated triggering of a sample event (a strain waveform) with different phase relationships between the interferometer retardation (position of the moving mirror) and the sample event. To obtain artifact-free spectra, the polymer response must be identical for every deformation cycle (48). The collected data are then sorted to reconstruct spectra characteristic of the polymer during different time intervals of the deformation cycle. The time resolved scheme that we have developed is tailored to studies of polymer viscoelasticity and therefore is flexible in the time resolution (10^{-4} to 10 seconds) and the strain waveforms applied (any repeatable function with a period corresponding to these time scales) (41,42). Further details of the TRS techniques are given in Chapter III.

Microstructural Response to Deformation in Poly(tetramethylene terephthalate) and Poly(ether ester)

Previously, infrared spectroscopy has been combined with WAXS and Raman studies to examine the reversible, stress-induced crystal-crystal phase transformation in poly(tetramethylene terephthalate) (49-51). Wide angle x-ray studies have determined the crystal structure and unit cell parameters of both the α and β crystal forms of poly(tetramethylene terephthalate) (51-53). Correlation of x-ray and IR results have identified infrared bands characteristic of the chain conformations of both the relaxed α phase and the strained β phase (27,54).

However, no direct morphological evidence had been published on the rate of α to β transformation when the sample is loaded and unloaded on a 1 second time scale. Therefore, a dynamic FT-IR study employing TRS was undertaken to follow the rate of α to β transformation. Additionally, in Hytrel®, a random-block copolymer of tetramethylene terephthalate and poly(tetramethylene oxide)(Mw=1000) (55,56), the existence of the α-β transition has been clearly demonstrated in our experiments. The strain dependence of the orientation of α crystalline, β crystalline, and amorphous tetramethylene terephthalate units and the relative amounts of α and β forms have also been determined.

CHAPTER II

LONGITUDINAL ACOUSTIC MODE STUDY OF ULTRA-ORIENTED POLYETHYLENE

Structure and Properties of Ultra-Oriented Polyethylene

In this section of the chapter, the motivation for a longitudinal acoustic mode (LAM) investigation of ultra-oriented polyethylene is presented. It has long been known that tensile properties of semicrystalline polymer fibers can be improved by drawing after the fiber has been spun. Accordingly, many "drawing" methods have been developed to attain improved mechanical properties. These methods include hot and cold drawing (5,57), solid state extrusion (3), solid state coextrusion (58), hydrostatic extrusion (59), and zone annealing and zone drawing (60). The experimental differences between the methods include whether pressure is applied, the temperature of deformation, and the use of temperature gradients. With each technique, variable experimental parameters usually include draw ratio, temperature, and strain rate as well as variations in the morphology, molecular weight, and molecular weight distribution of the polymer under study. Obviously, no study has managed to follow all of these variables and this study will be limited to an observation of some effects induced by varying the draw ratio for the solid state extrusion of polyethylene.

It is desired to correlate the draw ratio dependence of mechanical properties with changes in the sample morphology. This correla-

tion leads to a better understanding of the drawing process and will allow optimization of the mechanical properties. An explanation of the morphological changes accompanying drawing have been summarized by Peterlin (61,20). The transformation from an initial spherulitic morphology to the final fibrillar one has been described as a three phase process: 1) the plastic deformation of the original spherulitic structure, 2) the discontinuous transformation of spherulites into the fibrillar structure by micronecking, and 3) the plastic deformation of the fibrillar structure. In the fibrillar structure, microfibrils of lateral size 100-200 Å and several ten thousands of Å in length are composed of alternating crystalline and amorphous regions along the long axis (61). Within the microfibrils, a high degree of crystalline orientation exists. During micronecking, unfolding of the chains in the original lamellae occurs and results in some taut tie molecules which connect successive crystalline regions. This connectivity plays an important role in the mechanical properties (62,9).

A recent review described some of the changes in mechanical properties and morphology with draw ratio, DR, for solid state extrusion (3). The key feature is the linear increase in tensile modulus with DR in the range 10 to 40. When the DR increases from 1 to 10, the initial change from a spherulitic to a fibrillar morphology takes place. This change in structure is reflected by changes in crystallinity, melting point, and crystalline orientation function in the interval of DR from 1 to 15. However, very little further change in these parameters is observed with increasing draw ratio; therefore,

other observations are required to explain the increase in modulus with further increase in DR.

Structural models of the ultra-oriented fibers can be used to understand their morphology and their improved mechanical properties. Several proposed models are shown in Figure 2. The model of Gibson et al. is described as fibrillar stacks of crystallites, linked by intercrystalline bridges or as a continuous crystal containing disordered regions which are spaced periodically in the c-axis direction (62,8). The model incorporates the periodic density fluctuations observed by SAXS and a c-axis crystal thickness which increases with draw ratio and can exceed the long period. The increasing crystal continuity at higher draw ratios is expressed in terms of the amount and length of the intercrystalline bridges. The area fraction of intercrystalline bridges is estimated from the SAXS long period and WAXS 002 line broadening measurements and used together with a fiber reinforced composite model to calculate the sample modulus.

Other models are more qualitative and descriptive. Clark and Scott envision two stages in the drawing process (12,63). The first stage produces a "naturally drawn" fiber containing folded chain blocks and tie molecules. The folds are segragated into the amorphous region along with chain ends and tie molecules. The aggregation of defects gives rise to strong SAXS meridional intensity and allows stress to be concentrated in the tie molecules, causing crack propagation which results in low tensile strengths.

Figure 2. Structural models of the fibrillar morphology.
a. intercrystalline-bridge model, Gibson et al. (Ref. 8).
b. "natural drawn" fiber (lamellar block model), Clark and Scott (Ref. 12).
c. Peterlin's model (Ref. 61).
d. "super drawn" fiber (continuous crystal model (Ref. 12).

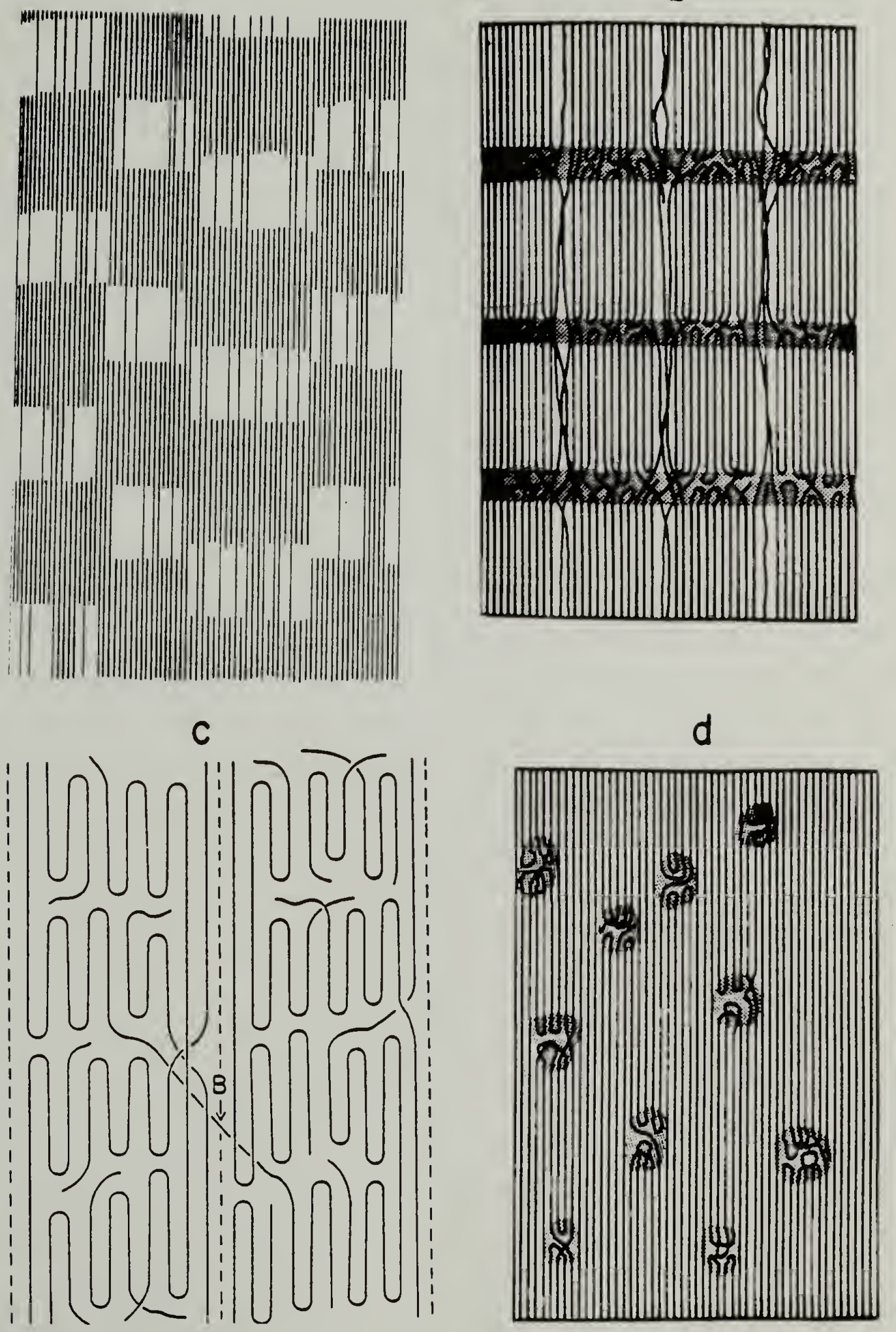

Figure 2

Additional drawing produces the "superdrawn fiber" described by the continuous crystal matrix model. The model is a lamellae-free, continuous crystal fiber with incorporated chain fold defects. The dispersal of folds throughout the crystal reduces stress concentration and inhibits crack propagation which results in high tensile strength (9). Porter had earlier proposed a similar continuous crystal model (11).

Peterlin's model retains periodic amorphous regions along the fibril axis which incorporate chain folds and tie molecules. A great number of taut tie molecules, constituting up to 50 percent of chains in the crystal lattice are responsible for the improved mechanical properties. According to Peterlin, the tie molecules are formed during chain unfolding of the starting lamellar material (20,61). In a later paper, Peterlin examines several of the proposed models in terms of expected deformation behavior (10). The tensile modulus and tensile strength predicted for each of the models are discussed in comparison with observed modulus values.

In summary, all of the models presented have several common features, including high degrees of crystallinity and crystal orientation. The models also incorporate chain folds, amorphous chains and extended amorphous chains (taut tie molecules) and/or intercrystalline bridges between successive crystals along the microfibrils. However, the models diverge on the exact nature and placement of the non-crystalline and connective features. For instance, in the intercrystalline bridge model and in the natural drawn fiber model,

the amorphous regions are quite distinct from the crystalline regions. This leads one to conclude that the crystals should be relatively free of packing and conformational defects. In contrast, the continuous crystal model has regions of high defect concentration distributed throughout the crystals which leads to a lower crystalline density.

The discussion of the Raman LAM technique presented in the next section will show that it is very sensitive to conformational defects in the crystals. The longitudinal acoustic mode, LAM, is a sensitive, new morphological tool to study microstructural features at the 50 to 500 Å level. Further consideration of the physical origin of LAM will reveal what information it can provide and how this information complements or supplements other techniques used to examine the fibrillar morphology.

A particular series of samples of solid state extruded polyethylene with draw ratios 12, 24, and 36 have been extensively characterized at the University of Massachusetts by several techniques (7,66) including small angle x-ray scattering (SAXS), wide angle x-ray scattering (WAXS), scanning (SEM) and dark field electron microscopy (DF-EM), and differential scanning calorimetry (DSC). Our Raman LAM analysis has clarified some structural aspects for these samples in particular and the fibrillar structures in general. In particular, the LAM results have shown that the crystals do not become more perfect at higher draw ratios. However, because of the apparent

disagreement between results from the various techniques, models which only explain certain aspects of the data are insufficient.

The Longitudinal Acoustic Mode

Introduction

Before comparing the LAM results with other techniques, it is necessary to understand the basics of the LAM technique and the features that it measures. The longitudinal acoustic mode measures the lengths of the extended, all-trans sequences (crystal stems). From the distribution of stem lengths, the thickness of the crystalline region can be measured. However, the LAM vibration is disturbed by non-trans conformations caused by kinks, jogs, or other conformational defects in the crystal (15). These defects effectively decouple the vibrations of the all-trans segments on either side of the defect (64,65). Therefore, if two different crystals of the same thickness (measured by small angle x-ray scattering (SAX) or electron microscopy) are compared, and one contains many more defects, then the stem length distribution measured by LAM will be broadened towards shorter lengths for the crystal with more defects. This example illustrates the fact that combining information measured by two techniques provides a much fuller understanding than either measurement alone.

The longitudinal acoustic mode (LAM) is a low frequency, Raman active vibration observed in many semicrystalline polymers. This mode has been described as "accordian-like" because of the atomic displacements which take place during the normal vibration (67,68). It is a cooperative vibration of a large number of atoms extending along the chain over distances of 100 Å or longer (69). This is in contrast to many localized normal vibrations that involve only a few atoms, e.g. CH_2 stretching. The frequency of localized normal vibrations vary little with changes in conformational sequence or crystallinity. However, the vibrational frequency of the LAM is extremely sensitive to the all-trans sequence length. Because the nature of the normal vibration will change drastically when the all-trans conformation is interrupted, the LAM measurements provide a quantitative length distribution of straight chain segments.

The earliest observation of LAM was in n-paraffins by Mizushima and Shimanouchi (70), who observed that the frequency is inversely proportional to the length of the all-trans sequences that traverse the paraffin crystals. They showed that the measured frequencies could be fitted to the expression for the longitudinal acoustic frequency of a thin elastic rod,

$$\nu = \frac{m}{2Lc}\left(\frac{E}{\rho}\right)^{1/2}$$

$$\nu = K/L \qquad (2.1)$$

where E is Young's modulus, ρ is the density, m is the vibrational

order, and L is the equilibrium rod length. The constants can be combined into K, with a value of 2838 $cm^{-1}/Å$ (75). Schaufele and Shimanouchi have observed the higher order, normal vibrations (LAM-3,5,7...) and demonstrated that their frequencies agree well with the calculated dispersion curve of the ν_9 and ν_5 branches of an infinite polymethylene crystal (71). Normal coordinate analyses have defined the atomic displacements of LAM and have shown that it consists of CCC angle bending and CC stretching (67,72). These studies confirmed that the odd-orders of the accordian-like vibration of an all-trans, straight chain segment are centrosymmetric and therefore Raman active.

In this section on LAM, the corrections which are required to determine the straight chain length distribution from the raw Raman LAM spectra are discussed. These include the subtraction of the background from the observed LAM and the application of frequency dependent intensity corrections (14). The interpretation of LAM in these ultra-oriented polyethylene samples requires an understanding of the effects of the chain folds at the lamellar surface and the effects of conformational defects in the crystals on the LAM frequencies.

The effects of folds and the lamellar surface

This sub-section summarizes previous studies of the influence of the lamellar surface on the LAM of n-alkanes and the effects of chain folds and the lamellar surface on the LAM vibration in polymers.

Olf, Peterlin, and Peticolas found LAM in the dilute solution

grown polyethylene single crystals (69), and in melt crystallized and cold drawn polyethylene (73). The observed frequencies were in the range of 10-40 cm^{-1} and were inversely proportional to the lamellar thicknesses (90 to 250 Å). In the case of polyethylene, the straight chain segments between the folds in the lamellae are considered to be the source of the finite chain segments responsible for the LAM. The vibrations are decoupled by the folds at the lamella surface and therefore the frequency reflects the lamellar thickness and is not dependent on the length of the polyethylene chain itself.

Olf et al. observed a lower intensity than predicted for the LAM-3 mode in polyethylene samples (73). They assumed that the reduction in intensity was due to the folds at the lamellar surface and proposed a composite rod model to describe the effects. To explain anomolies in the LAM results of an isotactic polypropylene extrudate, Hsu and Krimm have refined this model (74-76) to include masses added to the chain ends (folds) and perturbing forces acting on the ends of the vibrating chains. Other studies of end effects include a study of mixed n-alkanes by Chang and Krimm (77), normal coordinate analysis of various fold conformations by Chang and Krimm (16), a model for coupled rods with experimental results by Strobl and Eckel (78), and coupling of the normal modes of two all-trans segments with the normal modes for various fold conformations (79). However, it is most probable that the results obtained for paraffins are not directly applicable to polyethylene.

Testing the applicability of the LAM technique for microstructural determination in semicrystalline polymers is hampered by the difficulty in obtaining polyethylene data such as LAM frequencies and intensities, SAXS crystal thickness, and chain tilt angle in the lamellae to the same degree of precision that is available for the n-paraffins. In a study of these effects in polyethylene, Glotin and Mandelkern compare the frequencies of LAM-1 and LAM-3 modes for C_{94} n-alkane, quenched low molecular weight polyethylene fractions, and solution and isothermally crystallized high molecular weight polyethylene fractions (80). The effect of chain folds and forces on the ends of the vibrating segments shifts the frequency of the LAM-1 and LAM-3 from their theoretical values. The perturbation of the LAM-1 frequency in C_{94} n-alkane is 3.2 cm^{-1}, from the expected value of 24.4 to the measured one of 27.6 cm^{-1}. The ratio of LAM-3 to LAM-1 frequencies is 2.69 instead of 3.00. Since the all-trans segment length in PE cannot be calculated directly as is the case for n-alkanes, and since they cannot be measured with a sufficient degree of certainty, the analysis centers on the quantity B, the ratio of LAM-3 to LAM-1 frequencies. Strobl and Eckel (78) have proposed the following equation to calculate the frequency of a perturbed rod.

$$\nu_m = m\,\nu_o + \frac{\Delta\nu}{m} \qquad 2.2$$

where ν_m is the observed frequency, m is the order of the LAM, ν_o is the unperturbed frequency, and $\Delta\nu$ is perturbation of the first order mode. The perturbation can be calculated from the measured frequencies

of LAM-1 and LAM-3;

$$\Delta\nu = \frac{9}{8}\left(\frac{\nu 3}{3} - \nu_1\right) . \qquad 2.3$$

For quenched low MW polyethylene fractions, solution crystallized samples, and melt crystallized samples, the values for $\Delta\nu$ are 2.0 to 3.0 cm^{-1}, 1.0 to 1.5 cm^{-1}, and 0.2 to 0.6 cm^{-1}, respectively. B values for the same three samples are 2.70 to 2.80, 2.83 to 2.88, and 2.82 to 2.93, respectively. A comparison of quenched low MW fractions with solution crystallized and melt crystallized high MW samples has shown the perturbations in frequency and in the ratio of LAM-3 to LAM-1 diminishes when the fold (lamellar) surfaces become more disordered. Therefore, the surface effects may be large for n-paraffins, but their magnitude decreases as the surface layer becomes more irregular and apparently may be ignored with less error in the case of most polyethylene samples.

Chain length and frequency distributions

In this sub-section the quantitative relationship between the LAM bandshape and the straight chain length distribution is presented. For either drawn or extruded samples, the distribution in chain segment lengths is sufficiently broad so that it may be obtained from the LAM bandshape without deconvoluting the natural line width of the vibration or instrumental broadening. The natural line width of a specific LAM vibration was determined to be 1.45 cm^{-1} by Glotin and Mandelkern for a chain length approximately 400 Å long (80). This is

lower than the value of 2.5 cm^{-1} previously reported by Snyder (14).

In order to obtain the true straight chain segment length distribution, first the background intensity from Rayleigh scattering must be removed and then the band shape must be corrected to give the length distribution. The corrections were shown by Snyder and Scherer (13) to have the following form:

$$I_\nu^{obs} = A \frac{(\nu_o - \nu)^4}{\nu B_\nu} S(\nu) \qquad (2.4)$$

where I_ν^{obs} is the observed intensity at frequency ν, A is a constant containing sample geometry, ν is the Raman frequency and ν_o is the incident laser frequency. The scattering efficiency is given by $(\nu_o - \nu)^4$, and is taken as a constant over the frequency range of interest. $S(\nu)$ is the Raman scattering activity of the chains in which the LAM occurs at frequency ν. The term $\nu \cdot B_\nu$ results from considering the relative population of the low lying vibrational states due to thermal energy (65). B_ν is defined as

$$B_\nu = 1 - \exp(-hc\nu/k_B T) \qquad (2.5)$$

where h is Planck's constant, c is the speed of light, k_B is the Boltzmann constant, and T is the sample temperature. The value of $k_B T/hc$ is 200 cm^{-1} at room temperature. Equation 2.4 can be rearranged to give

$$I_\nu^{\alpha} = A' \nu B_\nu I_\nu^{obs} \qquad 2.6$$

where I_ν^{α} is the frequency-temperature corrected intensity and is pro-

portional to the scattering activity. The scattering activity is inversely proportional to the number of CH_2 groups in the straight chain segment (71) and consequently is also inversely proportional to the length, ℓ, of the straight chain segment. Since Equation 2.1 shows that ℓ is inversely proportional to ν, $S(\nu)$ must be proportional to ν. This allows the number of chains with LAM at frequency ν (expressed in terms of the straight chain length distribution $F(\ell)$) to be determined from I_ν^{obs} and I_ν^{α} as shown in equations 2.7 and 2.8 respectively.

$$F(\ell) = A''\nu^2 B_\nu I_\nu^{obs} \qquad (2.7)$$

$$F(\ell) = A''\nu I_\nu^{\alpha} \qquad (2.8)$$

Equations 2.6, 2.7, and 2.8 are important since they allow the distribution of LAM frequencies to be transformed into distributions of straight chain segment lengths.

Snyder and Scherer also show that

$$I_T \simeq K' \cdot L_T \qquad (2.9)$$

That is, the total integrated observed LAM intensity, I_T, is proportional to the total length of trans segments in the sample, L_T. Independently, Strobl and Eckel have derived the conservation of the integrated intensity by a classical treatment of polarizability change during the LAM vibration (68). In a study of melt quenched mixtures of polyethylene 1000 and 2000 fractions, Shu et al. have

experimentally confirmed that the integrated intensity of the LAM was conserved (64). Because all-trans segments of reasonable length are usually in the crystalline regions, the integrated LAM intensity should be proportional to the crystallinity.

The length distribution, $F(\ell)$, can be used to describe one aspect of sample morphology and should be preferred over I_ν^{obs} for presentation of the data. Because $F(\ell)$ gives the number of chains at each length ℓ, it is a number average distribution of segment lengths, i.e. a short segment counts as much as a long segment. However, the longer segments are given more consideration than the shorter ones in the weight or volume distribution.

$$P_n(\ell) = n(\ell) \,/\, \sum_{\ell} n(\ell) \qquad 2.10$$

$$P_n(\ell) \propto F(\ell)$$

$$P_w(\ell) = w(\ell) \,/\, \sum_{\ell} w(\ell)$$

$$P_w(\ell) = n(\ell)\cdot\ell \,/\, \sum_{\ell} [n(\ell)\cdot\ell] \qquad 2.11$$

$$P_w(\ell) \propto F(\ell)\cdot\ell$$

The term $n(\ell)$ is the number of chains of length ℓ, $w(\ell)$ is the weight of chains with length ℓ, $P_n(\ell)$ is the probability that a given chain is of length ℓ, and $P_w(\ell)$ is the probability that an infinitesimal volume element would be occupied by part of a chain with length ℓ.

$F(\ell_i)$ is multiplied by ℓ_i to go from the number distribution, $P_n(\ell)$, to the weight distribution, $P_w(\ell)$. This has the same result

as dividing $F(\ell)$ by ν_i since $\ell_i=a/\nu_i$ and equation 2.8 shows that $I_\nu^\alpha \propto F(\ell)/\nu$. Therefore, I_ν^α is proportional to the weight distribution of chain lengths.

Subtraction of the baseline

As mentioned earlier, to apply the corrections to the intensity, the background contribution must first be subtracted. The low frequency baseline intensity is usually attributed to stray light at the incident laser frequency which reaches the detector. If this were simply the case, then the shape of the baseline at low frequency would be independent of the sample and could be measured once and scaled to fit any sample spectra. However, the shape of the low frequency baseline is known to depend both on the sample geometry and sample temperature (81-83).

The shape of the stray light curve is known in the region a few wavenumbers about $\Delta\nu=0$ and the shape of the Brillouin scattering contribution to the "Rayleigh line" can also be measured in this region (84). However, these contributions cannot be extrapolated reliably enough over the regon $\Delta\nu=2$ to 100 cm^{-1} to be of much use in background subtraction. Part of the problem is that the LAM intensity is at least 10^{14} times smaller than the Rayleigh scattering and any error in extrapolating the background overwhelms the LAM intensity (85).

The approaches taken to overcome this problem include fitting the baseline either mathematically or visually. Mathematical fitting often includes fitting the LAM peaks; but there is no reason to

expect the LAM peaks to fit any prescribed curve - polynomial, gaussian, or Lorentzian, since the shape is determined by the distribution of straight chain lengths in the sample. Most fitting approaches often make assumptions about the baseline away from the center of the LAM peak. One example is to assume the LAM intensity approaches zero at the wings of its peak. This may be acceptable for n-alkanes and polyethylene single crystals but is less acceptable for more disordered materials. Another approach is to measure the baseline for one sample and to assume that it will apply to another sample. A method that applies to transparent, highly oriented samples relies on the fact that no LAM intensity is expected in its VH spectrum, only in VV (13). Then the scaled VH spectrum can be subtracted from the VV spectrum to yield the expected LAM band. This approach appears attractive except for two problems. One, should the VV and VH background scattering exhibit the same shape in a highly anisotropic sample? Brilloun scattering results suggest that this is not the case (84). And two, if crystallite disorientation exists, it may depend on the segment lengths. The latter problem might arise during annealing of extruded samples where smaller crystals might disorient more readily than long ones. In any case, the results are only as good as the assumptions involving the subtractions.

One solution is to present only raw, unsubtracted spectra. This data is reliable but the reader will often mentally subtract a background of his/her choice to interpret the data. The next step is to state the assumptions and methods used in the background subtrac-

tions. This leaves the reader with more useful data but fails to address the uncertainties involved. The best solution would be to present the raw spectra, clearly show the backgrounds used, and to estimate the error involved in the subtractions. Usually part of the distribution has a shape that is maintained regardless of most background choices. Data at the center of the LAM peak is relatively unaffected by small changes in the baseline, while data at the peak wings is more sensitive to baseline shifts. Because of the approximate ν^3 factor involved during conversion of intensity to chain length distributions, the error in estimating the amount of short segments is much greater than for the long segments. Additionally, at the low frequency side of the LAM peak, the error may also be significant because the baseline intensity is larger and changes rapidly.

Even with experimental improvements such as holographic gratings and iodine-vapor cells to reduce the background intensity, it is still difficult to observe LAM clearly in some samples. Rabolt and Wang used a Fabry-Perot interferometer to observe the LAM in a sample of high-pressure crystallized polyethylene (86,87). The LAM was observed in the region 0.25 to 0.75 cm^{-1} with corresponding segment lengths of 5000 to 8000 Å. This may well be the lowest frequency LAM reported, but similar background uncertainties as mentioned earlier remain in the interpretation of this data.

The effects of conformational defects

The effects of conformational defects on the LAM have been mentioned in many papers (15,16,68,69,87-90). In two studies of crystal

melting, the change in LAM with increasing temperature has been analyzed (68,91). In both cases, the intensity of the LAM peak decreased with increasing temperature. What is generally believed is that the formation of a defect in the all-trans segment decouples the vibration of the two trans segments on either side of the defect and both segments vibrate at higher frequencies characteristic of their shorter lengths (69,88). For a random spatial distribution of defects in the crystal, the new bands will be broadly distributed on the high frequency side of the LAM (68). Normal coordinate analysis of chains containing defects by Chang and Krimm has confirmed that the two remaining trans segments vibrate at frequencies within 10% of that of an unperturbed sequence of equal length (16). This and other normal coordinate analysis of defects (15,90,92) show some change from the strictly longitudinal nature of LAM to include some transverse motion. This is generally considered to be due to coupling of LAM-like modes with other chain vibrations (87) and with normal modes of the defects (79,90). The following section presents an experiment which confirms the theoretical predictions of the effects of conformational defects on LAM.

Raman Analysis of Melt-Quenched Polyethylene

The length distribution of straight chains inferred from LAM measurements has been used to follow crystallization (86,93), melting (91), annealing (69), and drawing (88,94). To obtain accurate

interpretation of the LAM results, the effects of chain folds and conformational defects on the LAM vibration must be well understood. Experimental and theoretical studies have explained the effects of the lamellar surfaces and how they perturb the LAM vibration in n-alkanes. As stated previously, experimental evidence has shown that these effects are insignificant and may be ignored in studies of bulk crystallized polyethylene (80).

N-paraffins and narrow, low MW polyethylene fractions crystallize with fully extended chains when slow cooled. Quenching these samples from the melt will trap crystal defects which can be removed by annealing. In these samples, extensive crystal thickening is not expected during annealing because most chains are already extended. Normal coordinate analyses have shown that placing a conformational defect into an all-trans segment disrupts the LAM vibration and shifts the intensity to higher frequencies. In the case of random placement of the defects, the shifted intensity adds a continuous contribution to the high frequency background, causing a decrease in intensity of the main LAM peak. The experimental details of the study undertaken to confirm this are described here.

The Raman spectra were obtained with a Jobin-Yvon HG.2S Raman Spectrometer using slit settings of 4 by 100 μm giving a 1.5 cm^{-1} linewidth. The slit settings were chosen to maximize the rejection of the Rayleigh line while still maintaining sufficient throughput for good signal to noise ratios. The sample was illuminated with 200 mW of 5145 Å laser light from a Spectra Physics

model 165-08 argon ion laser. The plasma lines from the laser at approximately 65 and 78 Δcm^{-1} serve as a frequency reference for the spectra. The spectral signal was processed by photon counting and recorded on an analog chart recorder.

Polyethylene (PE) 1000 (Mn=980, Mw/Mn=1.1) from Polysciences, Inc. was placed in a melting point capillary and sealed. It was melted at 150°C for 20 minutes in an oil bath and quenched into liquid nitrogen. The capillary containing the sample was quickly transferred to the cold cell of the Raman spectrometer. The spectrum was taken at 130°K over the region 8 to 150 cm^{-1}. The sample was allowed to warm to room temperature for 15 minutes to anneal the sample, then cooled back down to 150°K and another spectrum was recorded.

Since both spectra were taken at similar temperatures, it is not necessary to correct the spectra for temperature effects when comparing them. In Figure 3 both spectra are shown; the features include the LAM-1 peak from 20 to 60 cm^{-1}, Argon plasma lines at 65 and 78 cm^{-1}, and the polyethylene lattice mode centered at 130 cm^{-1}.

The calculated frequency of fully extended 1000 MW polyethylene is 32 cm^{-1} and the observed peak at about 35 cm^{-1} confirms that even in quenched PE 1000 the chains are essentially fully extended (Figure 3a). A dotted line corresponding to the LAM of the annealed sample has been added to the quenched spectra. The region of intensity between the dotted line and the quenched spectra has been shifted to higher frequencies by conformational defects in the crystals. In the annealed spectra, Figure 3b, the defects have been removed and the

Figure 3. Low frequency Raman spectra of polyethylene 1000. Band-pass 1.5 cm^{-1}. Laser power, 200 mW at 5145 Å.
a. quenched in LN_2, measurement temperature of 130K
b. room temperature annealed, measurement temperature of 150K

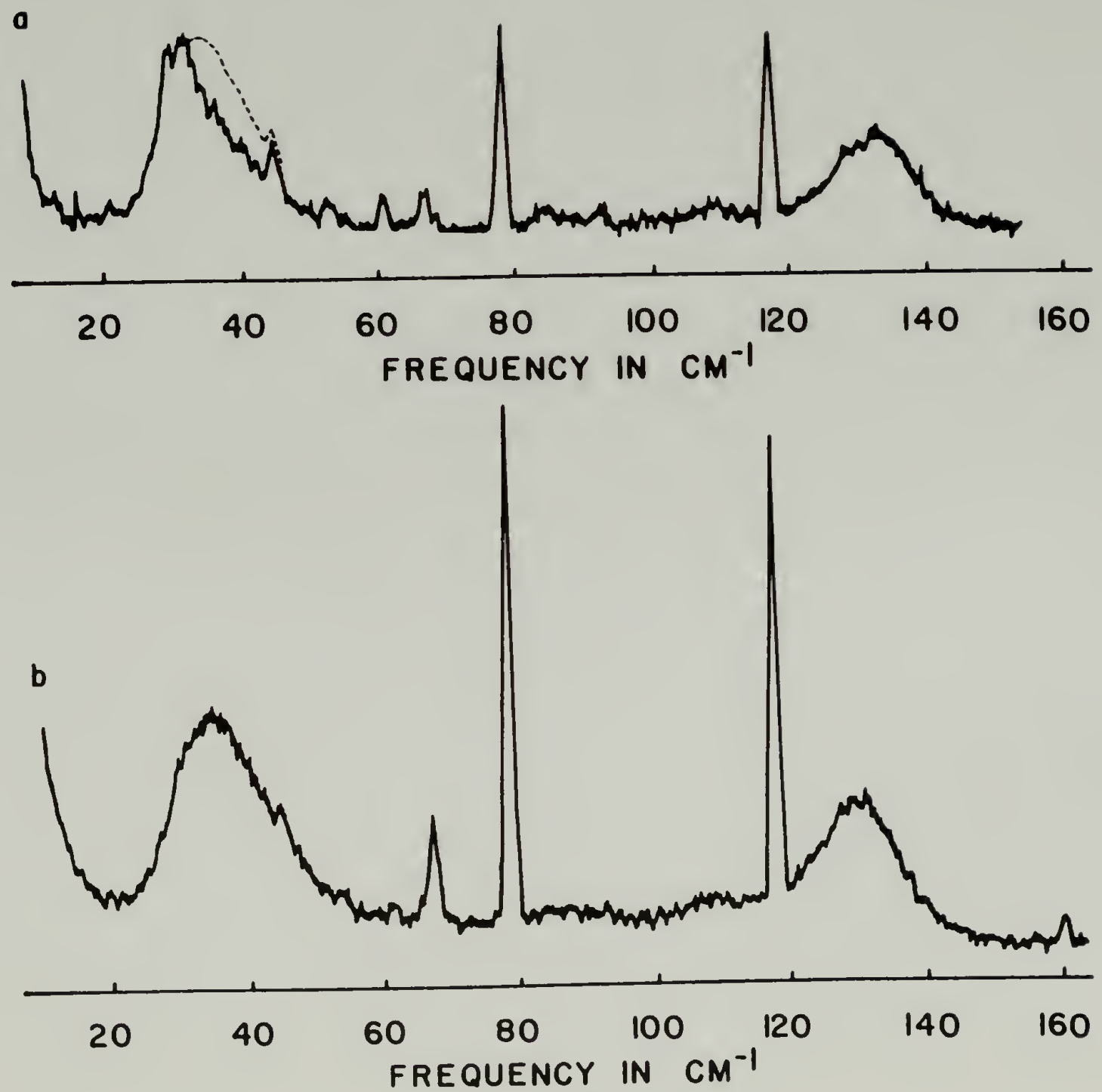
a
20
40
60
80
100
120
140
160
FREQUENCY IN CM⁻¹
b
20
40
60
80
100
120
140
160
FREQUENCY IN CM⁻¹

Figure 3

intensity is restored.

These results demonstrate that the normal coordinate analyses are correct in predicting higher frequencies for segments containing defects and that LAM is sufficiently well understood to be used for the measurement of chain length distributions of samples that have more interesting and complex morphologies. The LAM results obtained for a sample with a fibrillar morphology are given in the next section. The LAM of drawn PE is much broader than that of the PE 1000 sample and is similar to that obtained for solid state extruded polyethylene.

Raman Analysis of Drawn Polyethylene

In this section, a LAM experiment which follows changes in crystal stem lengths caused by the cold drawing of polyethylene is presented. The information obtained can be combined with other measures of the sample microstructure to gain a better understanding of the variables affecting the drawing process. Under optimal conditions, the quantitative distribution of crystal stem lengths can be obtained. But this requires reliable subtraction of background intensity and the correction of frequency and temperature effects. To facilitate this, the spectrometer was interfaced to a microcomputer data collection system described later in this chapter.

The details of sample preparation are given in reference 95. The LAM spectrum of polyethylene drawn 9.0X is shown in Figure 4c. The

Figure 4. LAM spectra of drawn polyethylene (9x)
a. annealed at 120°C at constant length.
b. annealed at 120°C with ends free.
c. cold drawn sample.

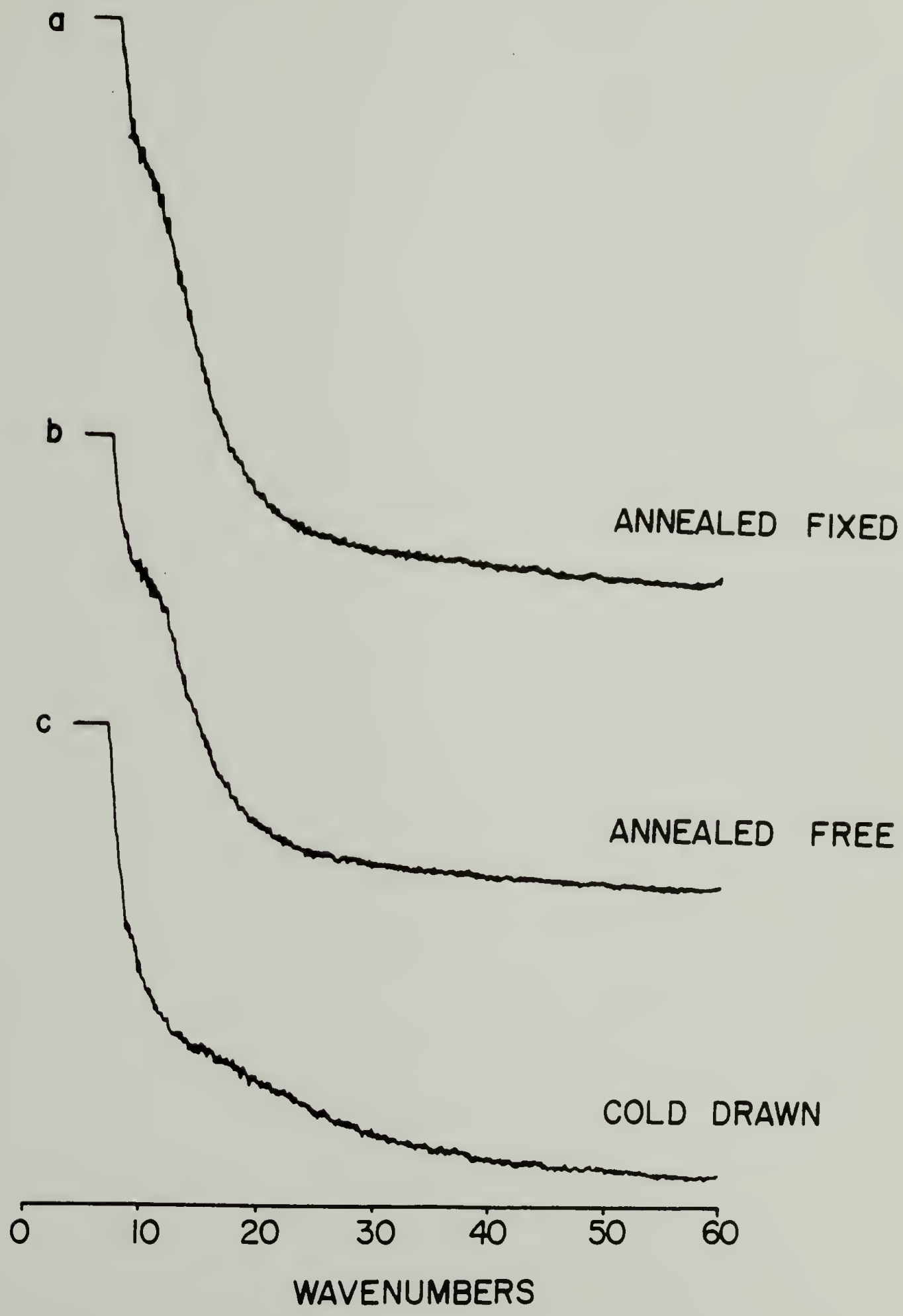
a
b
c
ANNEALED FIXED
ANNEALED FREE
COLD DRAWN
0
10
20
30
40
50
60
WAVENUMBERS

Figure 4

most obvious spectral feature is the very broad LAM peak which extends from 10 to 60 cm^{-1}. The lack of a distinct LAM peak shows that there is not a favored straight chain length and the breadth of LAM reflects the great degree of structural disorder in the drawn sample. Clearly, there are many defects in the crystals. Unfortunately, the broad nature of the distribution and the fact that the frequencies extend below 10 cm^{-1} tend to make any choice of baseline arbitrary and the subtracted data unreliable. However, some changes can be seen when the sample is annealed at 120°C with its ends fixed to prevent shrinkage (Figure 4a). During annealing, some of the defects move out of the crystals and the frequency distribution begins to show a peak at 10 cm^{-1} corresponding to a chain length of 300 Å. Annealing with the ends free seems to allow more reorganization and the resulting peak at 10 cm^{-1} is stronger, as seen in Figure 4b.

These measurements give qualitative information on the structure and effect of annealing in these drawn samples. The analysis required to give quantitative data is hindered by the uncertainty in the background subtraction. Attempts were made to use the iodine vapor filter technique to attenuate the scattered laser light entering the monochrometer (96). By attenuating the laser line, less stray light will be observed in the low frequency region of the spectrum. The design of the sampling chamber of the instrument limits the iodine cell length to less than 5 cm. The short path length limits the attenuation achievable and the shape of the cell makes it difficult to control the temperature and temperature gradients of the

cell surfaces. As a result, the iodine vapor tends to sublime on the optical faces of the cell which leads to low light transmission and reduces the concentration of vapor within the cell. The amount of improvement in the baseline is seen by comparing Figures 5a and 5b. The iodine cell reduces the baseline slope on the low frequency side of the LAM peak but still does not allow for reliable baseline subtraction. Similar difficulties exist in SAXS analysis of these samples. One dimensional SAXS intensity measurements will yield only an approximation of the long period because of the highly oriented nature of these samples (97,98). Quantitative orientation and crystallite dimensions must be obtained with pinhole geometry x-ray sources and a two dimensional detection system (98,99). However, such facilities only exist in a few laboratories (100).

Raman Analysis of Solid State Extruded Polyethylene

In this section, the microstructure of solid state extruded polyethylene samples with extrusion draw ratios of 12, 24, and 36X are examined. By starting with samples that have been previously characterized, the structural information obtained from LAM measurements can be directly compared to results of other techniques.

The detailed preparation methods and some properties of these solid state extruded samples are given in references 66 and 7. Alathon 7050 high density polyethylene (Mw=59,000, Mw/Mn=3) was crystallized into billets, then solid state extruded at 120°C as

Figure 5. Raman spectra obtained for solid state extruded polyethylene. Band-pass 1.5 cm^{-1}. Laser power, 200 mW at 5145 Å.
a. with iodine gas cell
b. without iodine gas cell

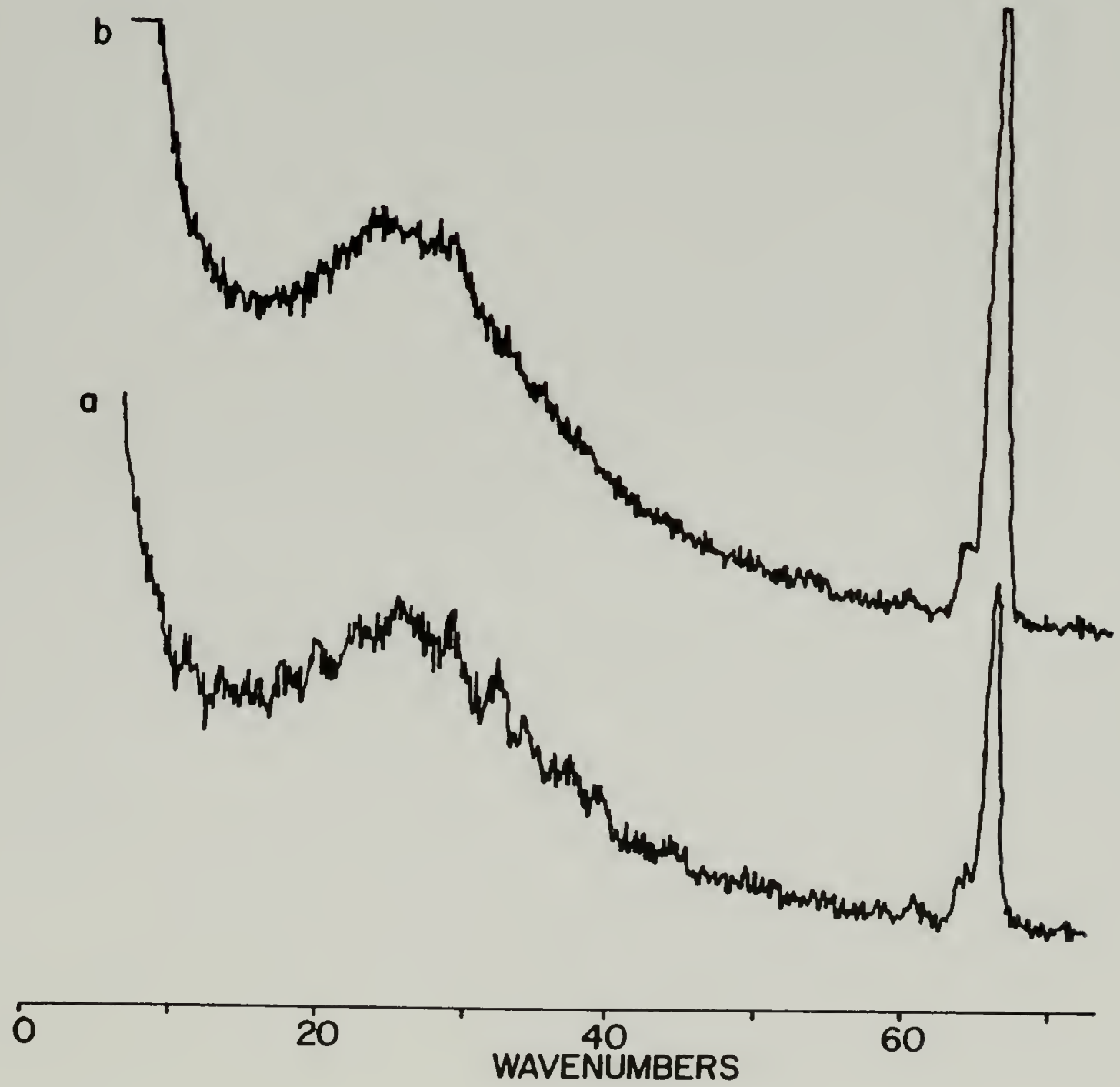

Figure 5

described in reference 66. The appearance of the samples ranged from translucent (12x) to very clear (36x). The LAM spectra were obtained using the microcomputer controlled Raman instrument described in the next section. Data points were taken every 0.1 cm^{-1} from 4 to 85 cm^{-1}. The data were transferred to a Nicolet FT-IR computer system and then analyzed. The sampling geometry used during collection of the spectra is shown in Figure 6.

The as-measured spectra are shown in Figure 7. The intensities have been scaled to the 1295 cm^{-1} peak height. It is evident that the straight chain segment distribution is narrower than in the drawn sample and that the peak shows some dependence on draw ratio. A combination of a sloping straight line, a gaussian and a Lorentzian peak centered at 0 cm^{-1} were fitted to remove the background from the LAM spectra. The background was chosen to fit the as obtained LAM spectrum in the 50 to 80 cm^{-1} region and in the 4 to 6 cm^{-1} region. No LAM peak is visible in the spectrum of the 36x sample collected with VH polarization because of its clarity and high orientation. Therefore, an estimate of the reliability and error of the background fit can be made by comparing the fitted function with the 36X VH spectra, as shown in Figure 8a. For the other spectra, the halfwidth and gaussian/lorenzian ratio were held constant while the peak intensity and sloping line were varied for "best fit" as shown for the 36X VV spectrum (Figure 8b). From Figures 8a and 8b, it can be seen that the fit is poorest at low frequencies. Because the baseline is so strong and rapidly changing in this region, no reliable estimate can

Figure 6. Scattering geometry to obtain polarized Raman spectra.

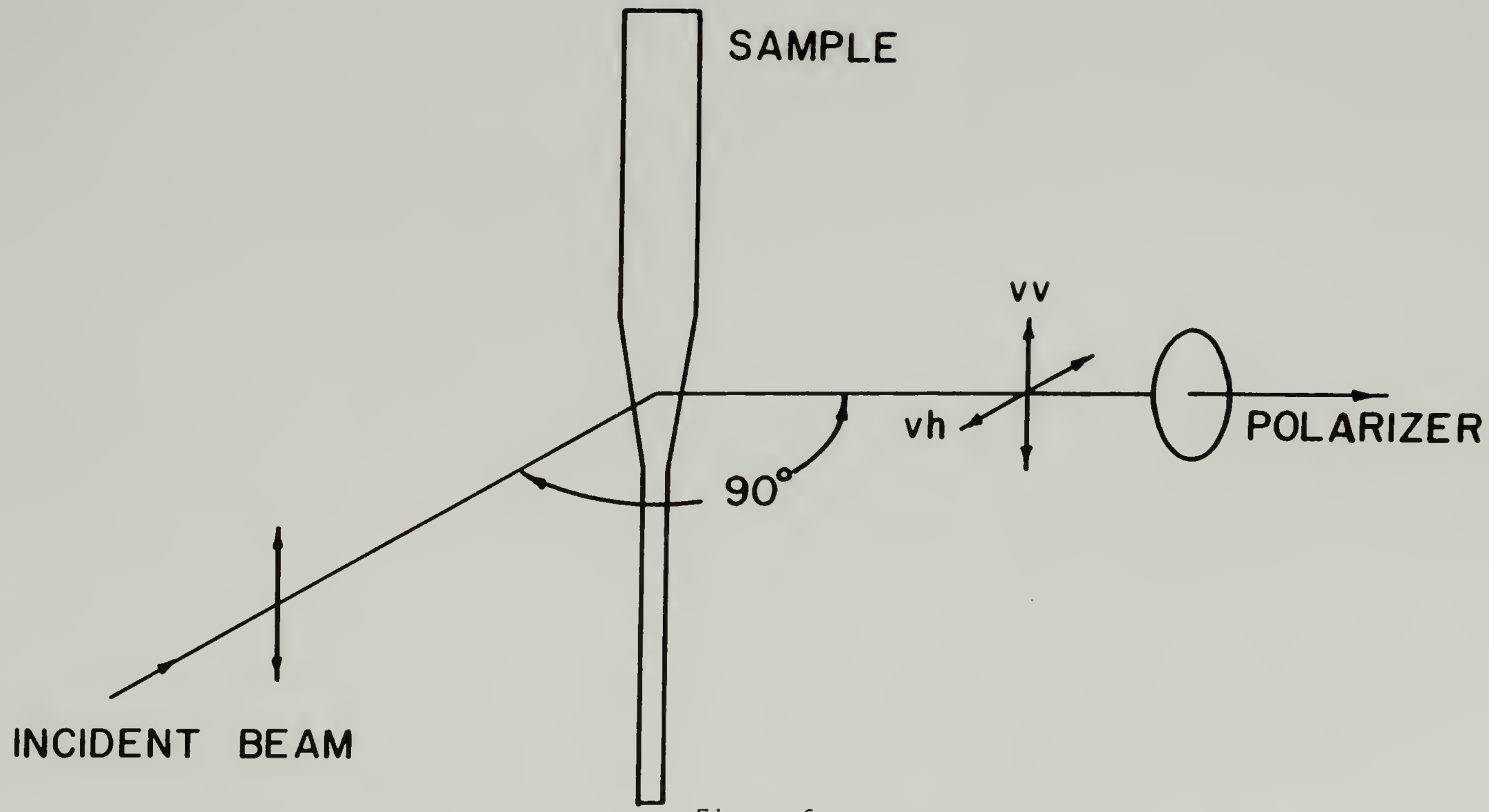

Figure 6

Figure 7. Raman spectra obtained for three solid state extruded polyethylene samples.
a. 12x draw ratio
b. 24x draw ratio
c. 36x draw ratio

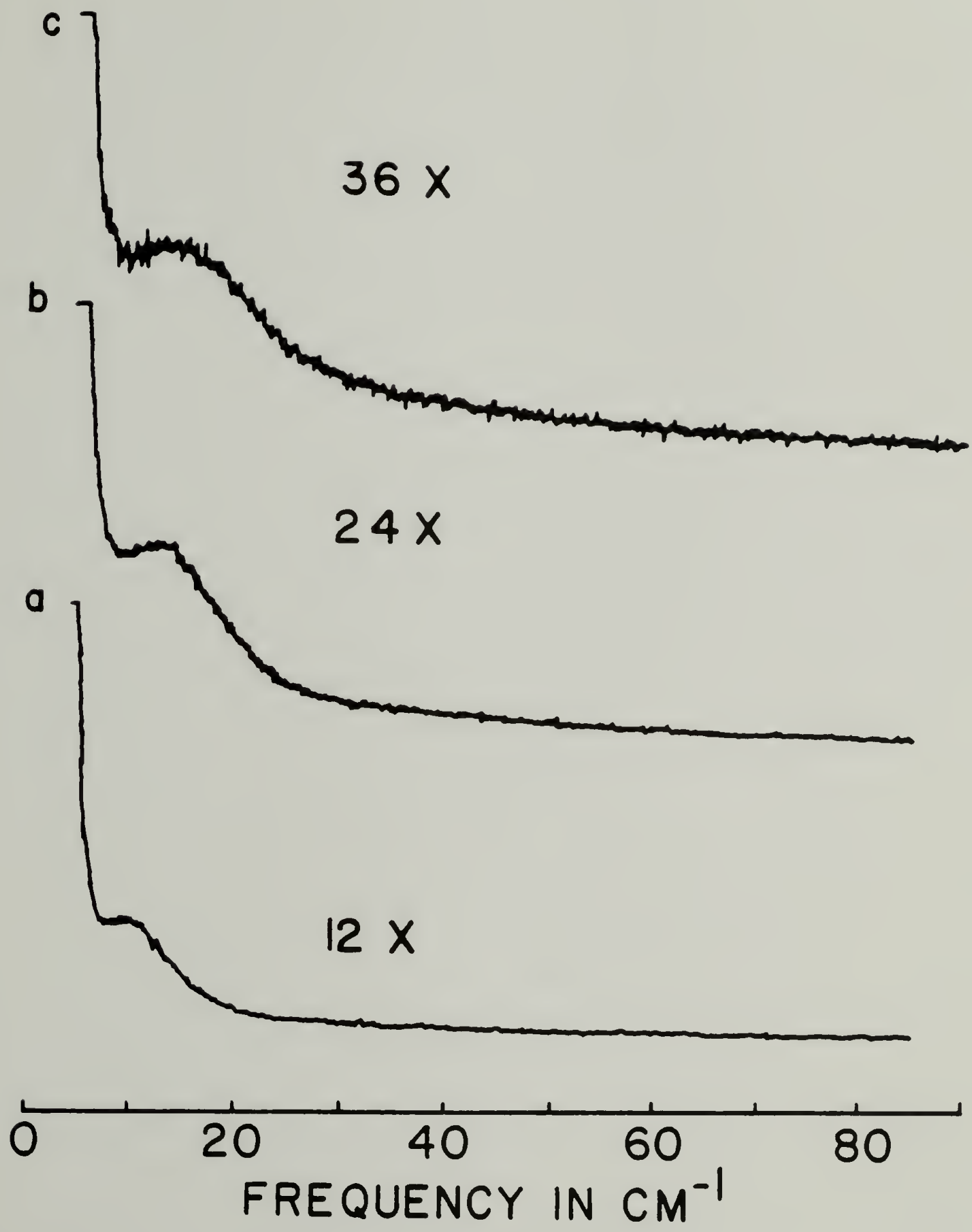

Figure 7

Figure 8. Fitted baselines for the Raman spectra obtained for polyethylene extrudates.
a. 36x VH geometry
b. 36x VV geometry

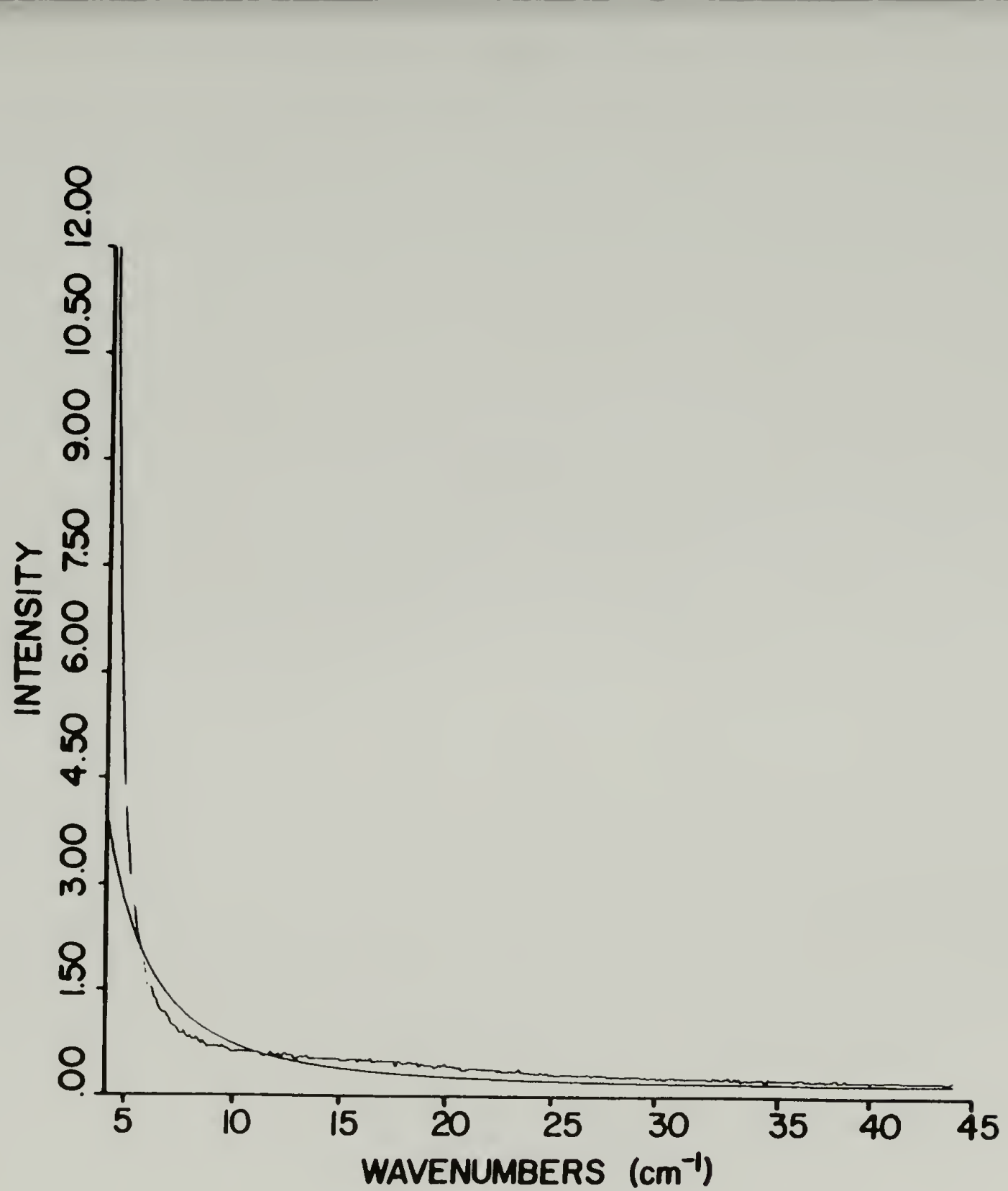
INTENSITY
.00
1.50
3.00
4.50
6.00
7.50
9.00
10.50
12.00
5
10
15
20
25
30
35
40
45
WAVENUMBERS (cm⁻¹)

Figure 8a

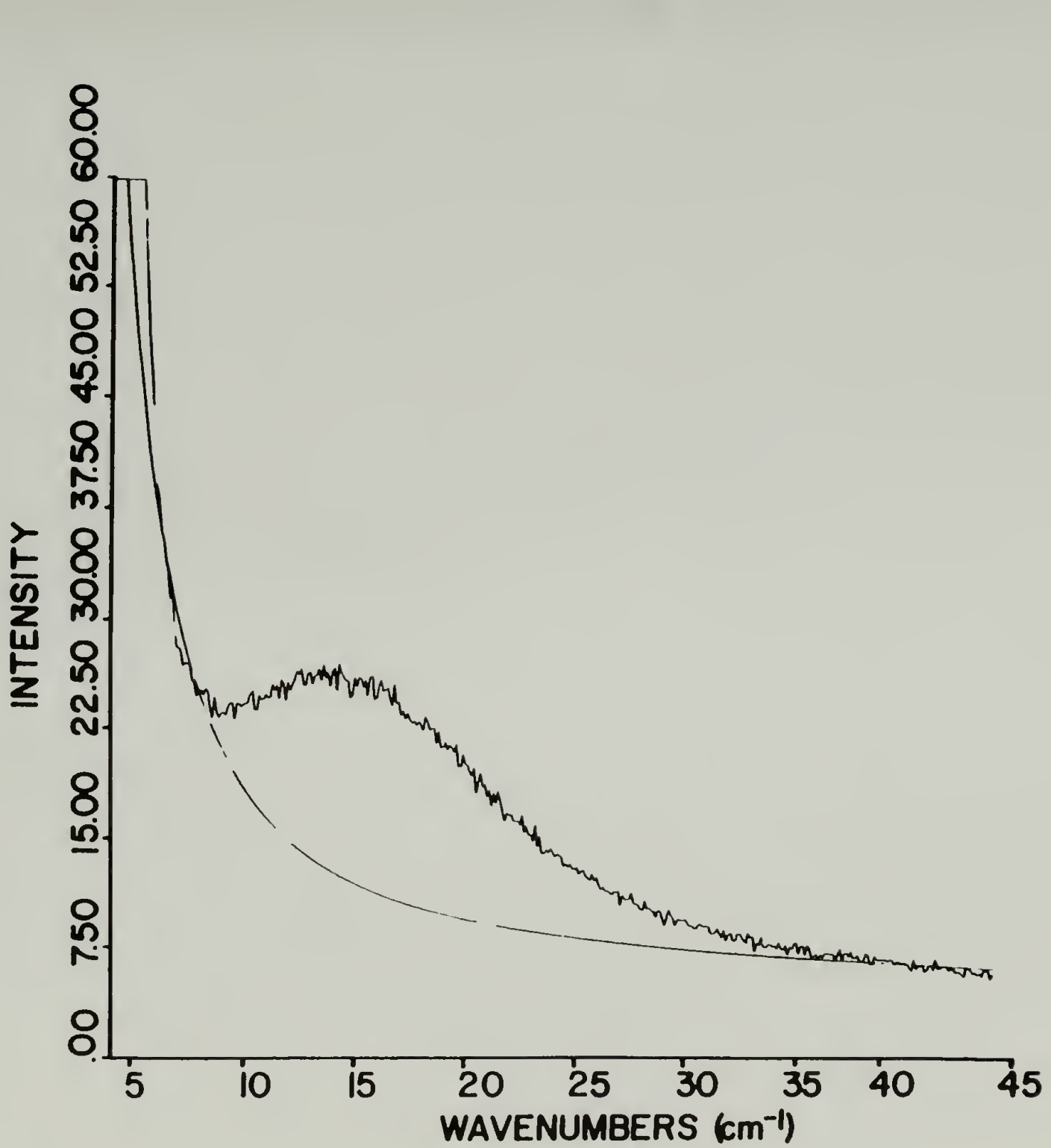
INTENSITY
.00
7.50
15.00
22.50
30.00
37.50
45.00
52.50
60.00
5
10
15
20
25
30
35
40
45
WAVENUMBERS (cm⁻¹)

Figure 8b

be provided below 5-6 cm^{-1}. At high frequencies, the uncertainty concerning the height and slope of the straight line portion of the baseline leads to large estimated errors. The data in the center region is fairly reliable as far as background subtraction is concerned.

In Figure 9, the LAM band of the 36X draw ratio sample is plotted in three forms: a) as I_ν^{obs}, the raw Raman spectrum with the background intensity subtracted, 2) as I_ν^{α}, the frequency-temperature corrected form which is also the weight distribution of straight chain segment lengths, and 3) as $F(\ell)$, the number distribution of straight chain segment lengths. Comparison of the three forms shows that the peak becomes broader and the peak maximum shifts to higher frequencies (shorter segment lengths) going from I_ν^{obs} to I_ν^{α} and $F(\ell)$.

LAM data for the three samples of draw ratio 12, 24, and 36X are presented in the form of I_ν^{obs} in Figure 10 and as I_ν^{α} and $F(\ell)$ in Figures 11 and 12, respectively. The draw ratio dependence of LAM width and the peak maximum becomes evident once the background has been subtracted (Figure 10). The LAM distributions are broadest when plotted as the number average distribution (Figure 12). The peak maximum of $F(\ell)$ (the most probable straight chain length) for each sample is listed in Table 1 along with results from SAXS, WAXS, and DF-EM measurements (7,66).

Discussion of results

The LAM data will be compared to results obtained by other techniques for these samples (7,66). The four techniques - LAM, SAXS,

Figure 9. Spectral correction of the LAM spectrum of the 36x polyethylene sample
a. $F(\ell)$
b. frequency temperature corrected, (I_{ν}^{α})
c. as subtracted

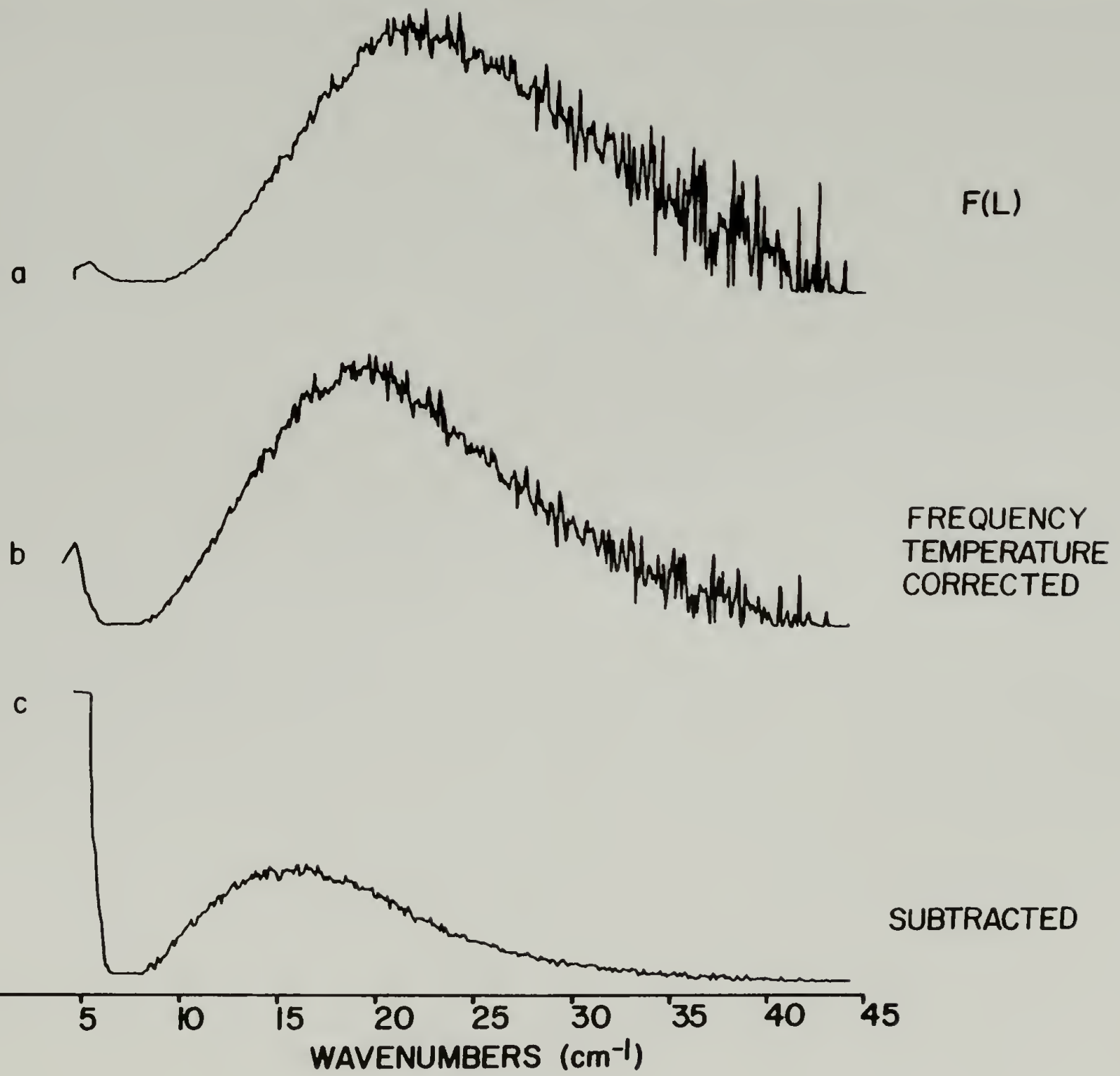
a
F(L)
b
FREQUENCY
TEMPERATURE
CORRECTED
c
SUBTRACTED
0
5
10
15
20
25
30
35
40
45
WAVENUMBERS (cm⁻¹)

Figure 9

Figure 10. Background corrected LAM peaks for the 12, 24, and 36X samples
a. draw ratio of 12
b. draw ratio of 24
c. draw ratio of 36

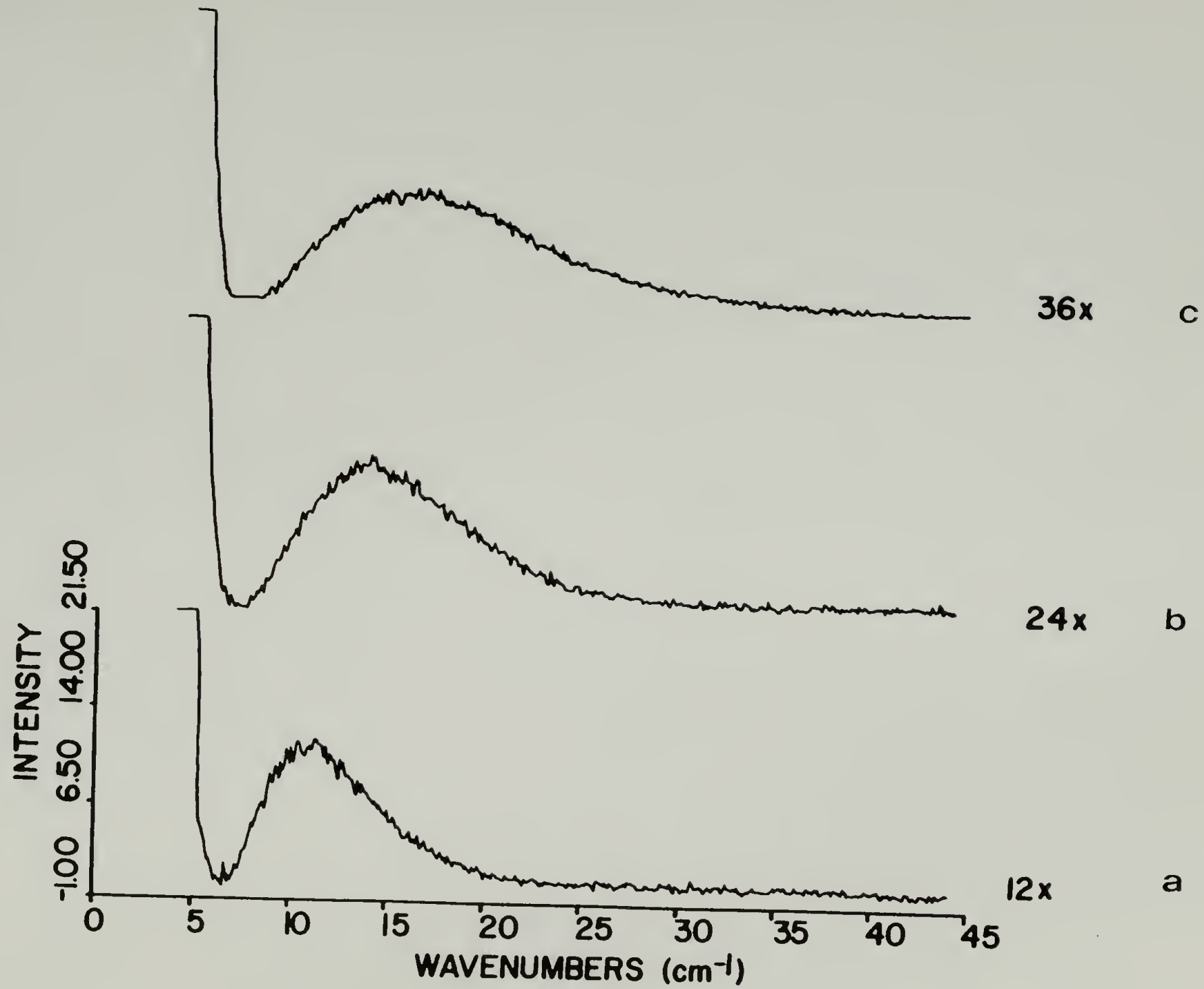
36x
c
24x
b
12x
a
INTENSITY
-1.00
6.50
14.00
21.50
0
5
10
15
20
25
30
35
40
45
WAVENUMBERS (cm⁻¹)

Figure 10

Figure 11. Frequency temperature corrected data (I_{ν}^{α}) for the 12, 24, 36X samples.
a. draw ratio of 12
b. draw ratio of 24
c. draw ratio of 36

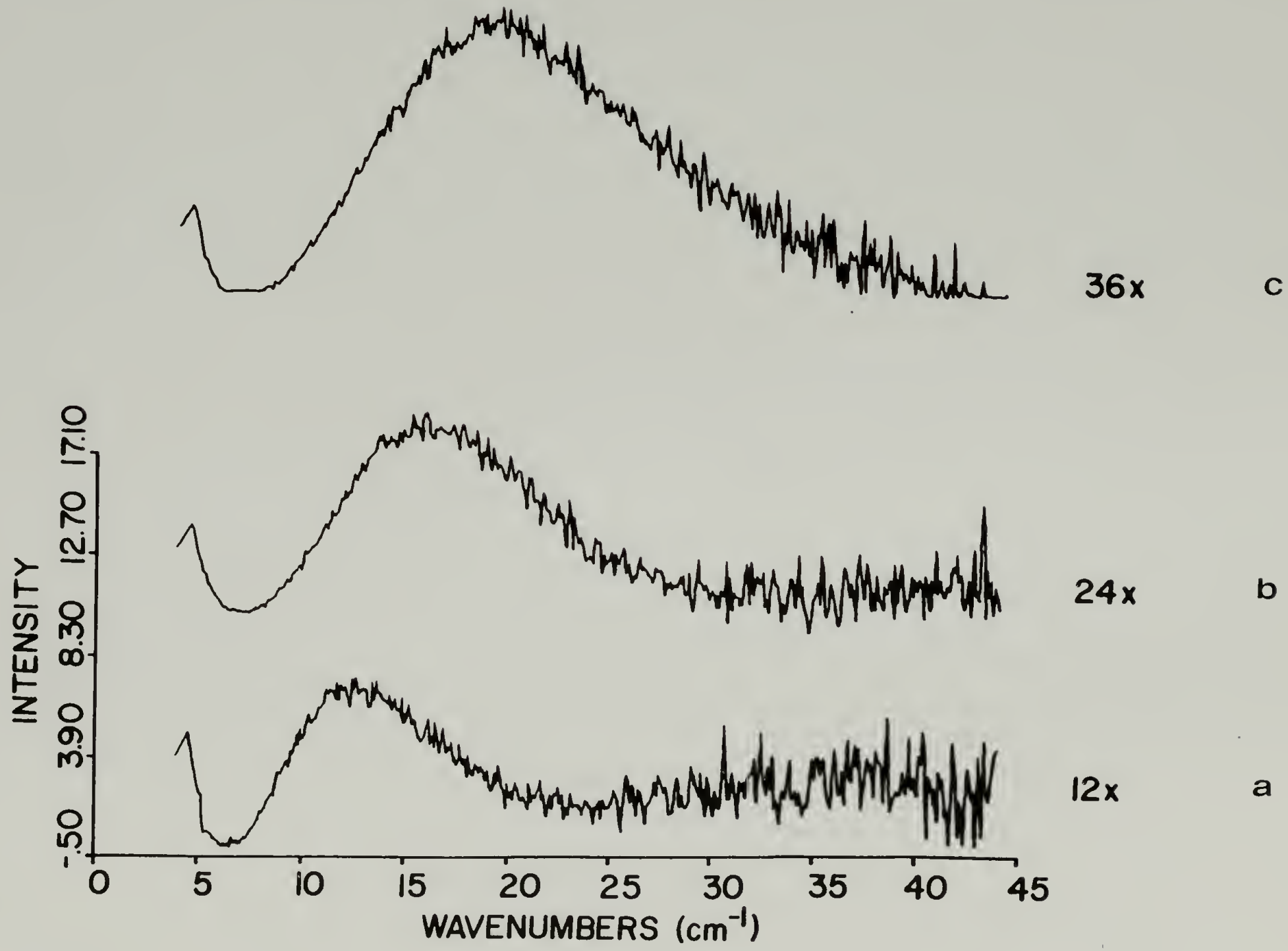
36x
c
24x
b
12x
a
INTENSITY
-.50
3.90
8.30
12.70
17.10
0
5
10
15
20
25
30
35
40
45
WAVENUMBERS (cm⁻¹)

Figure 11

Figure 12. F(ℓ) length distribution for the 12, 24, 36x samples
a. draw ratio of 12
b. draw ratio of 24
c. draw ratio of 36

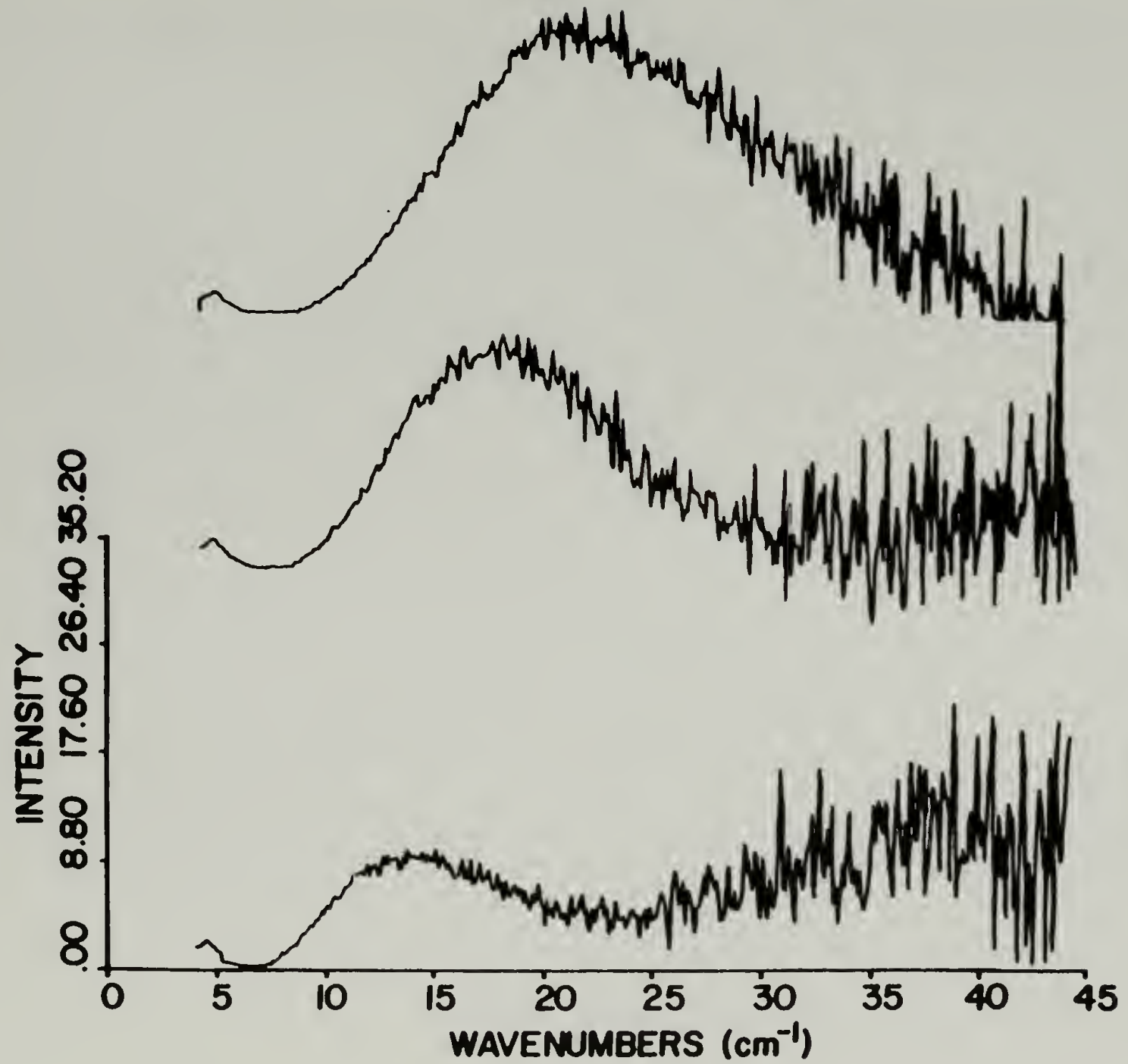
INTENSITY
.00
8.80
17.60
26.40
35.20
0
5
10
15
20
25
30
35
40
45
WAVENUMBERS (cm⁻¹)
36x
c
24x
b
12x
a

Figure 12

TABLE 1

Comparison of Measurements of Crystal Size

Draw Ratio EDR	LAM† ℓ_s	DF-EM* ℓ_c	WAXS-002** ℓ_c	SAXS** Long Period L	WAXS** Crystal Density ρ_c g/cm^3
12	230	270	300	349	.997
24	175	270	290	266	.995
36	150	390	400	237	.990

all lengths are in Angstroms

†The most probable straight chain segment length determined from the peak in $F(\ell)$.

*From reference 66.

**From reference 7.

WAXS, and DF-EM - measure different aspects of the sample morphology and any proposed structural model must incorporate the results obtained from all of these techniques. The LAM results show that the stem length distribution becomes broader and shifts to shorter lengths at higher draw ratios. These results are contrary to the expected increase in sample perfection at higher draw ratios (3). Several possible structures may be proposed to interpret the combined results.

One interpretation is that the amount of defects in the crystals increases for samples deformed to higher draw ratios. The presence of defects in the crystals would shift the LAM stem length distribution to shorter lengths and explain the decrease in crystalline density as measured by WAXS (Table 1). The SAXS long period decreases with increasing DR which is also consistent with the LAM results. In contrast, both DF-EM and WAXS-002 integral breadth measurements show an increase in the average crystal thickness with DR. However, neither of these two techniques is very sensitive to the presence of conformational defects in the crystals.

An alternate explanation is a bimodal distribution of crystal thickness. The model of Gibson et al. (Figure 2) has thin periodically spaced crystals that would give rise to the SAXS and LAM results while the thicker non-periodic intercrystalline bridges would account for the WAXS-002 and DF-EM results. The LAM of these longer crystals may be too close to the Rayleigh line to be resolved in the Raman spectra obtained in the present study. The broad length distribution and non-periodic nature of the long crystals result in a lack of

distinct SAXS or Raman peaks. However, the well ordered crystalline regions of Gibson's model are inconsistent with the observed decrease in crystal density and the broadness of the LAM.

Clark and Scott have proposed that, at higher draw ratios, the defects and amorphous chains are not segregated into regularly spaced regions, but are more evenly distributed throughout the crystals (12). This concept is certainly in agreement with the observed decrease in the SAXS invariant (7), the drop in crystal density, and the broadening of the LAM at higher draw ratios. However, from the description of their model it is difficult to interpret the changes in crystal length with draw ratio which are measured by WAXS 002 line broadening and DF-EM.

None of the models are totally consistent with all of the experimental data. Additionally, it seems that the models were developed to address only a few of the results and it is difficult to interpret them in terms of other techniques. For example, the model of Gibson et al. was developed to predict the modulus by incorporating data from the SAXS WAXS crystal size measurements. Their model does not explain how the crystal defects (observed by LAM and crystal density measurements) should be incorporated into the crystalline regions.

Based on the LAM results, we favor a model with a low degree of structural regularity. Essentially random placement of conformational defects within the crystals would be consistent with the breadth of the LAM distribution. It would be difficult to develop a detailed

model of the fibrillar morphology and the drawing or solid state extrusion processes based on just these few samples. However, by varying parameters such as the initial morphology of the polymer and processing conditions, different aspects of the fibrillar structure and deformation process may be revealed if each of the samples is sufficiently well characterized. Before closing this chapter, the opportunity presented by these well characterized 12, 24, and 36X draw ratio samples will be used to compare Raman chain segment orientation with the x-ray orientation measurements.

Raman Orientation Measurements

Polarized Raman measurements were used to measure the orientation of chain segments. For a transparent, uniaxially oriented polyethylene sample, the symmetric CH_2 stretching vibration (A_g symmetry) at 2850 cm^{-1} contributes only to the VV spectrum, while the CH_2 asymmetric stretching vibration of B_{1g} symmetry at 2885 cm^{-1} contributes only to the VH spectrum.

In samples with less than perfect orientation, the depolarized scattering of the asymmetric stretching mode contributes to the VV spectrum. Snyder and Scherer have described a model in which all chains are disoriented by the same angle from the fiber axis (88). From r, the ratio of peak heights of the 2885 and 2850 cm^{-1} modes in the VV spectrum, they have calculated θ, the average disorientation

angle of the polyethylene chain segments.

$$\theta = \cot^{-1}[(4.40 - 3.89r)/r]$$

In order to obtain accurate measurements, the polarization of the incident and scattered light must not be scrambled, which is indeed the case for the solid state extruded samples. The VV polarized spectra of the CH_2 stretching region are shown for the 12, 24, and 36X solid state extruded samples in Figure 13. The intensity of the 2885 cm^{-1} peak decreases rapidly with increasing draw ratio and is smaller than the noise level by 36x draw ratio. The average angles from Raman measurements are given in Table 2 along with WAXS (110) azimuthal half orientation angles from ref. 7. The values agree very well for 12 and 24 DR but the LAM gives a value of less than 2° for 36 DR compared with 5° for WAXS. At extremely high orientations, the WAXS instrumental broading becomes a significant limitation. However, Raman intensity ratios as small as 0.5% can be easily measured, allowing a determination of disorientations of less than 2 degrees. Since the x-ray measurements give the bulk orientation and the Raman orientation is determined from scattering near the surface, the disagreement between results may reflect a difference in orientation of the surface and core of the 36X solid state extruded sample.

Comparisons of Raman intensity between different samples require an internal standard to be used for normalization since the exact scattering volume cannot be determined. The peak height or area used

Figure 13. Polarized Raman spectra in the CH_2 stretching region of solid state extruded polyethylene samples of draw ratio 12, 24, and 36x.
a. draw ratio of 12
b. draw ratio of 24
c. draw ratio of 36

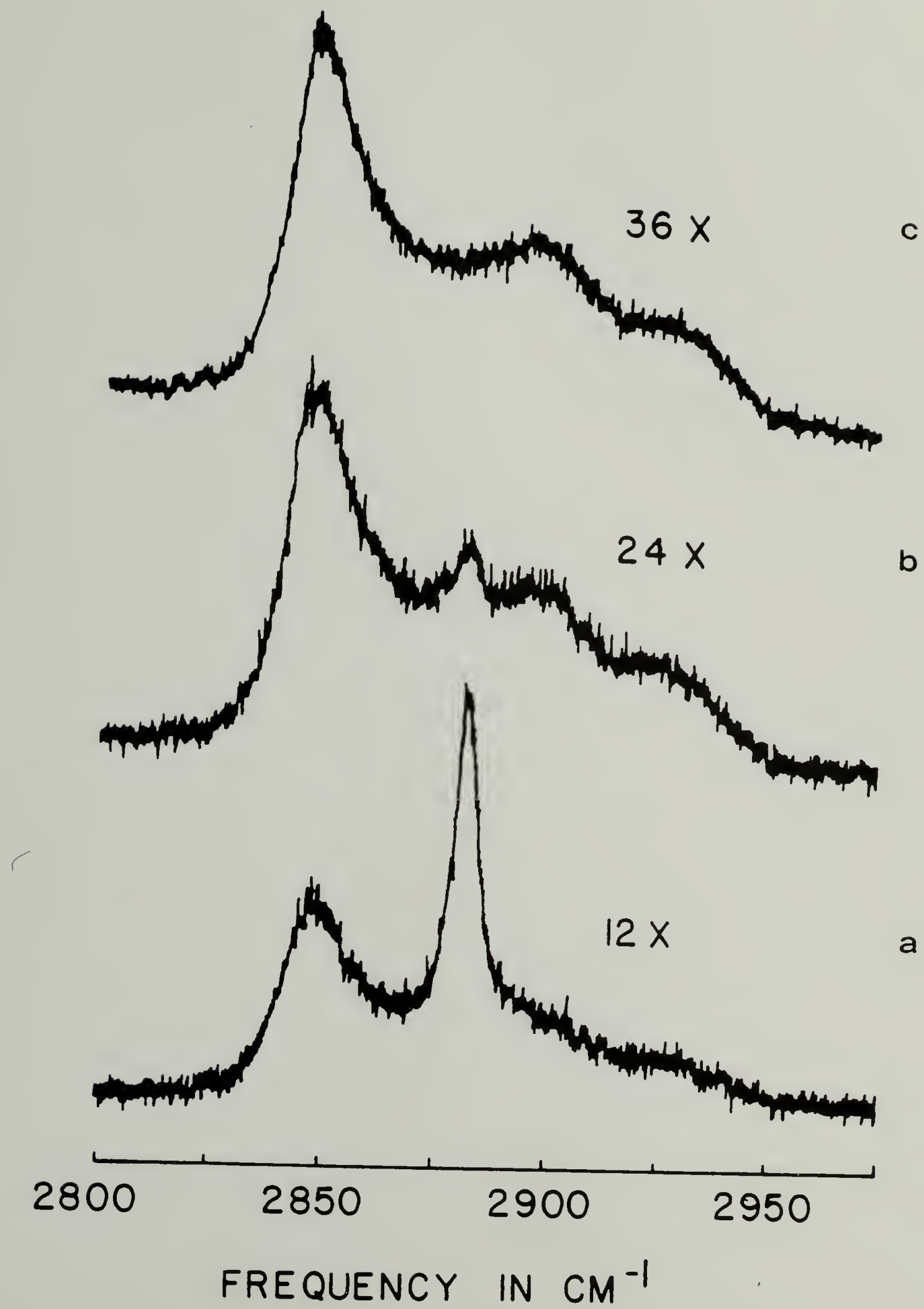

Figure 13

TABLE 2

Comparison of Orientation Measurement by Polarized Raman Scattering and Wide Angle X-Ray Scattering for Solid State Extruded Polyethylene

Extrusion Draw Ratio	12	24	36
Raman Orientation	17°	6°	<2°
WAXS Orientation*	17°	6°	5°

*Data from reference 7.

should be insensitive to conformation and orientation of the molecules. For polyethylene, the 1295 cm^{-1} CH_2 twisting mode has often been used as the internal standard (64,68) because of the flat dispersion curve of this mode (101). There are actually two peaks in this region, a narrow peak at 1295 cm^{-1}, corresponding to crystalline chains and a broad band with its peak at 1300 cm^{-1} corresponding to amorphous chains. Using only the peak at 1295 cm^{-1} gives the crystalline contribution (102,103) while integrating from 1260 to 1350 cm^{-1} gives a standard independent of crystallinity (68). Either is an appropriate standard for opaque, unoriented samples where the polarization of the light and symmetry of the scattering tensor do not have to be considered.

For oriented samples which do not scramble the polarization of the incident and scattered light, the internal standard used should either have the same form of the scattering tensor as LAM (strong CC, chain axis component) or be independent of orientation.

In the following section, the data collection system which was built and interfaced to the Raman spectrometer is described. A data collection system was required to convert the as-obtained Raman LAM spectra into straight chain length distributions.

The Raman Spectrometer-Computer Interface

The general motivation for interfacing a Raman instrument with a computer system is to automate data acquisition, allow for improved

signal to noise ratios, and to perform data storage, analysis, and reduction. For this low frequency Raman study in particular, background subtraction and intensity corrections are required to convert the LAM spectra to straight chain distributions.

Commerical and custom-built data acquisition systems for Raman instruments have been described (104-106) and both types of systems work well, but the commercial systems are expensive and not as flexible as is sometimes required. In most Raman experiments, the rate of data collection rarely exceeds a few data points per second and can easily be handled by microprocessor-based systems. The most recent 16-bit microcomputers are as powerful as earlier minicomputers and the 8-bit Z-80 system described here is adequate for all required tasks except large numerical computations.

Hardware and software development time and cost were reduced by utilizing available hardware and existing software wherever appropriate. A Jobin Yvon (JY) HG.2S monochromator was used with a Jobin Yvon controller. The controller provides full manual control of wavenumber scanning and slit openings. It also conditions computer pulses to control wavenumber scanning. But, from our experience, the JY external control interface is not well designed and can be susceptible to pulse reflections and noise. Therefore, reliable unattended coadding of scans for S/N improvement is not practical without a feedback of wavenumber position (JY provides signals which can be decoded to achieve this function, but our design does not use them). Almost equivalent S/N improvement is possible by taking one slower scan

instead of many faster ones. However, this method does not provide as much reduction of low frequency noise and instrumental drift.

A Cromenco System Three microcomputer with an added Cromenco TUART, 2 serial and 2 parallel input/output board was used to control the wavenumber scanning and to record digital intensity values. The photons are detected by a RCA C31034 photomultiplier in a cooled housing (Products for Resarch model TE 104 TS-RF). The PMT signal is processed by a PAR 1120 amplifier-discriminator before passing to a PAR 1105 analog ratemeter and finally to an analog strip chart recorder. The PAR 1105 also provides a digital pulse for each photon; these pulses are counted by a Canberra model 1773 digital scaler. The counting period is set by the computer through a timer which was designed and built in the laboratory (Figure 14). The 4 MHz crystal oscillator driven timer allows intervals from 0.1 to 9.9 seconds with accuracy better than 0.1 millisecond. The connections between the monochromator, digital photon counter, interval timer, and the microcomputer are shown in Figure 15.

The control software was written in Pascal/MT 3.0, a compiled, high level language which includes extensions allowing easy control of external devices. This language combines ease of development with adequate program execution speed, making the use of assembly language subroutines unnecessary. The source code and explanation of the control program are given in the Appendix.

During data collection, the control program steps the monochromator to a point, starts the timer and scaler, and at the end of the

Figure 14. Schematic of the timing circuit for Raman data collection.

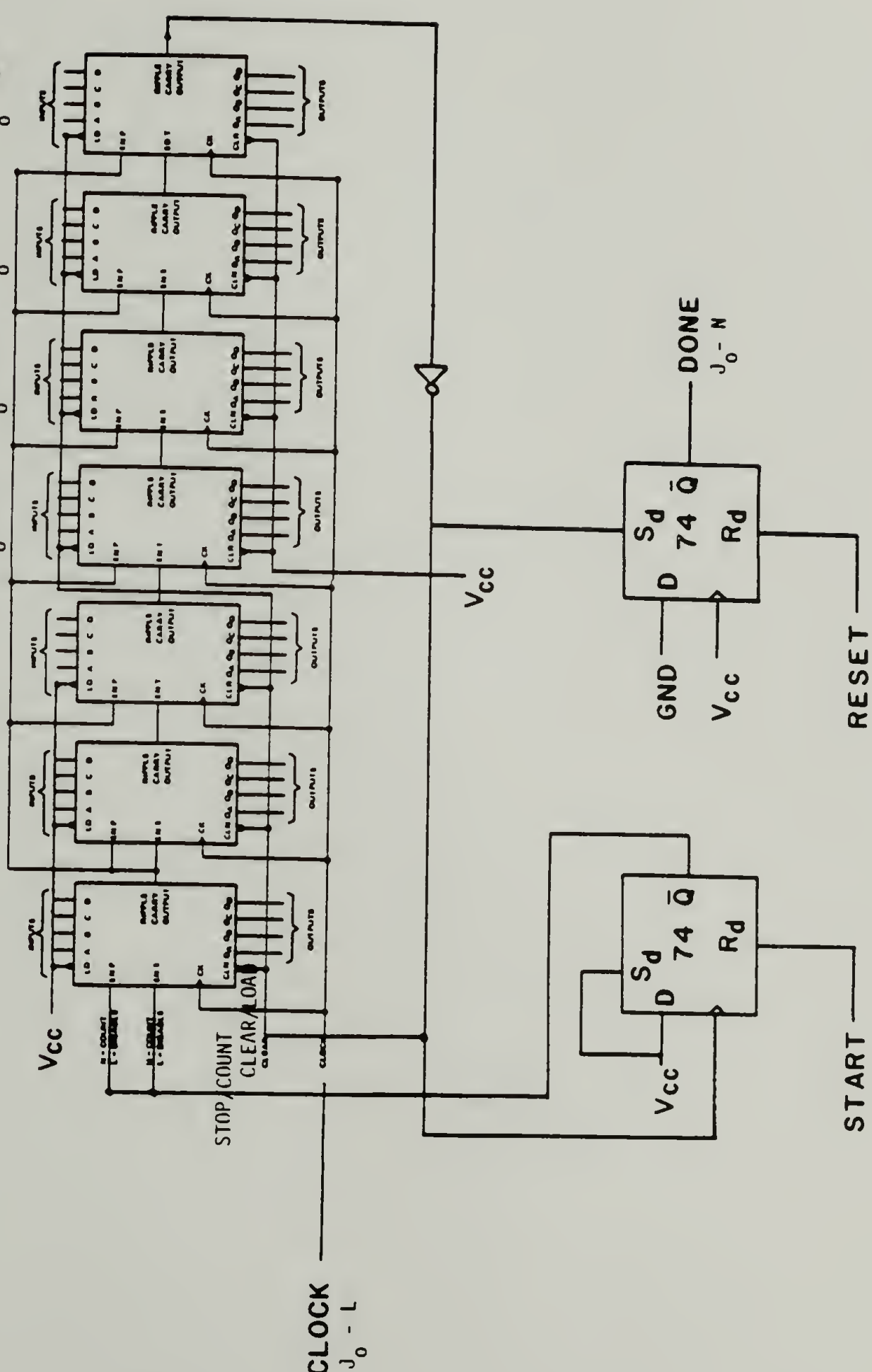
J_0 1-4
J_0 5-8
J_0 9-12
J_0 13-16
V_{CC}
STOP/COUNT
CLEAR/LOAD
CLOCK
J_0 - L
S_d
D 74 $\bar{Q}$
R_d
GND
V_{CC}
DONE
J_0 - N
RESET
J_0 - P
V_{CC}
START
J_0 - M

Figure 14

Figure 15. A block diagram of the Raman data collection system.

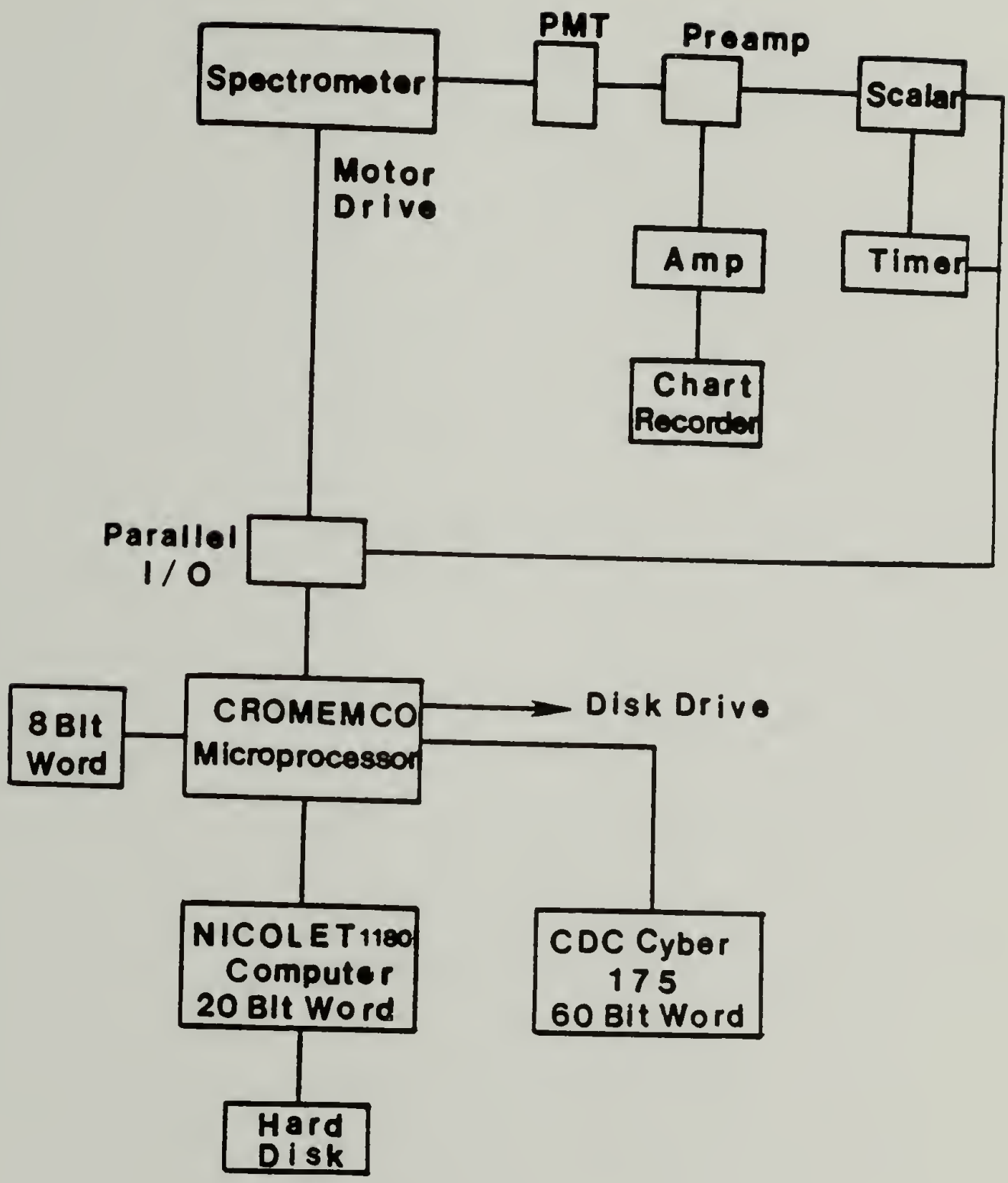
Spectrometer
PMT
Preamp
Scalar
Motor
Drive
Amp
Timer
Chart
Recorder
Parallel
I/O
8 Bit
Word
CROMEMCO
Microprocessor
Disk Drive
NICOLET 1180
Computer
20 Bit Word
CDC Cyber
175
60 Bit Word
Hard
Disk

Figure 15

time interval reads in the photon counts from the scaler, stores the value, and moves the monochromator to the next point. The completed spectra are recorded on floppy disk files at the end of each scan.

The spectra are retrieved from floppy disk files and transferred via an RS-232 serial port to a Nicolet 7199 FT-IR system or to a Control Data Corp. Cyber 175 or 720 computer system at the University of Massachusetts. Software development was minimized and the expense of graphic hardware was avoided by using existing programs on these systems for the analysis and plotting of results. Programs were written on the Nicolet to subtract the background of the LAM spectrum and to correct the subtracted spectra for frequency and temperature effects, converting them to I_{ν}^{α} and $F(\ell)$.

Conclusion

The LAM technique is a morphological tool that can be used to measure features at the 50 to 500 Å scale in semicrystalline polyethylene. The length distribution of straight chain segments is determined from the frequency distribution of the LAM mode. The effects of crystal defects on the LAM vibration were clearly shown in a study of quenched, narrow low MW fraction of polyethylene. The vibration is perturbed by conformational defects and the intensity is redistributed in the high frequency, short segment length region as had been theoretically predicted. Measurements in a model system agree with normal coordinate analysis of defects, providing con-

fidence in the interpretation of LAM for more complex samples.

The uniqueness and applicability of the technique is illustrated by the examination of drawn polyethylene. The broad LAM reflects the great amount of disorder in the as-drawn samples. Interpretation of structural changes are consistent with reduced disorder and a decrease in conformational defects with annealing. The problem of reliable baseline correction is presented and a workable solution is discussed.

LAM results for polyethylene solid-state extrudates showed increasing defect content and a shift to shorter, all-trans segments with increasing draw ratio. The LAM information was examined in conjunction with data from other techniques. Taken together, this data has shown that there are more crystalline defects and less structural regularity than is suggested by the models of the fibrillar morphology. Because of the unique information which the LAM results contain, the LAM technique should be included in any comprehensive study of the structure and properties of ultra-oriented polyethylene.

C H A P T E R I I I

INFRARED STUDIES OF POLYMER DEFORMATION

Introduction

The mechanical properties of polymeric materials are of considerable importance in their engineering applications. In this respect, an understanding of the microstructural mechanisms involved in polymer deformation is a prerequisite to reasonable structure-property-morphology correlations. Rheo-optics, an extremely powerful method for the study of polymer deformation and relaxation phenomena, measures the relationship between stress, strain, and an optical quantity (for example, birefringence, IR absorption, light scattering, or x-ray diffraction). The optical quantity is measured simultaneously with the stress and strain and followed as a function of time (21,25,107-109). The advent of rapid scanning FT-IR systems has expanded the applicability of vibrational spectroscopy in rheo-optical studies.

Early infrared rheo-optical studies examined simple semicrystalline materials. For example, the orientation rates of the amorphous chains and the a and b crystal axes in polyethylene have been established (23,24,110). In this case, the results are similar to those obtained from the combination of WAXS and birefringence techniques (18,107). In more complex materials such as polyurethanes

containing amorphous hard segments, use of only wide angle x-ray and birefringence cannot provide an adequate understanding of deformation behavior. In polyurethanes, infrared methods have determined hard and soft segment orientation as well as the quantity and strength of hydrogen bonding (31,34,111,112). In these copolymers and in polymer blends (113-115), the selectivity of infrared spectroscopy (the ability to distinguish between different chain segments and between chains in different conformations) is a great advantage.

The main emphasis of this chapter is the description of a newly developed time resolved spectroscopy (TRS) technique which has been designed for polymer rheo-optical studies. A discussion of the limitations of previous time resolved spectroscopy methods illustrates the necessity for the development of a new TRS method for infrared rheo-optical studies of polymer viscoelasticity. In our studies, the chain segment orientation is determined from polarized infrared spectra. Therefore, a summary of orientation measurement by infrared dichroism is presented. Next, the experimental considerations which constrain dynamic measurements are discussed. This is followed by a description the hardware used for the infrared rheo-optical experiments.

Infrared Orientation Measurement

The theory of polarized infrared measurements which are used to follow chain segment orientation is briefly summarized here (35-37). The attenuation of infrared radiation passing through a sample is

described by the absorbance, A, which is equal to $-\log(I/I_o)$ where I_o and I are the incident and transmitted intensities, respectively. For an unoriented sample, A is given by equation 3.1a where ε is the molar extinction coefficient, c is the molar concentration, and b is the pathlength in the sample. For an oriented sample the absorbance also depends on the angle between the transition dipole moment and E, the electric field vector of the polarized incident radiation. If the transition dipole moment is oriented along a bond axis, then $A_{\parallel}$ and $A_{\perp}$, the absorbances for infrared radiation polarized parallel and perpendicular to a reference direction, z, are given by equations 3.1b and 3.1c. In this case, the bonds are assumed to lie within a plane normal to the propagation direction of the incident radiation. θ_z is the angle between the bond and the reference direction z. The structural absorbance, A_o is given by Equation 3.1d and is independent of the orientation of the bonds within the sample.

$$A_o = \varepsilon \cdot b \cdot c \qquad (3.1a)$$

$$A_{\parallel} = A_o \overline{\cos^2\theta_z} \qquad (3.1b)$$

$$A_{\perp} = A_o \overline{\sin^2\theta_z} \qquad (3.1c)$$

$$A_o = A_{\parallel} + A_{\perp} \qquad (3.1d)$$

If the bonds are not constrained in the normal plane, but are free to orient at any angle ϕ with respect to the radiation propagation direction, then $A_{\perp}$ is given by equation 3.2a and $A_{\parallel}$ is given by 3.1b. When rotational symmetry about the reference axis z is assumed

(as in uniaxial extension), then equation 3.2b gives $A_\perp$, while $A_\parallel$ is still given by 3.1b, and A_o is given by equation 3.2c.

$$A_\perp = A_o \overline{\sin^2\theta_z}\ \overline{\cos^2\phi} \tag{3.2a}$$

$$A_\perp = \frac{1}{2} A_o \overline{\sin^2\theta_z} \tag{3.2b}$$

$$A_o = A_\parallel + 2A_\perp \tag{3.2c}$$

The orientation can be expressed in terms of an average orientation angle derived from Equation 3.3.

$$\cot^2\theta = \frac{A_o \overline{\cos^2\theta}}{A_o \overline{\sin^2\theta}} = \frac{A_\parallel}{2A_\perp} \tag{3.3}$$

However, polymer orientation measured by infrared is usually expressed as the orientation function F, given by $P_2(\cos\theta_z)$ where P_2 is the second order Legendre polynomial.

$$F = P_2(\cos\theta) = \frac{3\overline{\cos^2\theta} - 1}{2}$$

$$F = \frac{A_o}{A_o}\left[\cos^2\theta - \frac{1}{2}(1 - \cos^2\theta)\right]$$

$$F = \frac{A_\parallel - A_\perp}{A_o} = \frac{A_\parallel - A_\perp}{A_\parallel + 2A_\perp} \tag{3.4}$$

The value of F varies from +1 to zero to -1/2 for orientations that are parallel, random, and perpendicular, respectively. Experimentally, the dichroic ratio, D, defined as $A_\parallel/A_\perp$ is often reported and Equation 3.5 which gives F in terms of D can be obtained by dividing the

numerator and denominator of equation 3.4 by $A_\perp$.

$$F = \frac{D - 1}{D + 2} \qquad (3.5)$$

These equations give the orientation of transition dipole moments but the orientation of the chain axis is the desired quantity. When the angle γ between the chain axis and the transition dipole is known, the corrected expression becomes

$$F = \frac{D - 1}{D + 2} \Big/ \frac{D_o - 1}{D_o + 2} \qquad (3.6)$$

where $D_o = 2\cot^2\gamma$ (35). Samuels has discussed experimental methods of determining D_o from infrared and x-ray results (36,37).

General Overview of Infrared Rheo-Optics

Infrared rheo-optical measurements require a stretching device to deform the sample and a method to record the stress, strain, and infrared spectra. For experimental flexibility, the strain or stress applied to the sample should be fully programmable; this enables viscoelastic phenomena to be studied by constant load (creep), step strain (stress relaxation), sinusoidal strain (storage and loss measurement) and ramp strain (constant strain rate) experiments as desired (116). To obtain this flexibility, a closed loop, servo-hydraulic stretcher was designed and interfaced to the FT-IR system.

With this stretcher, an analog voltage from any source can be used to program the load or elongation of the sample. The desired waveforms, sine, triangle, ramp, or square, with frequencies from 10^{-4} to 10^{3} Hertz are supplied by a low frequency signal generator. External signal inputs to the signal generator enable the FT-IR to start, stop, or reverse the waveform. The load and elongation are measured by a load cell and a position transducer. These signals are digitized and stored under control of the FT-IR computer.

Two constraints affect the measurement of the infrared spectra; they are the rate of spectral acquisition and the spectral signal to noise ratio. The signal to noise (S/N) ratio increases with the square root of the measurement time (or the square root of the number of co-added scans per spectrum). The final S/N ratio must be high enough to reveal the spectral changes due to the applied strain. The measurement time required to achieve this S/N ratio depends on the magnitude of the spectral changes, the sample absorbance, and instrumental factors. High temporal resolution is needed to perform high strain rate experiments; two examples are 1) following the short time behavior in stress relaxation experiments and 2) determining the magnitude and phase of the polymer response in high frequency, sinusoidal strain experiments.

Infrared rheo-optical experiments utilizing FT-IRs fall into several categories depending on the time between successive spectra during the strain waveforms. The different categories are illustrated in Figure 16 where the relative time scales of the strain waveforms

Figure 16. Different time scales in infrared rheo-optical experiments
a. psuedo-static collection
b. rapid scan collection
c. unsorted time resolved collection
d. true time resolved collection

a) PSUEDOSTATIC

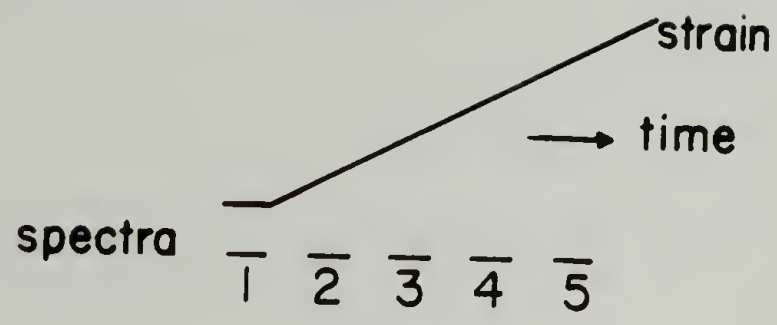

b) RAPID SCAN

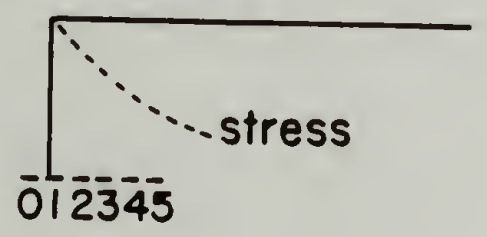

c) UNSORTED TRS

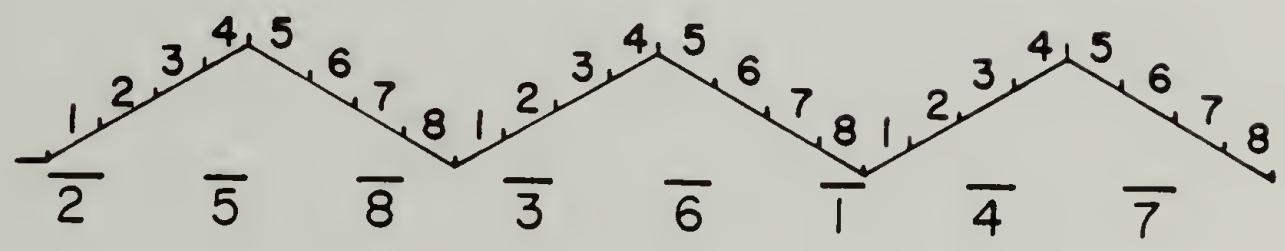

d) TRUE TRS

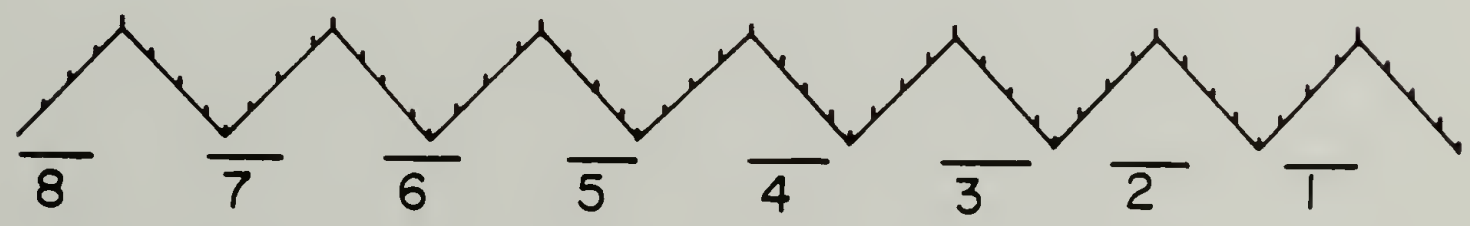

Figure 16

and the individual spectra are shown. In the psuedo-static case, the sample is near equilibrium; this allows spectral signal averaging to be done while simultaneously satisfying the conditions of adequate temporal resolution and high S/N ratio. Furthermore, the FT-IR software overhead associated with each spectrum and the time needed to obtain the stress and strain values are small compared to either the time between successive spectra or the time needed to collect each spectrum. In the rapid scan case, successive spectra are obtained through the use of special collection software; the maximum collection speed is limited only by the access time of the hard disk or the interferometer scan rate. The number of coadded interferograms needed to achieve the necessary signal to noise ratio determines the final time resolution. In rapid scan, there is a clear trade-off between signal to noise ratio and time resolution (which can be as fast as 0.5 seconds). In the psuedo-static and rapid scan methods, the total time of the experiment and the strain waveform are the same (Figure 16a and b). However, in the time resolved spectroscopy (TRS) methods, the experiment lasts for many cycles of the strain waveform (Figure 16c and d). The TRS methods require identical sample responses for each strain cycle. Therefore, irreversible changes in the sample can only be followed by the psuedo-static or rapid scan methods. The first of these TRS methods, unsorted time resolved, is used to achieve time resolutions ranging from that corresponding to many scans to that for a single interferometer scan (<100 msec) while allowing signal averaging to improve S/N ratios. In unsorted TRS, the FT-IR acts as a

boxcar signal averager; the strain cycle is divided into equal intervals of time and each collected interferogram is coadded to an interferogram file coresponding to the same time interval of the strain cycle. The hardware and software used for data collection are the same as for the second TRS method, true time resolved spectroscopy. In true TRS, the desired time resolution is shorter than the time required to collect a single interferogram (50 to 1000 msec). Once again, the strain waveform is divided into time intervals and the collected interferograms are co-added into files depending on the strain interval in which the interferogram began. When enough scans are coadded into each file, the interferogram points are shuffled so that interferograms of constant strain are formed and these are transformed to yield spectra corresponding to the different strains.

In summary, the psuedo-static and rapid scan experiments are used for experiments with moderate requirements for time resolution and where the sample deformation is irreversible. Unsorted TRS measurements give improved S/N ratios of short time events and true TRS enables both good S/N ratios and very short time resolution. The hardware and software used to accomplish these methods are described in the following sections.

Description of the Infrared Rheo-Optical Experiment

Our instrument is a standard Nicolet 7199 Fourier transform infrared spectrometer employing a model 7000 optical bench capable of

high spectral resolution and fast data collection. The interferometer scan velocity and scan length are set by the FT-IR software; together they determine the scan period. Typically, a single, 4 cm^{-1} resolution scan can be taken every 500 msec. One hundred msec of this time is required for the actual sampling of the interferogram and the other 400 msec are necessary to stop, return, and restart the moving mirror of the interferometer. A broad band, LN_2 cooled, MCT detector was used to give a high S/N ratio. The processor is a 20 bit word Nicolet 1180 minicomputer with 80K words of main memory. In most kinetic studies, large amounts of data are usually acquired in a short time; therefore two Diablo 44B 5Mb fixed/5 megabyte removable cartridge disk drives and a Kennedy 9800, 9 track, 1600 bpi magnetic tape system are used for spectral storage. A 20 bit parallel input/output interface board (Nicolet 308) is used for controlling the stretcher function generator, to access stress and strain information from an external A/D converter, and to control the external time resolved interface. All of the individual I/O lines are accessed by the 1180 computer through programs written in assembly language. These programs are callable by higher level languages such as BASIC or FORTRAN and can be incorporated into the FT-IR operating software. Thus an entire experiment can be programmed to run conveniently and precisely with little operator involvement.

The hydraulic stretcher is shown schematically in Figure 17. This stretcher is small enough to fit in the sampling compartment of

Figure 17. A diagram of the closed loop servo-hydraulic stretcher.

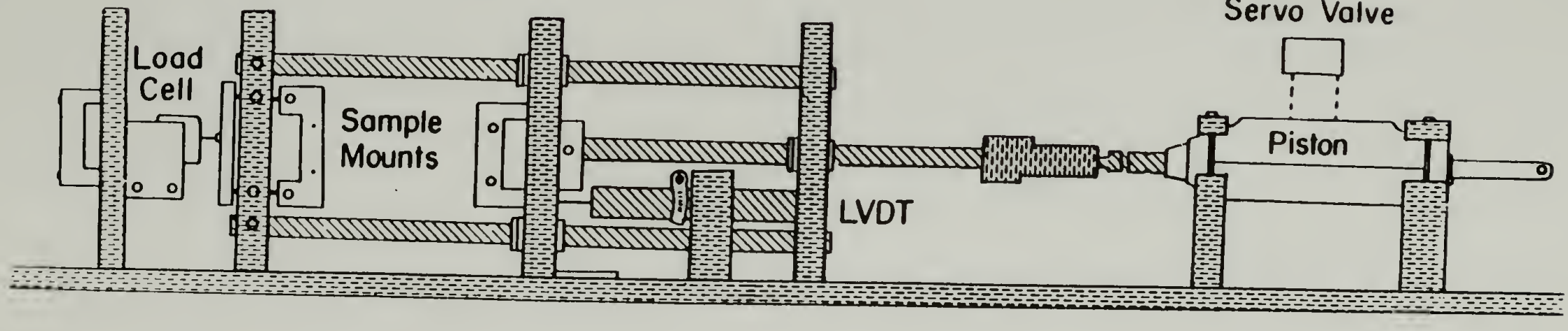

Figure 17

the regular Nicolet 7000 optical bench. The entire stretcher is attached to a single base plate and thus slides easily into and out of the spectrometer. A platform straddling the FT-IR sample area and attached directly to the floor was used to isolate the stretcher vibrations from the FT-IR optical bench. The sampling area is enclosed by a separate cover to maintain the spectrometer purge. The polymer films (30 mm x 10 mm x 5-50 μm) usually used in transmission experiments are stretched between the sample mounts. The moving mount is mechanically coupled to the hydraulic piston to ensure fast and accurate response. Rotation and misalignment of the sample mounts is eliminated by a pair of stabilization rods. The hydraulic power unit and accumulator to drive the hydraulic piston deliver at least 2.5 gallons/minute of flow at a pressure of 1200 pounds per square inch. The double acting hydraulic cylinder has an effective piston area of 0.7 in^2 and a stroke of 2 inches. The hydraulic flow is controlled by a MOOG model 30 servovalve rated at 1 gallon per minute flow rate (117). This should give a maximum piston velocity of 5 inch/sec. The piston acceleration is limited by inertial effects within the servovalve and hydraulic system. MOOG specifications show a -3 db point in the servovalve frequency response at 80 hz. The servovalve is controlled by a MOOG model 82-300 dc servocontroller which accepts a load or position feedback signal. The measured phase lag between the function generator signal and the piston displacement is 5 degrees for a sine wave of 20 hertz and 0.1 inch displacement amplitude. The load is measured by a Data Instruments JP10 load cell

(rated at 10 pounds) attached to the fixed sample jaw through two stabilization rods which eliminate jaw rotation and reduce the torques acting on the load cell. The moving jaw position is measured by a Trans-Tek 243-000 DC to DC linear variable differential transformer position transducer (DCDT). The analog signal outputs from the load cell and DCDT are digitized and accessed through the parallel I/O port of the Nicolet computer.

Electric cartridge heating elements are attached to a removable cover enclosing the sampling area. A programmable temperature controller and a flow of cooled N_2 gas allows deformation experiments to be carried out at temperatures between -20 and 200°C.

In order to carry out infrared rheo-optical experiments, both the spectrometer movements and the stroke and applied force of the stretcher must be closely monitored and controlled. The entire interface between various components used in the experiments is shown schematically in Figure 18. The data collection software supplied by Nicolet was modified to record the sample load and elongation for each file as it is collected. Figure 19 shows the control electronics which include the analog to digital converter and the analog multiplexer. The load cell signal is amplified sixty times by an AD521 instrumentation amplifier. The amplified load signal and the DCDT elongation signal pass to the DD7510DI protected analog switch which allows any of four signals to pass through to the A/D converter depending on the TTL signals received from parallel I/O port bits 18-15. The analog signals are digitized by an AD572 12 bit successive

Figure 18. Block diagram of the electronic components of the infrared rheo-optical set up.

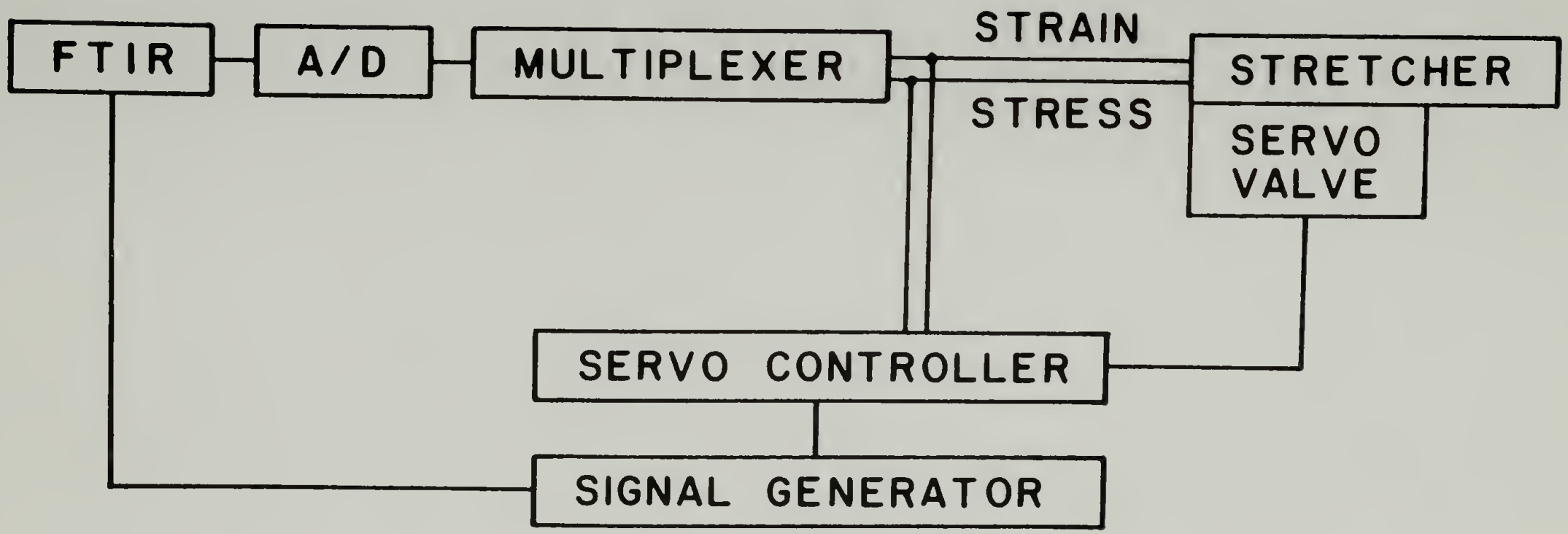
FTIR
A/D
MULTIPLEXER
STRAIN
STRESS
STRETCHER
SERVO VALVE
SERVO CONTROLLER
SIGNAL GENERATOR

Figure 18

Figure 19. The schematic diagram of the control electronics and the interface to the Fourier transform infrared spectrometer.

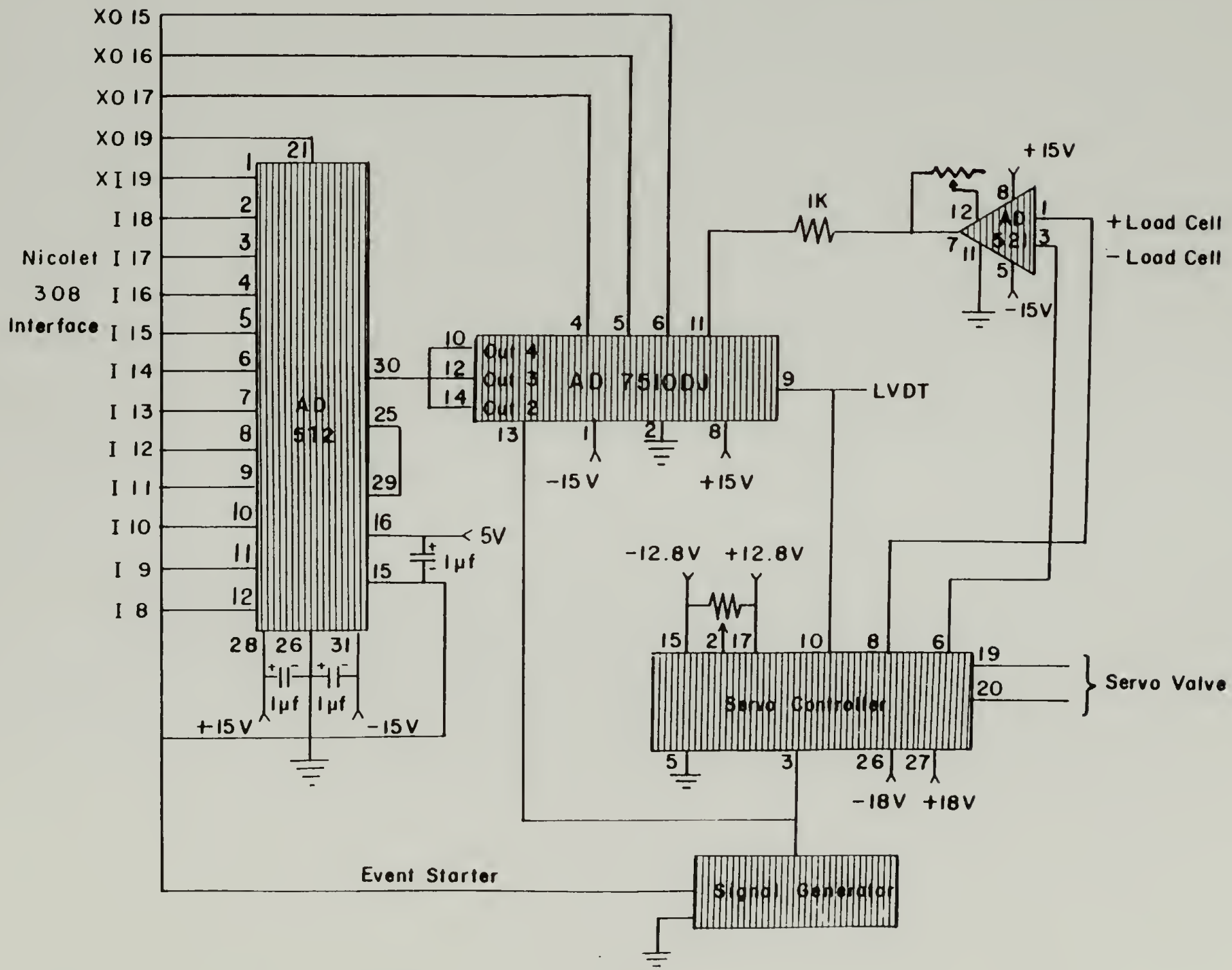
XO 15
XO 16
XO 17
XO 19
XI 19
I 18
Nicolet I 17
308 I 16
Interface I 15
I 14
I 13
I 12
I 11
I 10
I 9
I 8
AD 512
21
1
2
3
4
5
6
7
8
9
10
11
12
25
29
30
16
15
28
26
31
5V
1µf
1µf
1µf
+15V
-15V
AD 7510DJ
Out 4
Out 3
Out 2
4
5
6
11
10
12
14
13
1
2
8
-15V
+15V
1K
+15V
AD 521
8
12
7
11
1
3
5
-15V
+Load Cell
-Load Cell
LVDT
9
-12.8V
+12.8V
15
2
17
10
8
6
19
20
Servo Controller
5
3
26
27
-18V
+18V
Servo Valve
Event Starter
Signal Generator

Figure 19

approximation analog to digital converter set for a 10 volt range. The A/D conversion is initiated by parallel I/O bit 19 and requires 25 µsec to complete. The load and elongation are sampled sequentially with about 35 µsec of delay between the two values; for most of our experiments this delay is negligible. The load and elongation values are digitized at the start of each rapid scan file or at the end of each regular data collection file. The data can be stored in a common data area in main memory and/or in the file status block, a group of 352 words that are stored with each FT-IR file on the hard disk. The values can then be recalled later for analysis.

Time resolved spectroscopy

General overview of time resolved spectroscopy. Because of its multiplex advantage and high throughput, FTIR has a higher speed of spectral acquisition than dispersive instruments. This has been shown numerous times in the literature both theoretically and experimentally. Even so, when observing short time phenomena, it is necessary to reduce the S/N ratio (by decreasing the number of scans coadded and the time to collect each scan) and/or spectral resolution to achieve better time resolution. The limit of rapid scan FTIR is reached when the time period required for one scan of the moving mirror is longer than the desired time resolution. The development of time resolved spectroscopy, TRS, has led to vastly improved time resolution in FT-IR.

The principles representing several approaches to TRS have been published (43-47). TRS observes time varying phenomena (polymer

deformation, laser or electron beam induced chemical events, etc.), which are referred to as the sample event. Each of the TRS techniques divides the sample event cycle into discrete elements of time, t_i (Figure 20b). A normal interferogram $I(\delta_j)$ is composed of points from j=1 to the maximum number of data points, NDP, each taken at equal intervals of the retardation, δ (Figure 20). During a TRS experiment, the interferogram points, $I(\delta_j,t_i)$ are a function of both time and retardation. Varying methods exist for collecting $I(\delta_j,t_i)$, the interferogram points for all j and i. The collected interferogram points are sorted to reconstruct interferograms corresponding to each time, t_i. The resulting interferograms then contain data points from 1 to NDP, all collected during particular t_i's. These interferograms are Fourier transformed to give spectra describing the sample at times t_i.

The first reported TRS results were taken with a step scanning interferometer (43,44). With this type of interferometer, the moving mirror is positioned to the starting retardation and then the IR signal is sampled at each of the times, t_i, during the sample event cycle. The value for each t_i may be improved by signal averaging over many sample event cycles. Next, the retardation is incremented and the signal is recorded for all t_i's. The increment and sample process continues until all interferogram points (with retardations δ_i) from 1 to NDP at all times t_i have been sampled. The complete set of data $I(\delta_j,t_i)$ is sorted to form interferograms of constant time which are transformed into spectra for each t_i.

Figure 20. An interferogram (a) and the waveform (b), for a time resolved spectroscopic experiment with experimental conditions as stated in Table 4.

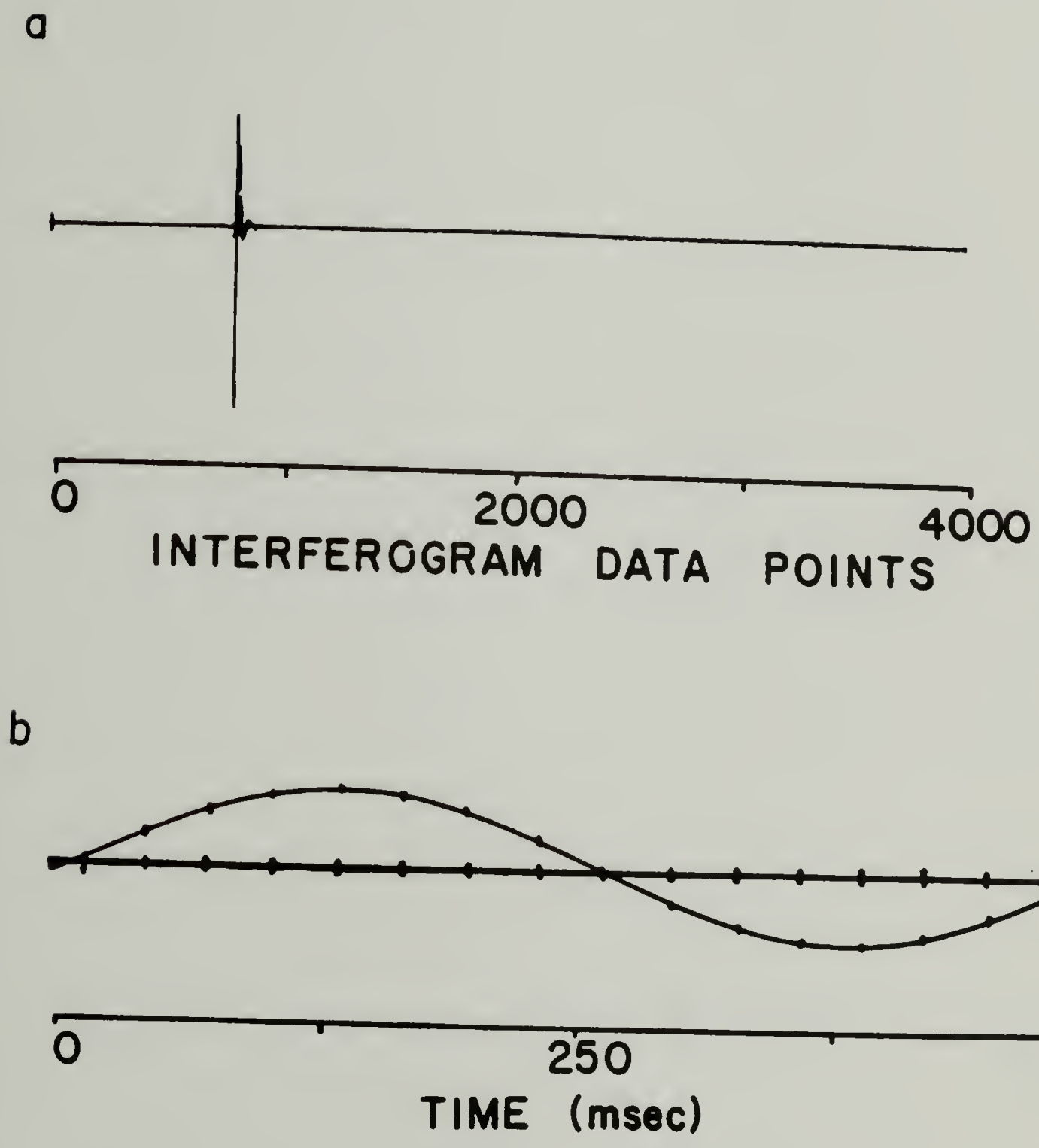

Figure 20

The step scanning TRS approach has the advantage that the time resolution is limited only by the digitization rate of the infrared signal. Furthermore, the sampling scheme is very flexible and places few (if any) constraints on the duration and type of sample event cycle chosen. The disadvantage is the lack of commercially available step scanning FT-IRs. However, this experiment demonstrated the advantages of TRS, i.e., increased time resolution and signal averaging to improve S/N ratios.

A different approach was taken by the commercially available time resolved spectroscopy packages for use with rapid scanning interferometers (40,45-47,118). In these experiments, an extra circuit is added which controls the start of the sample event cycle. Initially, the sample event cycle is triggered by the start of each interferometer scan (Figure 21). Many scans can be coadded with the sample event retriggered at the beginning of each scan. During each scan, the interferogram is sampled at each t_j. For the next set of scans, a time delay, Δt, is imposed between the start of the scan and the start of the sample event cycle. For each successive set of scans the time delay is increased by Δt. This continues until all time elements have been collected at all the interferogram points. If the sample event is shorter than the scan time, the sample event cycle may be triggered several times per scan to reduce the amount of time required to collect all the data (40,45,47).

Several limitations exist in this approach: 1) The start of the sample event cycle must be triggered at each cycle by the special TRS

Figure 21. Scheme of commercial time resolved spectroscopy. The sample event is shown in place of the interferograms. The start of the sample event is displaced by Δt for each file. Experimental conditions are given in Table 4.

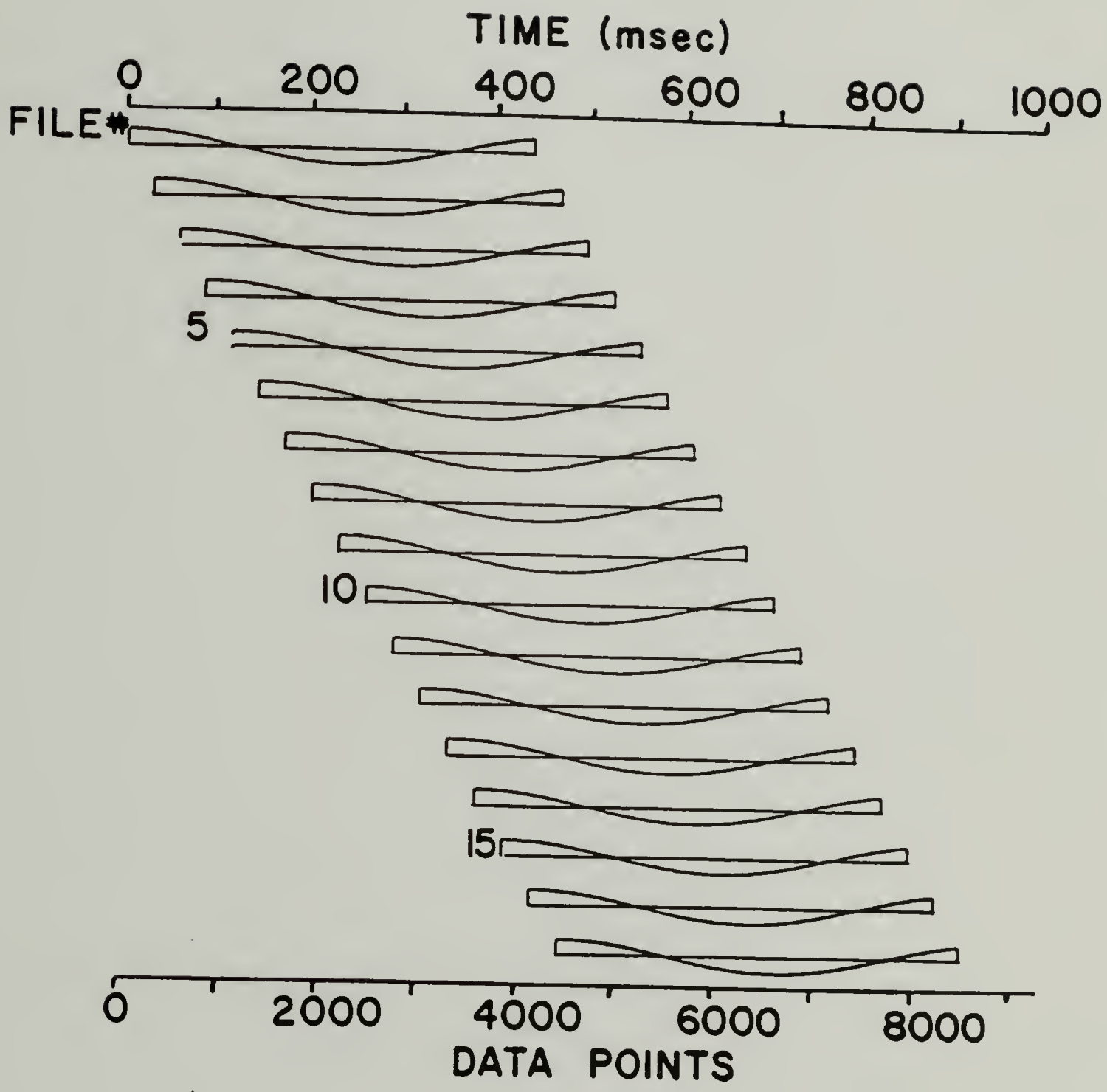
TIME (msec)
0
200
400
600
800
1000
FILE#
5
10
15
0
2000
4000
6000
8000
DATA POINTS

Figure 21

circuit. Therefore, this method precludes the use of continous sample event cycles (such as the sine waves used in dynamic viscoelastic measurements). 2) The whole sample event cycle must be completed between the time the interferometer scan starts and the time the moving mirror reaches the point of zero path difference, ZPD, in the interferometer. This time period is less than 30 msec on our instrument at the standard mirror velocity. The interferograms corresponding to sample event times, t_i, greater than 30 msec will not include points at or before the ZDP region and these interferograms are difficult to coadd and to phase correct during Fourier transforms. Therefore, flexibility is reduced in choosing the duration of the sample event cycle (a large range of cycle times is desirable in viscoelastic studies). 3) Finally, the experiment is based on the software provided with the FT-IR instruments which is difficult to adapt to a variety of experiments.

Development of a new time resolved spectroscopy technique. In this new approach, the start of the sample event cycle is not triggered by the start of each scan. Instead the sample event cycle runs continuously and independently of the interferometer. The sample event cycle is divided into time intervals, t_i over which the sample event is considered constant, by a counter and a clock. If T_o is the duration of the sample event and Δt is the desired width of the time interval, then there will be $N_o=T_o/\Delta t$ different time intervals. N_o may not exceed 256 with our present hardware (Figure 22). At the beginning of each sample event cycle, the counter is set to zero,

Figure 22. Schematic diagram of the time resolved spectroscopy experiment.

TIME RESOLVE BLOCK DIAGRAM

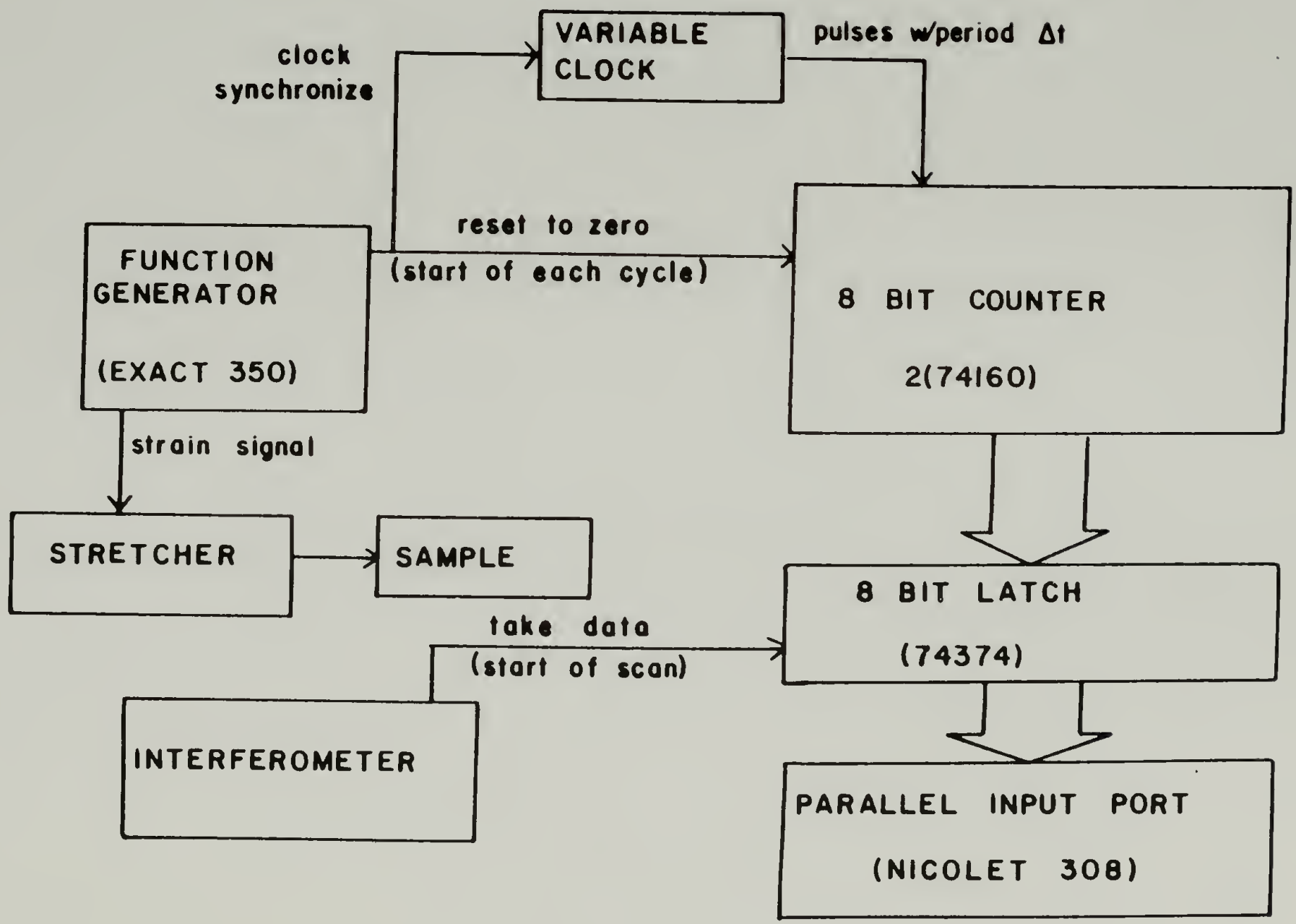

Figure 22

and then receives a clock pulse every Δt seconds. At the start of each scan (signaled by the Take Data pulse (TKDA) from the interferometer) the counter value is latched. The latched count value represents t_i at the start of the scan. This count value is read in at the end of the scan and stored with the interferogram. The stored count value will be used later to calculate the time corresponding to all the other data points in that interferogram. The count value of each collected file depends on the random correlation between the sample event cycle and the interferometer movement. The signal-to-noise ratio of the data may be improved by coadding scans which started during the same t_i. Interferograms are collected and coadded until a sufficient number of scans have been coadded into each of the N_o different files. After the collection is finished, the interferogram files are sorted to construct interferograms of constant time. This is accomplished by assuming that during the interval Δt, the sample event is stationary. Δt was defined above to be the spacing between t_i and t_{i+1}. The interferograms are broken into blocks of points - each block collected over a period Δt. N_1, the number of points per block is given by $\Delta t/t'$ where t' is the time spacing between each data point in the interferogram. t' is normally 28 μsec but can range from 14 to 250 μsec by varying the mirror velocity. If an unsorted interferogram has NDP points, then it will be made up of NDP/N_1 blocks. The first block corresponds to time t_i (relative to the beginning of the sample event cycle), the second block to time $t_i + \Delta t$, the next block to $t_i + 2\Delta t$, and so on (Figure 23).

Figure 23. The relationship between files collected under time resolved spectroscopy when the interferogram has been replaced by the strain. The segments between the diagonal lines represent interferogram points at constant time. Experimental conditions are given in Table 4.

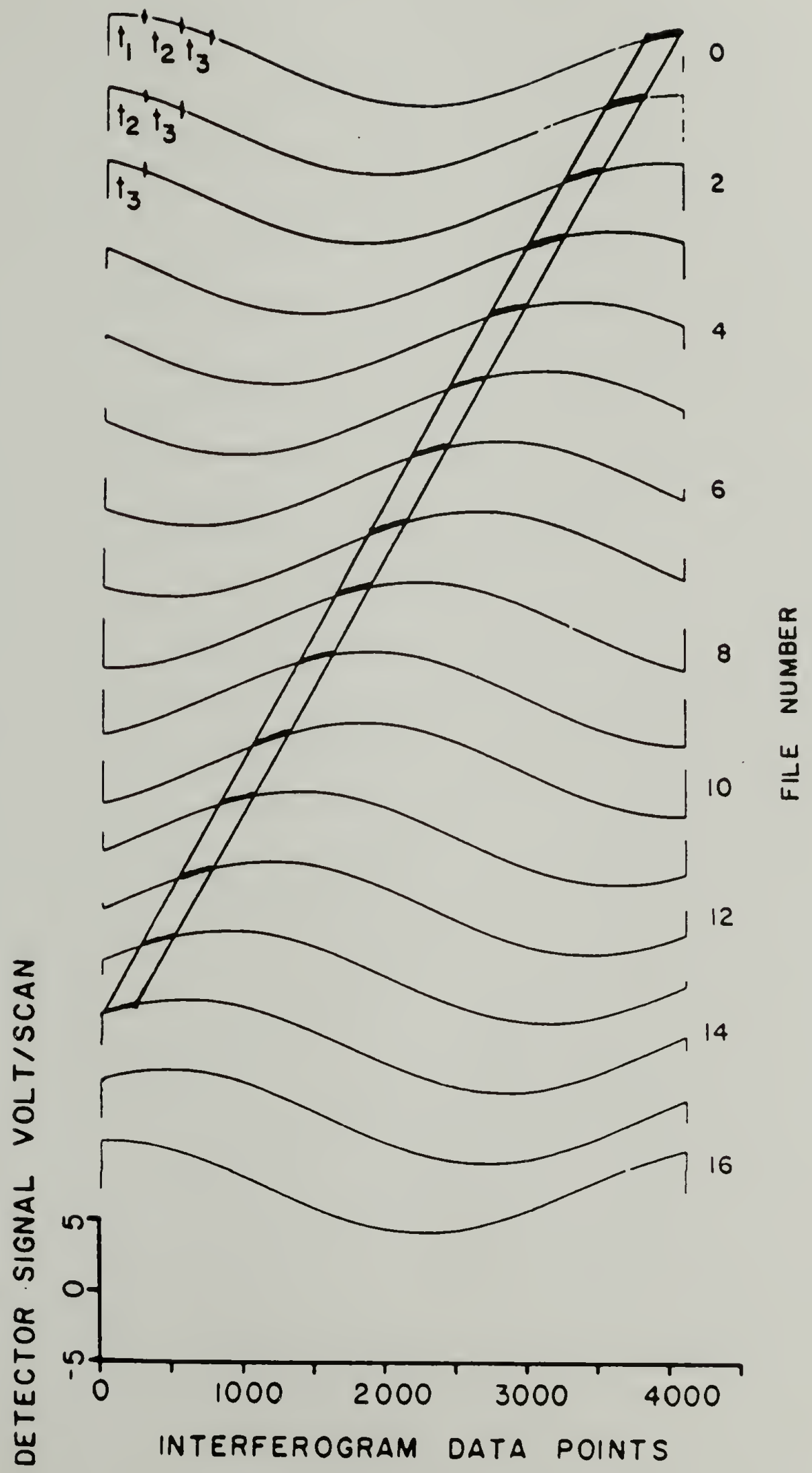
t_1 t_2 t_3
t_2 t_3
t_3
0
2
4
6
8
10
12
14
16
FILE NUMBER
DETECTOR SIGNAL VOLT/SCAN
-5
0
5
0
1000
2000
3000
4000
INTERFEROGRAM DATA POINTS

Figure 23

Since the time relationship between interferogram files and between blocks in each file is clearly defined, separate interferograms may be reconstructed for each time element t_i. In Figure 23 the blocks needed to reconstruct a particular time element are shown between the diagonal lines.

It should be mentioned that the start of the scan can occur any time during the interval Δt, but on the average it will occur in the middle. Therefore, the true time (relative to the beginning of each sample event cycle) associated with i^{th} individual file will be $t=(t_i + 0.5\Delta t) \pm 0.5\Delta t$. This error is due to the uncertainty of exactly when in the time period Δt the scan started. Note that the error is proportional to Δt; therefore, Δt should be reduced until the error level is acceptable. Also, in the sorting process, NDP/N_1 (the number of blocks) might not be a whole number and therefore a smaller block of less than N_1 points will be left at the end of each file of interferogram points collected. These points are discarded with a small decrease in spectral resolution.

To collect the data, the assembly language program (DATCOL) supplied with the FT-IR by Nicolet was modified to read in the counter value (through a model 308 20-bit parallel I/O port) at the end of each scan and to store it into a file status block memory location. Next, the data (in the sample file) must be coadded to the proper file (the destination file). This is done by a program written in the FT-IR macro which examines the counter value in the status block and sets the proper destination file to coadd the sample file into. Next

the coadd command is executed, which adds the sample and destination files and stores them back into the destination file. A sample program which does this is shown:

CLS	the interferogram data is collected into the sample file, along with the counter value
DFN=NSD	the counter value is obtained from the sample file and the destination file is set accordingly
CAD	this coadds the sample file into the destination file

While this sequence is being carried out, the sample event and the interferometer continue; however, no interferograms are collected. After the FT-IR software is finished coadding, it collects the next full interferogram.

The sorting of the files is done by a Fortran program on the Nicolet computer. The time required to sort the files is much shorter than the time required to collect the files.

The unsorted TRS method which was mentioned earlier is essentially the same as the TRS method just described. However, in unsorted TRS, Δt, the time between clock pulses is longer than the time to scan one interferogram (NDP x t'). The collection of files is the same as with true TRS, but the interferograms do not have to be sorted before they are Fourier transformed into spectra. The conditions for a typical unsorted FT-IR experiment are given in Table 3.

TABLE 3

Typical Experimental Conditions for
Unsorted Time Resolved Spectroscopy (TRS)

TRS Parameters	
clock period (time resolution)	126.4 msec
sample event period	1000 msec
time/interferogram data point	28.3 μsec
NDP, number of points in interferogram	4096
number of scans coadded to each file	*

TRS Relationships	
number of clock periods/sample event	7.91
time/scan	116 msec
number of clocks/scan	0.91 ǂ
number of data points/clock period	>4096 ǂ

*This is determined by the signal to noise requirements.

ǂSince the time per scan is less than the time resolution, i.e. the whole interferogram (4096 points) is collected in less time than one clock period (126 msec), the collected interferograms do not have to be sorted.

Testing the operation of the newly developed technique. Several tests were designed to evaluate the correct operation of the hardware and software associated with interferogram collection and sorting. The initial test was designed to check the operation of the counter and the associated circuits which divide the sample event into time elements t_j. A sine wave from the signal generator was used as the sample event and fed into the infrared signal path after the high and low pass filters. This allowed the sine wave to be sampled and stored as if it were an interferogram. The experimental parameters are summarized in Table 4. Using the TRS collection software, the interferograms of Figure 23 were collected. Figure 23 shows a series of sine waves each shifted by ΔT relative to its neighbors. This shows the time t_j of each interferogram was correctly determined. The sorting algorithm and program were tested by using the series of "interferograms" collected above. The sorted files should consist of identical segments of the sine curve. This is indeed found to be true, as shown in Figure 24.

Tests with real interferograms of polymer samples serve to assess the signal to noise ratio to be expected in actual experiments and to check for spectral artifacts in our time resolved method. Spectral artifacts in TRS spectra have been observed due to changing sample conditions which cause discontinuities or fluctuations in the interferograms. When these interferograms are sorted and transformed, they give rise to spectral artifacts and noise (48,119). In our experiment, if too large a change in the sample spectra occurs during

TABLE 4

Experimental Conditions used for the
Time Resolve Test Spectra

TRS Parameters

clock period (time resolution), Δt	30.8 msec
sample event period	500 msec
time/interferogram data point	113.2 μsec
NDP, number of points in interferogram	4096
number of scans coadded to each file	12 minimum, 35 average

TRS Relationships

number of clock periods/sample event	16.2
time/scan	463.6 msec
number of clocks/scan	15.1
number of data points/clock period	271

Figure 24. Result of sorting the interferograms in Figure 23. Each file is made up of 15 segments of 271 points.

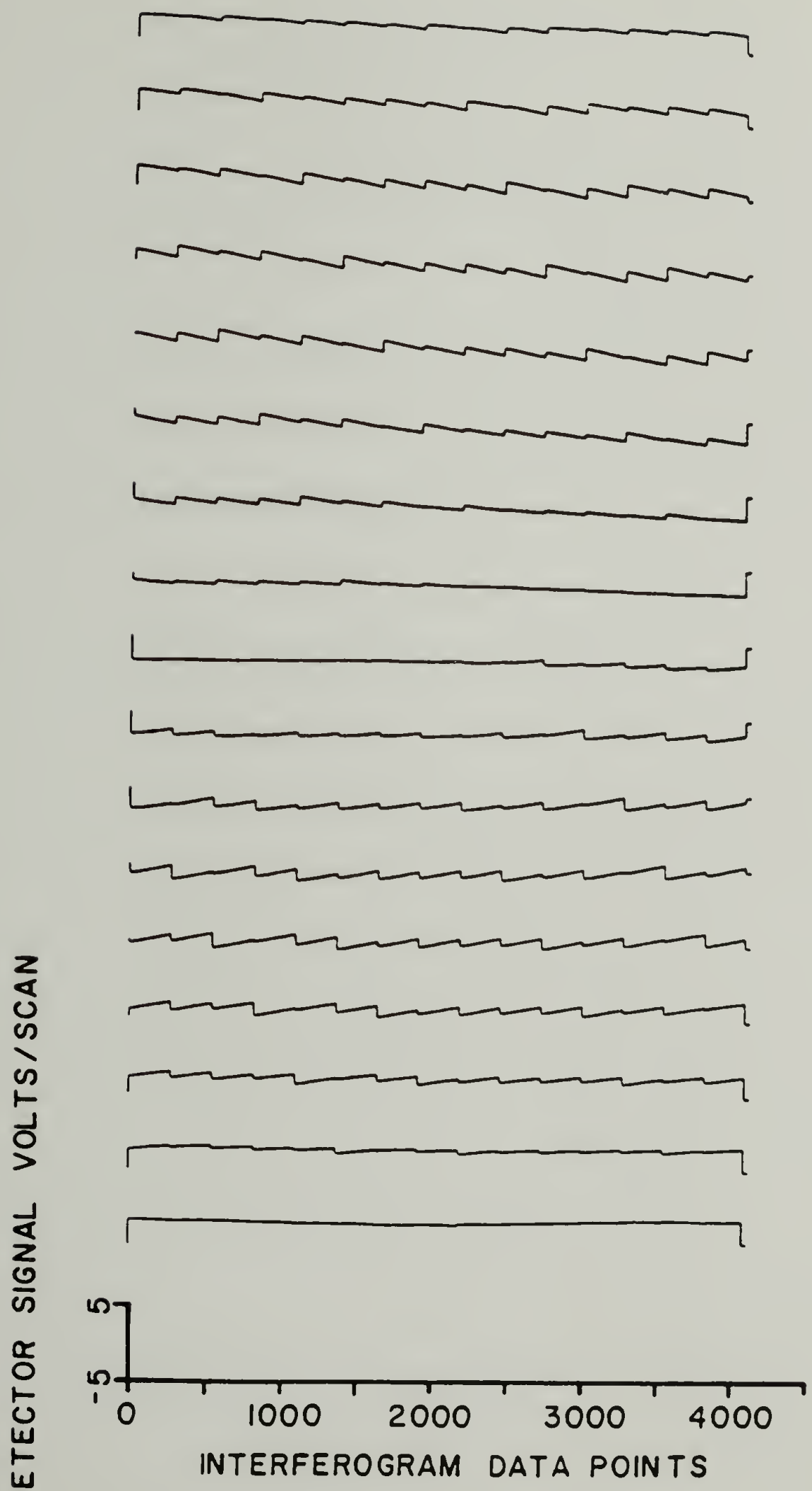
DETECTOR SIGNAL VOLTS/SCAN
5
-5
0
1000
2000
3000
4000
INTERFEROGRAM DATA POINTS

Figure 24

the time interval Δt, spectral artifacts may occur. Two tests were performed to check for artifacts: Test 0) The stretcher was used to move a polymer film into and out of the path of the infrared beam. The TRS spectra will show changing heights of the polymer peaks when plotted in transmittance, Figure 25a. However, when they are plotted as single beam spectra, the single beam "profile" will remain largely unchanged with the only changes occurring at the vibrational bands as shown in Figure 25b. Test 1) A more rigorous test would have larger changes in the sequence of single beam spectra. A polymer film was fixed in the beam and an opaque film was moved into and out of the beam producing the single beam spectra of varying heights shown in Figure 25c. In this case, if there are no artifacts, each of these single beam spectra will give identical absorbance spectra with only a baseline shift. This is indeed true as shown by the five lower spectra in Figure 25d. None of the collected spectra in Figures 25a-d show any evidence of "new peaks" which were artifacts in an earlier TRS experiment (48). During actual polymer deformation experiments, the changes in the single beam spectra during Δt are expected to be much less than in either of these two tests and therefore the occurence of spectroscopic artifacts is unlikely. These tests also have measured the experimental S/N ratio in TRS which helps to assess the reliability of the spectroscopic differences observed by TRS.

Discussion of the results. The new TRS method enables the use of continuous sinusoidal strains. This allows results of our FT-IR rheo-

Figure 25. Tests of the newly developed time spectroscopy
a. transmittance spectra of polymer film moving into the IR beam
b. single beam spectra of the transmittance spectra in (a)
c. single beam spectra of fixed polymer film with an opaque object moving into the beam
d. absorbance spectra of the single beam spectrum of the single beam spectra in (c) with a noise spectrum shown at top

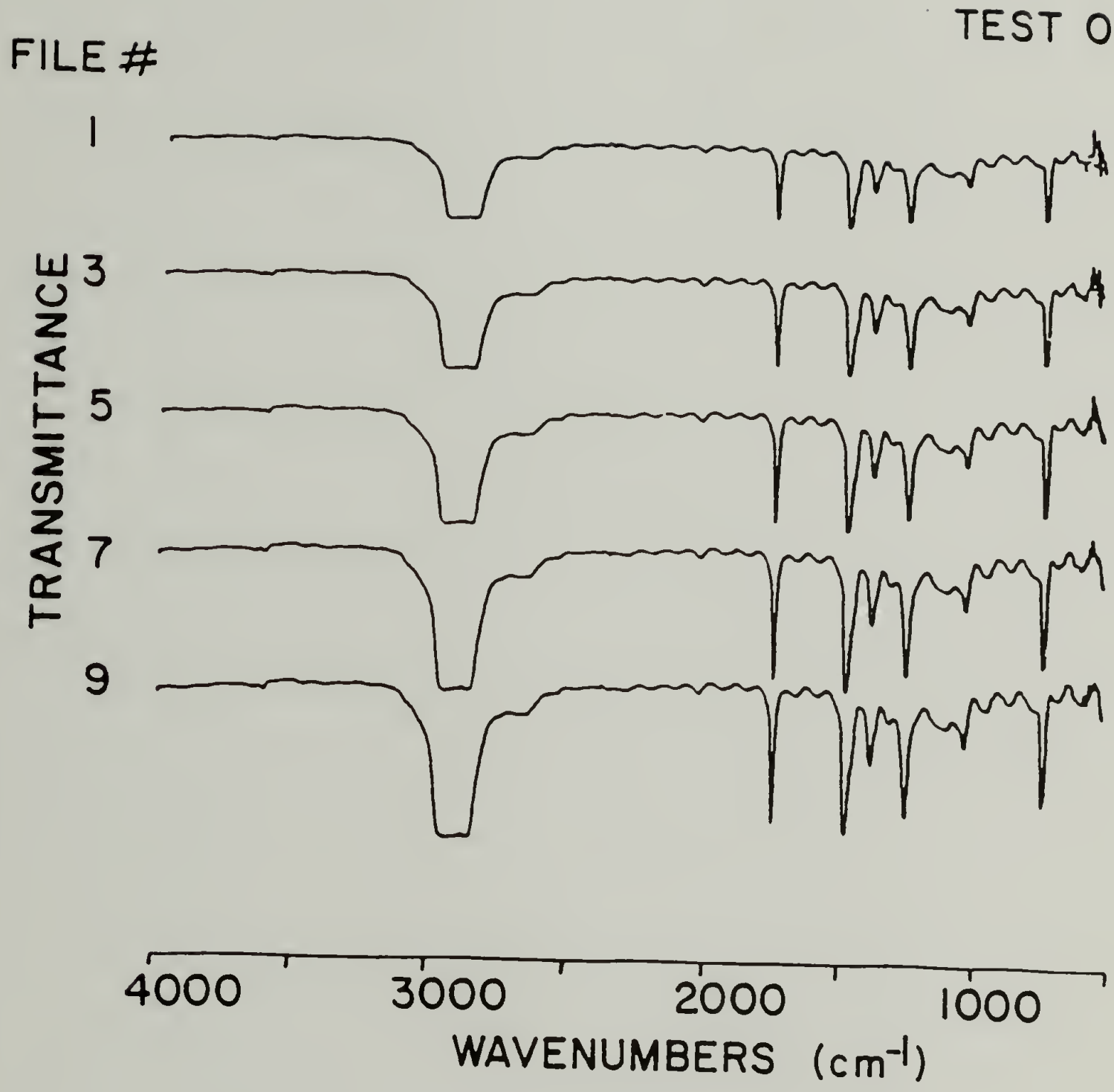
TEST 0
FILE #
1
3
5
7
9
TRANSMITTANCE
4000
3000
2000
1000
WAVENUMBERS (cm⁻¹)

Figure 25a

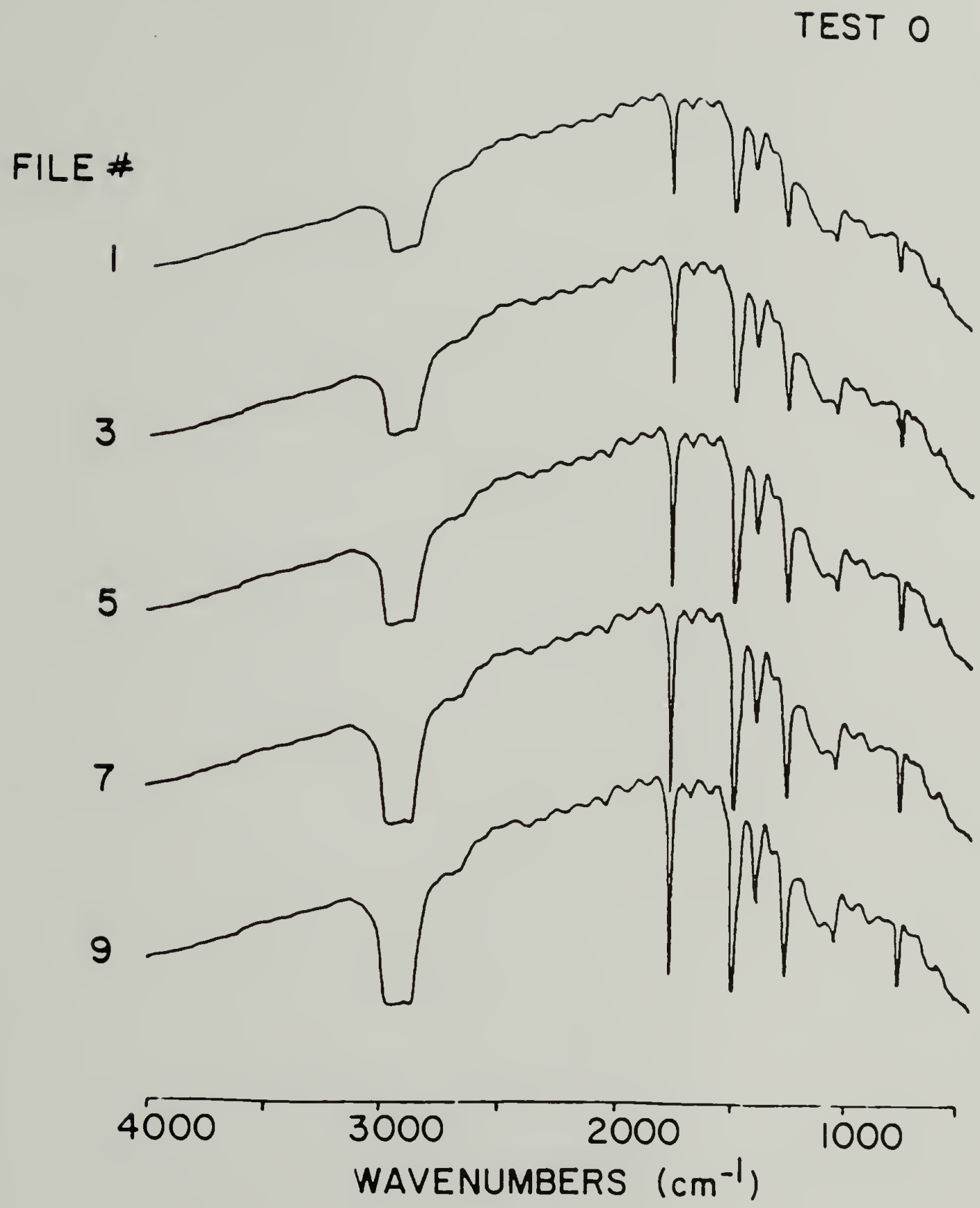

Figure 25b

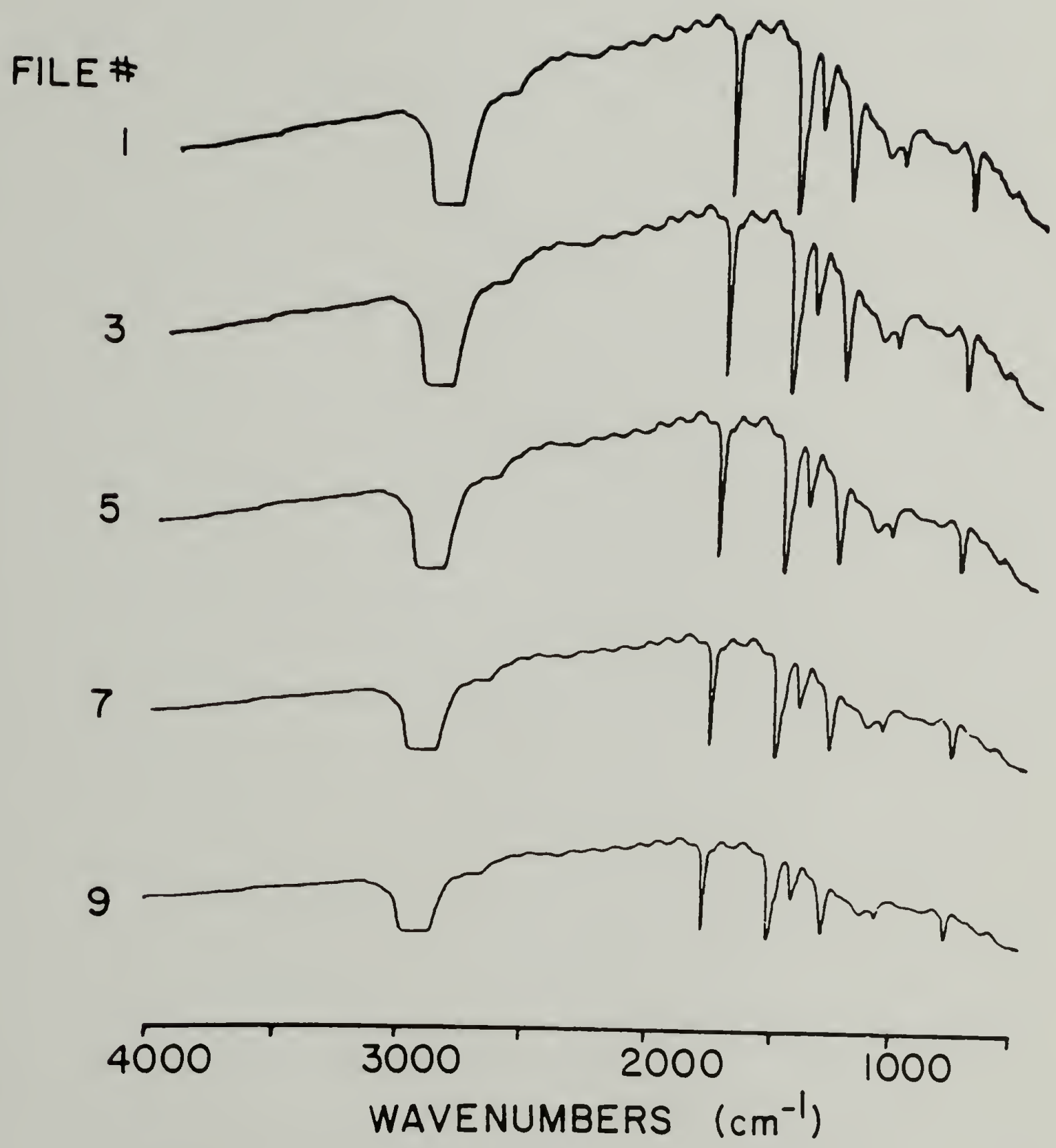

Figure 25c

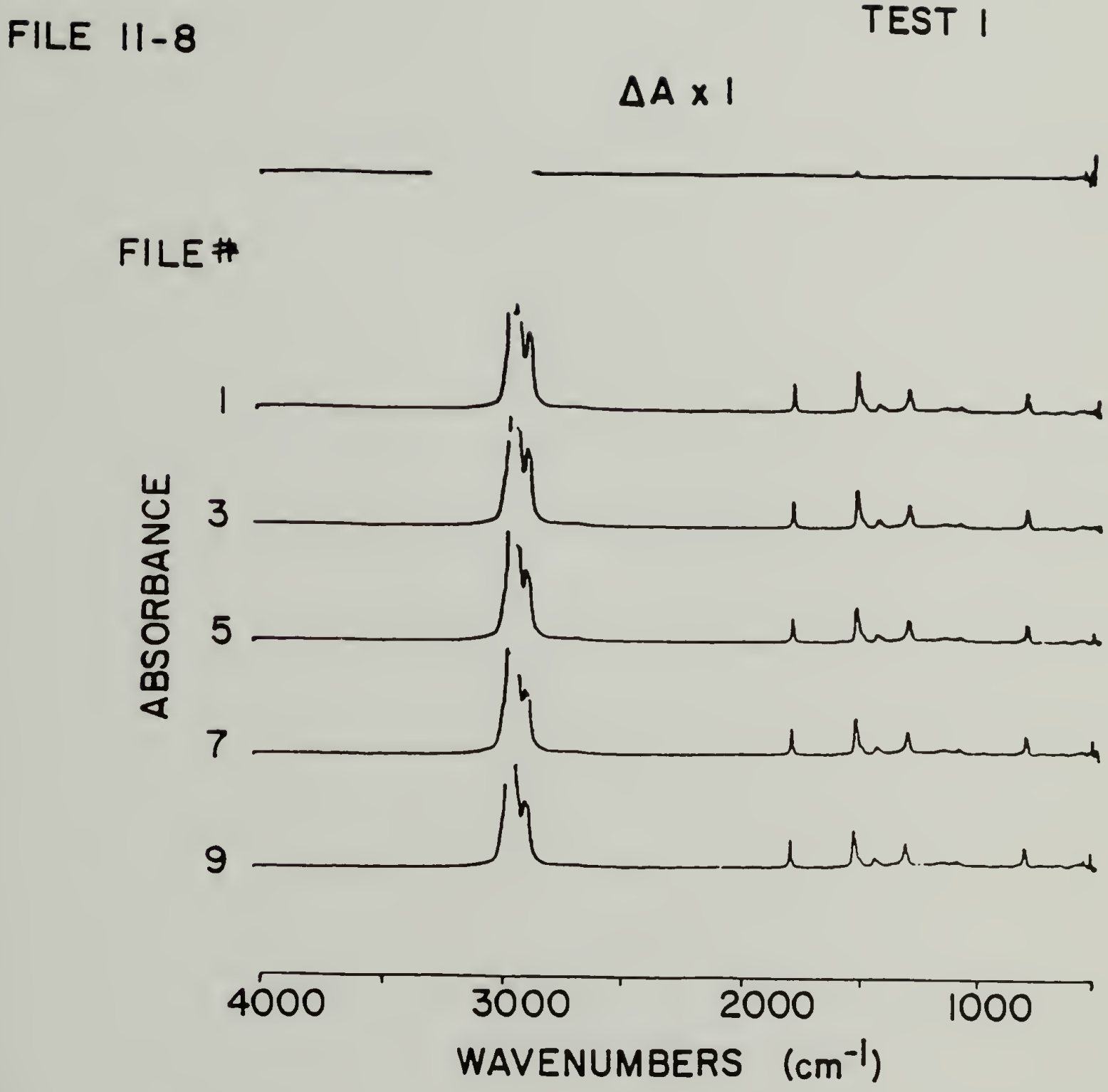
FILE 11-8
TEST 1
ΔA x 1
FILE #
1
3
5
7
9
ABSORBANCE
4000
3000
2000
1000
WAVENUMBERS (cm⁻¹)

Figure 25d

optical experiments to be compared directly with traditional dynamic mechanical experiments. Furthermore, the wide range of time resolutions available (0.1 msec to 10 sec) is also desirable for viscoelastic studies in which the response is often plotted vs. log time.

An example of results obtained by this TRS method are shown in Figure 26. Low density polyethylene was chosen for this experiment because its rheo-optical behavior is well characterized (18,120,121). The crystalline orientation is known to lag behind the applied strain and can be followed by the dichroism of the CH_2 bending vibration in the 1400 cm^{-1} region. A slow cooled, low-density polyethylene film was prestrained 5% and a 3% amplitude 0.5 Hz dynamic strain applied. A series of 18 parallel and 18 perpendicular time resolved spectra were obtained and the dichroic ratios of the CH_2 bending region are plotted in Figure 26. Fitting the data to a cosine wave showed a 70° phase lag between the orientation and the applied strain. The phase delay is consistent with previously reported x-ray and birefringence data (18). Additional TRS results are presented in Chapter IV.

The poor quality of the fit to the cosine curve in Figure 26 demonstrates the need for improved S/N ratio in TRS. One approach to the improvement of the S/N ratio is the use of the polarization modulation technique which is discussed in Chapter V. A more obvious approach is to signal average more scans by collecting for a longer time period. Another possibility is to improve the time efficiency of the collection. Table 4 shows that there is an uneven distribution of

Figure 26. The measured orientation function for the 1470 cm^{-1} bending vibration of polyethylene in a 0.5 Hertz time resolved experiment.

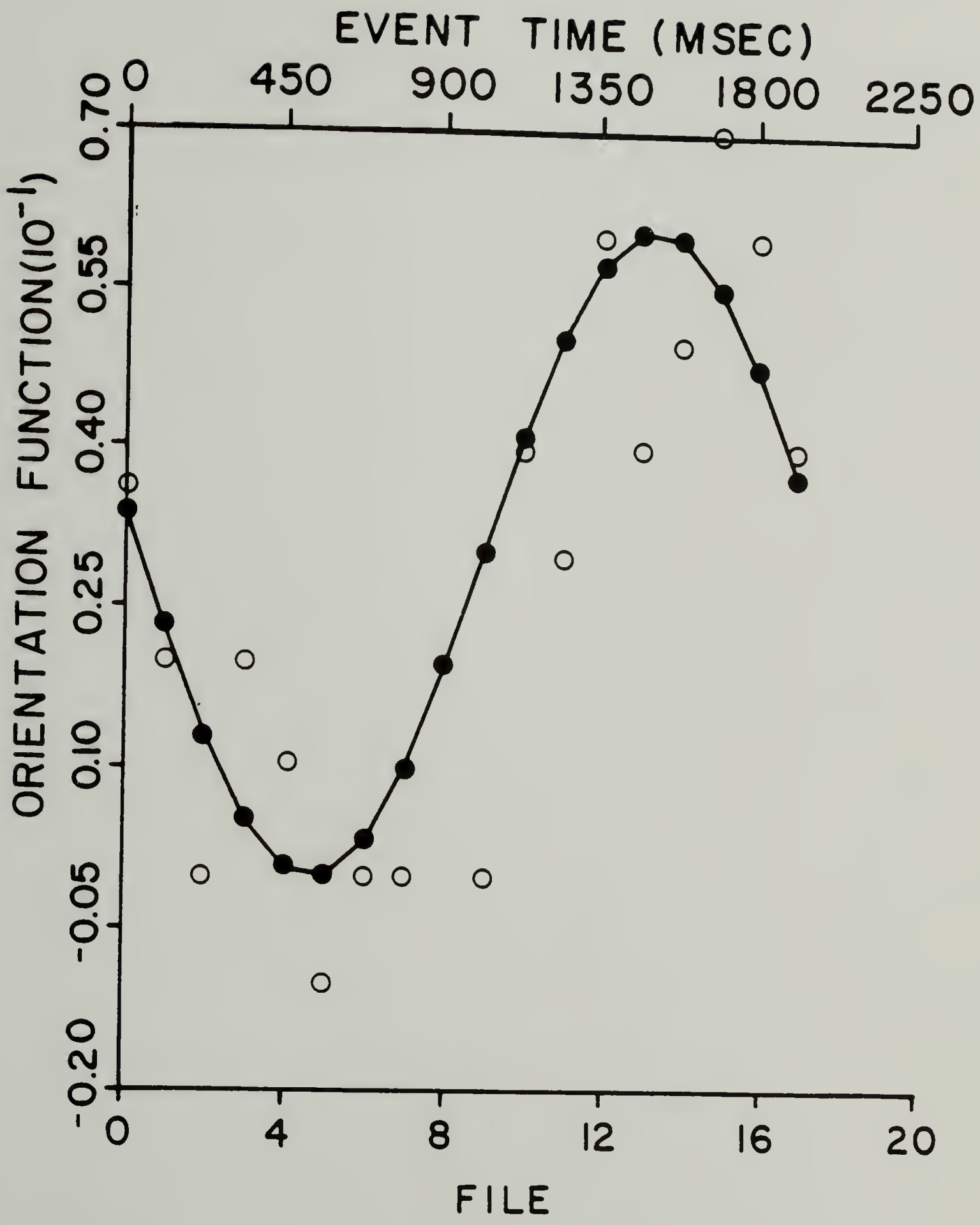
EVENT TIME (MSEC)
0
450
900
1350
1800
2250
ORIENTATION FUNCTION(10⁻¹)
0.70
0.55
0.40
0.25
0.10
-0.05
-0.20
0
4
8
12
16
20
FILE

Figure 26

the number of scans coadded into the different files. This non-random distribution of collected counter values is probably caused by the fact that the time required to coadd the scan depends on its clock value. This dependency occurs because the hard disk access time is different according to where the destination file is located. This non-randomness has been eliminated by moving the sample file (where the data is collected) to another location on the disk. This modification has resulted in at least a three-fold reduction in the time required to collect a minimum number of scans into each destination file.

Another problem is that the original data collection macro program would abort when the successive interferograms did not correlate. Modifications to this macro now allow these shifted interferogram peaks to be coadded by using the phase calculate command to measure the peak position and the special put/get commands to align the peaks. This allows collection even when the peak location is not stable. The final problem involves the software execution time necessary for coadding; it slows down the collection rate by a factor of three to six over the regular data collection. This overhead can be reduced by better hardware (a faster disk), better software (coadding the interferograms directly in the main memory or by having the collection and coadd routines call each other directly instead of through the macros) and/or by modified collection schemes (perhaps collecting a whole disk of files before sorting them). These gains could reduce the software execution time so that the collection rate

is only limited by the interferometer scanning rate.

In a different approach, Molis et al. have developed a TRS scheme in which the sample event period is matched to the interferometer scan period by an external microprocessor (122). The regular collection software is used so that there is no penalty in data collection efficiency. This method has traded more limited time scales (0.5 to 5 second sample event cycles) for highly efficient data collection.

Conclusion

The new TRS method described in this chapter has been specifically designed for polymer rheo-optical studies. The flexibility in choice of strain waveforms and time scales is greater than in the available commercial TRS packages. Results of initial experiments on polyethylene agree with data from other methods and the data presented on poly(tetramethylene terephthalate) in Chapter IV provide direct evidence regarding the rate of the crystal-crystal phase transition in that polymer. The technique should have general application in understanding viscoelastic phenomena in complex polymer systems and can also be used to study piezoelectric and liquid crystalline materials in electric fields.

C H A P T E R I V

INFRARED DEFORMATION STUDIES OF POLY(TETRAMETHYLENE TEREPHTHALATE) AND POLY(ETHER ESTER)

Introduction

Infrared rheo-optical studies of poly(tetramethylene terephthalate) (4GT) and a random block copoly(ether ester) copolymer, Hytrel®, are presented in this chapter. These studies have emphasized the assessment of the rate and amount of the stress induced, reversible, crystal-crystal phase transformation in both the homopolymer and the copolymer. Although this solid-solid phase transition (α to β) has been found for the homopolymer, its existence in the copolymer has not been demonstrated previously. Since 4GT served as one of the components, and is in fact the crystallizable portion, its deformation induced structural changes significantly influence the mechanical properties of the copolymer. By using the newly developed infrared rheo-optical methods, the overall mechanical behavior is interpreted in terms of the transformation mechanism and the orientation of both the hard and soft segments.

Structure and Morphology of Hytrel®

The synthesis of Hytrel®, a random block copoly(ether ester), occurs by a condensation reaction (55,123). The hard segment is

tetramethylene terephthalate, which crystallizes into the triclinic α unit cell of poly(tetramethylene terephthalate) (51,124,125). The non-crystalline hard segments form a compatible amorphous domain with the soft segment, poly(tetramethylene oxide) (Mw = 1000). Several morphology studies of these poly(ether esters) have been published (55,56,124-127).

The morphology of Hytrel® is similar to many semicrystalline polymers. Hytrel® can form spherulites when cooled slowly from the melt (124,125) and, when annealed, shows a typical increase in lamellar spacing with temperature (128). However, because Hytrel® is a random block copolymer, a distribution of hard segment sequence lengths which depends on the mole fraction of hard segments exists (55,128). This sequence length distribution causes some aspects of the copolymer morphology to differ from the typical crystallization behavior of a semicrsytalline polymer. These differences occur because some hard segment sequences are too short to be incorporated into the crystalline lamellae (125,128,130). For example, in the copolymer, isothermally crystallized spherulites stop growing long before they impinge on each other. This occurs when the hard segments which are long enough to crystallize at the particular temperature have been depleted. Even though there are still more hard segments available, they are in sequences too short to crystallize at these crystallization conditions. If the temperature is reduced further, additional segments can then crystallize (124,125). In general, samples crystallized at high under-coolings exhibit an ill-defined structure of

interlocking lamellae resulting from the high nucleation densities (125).

Hytrel® is used as an impact toughened plastic or as a thermoplastic elastomer in which the hard segment crystals act as crosslinks connecting the soft segments. Therefore, the mechanical properties of Hytrel® in terms of stress or strain depend very much on the relative compliance of each phase. When highly stressed, the hard segment domains can break apart, causing irreversible changes in the sample. Since the relative α and β content of 4GT is determined by the stress in the crystalline regions, by using our spectroscopic techniques we have a unique opportunity to directly measure and interpret the stress distribution in a copolymer of complicated morphology undergoing uniaxial deformation.

The α - β Transition in Poly(tetramethylene terephthalate)

A study of Hytrel® is necessarily related to a clear understanding of the mechanical properties, morphology, and α-β transition of the homopolymer 4GT. The influence of the α-β transition on the mechanical properties of 4GT can be illustrated by comparing its stress-strain curve with the similar polyesters, poly(trimethylene terephthalate) (3GT) and poly(ethylene terephthalate) (2GT). As a result of this phase transformation, a stress plateau occurs in the stress-strain curve of 4GT extending from 2 to 10 percent strain (131). The differences in the mechanical behavior of these three polyesters resulting from their chain conformations can be interpreted in terms of the changes observed in WAXS fiber repeat period with

applied strain (49). In 2GT, little change in the fiber repeat with strain is expected or observed, therefore, the modulus is quite high. 3GT shows a large linear increase in the fiber repeat, suggesting a continuously changing conformation in response to the strain. In contrast to 3GT, 4GT shows a more abrupt change in fiber repeat resulting from the stress induced transition from one conformation to a second (49). The stress plateau and the dramatically lower modulus of 4GT compared to 2GT is a result of this transition in 4GT.

The conformation of the four adjacent methylene groups in the α form is nearly gtg' and the β form conformation is approximately ttt (132). X-ray diffraction studies of the α-β transition in 4GT have shown that during transformation from the α to the β form, the c-axis of the unit cell increases from 11.6 to 13.0 Å, a 12% increase in length (49). The relative amount of α and β crystalline structures can be determined from the intensity of the $(\bar{1}04)$ or $(\bar{1}06)$ reflections of each structure (49).

The different conformations of the α and β structures are reflected in their infrared and Raman spectra. The largest conformational changes occur in the tetramethylene sequence and correspondingly the vibrational modes which involve them are the most sensitive to the microstructural changes. The conformationally sensitive IR bands of the α form are the CH_2 rocking modes(917 and 752 cm^{-1}), the CH_2 bending modes (1350 and 1383 cm^{-1}), and the wagging modes (1450 and 1460 cm^{-1}). For the β form, these bands appear at 960, 840, 1375, 1393, 1470, and 1484 cm^{-1} respectively (27). These

band assignments have been established in previous studies of several tetramethylene terephthalate model compounds (133). Since the vibrational bands are characteristic of local chain conformation, vibrational spectroscopy provides the high selectivity needed to monitor the microstructures when the sample is deformed macroscopically. In fact, previous spectroscopic studies have attempted to clarify the relationship between the α - β transition and the overall stress relaxation (134), hysteresis in the phase transition (135), and the extension of amorphous chain segments in 4GT (49). It has been established that when amorphous 4GT is elongated to 350% a significant amount of β structure is formed from chains which were previously amorphous. Upon removal of the stress, the amount of β form did not decrease. The failure of the β form to return to the α form may be due to one of two reasons. First, the crystal stress may be "locked in" by the glassy amorphous material, or second, as suggested by Siesler, chains in the amorphous state do not have intermolecular crystal packing considerations to drive them back into the more stable α form (136).

Although the hysteresis cycle of the α-β transition has been studied by a number of investigators (54,131,134,137-139), the results were inconclusive because the contributions of the plastic deformation in the amorphous and crystalline regions and the α - β transformation to the hysteresis have not been separated. This point is illustrated with stress-strain data taken from Siesler's paper (Figure 27) (135). The difference in area under the loading curve and the unloading curve gives the total hysteresis. Only when a reloading curve is shown

Figure 27. A stress strain curve illustrating the observed hysteresis for poly(tetramethylene terephthalate) (data from Ref. 135).
a. loading curve
b. unloading curve
c. reloading curve

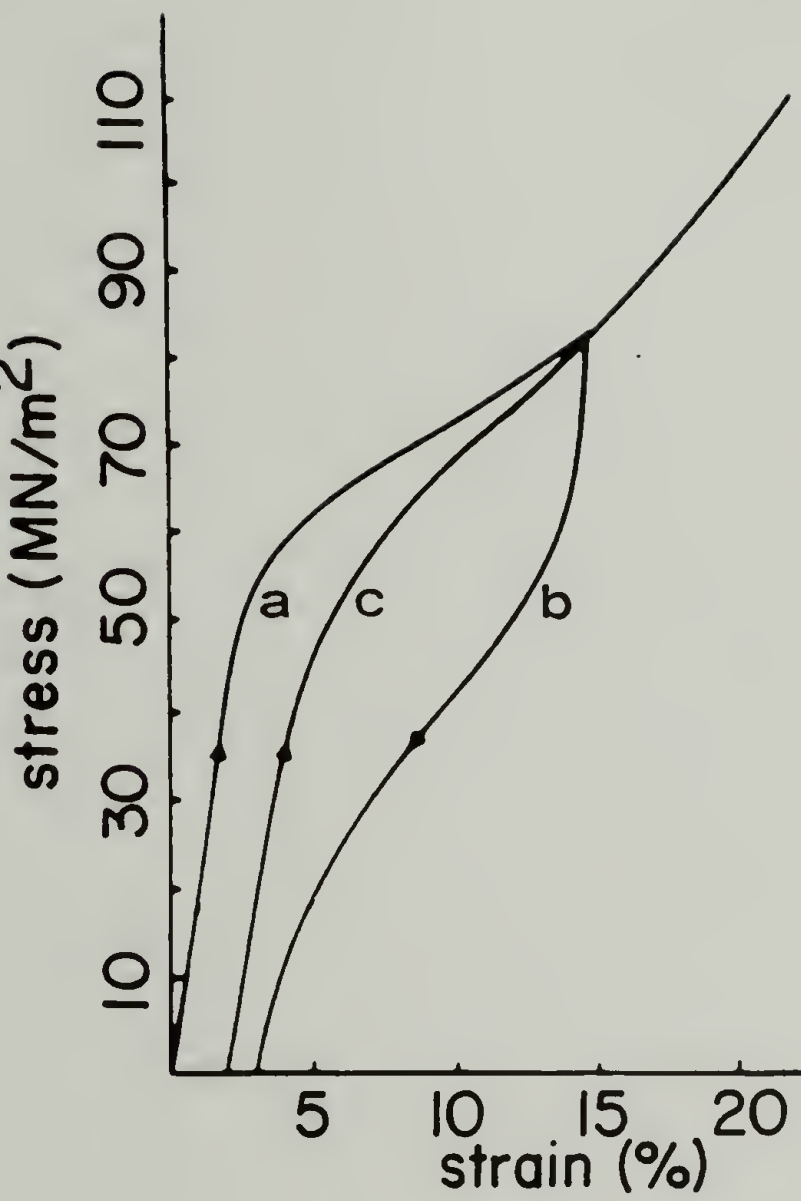

Figure 27

can one begin to separate the plastic deformation from the intrinsic α-β hysteresis. The area between the loading and reloading curves is attributed to plastic deformation and the area between the reloading and unloading represents α-β hysteresis. Without measuring the reloading curve, the total hysteresis would be wrongly attributed to the α-β transition.

Theoretical studies have attempted to interpret the thermodynamics and kinetics of the α-β transition (54,138-140). The stress hysteresis associated with the transition is taken as evidence of a cooperative phenomenon. Tashiro et al. modeled this phase transformation as a first order thermodynamic transition (138). The functional dependence of the free energy and theoretical stress-strain curves associated with their model are shown in Figure 28. It was demonstrated that for stresses above a critical value, F*, the free energy of the β form is lower than the α form. The sample is all α below the critical stress, then at the stress plateau the β content increases linearly with strain until 100 percent β is reached. Afterwards, the stress again increases with strain. From the variation of measured critical stress with temperature, the enthalpy and entropy of transition per mole of monomer unit were found to be 5.1 kJ/mole and 12.6 J/mole °K, respectively. However, this model fails to predict the observed hysteresis in the transition and the agreement of the theory and experiment is poor above 60°C.

A different model presented by Brereton et al. attempts to explain the observed hysteresis (54). This model treats the α - β

Figure 28. The functional dependence of free energy and the theoretical stress curve for the first order phase transition model of Ref. 138.

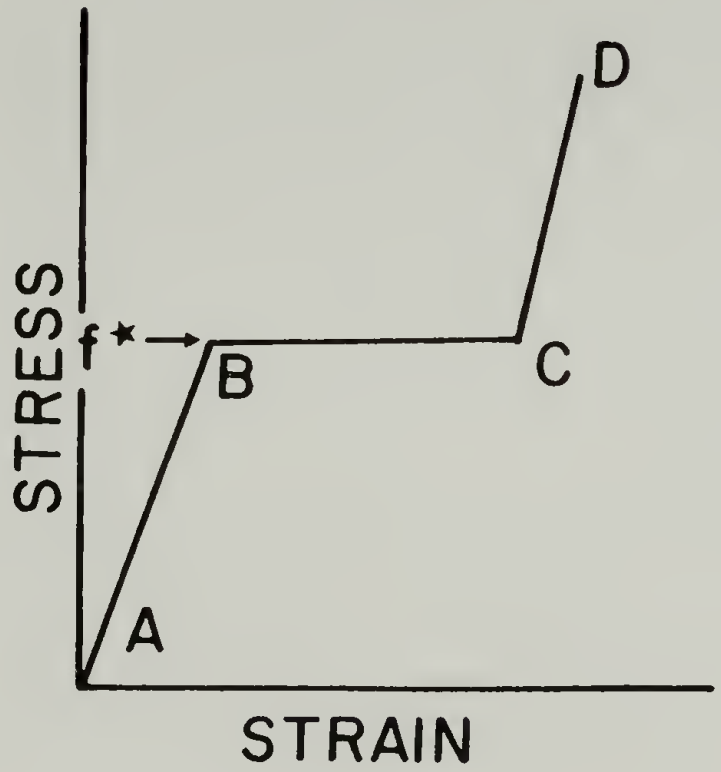

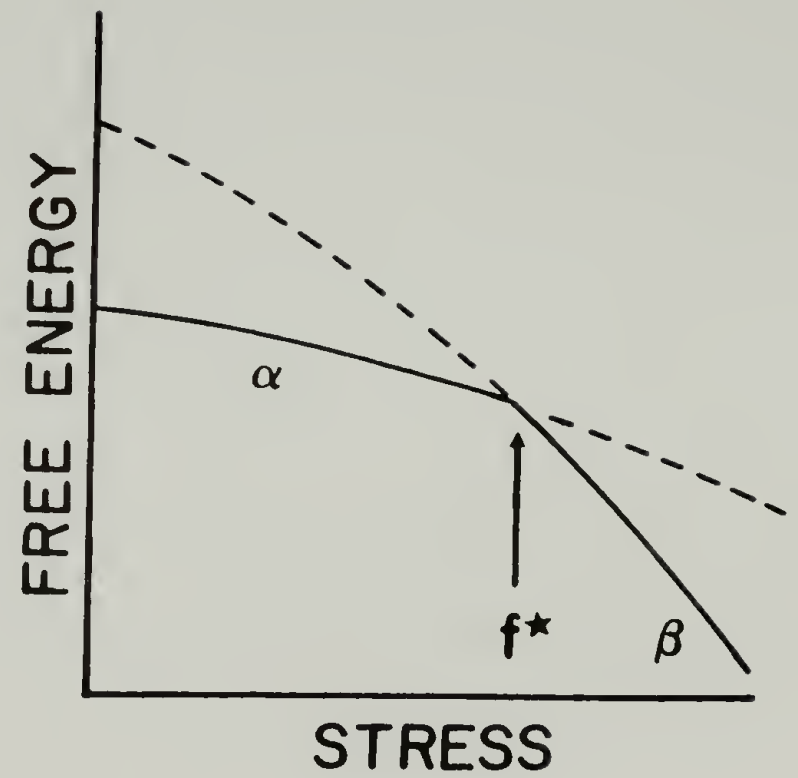

Figure 28

transformation as a cooperative phase transition. Their hypothesis states that the energy difference between the α and β forms at constant temperature not only depends on stress but also depends on the relative amounts of the α and β forms already present. Their theory gives the free energy of the α and β forms as $G_\alpha = G_{\alpha o} + V_\alpha \sigma_L$ and $G_\beta = G_{\beta o} + V_\beta \sigma_L$. The free energy of the α and β states is altered by σ_L, the local stress, given by $\sigma_L = \sigma + K \cdot m$. The local stress arises from crystal lattice packing energies, i.e. the total free energy of a single chain segment is lower when the neighboring chains in the crystal lattice have the same conformation (α or β). As the crystals transform from all α to all β, m, given by $(x_\beta - x_a)/(x_\beta + x_\alpha)$ varies from -1 to +1. The x_β and x_α refer to the volume fractions of β and α phases respectively. The factor K gives the strength of the cooperative interactions. The equations were solved to determine m as a function of stress. A family of hysteresis curves at different temperatures which fit the experimental data were obtained (27). The parameters that control cooperativity in this mode were then determined by fitting the observed hysteresis behavior.

In the interpretation of the experimental results, neither Tashiro or Brereton considered the effects of non-uniform crystal stress distribution or amorphous viscoelasticity on the α-β transition.

Rate of the α-β Transition

Experiments measuring the rate of α-β transition fall into two groups: 1) experiments directly measuring the amounts of the α and β forms as a function of strain, and 2) experiments that do not measure the α and β content, but imply from the data that the α-β transition is taking place. An experiment of the second type by Davies et al. attributes the strain dependence of J' and J" in a 10 Hz dynamic mechanical experiment to the α-β transition (137). Although the experimental data agree with the theoretical predictions, several problems exist: 1) the model does not distinguish between crystalline and amorphous regions (which will have very different interchain interactions and mobilities); 2) although the model incorporates a transformation between two conformations with different chain extensions and energies, these two states need not correspond to α and β states. The latter deficiency is clearly demonstrated by NMR studies. In that case, thermally activated rotational motion of the methylene sequences in 4GT has been observed on a 10^{-5} second time scale; but, the motions do not correspond to a transition between the α and β states (141-143).

There are virtually no experiments which have directly measured the rate of α-β transition. Siesler attempted to follow the dynamics of the α-β transformation in a FT-IR experiment (54). The 60 second ramp strain (0 to 20%) used in that experiment resulted in a 120 second loading-unloading cycle. The IR results did not show any time

dependence on this time scale (120 seconds). An x-ray diffraction study was also attempted without success (54). Time-resolved spectroscopy (TRS) can be used to obtain a better estimate of the transformation rate. As described in the previous chapter, the TRS techniques can be used to obtain spectra of improved time resolution and significantly higher signal to noise ratios. These techniques require many strain cycles to be applied to the sample. A stringent requirement is that the sample response be exactly the same for each strain cycle. For each particular sample, there are upper limits on the strain rate, the strain amplitude, and the number of strain cycles that can be applied and yet retain repeatable sample response. An additional condition requires that the deformation imposed on the sample will produce a large enough spectral change to be measured with a good signal to noise ratio. For the 4GT films used, these conditions were satisfied with a one Hertz triangle wave with a three percent strain amplitude. These experimental conditions result in a 6 percent/second strain rate and were applied for about 1500 cycles (25 minutes). The results of this one second time scale IR experiment are described later in this chapter.

Experimental

Valox 310 poly(tetramethylene terephthalate) was supplied by the General Electric Company. The sample was dried for 4 hours at 120°C in vacuum to remove moisture, then pellets were melt-pressed and

quenched into cold water forming thin, ca. 50 μm films. The films were then drawn 2.5X at 120°C to align the crystals in the stretch direction, giving more effective coupling of the applied forces to the chains in the crystal. The film was mounted in the stretcher and a static pre-strain of 2 percent was applied. A periodic triangle strain waveform with a 3 percent amplitude and a 1 second period was applied to the sample. The unsorted TRS technique was used for collection of the spectra. A time resolution of 126.4 msec was used to produce eight spectra during the strain cycle. In unsorted TRS, the time to collect an interferogram (116 msec) is less than the time resolution (126.4 msec) and therefore the interferograms do not have to be sorted. The spectra were taken at 4 cm^{-1} resolution with at least twenty scans coadded into each file to attain high signal to noise ratios. The resulting interferograms were Fourier transformed, ratioed against a background file, and converted into absorbance spectra. The experimental TRS parameters are summarized in Table 5.

A sample of Hytrel® containing 83 weight percent hard segment was dried for two hours in vacuum at 120°C. The sample was melt pressed at 224°C for 2 minutes and then quickly air cooled to room temperature. The deformation behavior was characterized using the stretcher and FT-IR system described in Chapter III. The sample was elongated at a constant strain rate (0.02%/sec) up to 25% strain, then the strain was decreased (at the same rate) until the sample load reached zero. A series of fifty spectra, alternating between parallel and perpendicular polarization were obtained. The spectra were taken

TABLE 5

Experimental Time Resolved Parameters used for the Rate Determination of the α-β Transition

TRS Parameters	
clock period (time resolution)	126.4 msec
sample event period	1000 msec
time/interferogram data point	28.3 μsec
NDP, number of points in interferogram	4096
number of scans coadded to each file*	21 minimum, 45 average

TRS Relationships	
number of clock periods/sample event	7.91
time/scan	116 msec
number of clocks/scan	0.91 ǂ
number of data points/clock period	>4096 ǂ

*This is determined by the signal to noise requirements.

ǂSince the time per scan is less than the time resolution, i.e. the whole interferogram (4096 points) is collected in less time than one clock period (126 msec), the collected interferograms do not have to be sorted.

at 4 cm^{-1} resolution and required 25 seconds each to collect. To obtain dichroic results, each parallel spectrum was divided by the average of the perpendicular spectra preceeding and following it.

Discussion of Results

Rate of α-β transition

The combination of IR and WAXS studies has established that the 917, 938, and 960 cm^{-1} bands are due to the α, amorphous, and β phases, respectively (138,144). A typical spectrum of 4GT in the 900 to 1000 cm^{-1} region is plotted in the bottom of Figure 29. The height or area of these peaks can be used to follow the amount of each phase present. To reveal the changes in the spectra with strain more clearly, the first file (minimum strain) was subtracted (1:1 ratio) from all the files. The differences spectra are scaled 6.6 times and plotted in Figure 29. The results are summarized in Figure 30, where the applied strain, the increase in β content, and the decrease in α content are plotted as a function of time. The changes in the amount of each phase were determined by the area above or below the baseline indicated on each spectrum. The baselines were chosen to match the spectra at 1000 cm^{-1}, a region where no peaks are present. The baseline uncertainties are reflected in the error bars of Figure 30.

The TRS spectra show no evidence of delay between the strain and phase transformation when loaded and unloaded in a one second cycle.

Figure 29. The CH_2 rocking region of the infrared spectra collected by the time resolved spectroscopic technique of PTMT - eight successively subtracted spectra. Experimental conditions given in Table 5.

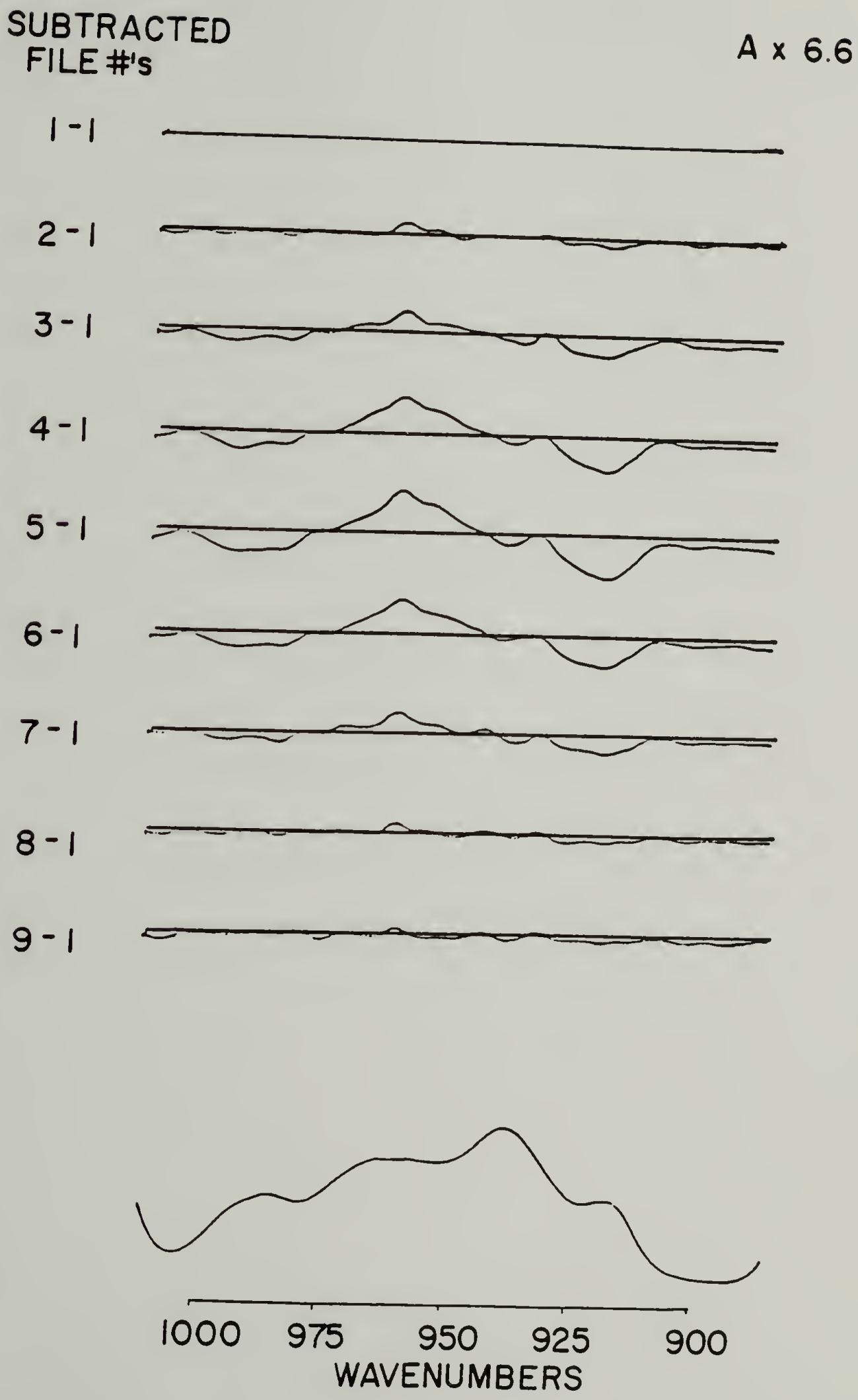
SUBTRACTED
FILE #'s
A x 6.6
1-1
2-1
3-1
4-1
5-1
6-1
7-1
8-1
9-1
1000
975
950
925
900
WAVENUMBERS

Figure 29

Figure 30. Summary of time resolved spectroscopic results for PTMT
a. applied strain
b. increase in β crystal form
c. decrease in α crystal form

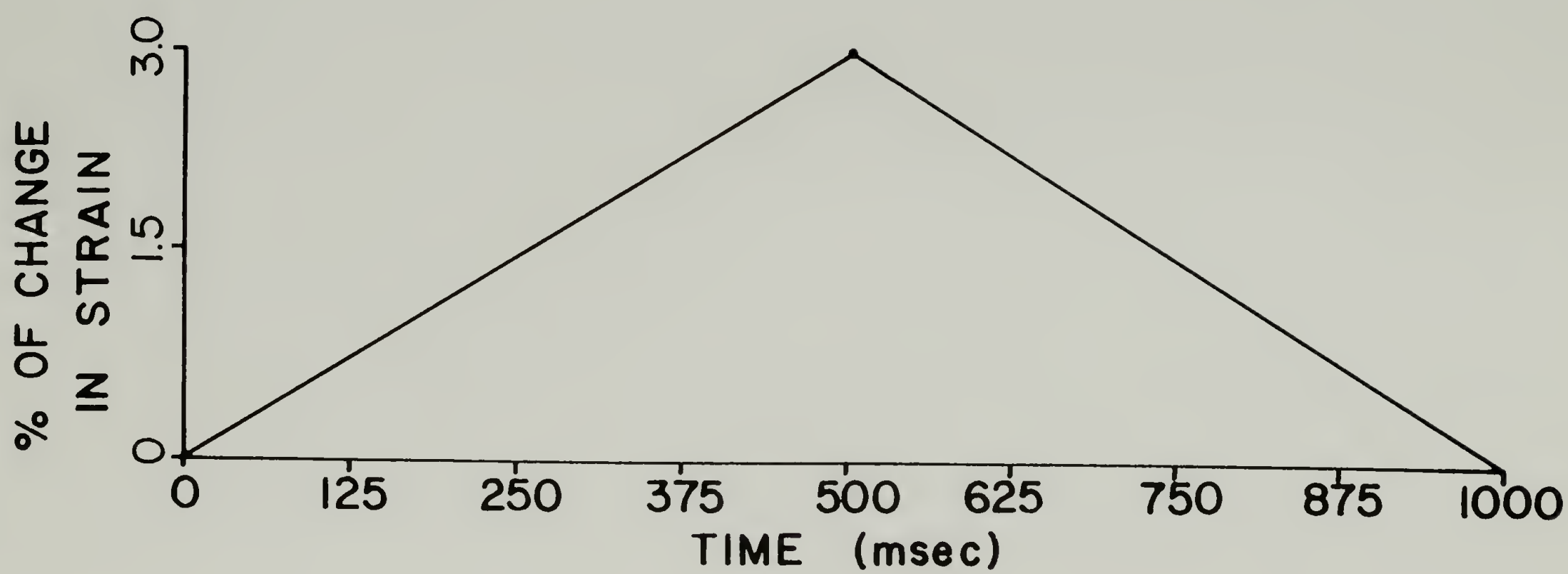
% OF CHANGE IN STRAIN
0
1.5
3.0
0
125
250
375
500
625
750
875
1000
TIME (msec)

Figure 30a

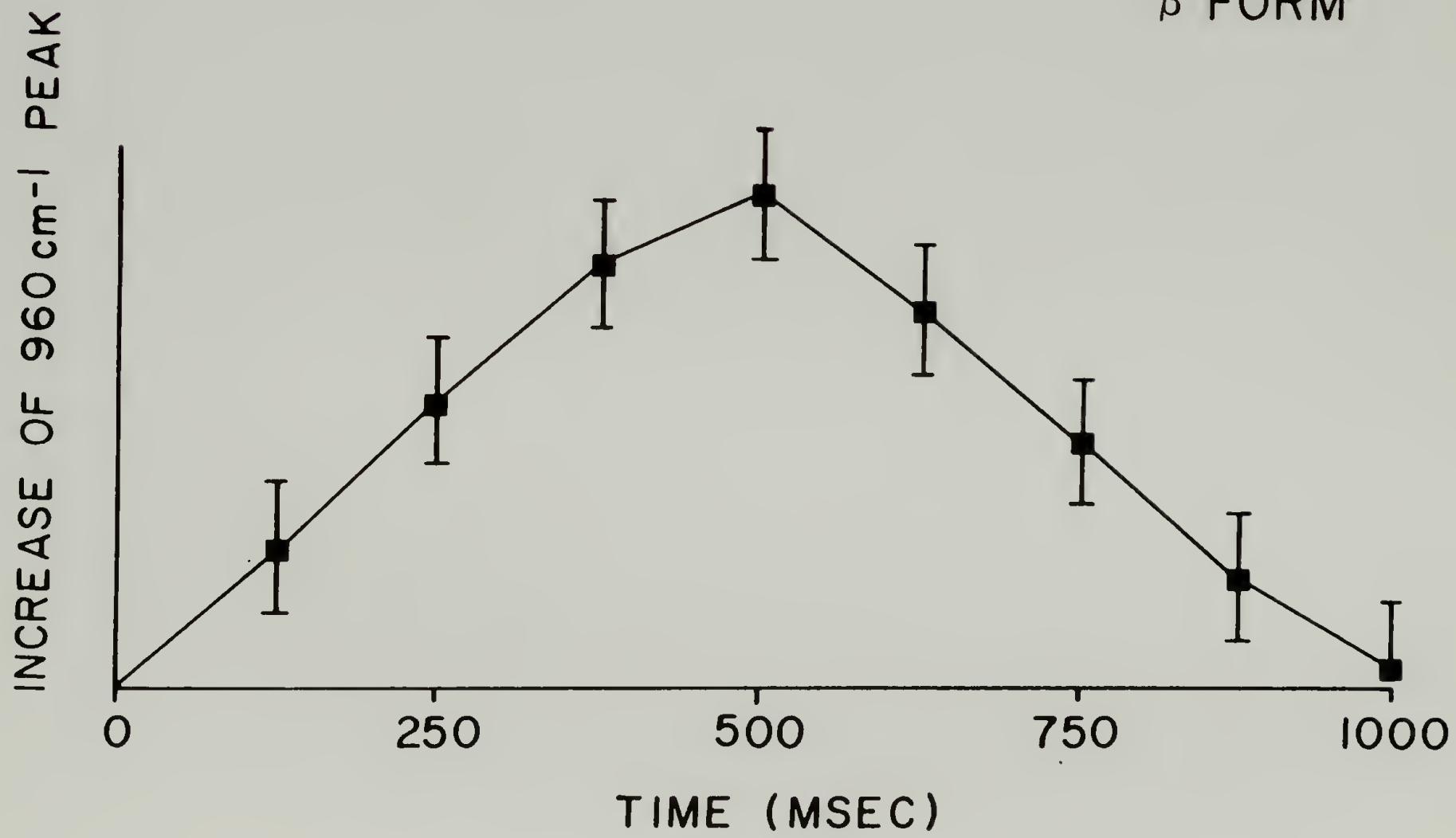

Figure 30b

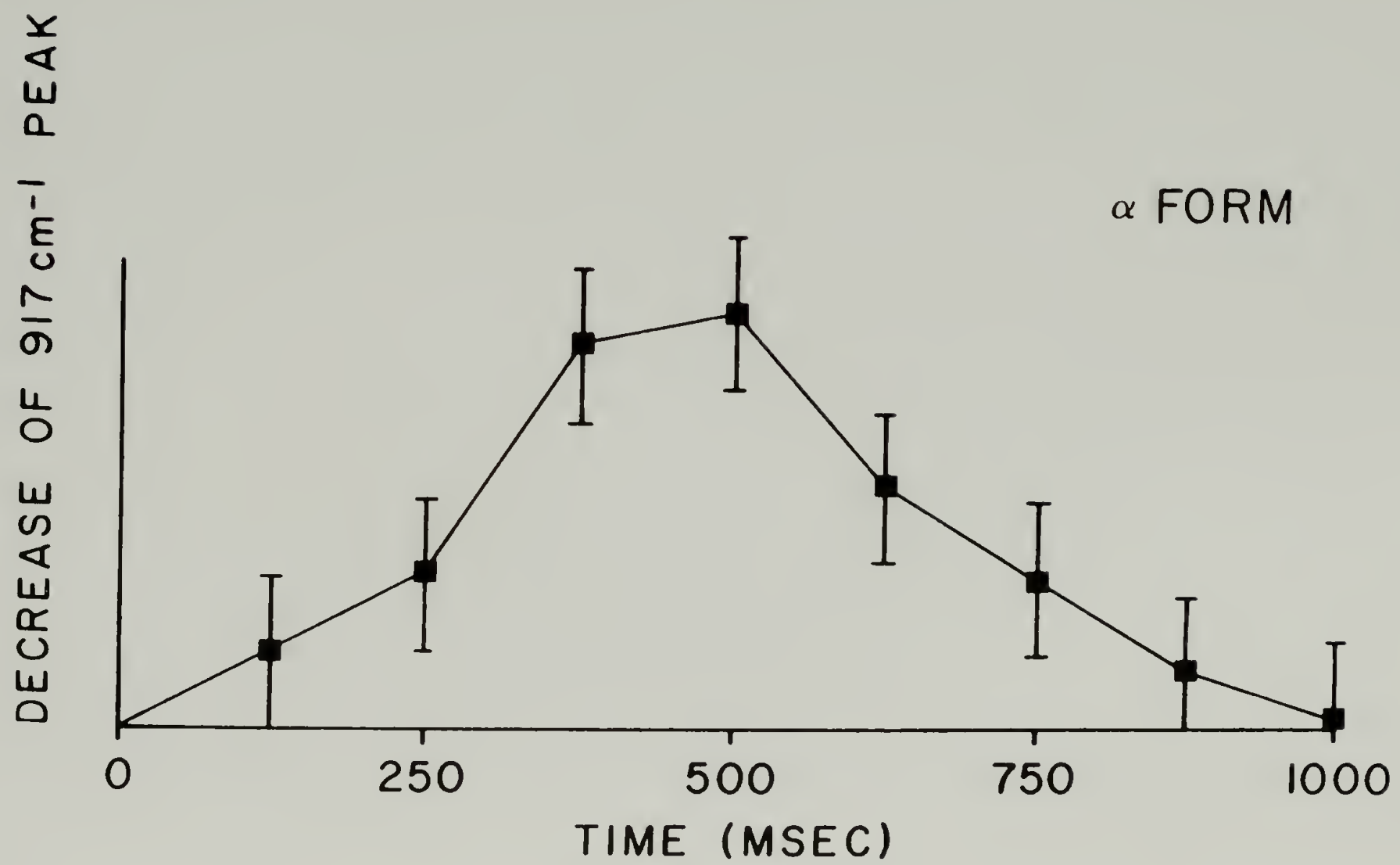

Figure 30c

The amount of α that is converted into β follows the strain very closely (Figure 30). The 3% dynamic strain produces a 6 percent increase in the height of the 960 cm^{-1} β peak. In this experiment, the effects of decreasing film thickness and change in orientation with strain were not taken into account. At low strains, these effects are small enough to be overlooked. However, in the study of Hytrel® which follows, the strains are larger and these effects are included in the analysis of the data.

In order to determine the transition rate, the experiment must be as fast or faster than the time associated with the phase transition. This condition has yet to be achieved. It may be possible to increase the time resolution of IR rheo-optical experiments for 4GT, but the strain amplitude may have to be decreased at higher frequencies of deformation to ensure repeatability of sample response. A resolution of 10 msec with a 10 Hertz strain wave probably can be reached using the present experimental set-up. Because the lower strains used at higher frequencies of deformation produce very small spectral changes that are difficult to measure, a major improvement in the TRS rheo-optical experiment would be required for frequencies much greater than 10 Hertz.

The development of intense synchrotron x-ray sources has improved the time resolution of WAXS rheo-optical experiments. Brown et al. have presented results of a WAXS study of the α-β transition in 4GT (145). Their results also did not indicate any delay in the phase transformation relative to the strain applied. At present, the time

resolution in x-ray experiments is limited by the rise time, 100 msec, and the persistence time, 1 second, of the phosphors used in the x-ray image intensifiers (146). Development of a better detector should produce interesting dynamic WAXS results in the future.

Infrared rheo-optical analysis of Hytrel®

A large hysteresis occurs in the stress-strain curve shown in Figure 31a. The orientation behavior of each phase is reflected by the changes in dichroic ratios plotted versus strain in Figures 31b-e. By using the peak heights of the 917, 960, and 938 cm^{-1} methylene rocking bands, the orientation of α crystalline, β crystalline, and amorphous tetramethylene terephthalate chain segments can be followed. The average sample orientation is determined from the dichroic ratios obtained from the integrated area of the entire CH stretching region. The transition dipole moments of the CH stretching vibrations are perpendicular to the chain axis while the methylene rocking vibrations are parallel to the chain axis (27). The increasing dichroic ratios of the 938 and 960 cm^{-1} bands show the chain segments are orienting parallel to the stretching direction. The 917 cm^{-1} α form peak shows increasing perpendicular orientation to the stretching direction. This behavior will be shown to be a result of the α to β transformation. The 960 cm^{-1} band dichroism shows a large hysteresis with strain while the dichroism of other bands shows no clear evidence of hysteresis.

Figure 31. Results of infrared rheo-optical study of Hytrel®. (▲) increasing strain, (■) decreasing strain.
a. force-strain curve
b. dichroic ratio-strain curve for the integral of the entire CH_2 stretching region
c. dichroic ratio-strain curve for the 960 cm^{-1} peak
d. dichroic ratio-strain curve for the 938 cm^{-1} peak
e. dichroic ratio-strain curve for the 917 cm^{-1} peak

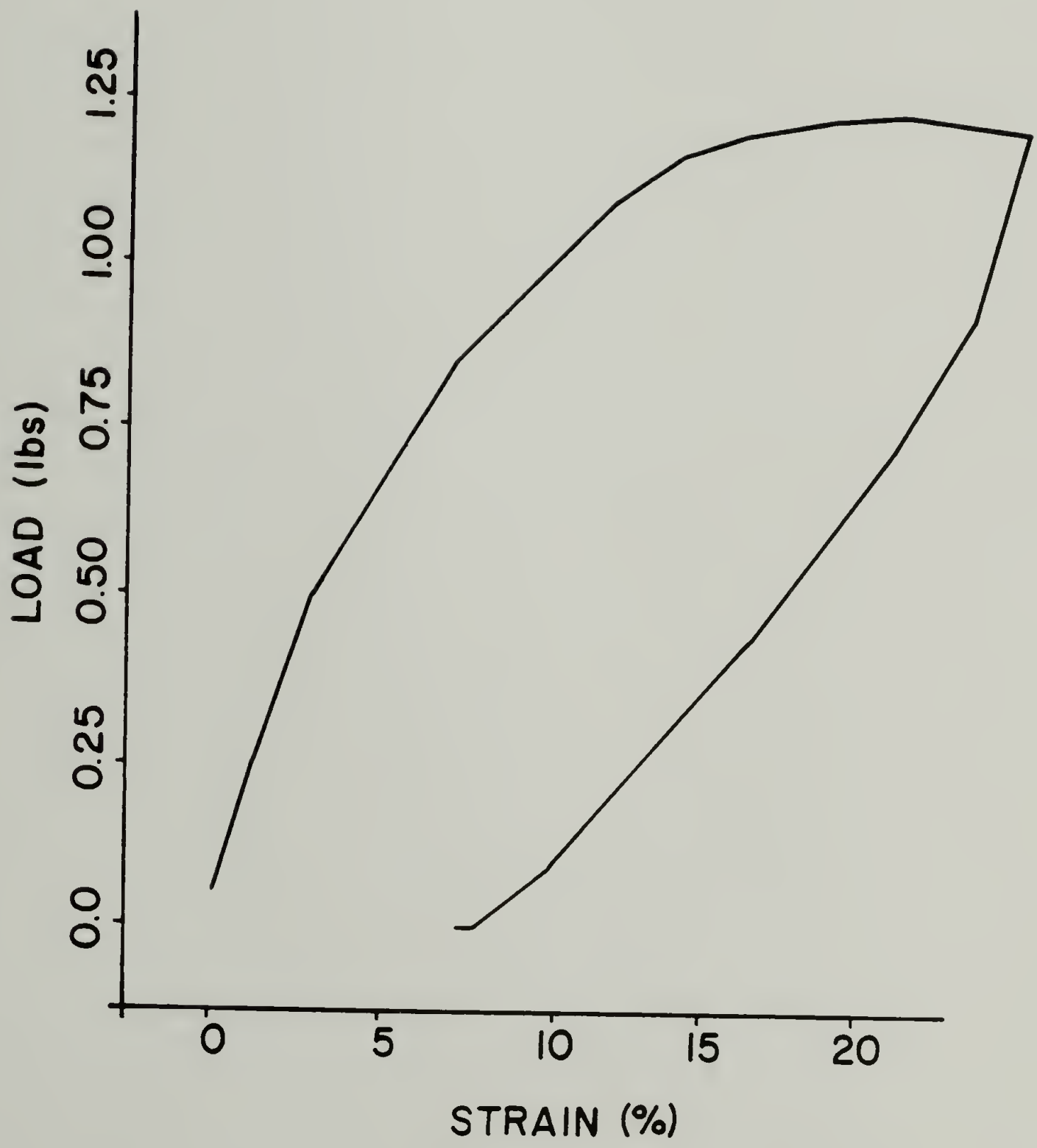

Figure 31a

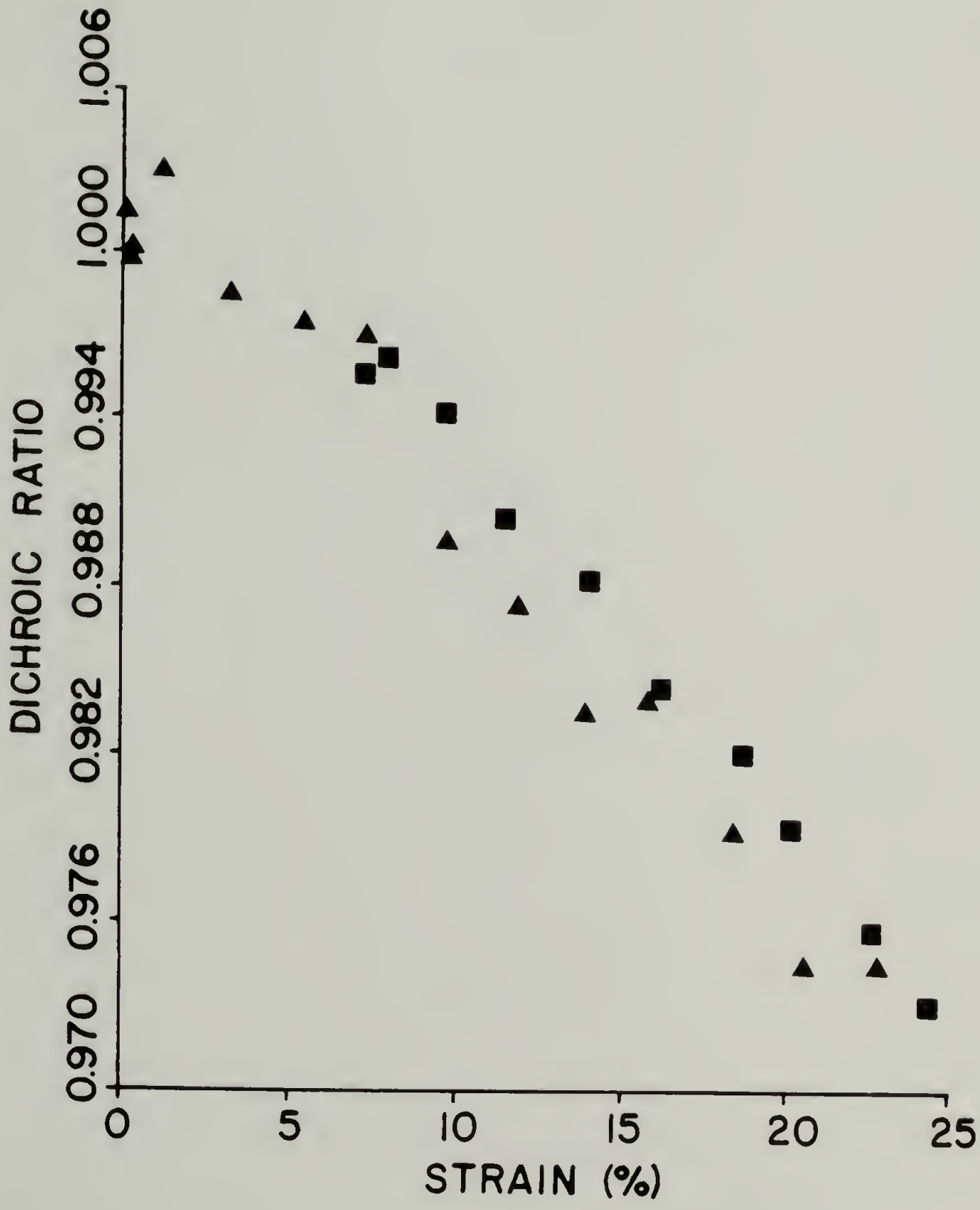
CH STRETCHING VIBRATION
DICHROIC RATIO
1.006
1.000
0.994
0.988
0.982
0.976
0.970
0
5
10
15
20
25
STRAIN (%)

Figure 31b

960 cm^{-1} β DICHROISM

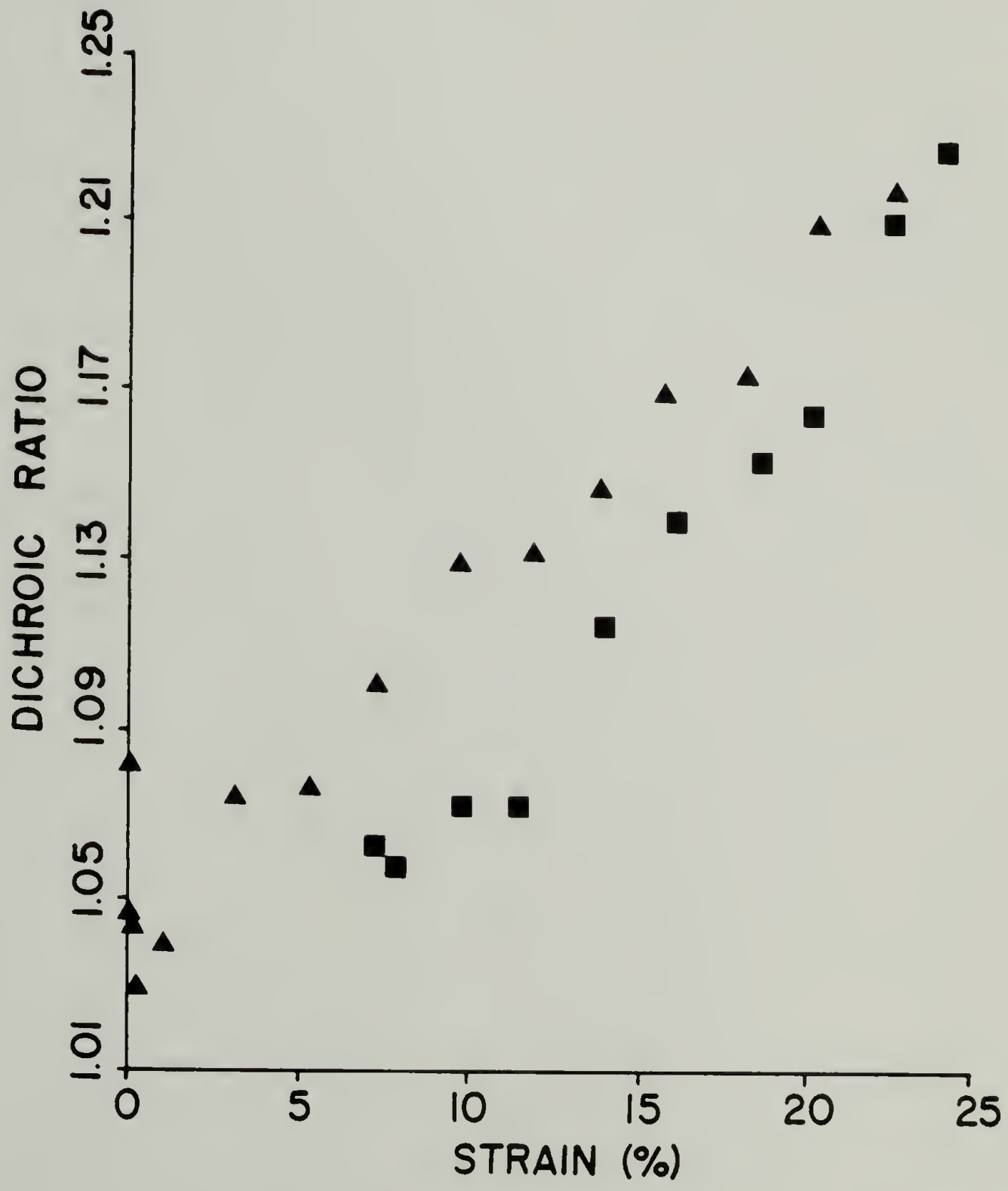

Figure 31c

938 cm^{-1} AMORPHOUS DICHROISM

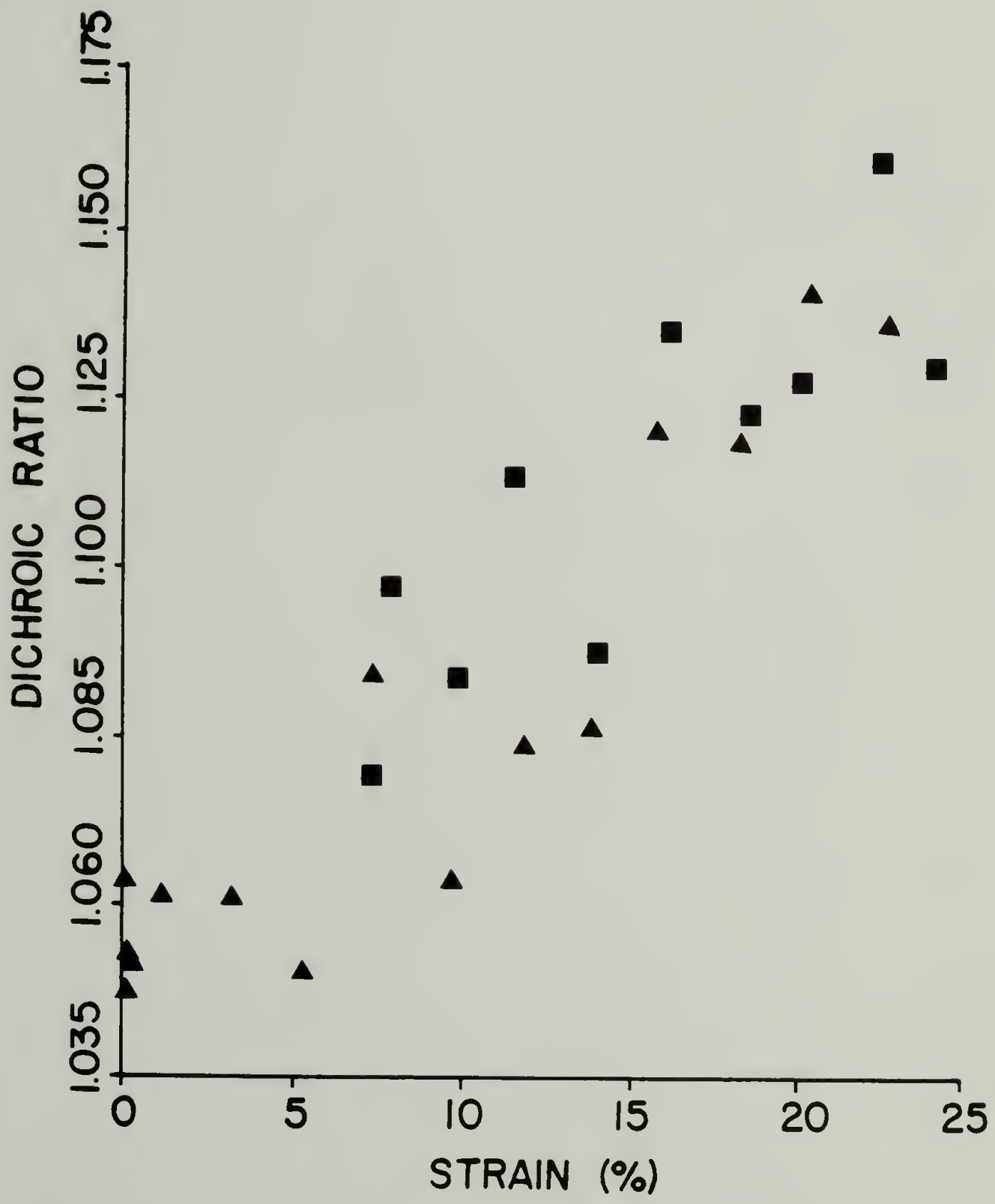

Figure 31d

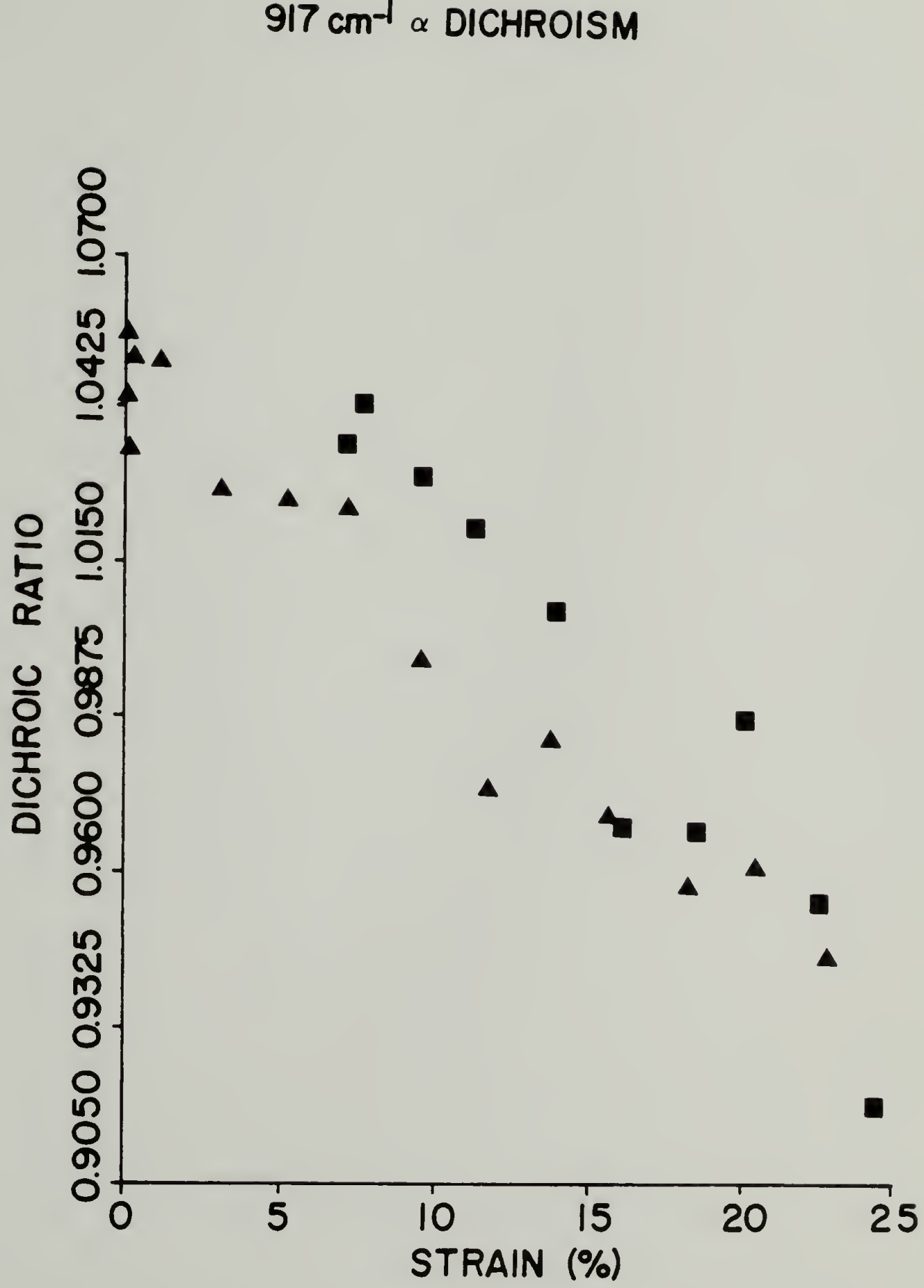
917 cm⁻¹ α DICHROISM
DICHROIC RATIO
0.9050
0.9325
0.9600
0.9875
1.0150
1.0425
1.0700
0
5
10
15
20
25
STRAIN (%)

Figure 31e

In order to follow the α to β transformation, the effects of crystal orientation must be taken into account. In Chapter III the structural absorbance, A_o, was shown to be independent of the sample orientation. A_o depends on the specific absorptivity, the sample thickness, and the concentration of each component. The structural absorbance is given by $A_o = A_{\parallel} + 2A_{\perp}$, when uniaxial symmetry of the deformation is assumed.

The structural absorbance is plotted vs. strain for the same four bands as the dichroism in Figures 32a-d. The change in A_o for the integral area of the entire CH stretching region reflects the decrease in sample thickness with strain. The increase in β content and the decrease in α content with strain is clearly shown by the change in their structural absorbances. There is no apparent change in A_o of the amorphous band (938 cm^{-1}); evidently the transformation of amorphous to β form that Siesler observed in 4GT homopolymer does not take place in Hytrel® at the stress levels present in our experiments.

The reduction in the α content causes an unexpected decrease in the α form dichroic ratio. The 917 cm^{-1} α band has its transition dipole moment along the chain axis (27), and its dichroic ratio, $A_{\parallel}/A_{\perp}$ is expected to increase as the chains orient in the stretching direction. However, the transformation of α-β depends on the orientation of the α crystallites with respect to the stretching direction. More of the crystals with their chain axes oriented along the stretching direction are expected to transform than are the unoriented crystals. Therefore, transformation of oriented α form into the β form is the

Figure 32. Structural absorbances for Hytrel®.
a. CH_2 stretching region showing decrease in film thickness
b. structural absorbance β form, 960 cm^{-1} peak
c. structural absorbance for the amorphous hard segments, 938 cm^{-1} peak
d. structural absorbance for the α form, 917 cm^{-1} peak

A_o of CH STRETCHING VIBRATION

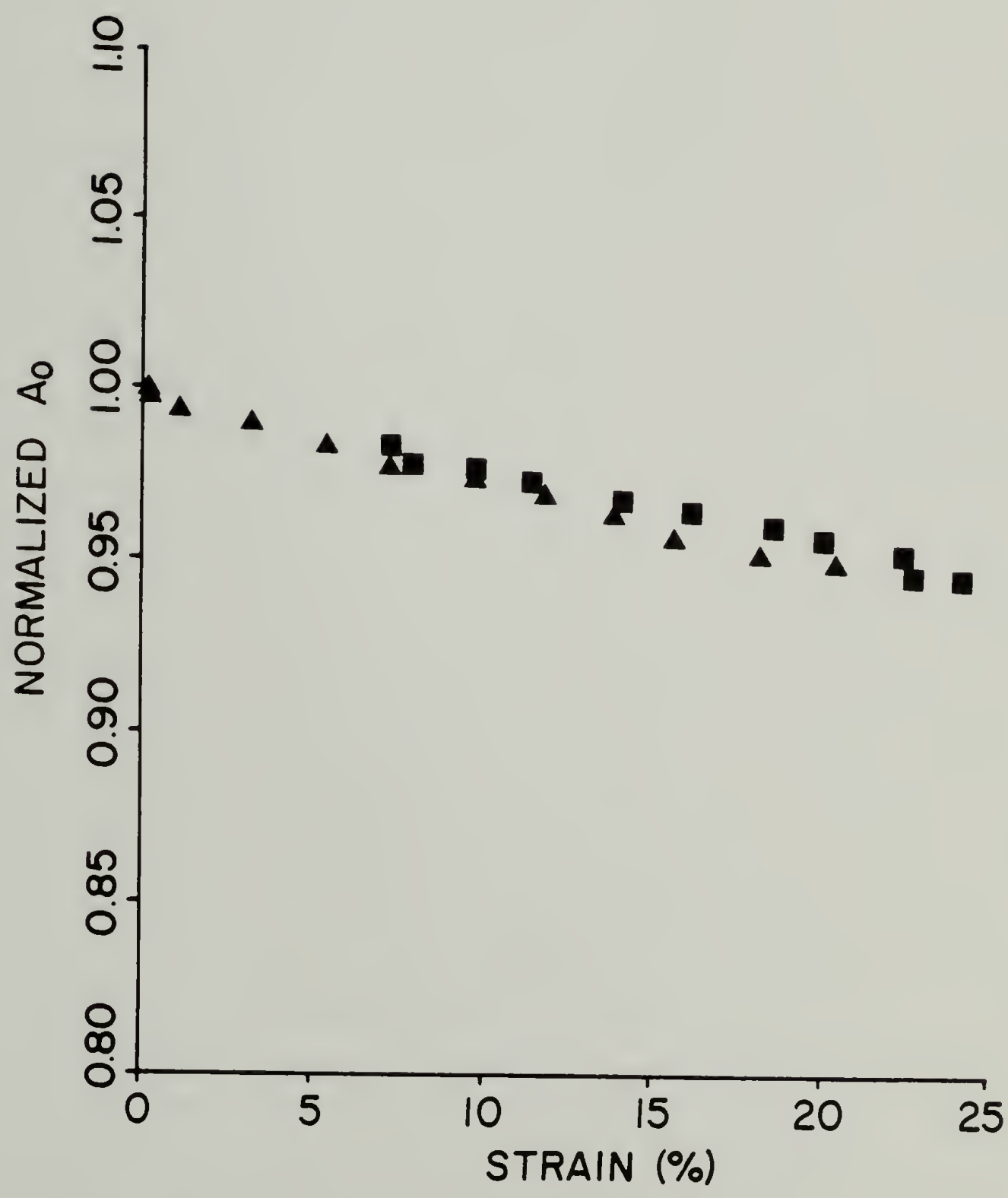

Figure 32a

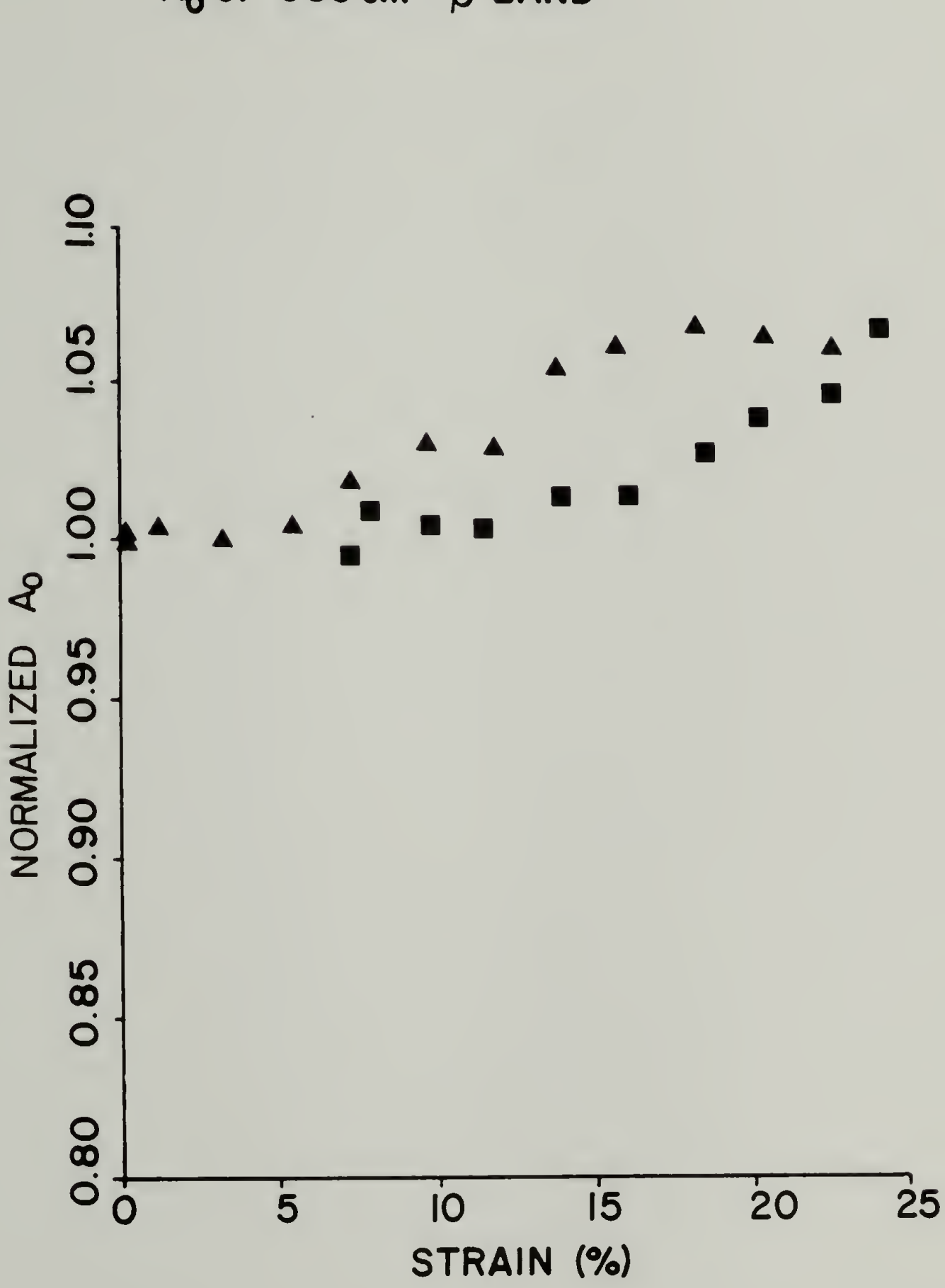
A_0 of 960 cm^{-1} β BAND
NORMALIZED A_0
0.80
0.85
0.90
0.95
1.00
1.05
1.10
0
5
10
15
20
25
STRAIN (%)

Figure 32b

A_0 of 938 cm^{-1}

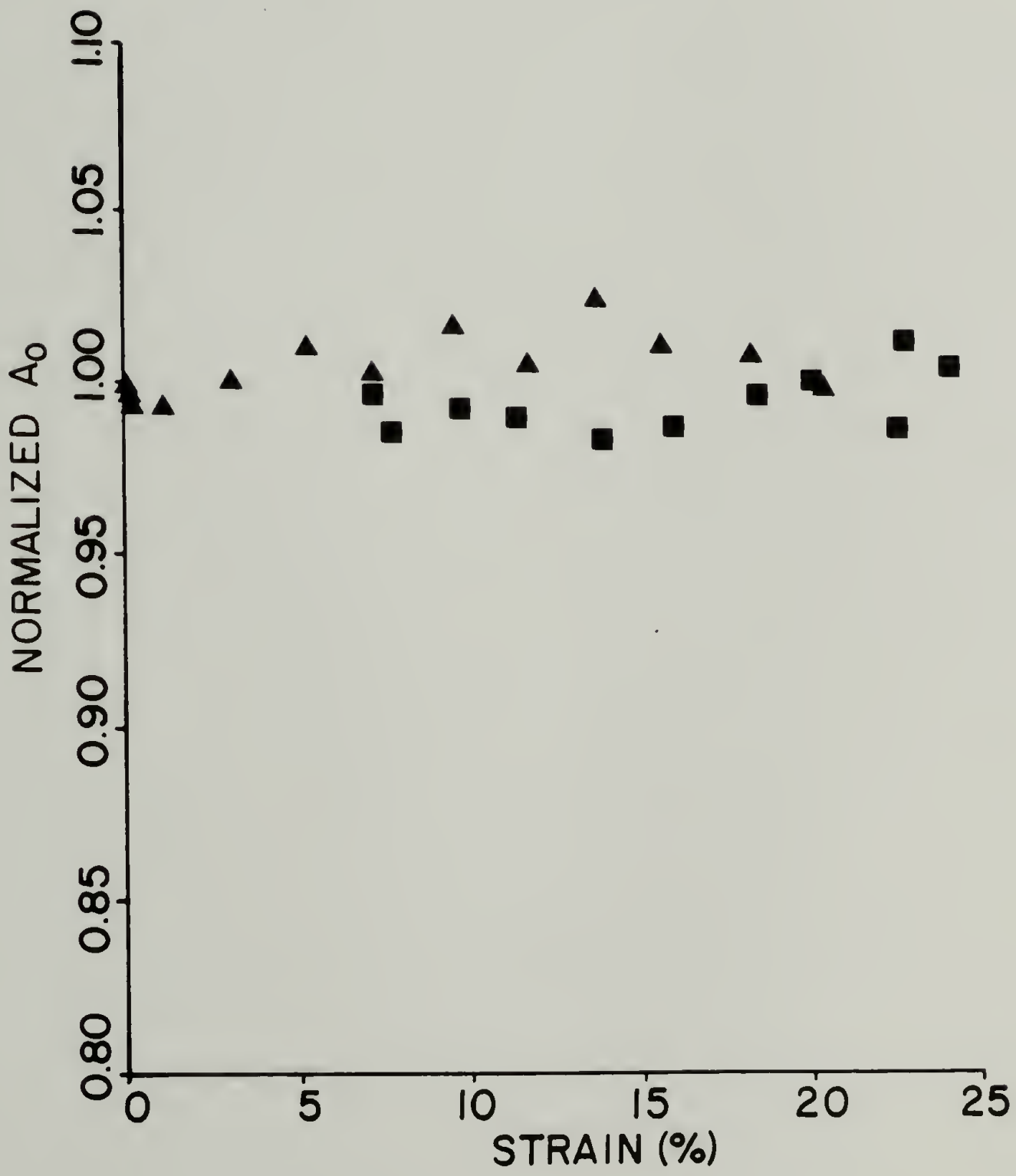

Figure 32c

A_0 of 917cm^{-1} α BAND

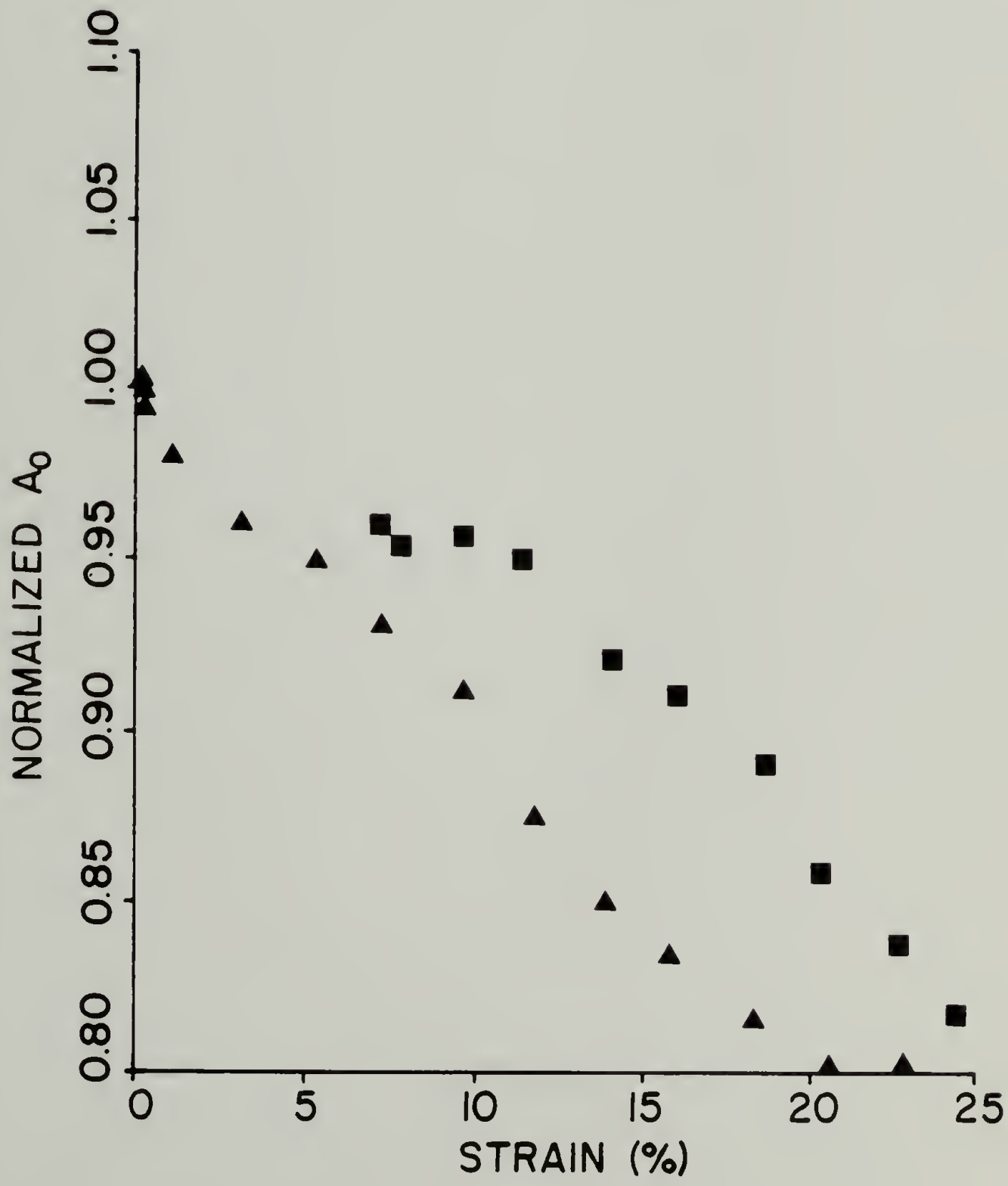

Figure 32d

cause of the decrease in $A_{\parallel}$ of the 917 cm^{-1} band. Few of the unoriented α crystallites are transformed, causing insignificant change in $A_{\perp}$. It can be concluded from these observations that the transformation of the crystals takes place faster than their rotation toward the stretching direction with the net result being the observed decrease in the α form dichroic ratio.

The hysteresis of the α and β forms as reflected by A_o contributes to the stress hysteresis of the overall sample. As mentioned in the previous section, a second loading cycle is required to determine how much of the hysteresis is due to plastic deformation.

Conclusion

Infrared rheo-optical experiments have been used to follow the reversible, stress induced, crystal-crystal phase transition in poly(tetramethylene terephthalate) and Hytrel®. The time resolved study of 4GT was not fast enough to measure the transition rate, but it does provide an improved limit on the measurement.

IR rheo-optical results as a function of strain obtained for Hytrel® clearly show the extent of the α-β transformation. By following the α and β content as well as the chain segment orientation in Hytrel®, the overall macroscopic properties were clearly interpreted in terms of microstructural changes.

C H A P T E R V

INFRARED DICHROISM MEASUREMENTS BY POLARIZATION MODULATION

Introduction

In polymeric materials, the orientation of chain segments is the most commonly measured quantity in infrared rheo-optical experiments and it is determined by measuring the absorbance of IR radiation polarized parallel and perpendicular to the stretching direction of a polymer film. The measurement is normally accomplished by taking two separate spectra (one of each polarization) and calculating their difference or ratio.

In infrared rheo-optical studies, the amount of noise in the obtained spectra is an experimental limitation. For the irreversible extension experiments, which are conducted by the rapid scan technique, the time resolution is controlled by two factors: the number of scans required to yield a signal to noise ratio, SNR, in each spectrum and the time required to switch between parallel and perpendicular polarizations. In the case of cyclic deformation experiments, low strain amplitudes must maintained to ensure the reproducible stress-strain behavior in the sample. The resulting small spectral changes lead to reduced SNR in the data.

Polarization modulation is a differential method which can be used to obtain the difference spectrum directly in a single

measurement. Polarization modulation is accomplished by alternately passing two differently polarized light beams through the sample. The detected signal is processed by a phase sensitive amplifier synchronized with the changing polarization, and turned into a signal which represents the intensity difference between the two polarizations. The main advantages of this technique are improved photometric accuracy and SNR and the convenience and improved time resolution which result from not having to collect two separate spectra. The purpose of this chapter is to evaluate the advantages of polarization modulation relative to subtraction for the measurement of polymer orientation.

Nafie et al. have published several papers describing the measurement of infrared circular dichroism by combining the polarization modulation with an FT-IR (147-150). Their results indicate that the FT-IR technique shows a definite advantage over the dispersive IR technique. The obtained circular dichroic spectra are of higher quality in both aspects, the spectral resolution and SNR (147,150). A brief examination of the spectral data indicated the detector noise to be dominant, even though additional noise coming from the modulation-demodulation process was noticed (147). Dowrey and Marcott have compared subtraction and modulation measurements of linear dichroism and they observed an improved SNR by modulation as well as elimination of certain artifacts associated with the subtraction spectra (151,152). Generally , the observed sensitivity increase for the modulation scheme has been attributed to a reduced dynamic

range in the experiment (39,147,153,154). However, no further elaboration is given. Therefore, the increase in sensitivity cannot be predicted from the experimental conditions. In this chapter, the improvement in sensitivity will be examined from a theoretical viewpoint in conjunction with experimental measurements.

Background of Differential Measurement

The general concept of modulating a signal to improve the quality of measurement is quite old. The intensity of a light beam is normally measured by passing it onto a detector which converts it into an electrical signal that is amplified. In the amplifier and in some detectors, there is a noise component with an amplitude inversely proportional to frequency (39). By chopping the light beam, the signal is shifted into the higher frequency region in which it is amplifed with less noise. In addition, AC amplication is less prone to drift and gain errors than DC amplification.

This concept was broadened to include double beam ratio spectrometers and other forms of differential measurements, where the absolute light intensity is no longer measured. Only the difference of two intensities is determined in these schemes. The two signals are alternately passed onto a single detector and a phase sensitive amplifier is used for producing the difference signal. The process of switching between the two signals produces the same benefits for the noise reduction as does chopping the signal. Furthermore, the

direct measurement of the difference signal requires a much smaller dynamic range than would be required to obtain the difference of the two separately-measured signals with the same accuracy.

The change in dynamic range requirements is illustrated by examining the measurement of circular dichroism (CD), which is the difference in the absorption of left and right circularly polarized (CP) light by chiral molecules. In many chiral molecules, when absorption peaks of about one absorbance unit are obtained for unpolarized light, the CD peak values are about 10^{-4} absorbance units (148-150). For demonstration purposes, assume the CD peak to be 1.1×10^{-4} A. The absorbance for right circularly polarized light might then be 1.00011 A and that for left CP light 1.00000 A. To be able to measure the CD peak with a 10:1 signal to noise ratio requires measurement to 10^{-5} absorbance units. Grosjean and Legrand developed polarization modulation measurement of CD spectra and in their approach, the left and right CP light beams were alternately passed through the sample (155,156). The CP light was produced and modulated by an electro-optical cell driven at 60 Hz. The detected signal was processed by a demodulator (a relay) also driven at 60 Hz. The demodulated output is a signal which corresponds to the difference on each cycle. The signal over 10^4 cycles can be averaged in three minutes producing a very accurate result. In the averaged signal, a dynamic range of only 10:1 is needed to preserve the signal to noise ratio for the modulation scheme while for the subtraction scheme a 10^5:1 dynamic range would be required. This example clearly illustrates the reduction in

dynamic range which can be achieved by modulation measurements. For both subtraction and modulation measurement, the total noise at the detector averaged over the measurement period must be 1 part in 10^5 or less to obtain the desired accuracy in the CD spectrum.

In addition to the advantage of the dynamic range reduction stated above, the modulation scheme eliminates several problems associated with the subtraction scheme in which the two spectra are measured sequentially in two different geometries. In rheo-optical experiments, errors may be caused by the change in the sample orientation between the measurement of the two spectra. Also, the time needed to switch between parallel and perpendicular polarization can lengthen the time between successive spectra, degrading the time resolution. Additionally, either the sample or, normally, the polarizer is rotated between successive measurements. Both experimental arrangements generate artifacts in the subtraction spectrum if the sample orientation or geometry and the intensities of the two polarized beams are not uniform over the area illuminated by the infrared beam. One such artifact that has been observed is film interference fringes which do not cancel out in the ratio or difference spectra (151). The modulation scheme is less vulnerable to these effects mentioned above, because the two polarization conditions are quickly repeated and averaged many times in a short time period. In some instances these additional effects can be more important than the SNR and dynamic range advantages realized by the use of polarization modulation.

Theory of Polarization Modulation

The application of polarization modulation to FT-IR is formulated here by following the work of Nafie and Vidrine (14). Let the sample be characterized by the two polarized components, $I_{\parallel}(\bar{\nu})$ and $I_{\perp}(\bar{\nu})$, where $\bar{\nu}$ is the wavenumber frequency of the infrared radiation. When a sinusoidal modulation is applied to these components at the frequency ω_m, the total intensity reaching the detector as a function of time and wavenumber is

$$I(\bar{\nu},t) = I_{dc}(\bar{\nu}) + I_{ac}(\bar{\nu}) \sin(2\pi\omega_m t) \qquad (5.1)$$

where the average intensity, I_{dc}, and the difference intensity, I_{ac}, are given by

$$I_{dc}(\bar{\nu}) = 0.5[I_{\parallel}(\bar{\nu}) + I_{\perp}(\bar{\nu})] \qquad (5.2)$$

$$I_{ac}(\bar{\nu}) = 0.5[I_{\parallel}(\bar{\nu}) - I_{\perp}(\bar{\nu})] \qquad (5.3)$$

The sinusoidal modulation is used in these formulae because it simplifes the analysis. The use of other modulation functions is permitted (147), and does not alter the basic picture of the scheme. The difference intensity, I_{ac}, which contains the desired information, is more meaningful if it is expressed in terms of A, the decadic absorbance. The expressions for single beam intensities become

$$I_{dc}(\bar{\nu}) = 0.5\ I_o(\bar{\nu})[10^{-A_{\parallel}(\bar{\nu})} + 10^{-A_{\perp}(\bar{\nu})}] \qquad (5.4)$$

$$I_{ac}(\bar{\nu}) = 0.5\ I_o(\bar{\nu})[10^{-A_{\parallel}(\bar{\nu})} - 10^{-A_{\perp}(\bar{\nu})}] \qquad (5.5)$$

where $I_o(\bar{\nu})$ is the single beam throughput of an open beam.. The ratio of I_{ac} to I_{dc} can be related to the absorbance difference spectrum:

$$I_{ac}/I_{dc} = (10^{A_\parallel} - 10^{-A_\perp}) /(10^{-A_\parallel} + 10^{-A_\perp})$$

$$I_{ac}/I_{dc} = \tanh[0.5(\ln 10)\ \Delta A_{\parallel\perp}] \qquad (5.6)$$

where $\Delta A_{\parallel 1}$ is $A_\parallel - A_\perp$. For small values of ΔA, the hyperbolic tangent may be replaced by its arguement with little error. With this approximation, equation 5.6 becomes

$$I_{ac}/I_{dc} = 1.1513\ \Delta A_{\parallel\perp} \qquad (5.7)$$

At the detector, the IR intensity $I(\bar{\nu})$ is converted into a voltage $B(\bar{\nu})$ as determined by the detector response function $R(\bar{\nu})$ (147).

$$B(\bar{\nu}) = R(\bar{\nu}) \cdot I(\bar{\nu}) \qquad (5.8)$$

The equations 5.1 through 5.8 are independent of the measurement scheme actually used to measure the spectra $I_{ac}(\bar{\nu})$ and $I_{dc}(\bar{\nu})$.

In an FT-IR, the interferogram is measured as a function of the retardation δ (the path length difference from the beam splitter to the fixed and moving mirrors). The interferogram may be expressed as $I(\delta)$, the infrared intensity at the detector, or as $V(\delta)$, the detector output in volts. The interferograms expressed by using the cosine integral

$$I(\delta) = \int_0^\infty I(\bar{\nu}) \cos [2\pi \bar{\nu}\delta - \theta(\bar{\nu})] \, d\bar{\nu} \qquad (5.9a)$$

$$V(\delta) = \int_0^\infty B(\bar{\nu}) \cos[2\pi \bar{\nu}\delta - \theta(\bar{\nu})] d\bar{\nu} \qquad (5.9b)$$

contain the phase factor, $\theta(\bar{\nu})$, of the individual wavenumber frequencies. It is often necessary to consider the interferogram as a function of time, V(t), rather than of retardation $V(\delta)$. The retardation δ, in cm, changes at a rate twice the velocity, u, of the moving mirror since the light travels both to and from the moving mirror. With the retardation $\delta(t)$ given by $2 \cdot u \cdot t$ the argument of the cosine in equation 5.9b becomes

$$\cos(2\pi\bar{\nu} \cdot 2ut - \theta(\bar{\nu})) \quad = \cos(\omega_{\bar{\nu}} t - \theta(\bar{\nu}))$$

where $\omega_{\bar{\nu}} = 4\pi u\bar{\nu}$. Equation 5.9b becomes

$$V(t) = \int_0^\infty B(\bar{\nu}) \cos(\omega_{\bar{\nu}} t - \theta(\bar{\nu})) \, d\bar{\nu} \qquad (5.10)$$

Equation 5.10 indicates that the detected interferogram signal is composed of a band of electrical frequencies in the audio region from 100 Hz to 10 KHz. The mirror velocity, u, ranging from 0.05 to 2.0 cm/sec determines the audio frequency, $\omega_{\bar{\nu}}$ of a given wavenumber. When sinusoidal modulation between $I_{\parallel}(\bar{\nu})$ and $I_{\perp}(\bar{\nu})$ occurs at ω_m, equation 5.10 becomes

$$V(t) = \int_0^\infty [B_{dc}(\bar{\nu}) + B_{ac}(\bar{\nu}) \sin \omega_m t] \cos(\omega_{\bar{\nu}} t) \, d\nu \qquad (5.11)$$

if the phase $\theta(\bar{\nu})$ is ignored.

The bandpass filters of the FT-IR pass only those signal com-

ponents corresponding to the range of wavenumbers from $\bar{\nu}_1$ to $\bar{\nu}_2$. The ω_m component (140 khz) is removed by the bandpass filters and the dc interferogram becomes

$$V_{dc}(t) = \int_{\bar{\nu}_1}^{\bar{\nu}_2} B_{dc}(\bar{\nu}) \cos[\omega_{\bar{\nu}} t - \theta_{dc}(\bar{\nu})] \, d\bar{\nu} \qquad (5.12)$$

where $\theta_{dc}(\bar{\nu})$, the dc phase, includes the electrical phase shifts added by the filters. The dc interferogram is Fourier transformed and phase corrected to give $I_{dc}(\bar{\nu})$, the dc single beam spectrum. The ac interferogram

$$V(t) = \int_{0}^{\infty} B_{ac}(\bar{\nu}) \sin(\omega_m t) \cos(\omega_{\bar{\nu}} t) \, d\bar{\nu} \qquad (5.13)$$

can be expressed as

$$V(t) = \int_{0}^{\infty} \frac{1}{2} B_{ac}(\bar{\nu})[\sin(\omega_m + \omega_{\bar{\nu}})t + \sin(\omega_m - \omega_{\bar{\nu}})t] \, d\bar{\nu} \qquad (5.14)$$

which is an amplitude modulated, double sideband signal with carrier frequency ω_m as shown in Figure 33. The detected signal (equation 5.11) is passed through a band pass filter centered at ω_m to separate the dc interferogram V_{dc} at $\omega_{\bar{\nu}}$. The signal is then sent to the mixer of the synchronous demodulator (a phase sensitive amplifier) with a reference signal of $\sin(\omega_m t)$. The mixer output passes through the FT-IR's band pass filters which isolate the signals of wavenumber frequencies from $\bar{\nu}_1$ to $\bar{\nu}_2$ to give

$$V_{ac}(t) = \int_{\nu_1}^{\nu_2} B_{ac}(\bar{\nu}) \cos[\omega_{\bar{\nu}} t - \theta_{ac}\bar{\nu}] \, d\bar{\nu} \qquad (5.15)$$

Figure 33. The expected distribution of Fourier frequencies in an interferogram of a polarization modulation experiment. Experimental conditions are mirror velocity 0.88 cm/sec, 400 to 4500 wavenumbers, and ω_m = 148 KHz.

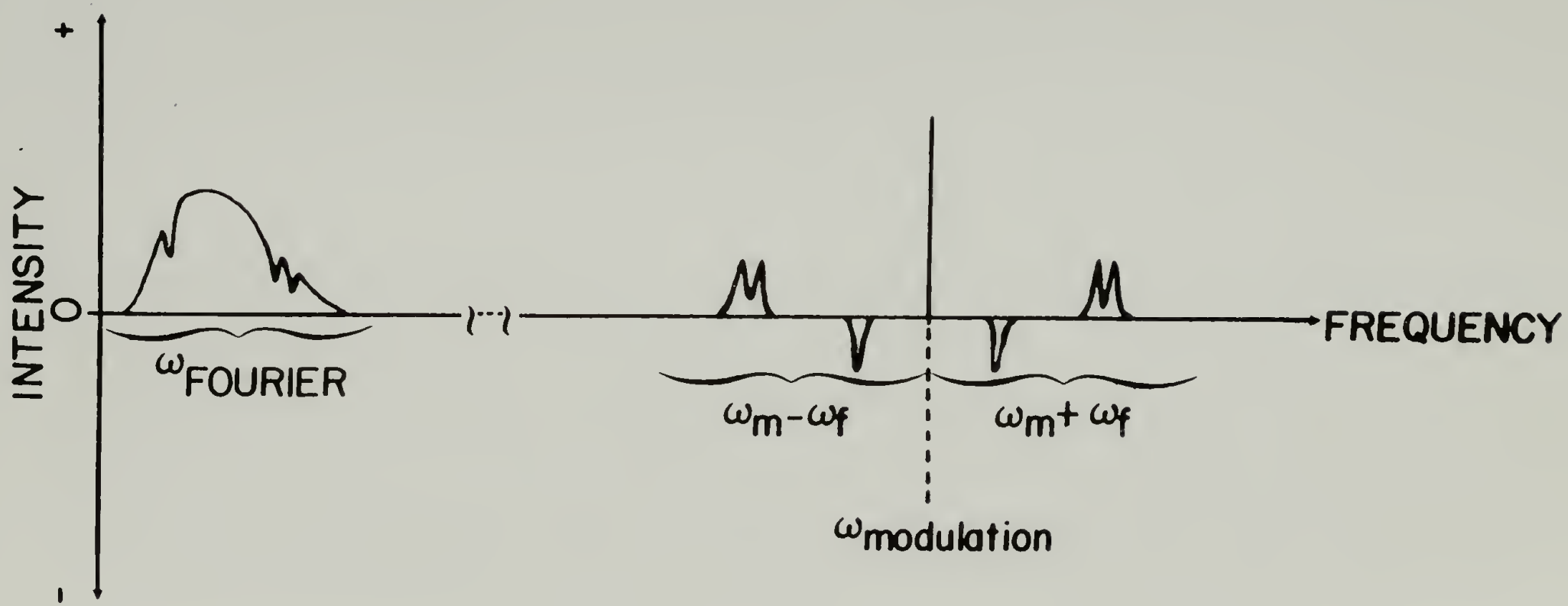

Figure 33

where $\theta_{ac}(\bar{\nu})$ is the ac phase which includes phase shifts from the ω_m bandpass filter and the mixer as well as those shifts present in θ_{dc}. The ac interferogram is Fourier transformed and phase corrected to give $I_{ac}(\bar{\nu})$, the ac single beam spectrum. Inadequate frequency response (too large a time constant τ) in the mixer can cause a frequency dependent attenuation in $V_{ac}(t)$:

$$V_{ac}(t) = \int B_{ac}(\bar{\nu}) \exp[-\omega_{\bar{\nu}}\tau] \cos[\omega_{\bar{\nu}}t - \theta_{ac}(\bar{\nu})] \, d\bar{\nu} \quad (5.16)$$

The frequency dependent attenuation of the filters and mixer can be calibrated separately and used to correct the results. Finally, the difference spectrum is obtained by dividing the Fourier transforms, I_{ac} and I_{dc},

$$FT[V_{ac}(t)]/FT[V_{dc}(t) \cong 1.1513 \, \Delta A_{\parallel 1}(\bar{\nu}) \quad (5.17)$$

as shown in equation 5.7.

A block diagram of the optics and electronics of the FT-IR polarization modulation experiment is shown in Figure 34. A more complete description of these elements will be given in the experimental section.

Photoelastic Modulator - Optics, Signals and Efficiency

Early differential measurements of linear dichroism employed dispersive spectrometers. The polarization was modulated by rotating

Figure 34. Block diagram of polarization modulation experiment.

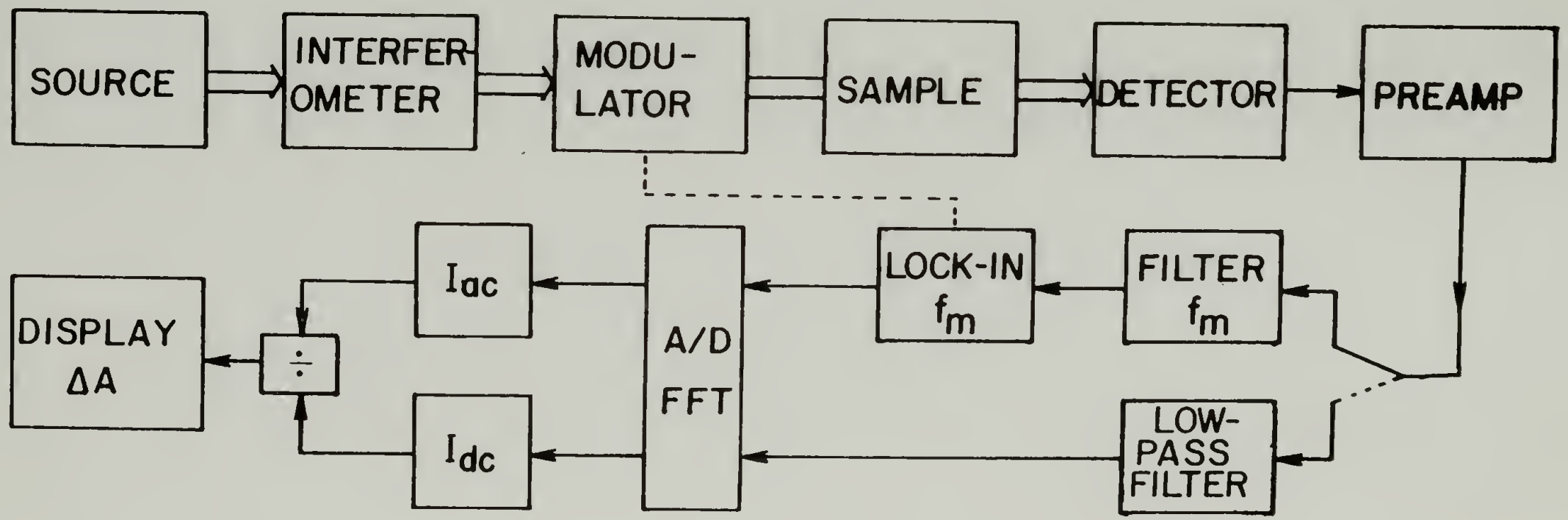
SOURCE
INTERFER-
OMETER
MODU-
LATOR
SAMPLE
DETECTOR
PREAMP
LOCK-IN
f_m
FILTER
f_m
I_{ac}
A/D
FFT
DISPLAY
ΔA
÷
I_{dc}
LOW-
PASS
FILTER

Figure 34

the polarizer (157), or by switching between the sample and reference beams with orthogonal polarizations (24,158), or by using photoelastic modulators (153,159). FT-IR differential polarization measurements require a clear separation of the interferogram signal frequencies ω_{ν} and the polarization modulation frequency, ω_m. Only the photoelastic modulator is capable of providing the 50 to 200 KHz modulation frequencies which are sufficiently high when compared to the interferogram frequencies which range from 100 Hz to 10 KHz depending on the mirror velocity and the infrared wavelengths (154,160).

The photoelastic modulator rotates linearly polarized incident light by ninety degrees when it acts as a half waveplate (160,161). It is an isotropic crystal if no stress is applied, and when it is subjected to a sinusoidal strain $\varepsilon=\varepsilon_0 \sin\omega_d t$ it induces a birefringence, $\Delta n=\Delta n_0 \sin\omega_d t$. Thus the phase difference (retardance), between light travelling along the two principal axes of the induced birefringence is given by $\alpha=\alpha_0 \sin\omega_d t$. An elliptically polarized light which can be separated into a circularly polarized component and a linearly polarized component is produced if a linearly polarized light is incident on the modulator. If its plane of polarization is in the direction bisecting the two principal axes, the amplitude of the circularly polarized output is given by $\sin \alpha_0$ and the linear component by $\cos \alpha_0$. The principal axes of the modulator are placed forty-five degrees from the parallel and perpendicular axes of the sample. With the modulator set to act as a halfwave plate, the perpendicularly polarized incident light is rotated to parallel and the parallel

polarized incident light is rotated to perpendicular.

The light from the source passes through the sample, the modulator, and an analyzer which is a parallel oriented polarizer before it reaches the detector. The parallel and perpendicular polarized beam transmitted through the sample are alternately passed through the analyzer to the detector by the action of the modulator dependent on whether it acts as an isotropic crystal or as a halfwave plate. If the modulator is driven by the frequency ω_d, the signal reaching the detector is given by

$$I(t) = I_{dc} + I_{ac} \cdot \cos[\alpha_o \sin\omega_d t] \qquad (5.18)$$

where I_{ac} and I_{dc} are given by equations 5.4 and 5.5. The cosine term can be expanded in terms of the even order spherical Bessel functions:

$$\cos[\alpha_o \sin\omega_d t] = J_0(\alpha_o) + \sum_{n=1}^{\infty} 2J_n(\alpha_o) \cos(2n\omega_d t) \qquad (5.19)$$

The zeroth order term, J_0, is a dc contribution. The lowest frequency ac term occurs at the frequency $2\omega_d$ because the linearly polarized component rotates at a rate twice the frequency ω_d applied to the modulator. The amplitude of the signal is determined by a mixer tuned to $2\omega_d$.

Since the birefringence of the modulator is not achromatic, only one wavenumber has the retardance varying from $+\pi$ and $-\pi$, or the polarization alternating precisely between fully parallel and fully

perpendicular. At other wavenumbers, the amplitude of oscillating retardance, α_o is given by

$$\alpha_o(\bar{\nu}) = 2\pi t\ \Delta n_o\ \bar{\nu}\ , \tag{5.20}$$

where t is the thickness of the modulator crystal and Δn_o is the amplitude of the induced birefringence. The modulation efficiency, η, is given by

$$\eta = 2\ J_2[\alpha_o(\bar{\nu})] \tag{5.21}$$

The Bessel functions J_o and J_2 are shown as a function of α_o in Figure 35.

The chromatic (wavenumber) dependence of the polarization modulation efficiency can be measured by placing the modulator between crossed polarizers. Let the first polarizer be parallel, with intensity $I_\parallel$ passing through it. The modulator receives the parallel intensity, $I_p = I_\parallel$ and the perpendicular intensity, $I_s = 0$. Using equations 5.2 and 5.3, both intensity components I_{dc} and I_{ac} are given by

$$I_{dc} = 0.5(I_\parallel + I_\perp) = 0.5\ I_\parallel$$

and (5.22)

$$I_{ac} = 0.5(I_\parallel - I_\perp) = 0.5\ I_\parallel$$

The modulator outputs, in accordance with Equations 5.18 and 5.19, are given by

$$I_p' = I_{dc} + I_{ac}\cos(\alpha)$$

and (5.23)

$$I_s' = I_{dc} - I_{ac}\cos(\alpha)$$

Figure 35. The zeroth and 2nd order Bessel functions.

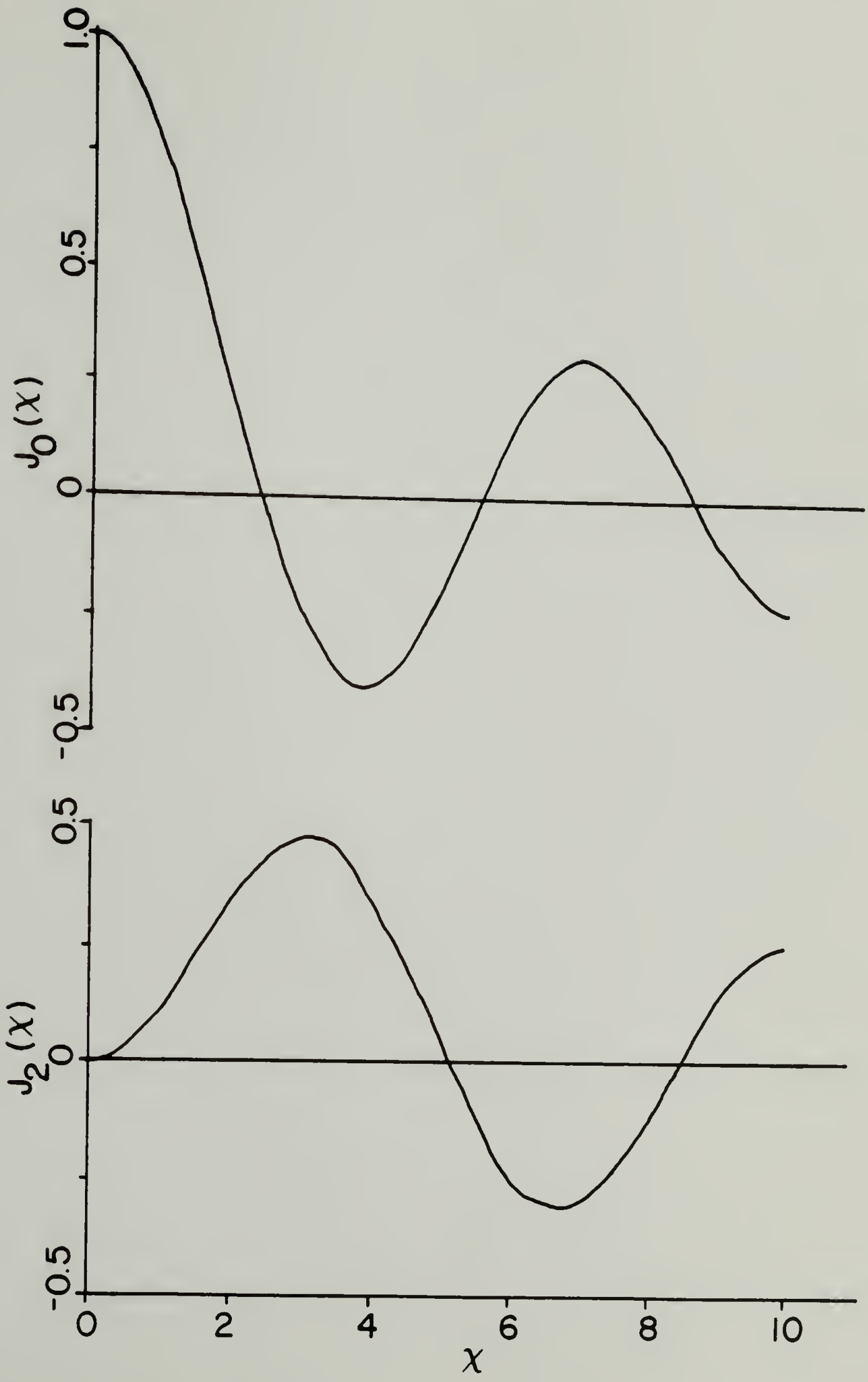

Figure 35

At zero retardance (α=0), the expected results $I_p' = I_\parallel$ and $I_s' = 0$ are obtained. Likewise, at halfwave retardance ($\alpha=\pi$), the intensities are $I_p' = 0$ and $I_s' = I_\parallel$. Only the perpendicular component, I_s', passes the second polarizer. Its intensity is expressed by

$$\begin{aligned} I_s'(\bar{\nu},t) &= I_{dc}(\bar{\nu}) - I_{ac}(\bar{\nu}) \cos[\alpha_o(\bar{\nu}) \sin\omega_d t] \\ &= I_{dc}(\bar{\nu}) - I_{ac}(\bar{\nu}) J_o[\alpha_o(\bar{\nu})] - 2I_{ac}(\bar{\nu}) \sum_{n=1}^{\infty} J_n[\alpha_o(\bar{\nu})] \cos 2n\omega_d t \end{aligned} \tag{5.24}$$

The ac component, single beam spectrum I_{AC}^*, at the frequency $2\omega_d$ is given by

$$\begin{aligned} I_{AC}^* &= 2\, I_{ac}(\bar{\nu})\, J_2[\alpha_o(\bar{\nu})] \\ I_{AC}^* &= I_\parallel(\bar{\nu})\, J_2[\alpha_o(\bar{\nu})] \quad , \end{aligned} \tag{5.25}$$

while the dc component spectrum obtained is given by

$$\begin{aligned} I_{DC}^* &= I_{dc}(\bar{\nu}) - J_o[\alpha_o(\bar{\nu})]\, I_{ac}(\bar{\nu}) \\ I_{DC}^* &= 0.5\, I_\parallel(\bar{\nu}) \left(1 - J_o[\alpha_o(\bar{\nu})]\right) \end{aligned} \tag{5.26}$$

These components, I_{AC}^* and I_{DC}^*, differ from the ideal intensities, I_{ac} and I_{dc}, given by Equations 5.2 and 5.3 and in Equation 5.22. The theoretical modulator efficiency is

$$\eta_{calc} = \frac{2\, J_2[\alpha_o(\bar{\nu})]}{1 - J_o[\alpha_o[\bar{\nu})]} \tag{5.27}$$

which may be compared with the observed efficiency η_{obs} determined by

$$\eta_{obs} = I_{AC}^*/I_{DC}^* \tag{5.28}$$

A set of calculated and measured modulation efficiency curves are given in Figures 36 and 37. In curves a-d, the maximum retardation, α_o has been set to π (halfwave) at wavenumbers, $\bar{\nu}_\pi$ of 10,000, 3330, 2000, and 1430 cm^{-1} respectively. In each curve the retardation at wavenumber $\bar{\nu}$ is calculated by $\alpha(\bar{\nu}) = \pi\bar{\nu}/\bar{\nu}_\pi$. There is good agreement between the observed and calculated curves for the case where J_2 is large and the term $1/(1-J_o)$ is small. However, for the case of small retardance as seen in curve a with ν_π at 10,000 cm^{-1}, the observed efficiency is much lower than the calculated efficiency. In this case, the calculated efficiency is dominated by the $1/(1-J_o)$ term. Equation 5.26 for I^*_{DC} shows that the factor $(1-J_o)$ is the term giving the time-independent fraction of light that passes through the crossed polarizers. Some additional light passes through the crossed polarizers because their polarization efficiency is less than 100%. The increase in I^*_{DC} caused by a lower value of n_{obs} than n_{calc} becomes more prominent as the retardance is smaller.

The measured efficiency will be noticeably lower only in those samples that show extreme dichroism. For less dichroic samples, the predicted value of I_{DC} will be fairly large and the effect of imperfect polarizers remain insignificant. The less dichroic case could be simulated with the polarizers crossed at an angle less than ninety degrees.

In the case of very small dichroism, the modulation index is dominated by J_2, and the I^*_{DC} term (equation 5.26) may be simplifed to $I_{dc}(\bar{\nu})$ since $I_{ac}(\bar{\nu}) << I_{dc}(\bar{\nu})$. In this case, it is possible to obtain

Figure 36. Calculated wavenumber dependence of modulation efficiency for half wave retardation at
a. 1.0 μm (10,000 cm^{-1})
b. 3.0 μm (3330 cm^{-1})
c. 5.0 μm (2000 cm^{-1})
d. 7.0 μm (1430 cm^{-1})

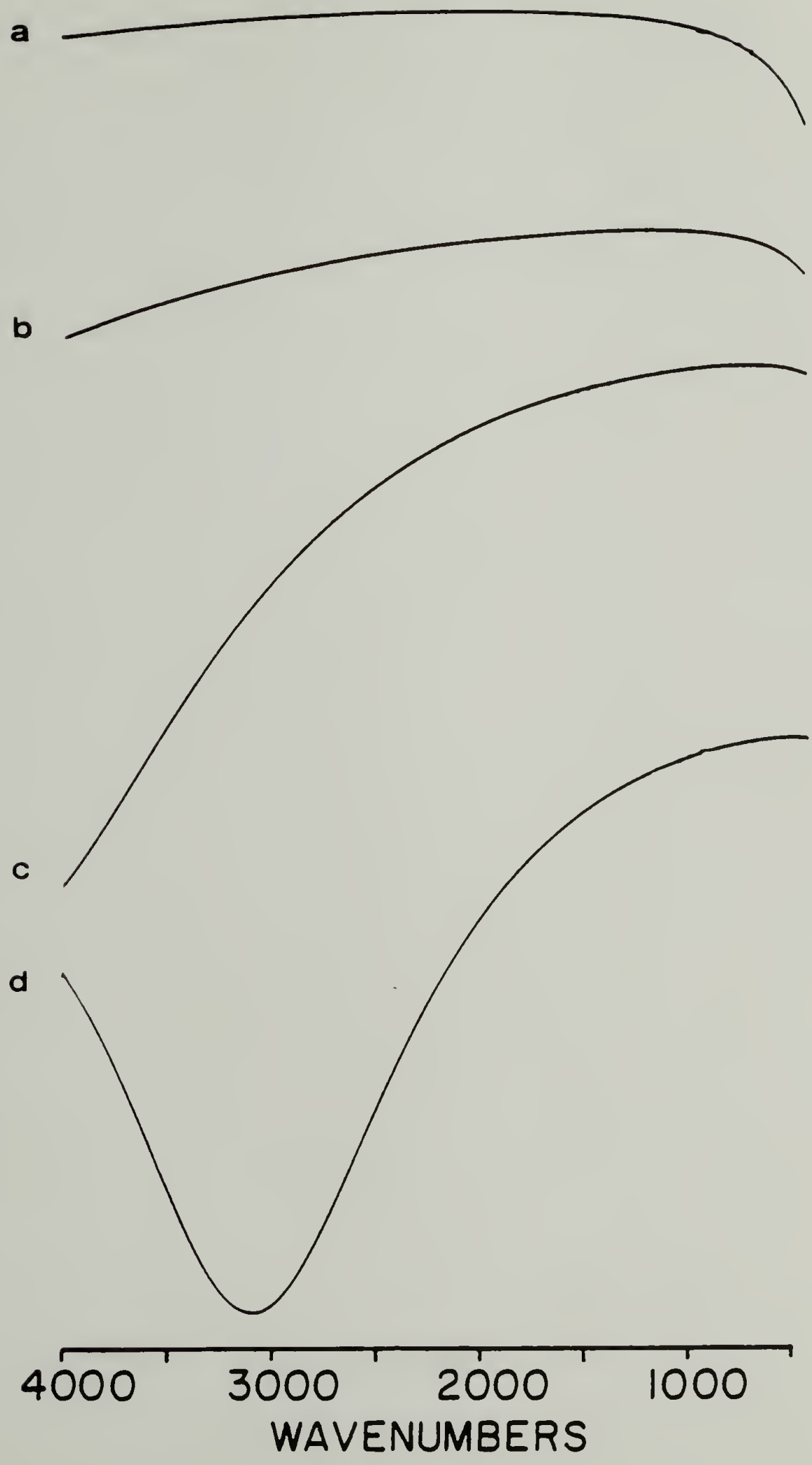

Figure 36

Figure 37. Measured wavenumber dependence of modulation efficiency for half wave retardation at
a. 1.0 μm (10,000 cm^{-1})
b. 3.0 μm (3330 cm^{-1})
c. 5.0 μm (2000 cm^{-1})
d. 7.0 μm (1430 cm^{-1})

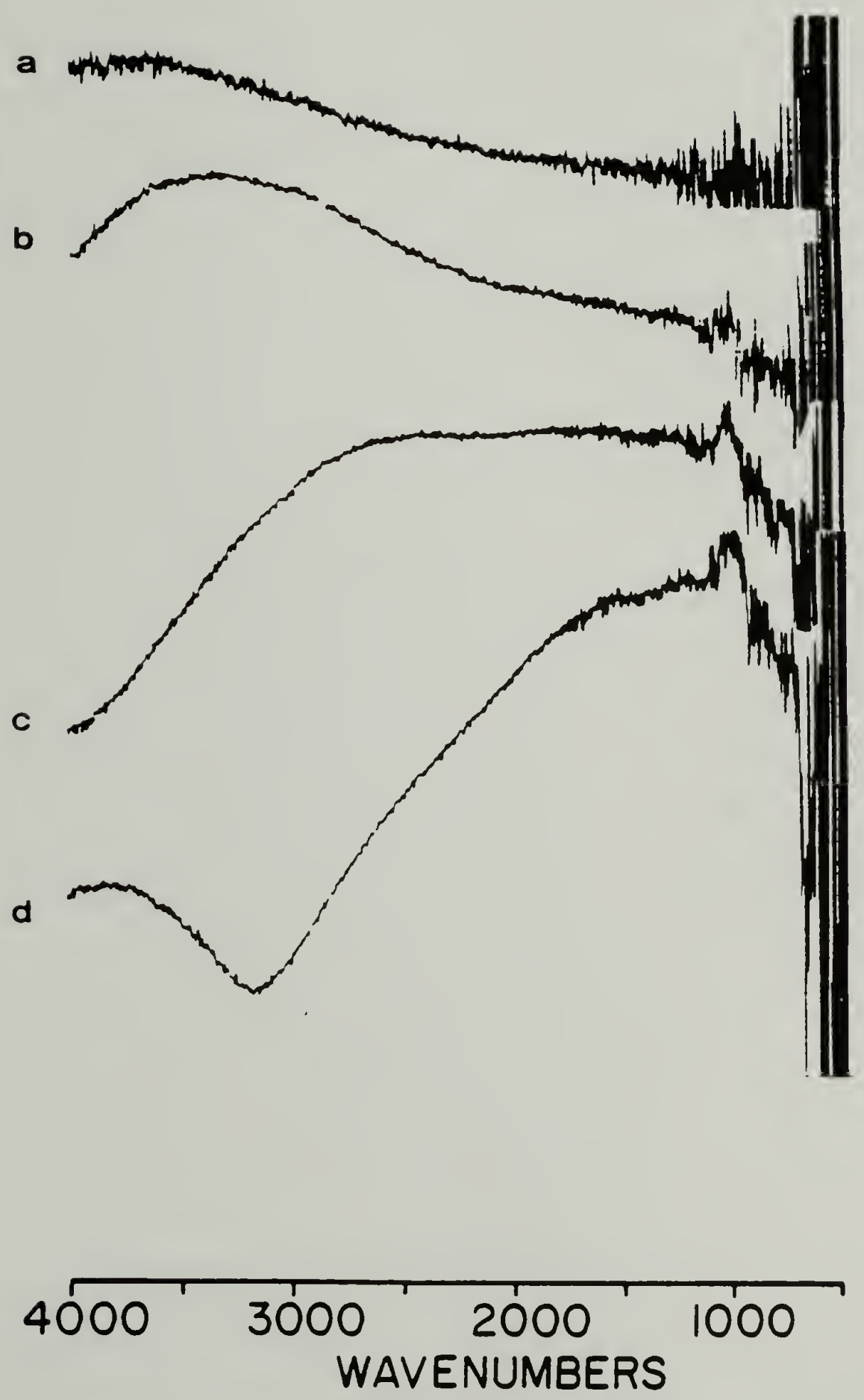

Figure 37

the measured curve of $J_2[\alpha_o(\bar{\nu})]$ by dividing I^*_{AC} by the spectrum of $I_{\parallel}(\bar{\nu})$ which is obtained by setting both the polarizers parallel and turning the modulator off.

Dynamic Range and Signal to Noise in Fourier Transform Infrared Polarization Modulation

The dynamic range and signal to noise considerations involved in difference (subtraction) and differential (modulation) measurements were briefly sketched in the background section of this chapter. A detailed treatment of this topic would be helpful. Since the analytical expression for the complete equations remains impractical, procedures for numerical evaluation of the dynamic range will be discussed. The results obtained for one sample cannot easily be extended to another, however, considerable insight on modulation spectroscopy can still be gained by examining them. The noise analysis in absorbance FT-IR spectroscopy is rather complex, as it includes the effect in the Fourier transform and the process of converting a single beam spectrum into an absorbance spectrum.

The mercury cadmium telluride (MCT) detector is the major noise source in our FT-IR system. Its noise level is independent of the light level falling on the detector (39,154). The detector noise which is contained in the measured interferogram signal is converted to a wavenumber distribution by the Fourier transformaton. The single

beam noise distribution can be determined by subtracting two single beam spectra. As seen in Figure 38, the noise is almost achromatic, i.e. little change is observed from 4000 to 400 cm^{-1}. The absorbance noise, however, is not achromatic and the effects that shape the absorbance noise distribution will be presented next.

The single beam noise, N_S, can be converted into absorbance noise, n_A, using equation 5.29a which follows from the definition of the absorbance, A, and its derivative, dA/dI;

$$n_A = - \frac{1}{I_o \ln 10} 10^A N_S \qquad (5.29a)$$

$$n_A = k\ 10^A N_S$$

$$A = -\log(I/I_o) \qquad (5.29b)$$

$$dA = - \frac{1}{I_o \ln 10} 10^A dI \qquad (5.29c)$$

Both the noise in the absorbance spectrum (equation 5.29a) and that in the transmission spectrum (eqn. not shown) depend on the reciprical of I_o, the background single beam spectrum (instrument throughput). In an open beam 100% line (the ratio of two background spectra taken under identical conditions), the noise level is highest where I_o is smallest (Figure 38b,c).

The noise level of a spectrum is commonly determined by examining a spectral region free from peaks. The deviation from the average in this region is taken to be the noise level. The knowledge of the true noise level is important in difference spectroscopy

Figure 38. Spectra (32 scans at 4 cm^{-1} resolution) showing the wavenumber dependence of
a. the single beam noise
b. the transmission 100% line
c. the single beam spectra

Figure 38a

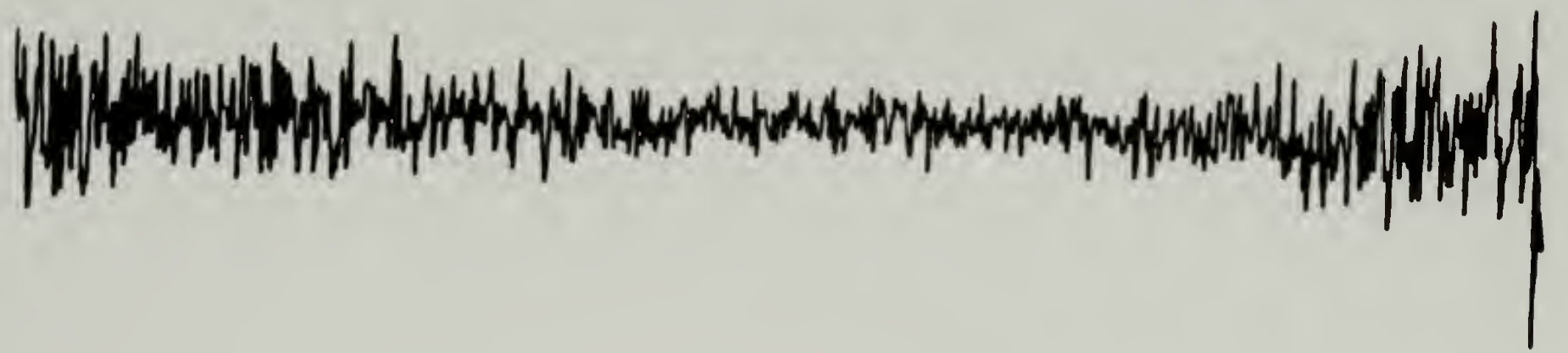

Figure 38b

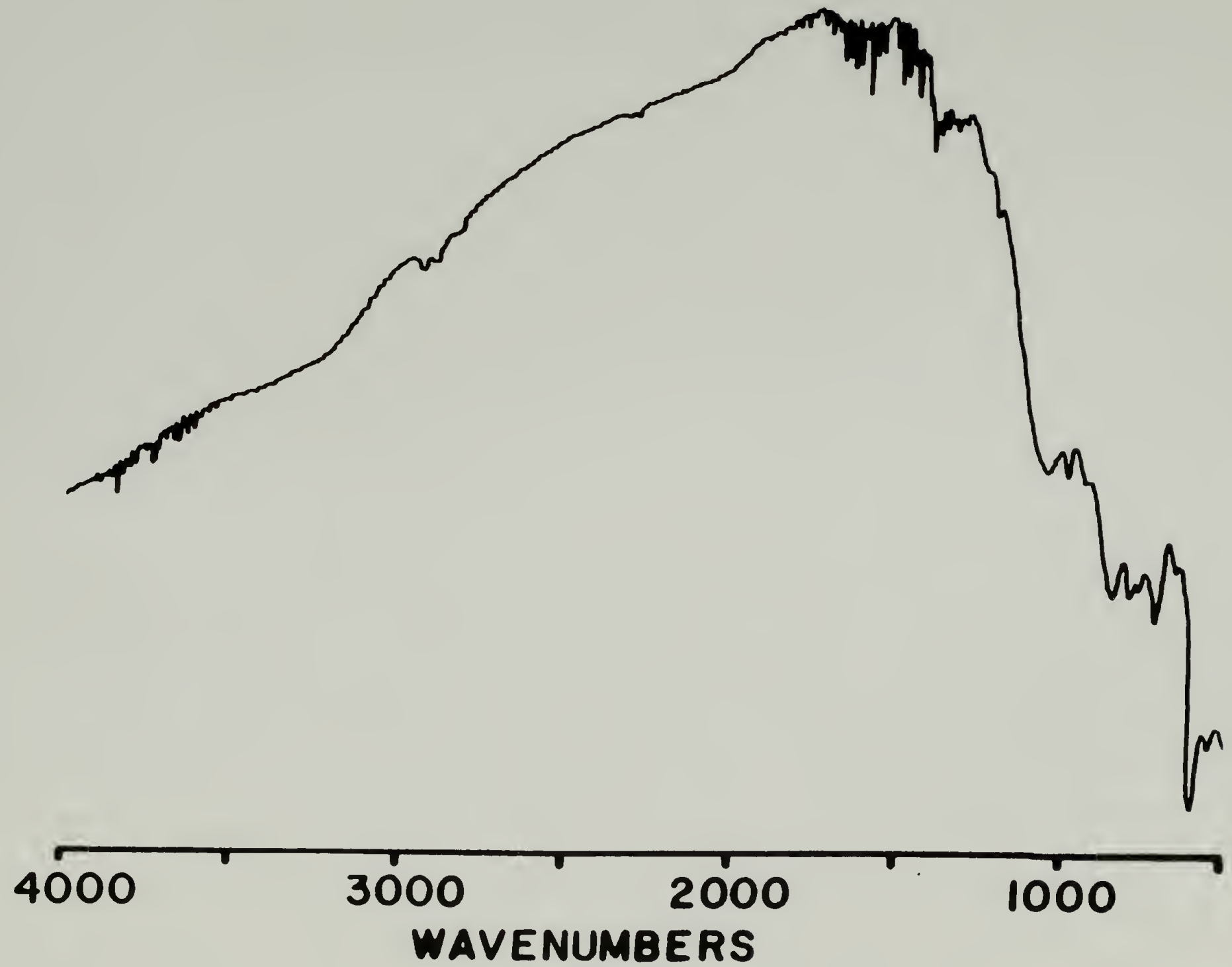

Figure 38c

because its spectral features have unfamiliar band shapes with small magnitudes. The noise level of a peak region may be considerably higher than other regions due to the 10^A dependence shown in equation 5.29a. Figure 39 shows the parallel spectrum and $A_{\parallel} - A_{\perp}$ measured by modulation and subtraction. The actual noise for each technique greatly increased at the peaks of the parallel spectrum. The actual noise can be determined by subtraction of two identical spectra. The noise may also be calculated from equation 5.29 when both $I_o(\nu)$ and $A(\nu)$ are taken into account.

In the introduction, it was mentioned that signal to noise ratio of subtraction and modulation should be equivalent. The proof is given below in the calculation of the SNR of both techniques. For the subtraction method, the noise in the difference spectrum is a combination of the noise in the two original spectra. The noise power from two separate sources can be added. Therefore, the adding of two separate noise sources of the same level gives $\sqrt{2}$ times the original noise level. For subtraction, the process is equivalent to the addition of two separate noise sources, and the absorbance noise is given by

$$n_{sub} = n_p + n_s = K\ 10^{A_s}\ N_s + K\ 10^{A_p}\ N_p$$
$$n_{sub} = \sqrt{2}\ K(10^{A_p} + 10^{A_s})N_s \qquad (5.30)$$

where A_p and A_s are the parallel and perpendicular absorbances and N_p and N_s, the parallel and perpendicular noise levels, are assumed to be equal. The absorbance signal is $S_{sub} = A = A_p - A_s$.

Figure 39. Spectra of an oriented poly(ethylene co-vinyl acetate) film (100 scans/file, 4 cm^{-1} resolution)
a. the parallel polarized spectrum
b. The difference spectrum ($A_{\parallel}$-$A_{\perp}$) obtained by the subtraction technique (spectra b - e are scaled 25 times spectra a)
c. the noise in (b) obtained by subtraction two difference spectra
d. the difference spectrum ($A_{\parallel}$-$A_{\perp}$) obtained by the modulation technique
e. the noise in (d) obtained by subtracting two difference spectra

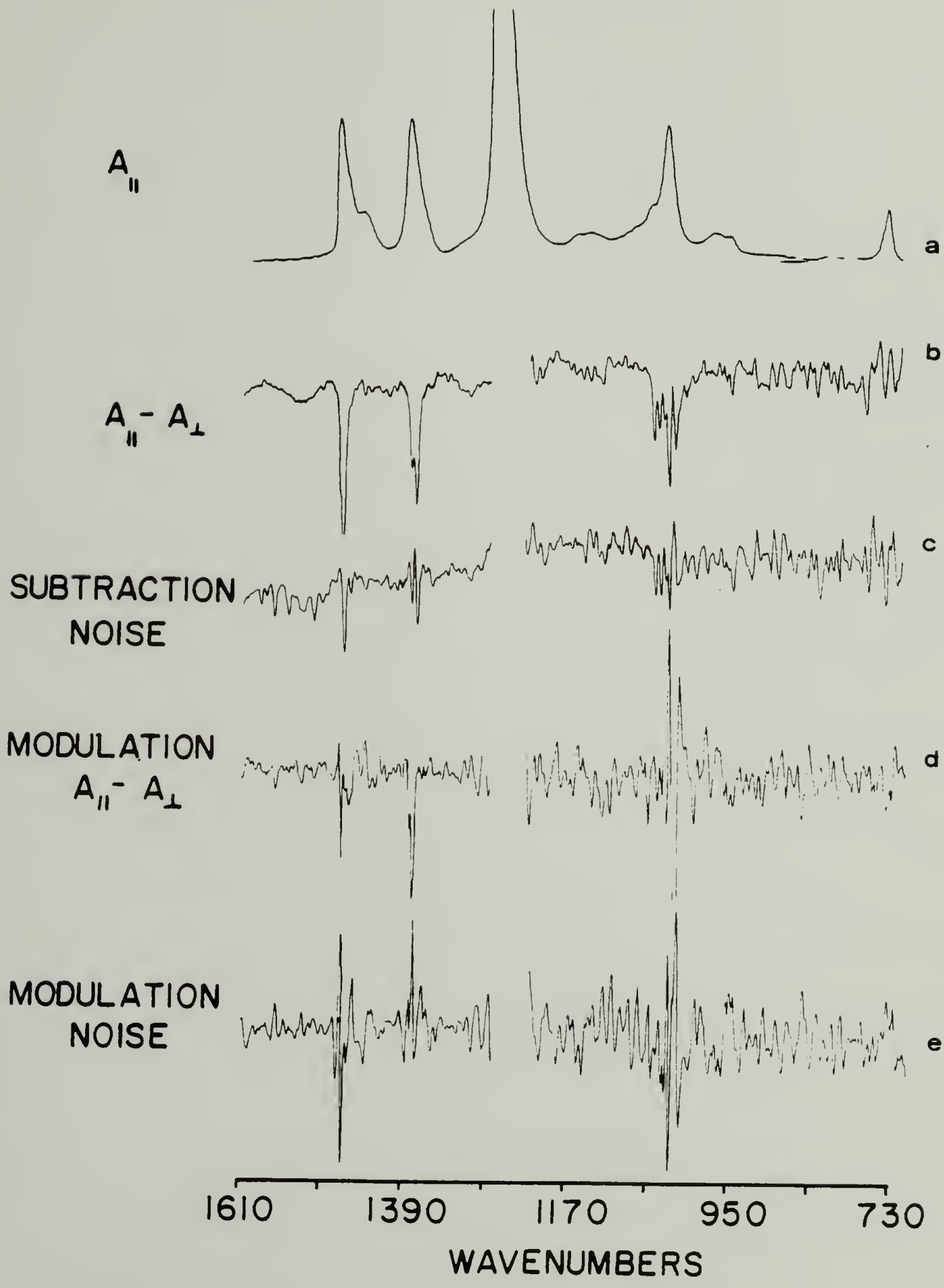
$A_{\parallel}$
a
$A_{\parallel} - A_{\perp}$
b
c
SUBTRACTION NOISE
MODULATION $A_{\parallel} - A_{\perp}$
d
MODULATION NOISE
e
1610
1390
1170
950
730
WAVENUMBERS

Figure 39

For the modulation method, the noise expression, N_{mod} follows from the derivative of the ratio;

$$R = I_{ac}/I_{dc} = x/y$$

and

$$\frac{dR}{dI} = \frac{\partial R}{\partial x}\frac{\partial x}{\partial I} + \frac{\partial R}{\partial y}\frac{\partial y}{\partial I} \quad .$$

Thus the noise n_{mod} is given by

$$n_{mod} = \frac{I_{ac}}{I_{dc}}\left(\frac{N_{ac}}{I_{ac}} - \frac{N_{dc}}{I_{dc}}\right) \quad , \tag{5.31}$$

where N_{ac} and N_{dc} are the noise in the single beam ac and dc spectra. Equation 5.31 can be simplifed if $N_{ac} \simeq N_{dc}$ and $I_{ac} << I_{dc}$;

$$n_{mod} \simeq \frac{N_{ac}}{I_{dc}} \tag{5.32}$$

Using the modulation signal, S_{mod}, given by

$$S_{mod} = \frac{I_{ac}}{I_{dc}} \tag{5.33}$$

the modulation signal to noise ratio, SNR_{mod}, is

$$SNR_{mod} = \frac{I_{ac}}{N_{ac}} = \frac{0.5\ I_o(10^{-A_p} - 10^{-A_s})}{N_{ac}} \tag{5.34}$$

Meanwhile, the subtraction signal to noise ratio, SNR_{sub}, is

$$SNR_{sub} = \frac{I_o\ \ln 10}{\sqrt{2}\ N_s}(A_p - A_s)/(10^{A_p} + 10^{A_s}) \ . \tag{5.35}$$

Since both expressions contain I_o and the noise level, these two factors can be brought over from the right hand side of the equations and the two results compared by plotting the quantity (SNR x Noise/I_o) for various values of A_s and A_p (Figure 40). As seen in Figure 40, the subtraction and modulation values are close for small values of (A_s-A_p). At larger values, the approximation used in the SNR expressions and that in equation 5.6 lose their accuracy. Thus the derivation seen for larger values can be considered insignificant. The plots demonstrate the SNRs are equivalent; there is no inherent signal to noise gain in modulation - any improvement must come from a reduction in the dynamic range requirements.

Next, the dynamic range and its effects on the measured signal to noise ratios will be considered. The measurement dynamic range is simply the ratio of the largest to smallest signal that can be measured. The spectral dynamic range is the ratio of the largest spectral feature to the RMS noise level (39). If the spectral dynamic range is greater than the measurement dynamic range, digitization noise (the difference between the measured and actual value) will be added to the spectrum. The spectral dynamic ranges of A_s, A_p, and ΔA can easily be determined from their absorbance spectra. However, in FT-IR it is not the absorbance dynamic range or even the single beam dynamic range that is important but the dynamic range of the interferogram.

To compute the dynamic range of the interferogram which is expressed by the Fourier transform,

Figure 40. Calculated signal to noise ratios for the subtraction and the modulation techniques.

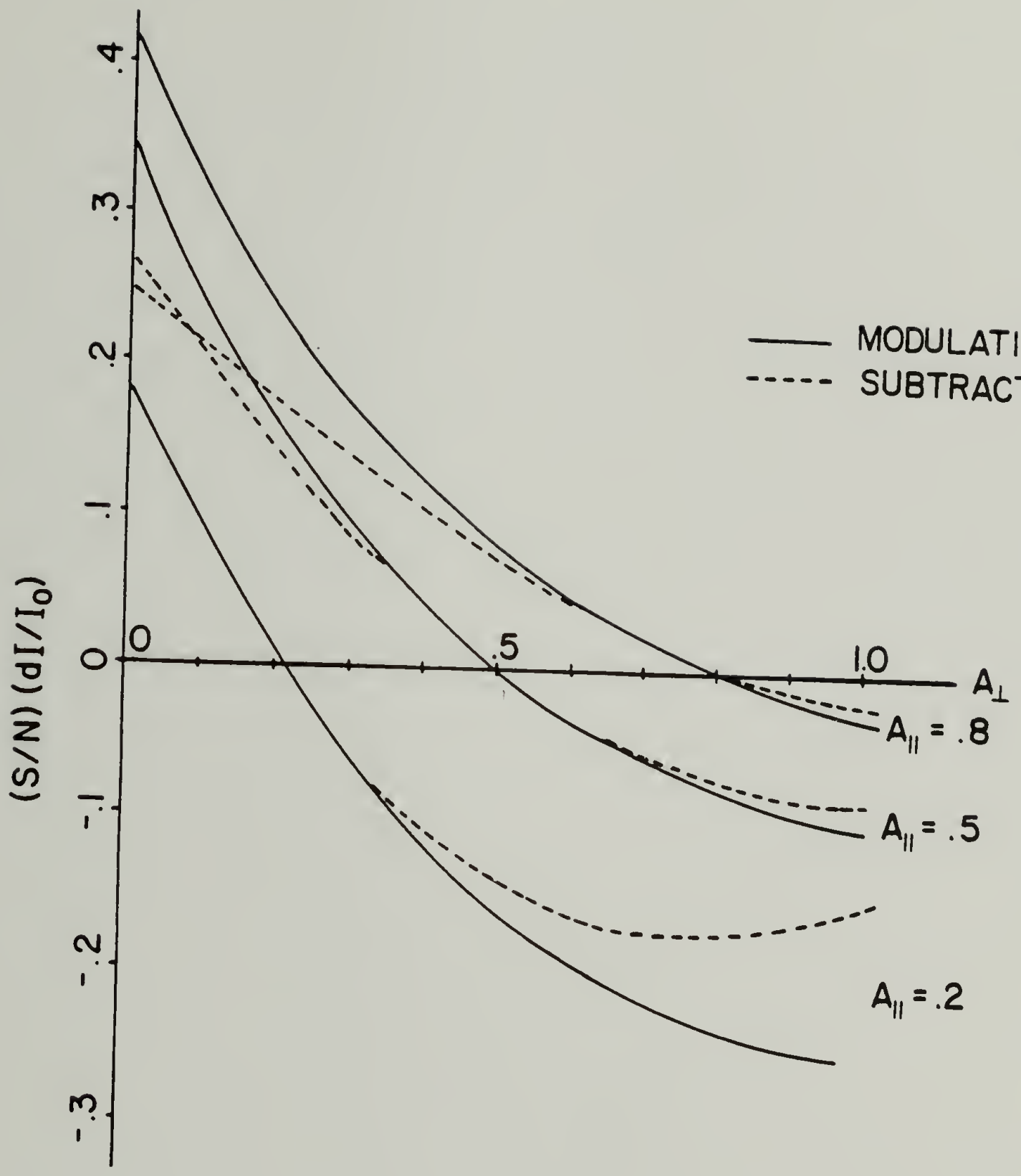

Figure 40

$$V(\delta) = \int_{\bar{\nu}_1}^{\bar{\nu}_2} B(\bar{\nu}) \cos[2\pi\bar{\nu}\delta - \theta(\bar{\nu})]\, d\bar{\nu} \qquad (5.36)$$

both the phase, $\theta(\bar{\nu})$ and $B(\bar{\nu})$ over the entire spectral region are required. The transform itself, however, has no utility in a general sense for the consideration of the dynamic range. The consideration may be simplifed by setting the phase to zero for all wavenumbers. The maximum value of the interferogram then occurs at δ=0 and is given by the integral of $B(\bar{\nu})$ from $\bar{\nu}_1$ to $\bar{\nu}_2$.

$$V(\delta)_{max} = \int_{\bar{\nu}_1}^{\bar{\nu}_2} B(\bar{\nu})\, d\bar{\nu} \qquad (5.37)$$

By assuming a flat $B(\bar{\nu})$, the integral is proportional to the number of resolution elements, N, given by $(\bar{\nu}_2 - \bar{\nu}_1)/\Delta\bar{\nu}$ where $\Delta\bar{\nu}$ is the spectral resolution. The smallest contribution to the interferogram comes from the single resolution element of minimum intensity:

$$V(\delta)_{min} = B_{min}(\bar{\nu}) \cos(2\pi\bar{\nu}\delta) \qquad (5.38)$$

If the cosine is set equal to one, the estimated interferogram dynamic range becomes N times the spectral dynamic range. This estimate provides an upper limit for the interferogram dynamic range. In fact, a factor of $\sqrt{N}$ times the spectral dynamic range has been suggested as a more realistic estimate (39,162). For a 4 cm^{-1} resolution spectrum from 400 to 4400 cm^{-1} the $\sqrt{N}$ is about 30.

Taking the numbers presented in the chapter introduction, $A_{\parallel}$ is 1.00000, $A_{\perp}$ is 1.00011, and ΔA is 1.1. x 10^{-4} and the requirement for 10:1 dynamic range in ΔA (10^5 : 1 in $A_{\parallel}$ or $A_{\perp}$) results in an inter-

ferogram dynamic range of 300 to 1 for modulation and 3×10^6 to 1 for subtraction. A 15 bit A/D converter has a dynamic range of 3.2×10^4 to 1 and could accurately sample the modulation interferogram. The dynamic range of subtraction, 3×10^6 to 1, cannot be handled directly by the same arrangement. However, it is unlikely that the 10^5 to 1 absorbance signal to noise ratio could be achieved in a single scan. This shortcoming is normally corrected by utilizing the fact that the signal to noise and the measurement dynamic range can both be improved by coadding scans (39). In the optimum case, the dynamic range can be expected to increase with the square root of the number of scans (39). Therefore, if 10^4 scans with a dynamic range of 3×10^4 to 1 were coadded, the dynamic range could be improved 10^2 times to 3×10^6 to 1. Thus, it is theoretically possible to use subtraction to directly measure a very small signal. However, in actual practice, these results are not always realized. Theory predicts that spectral signal to noise should decrease with the square root of the number of scans, i.e. noise is proportional to $N^{-0.5}$. This is observed initially, but after a large number of scans the noise begins to level off. This leveling off occurs when the detector noise level falls below that of another noise source which does not decrease with the number of scans, as shown in Figure 41. The possible noise sources include digitization noise and round off errors in the numerical computation process for signal averaging or for the Fourier transform. These effects set a limit on the SNR improvement

Figure 41. Theoretical decrease in spectral noise with number of scans.

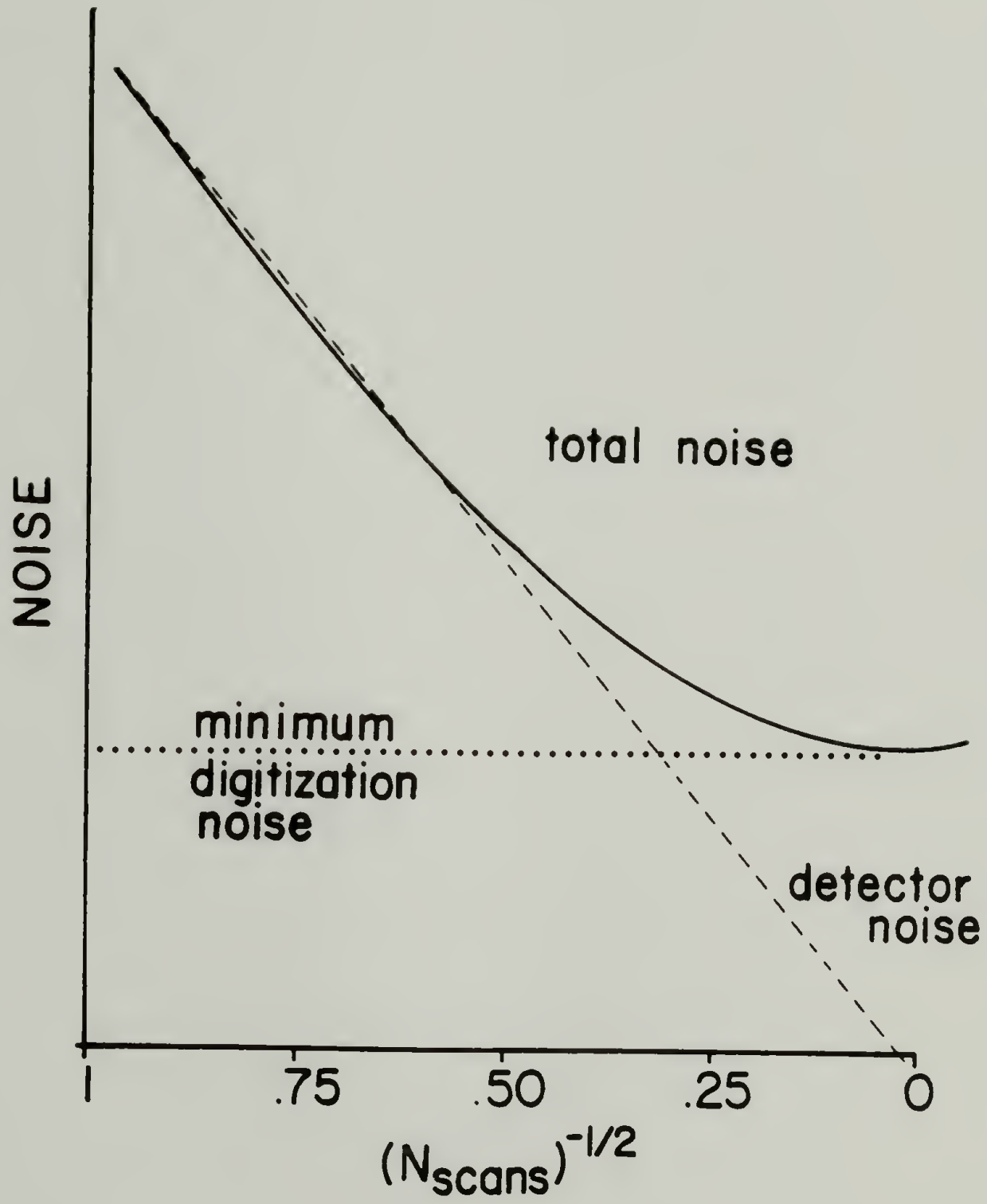
NOISE
total noise
minimum
digitization
noise
detector
noise
1
.75
.50
.25
0
$(N_{scans})^{-1/2}$

Figure 41

and on the dynamic range improvement. Figure 42 shows the decrease in noise for modulation and subtraction. The noise plotted versus $N^{-0.5}$ in Figure 42a shows the decrease to be linear up to 1000 scans. The method by which the data was plotted in Figure 42a is inconvenient since the data is highly compressed for large numbers of scans. In Figure 42b the data are plotted as the noise x $N^{0.5}$ versus N, and therefore are free from the vertical compression shown in the previous figure. In the second method of plotting the data, any uncertainty in measuring the noise is increased by $N^{0.5}$. In either case, the two plots show 1) that the noise is still continuing to decrease for both methods at 1000 scans, 2) the modulation noise is three to four times greater than the subtaction noise, and 3) a noise level of less than 2×10^{-4} absorbance units was obtained at 1000 scans by subtraction. The difference spectra ($A_{\parallel} - A_{\perp}$) of a highly oriented poly(p-phenylene benzobisthiazole) film shown in Figure 43 confirms the above conclusions.

The most significant result obtained in our study is the higher noise level obtained for modulation technique. This is principally caused by the optical losses of the modulator crystal and reduction in beam aperture. The observed difference spectrum between the two polarizations decreases at lower wavenumbers as the modulation efficiency falls off. At the same time the noise also increases at lower frequency as the modulator transmission decreases. Our results confirm that modulation fails to yield any theoretical signal to noise advantage over the subtraction technique and that in fact it is observed to operate at a disadvantage under these conditions. The

Figure 42. Comparison of the measured decrease in noise for the modulation and subtraction techniques
a. noise versus $(N_{scans})^{-1/2}$
b. noise $\cdot$ $(N_{scans})^{1/2}$ versus $(N_{scans})^{1/2}$

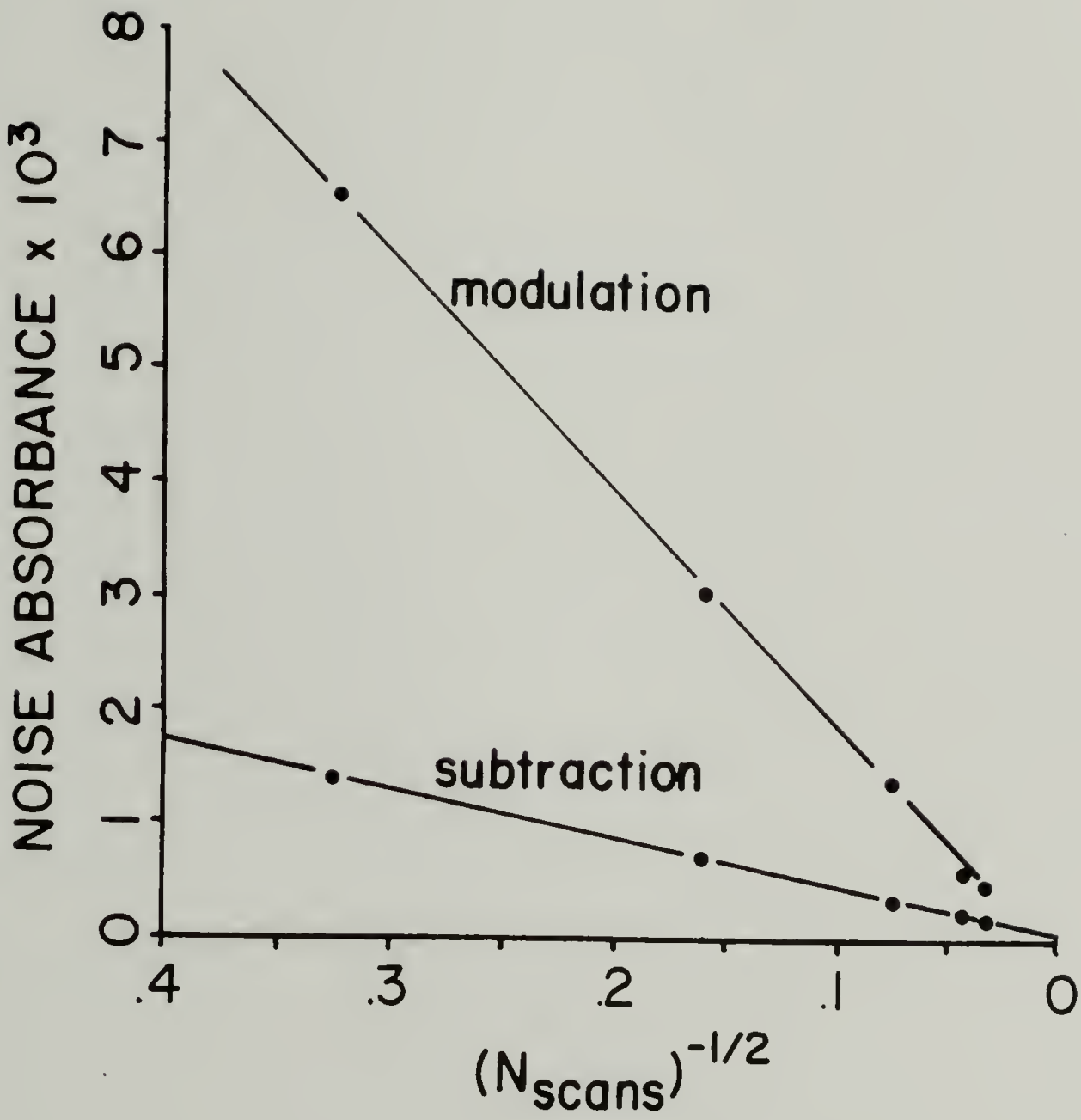
NOISE ABSORBANCE x 10³
0
1
2
3
4
5
6
7
8
.4
.3
.2
.1
0
modulation
subtraction
(N scans)^-1/2

Figure 42a

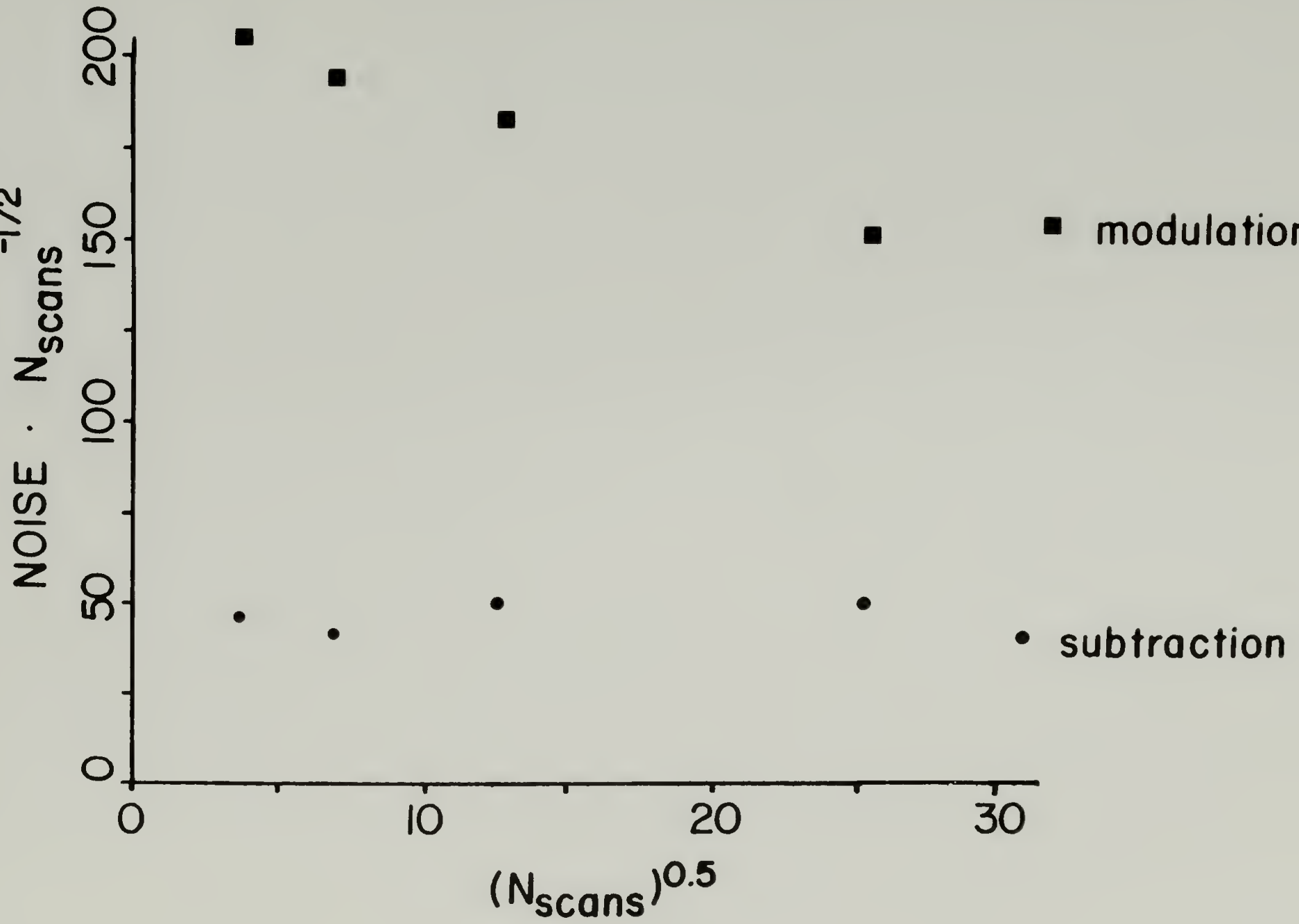
NOISE · $N_{scans}^{-1/2}$
0
50
100
150
200
0
10
20
30
$(N_{scans})^{0.5}$
modulation
subtraction

Figure 42b

Figure 43. The difference spectra ($A_{\parallel}$-$A_{\perp}$) for a highly oriented poly(p-phenylene benzobisthiazole) film which shows the difference in noise levels and spectral features (10 scans at 4 cm^{-1} resolution)
a. the subtraction technique
b. the modulation technique

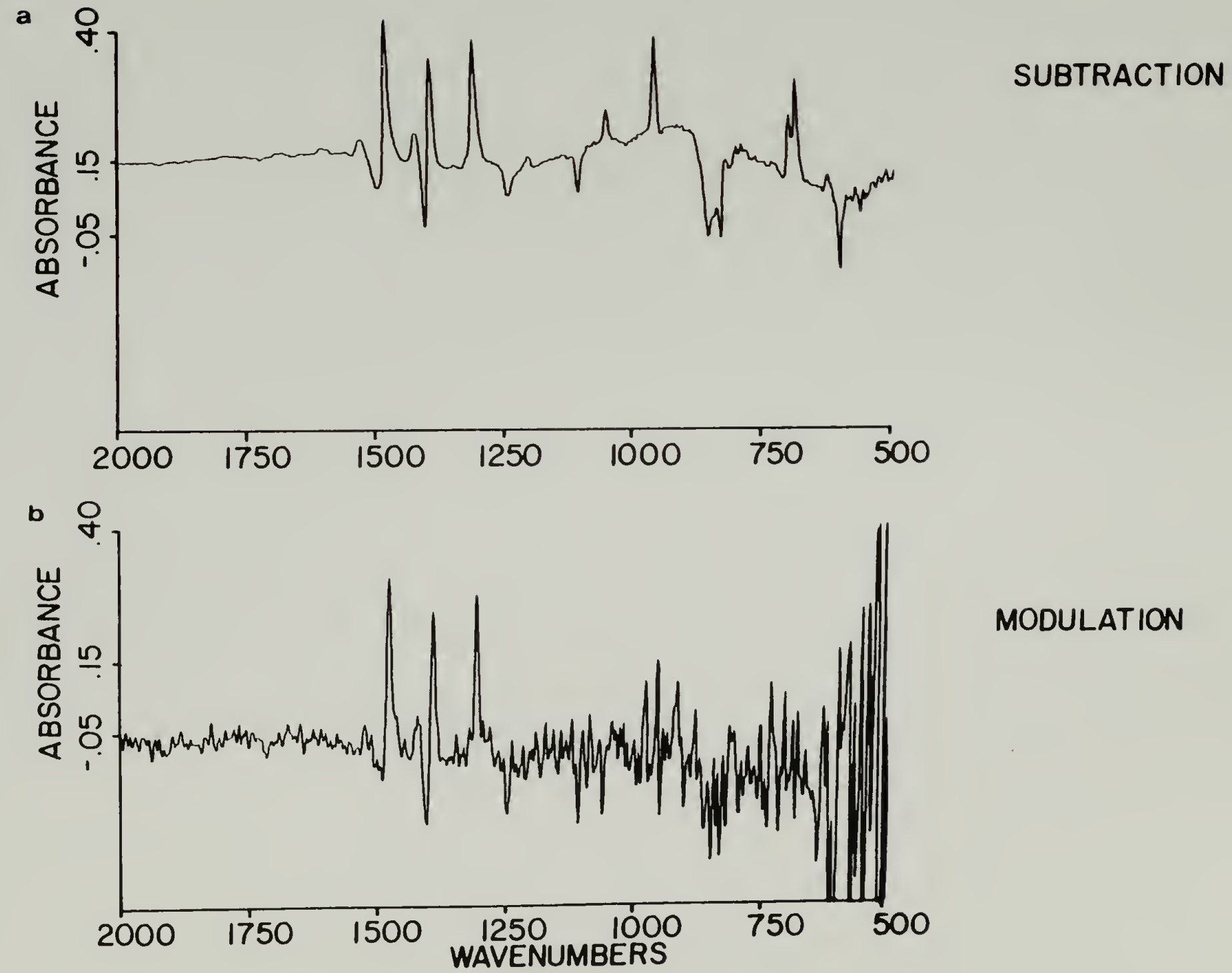
a
ABSORBANCE
.40
.15
-.05
2000
1750
1500
1250
1000
750
500
SUBTRACTION
b
ABSORBANCE
.40
.15
-.05
2000
1750
1500
1250
1000
750
500
WAVENUMBERS
MODULATION

Figure 43

plots of decreasing noise with number of scans show that subtraction can be used to measure a difference spectrum feature of 2 x 10-3 absorbance units with a 10:1 signal to noise ratio by coadding 1000 scans into the parallel and perpendicular files (this would take about 15 minutes).

In an earlier study of FT-IR polarization modulation, Marcott et al. reported that modulation produced better results than subtraction using one FT-IR spectrometer. But equivalent results for modulation and subtraction were obtained on a second FT-IR system (152). The relative merits of the two techniques depends on the sensitivity and noise level of the detector as well as the overall throughput of the spectrometer. The relative merits of the two techniques depend very much on the spectrometer throughput and the amplitude of detector noise. If the FT-IR instrument throughput and detector area are properly matched, it may be possible to increase the aperture opening to compensate for the optical losses of the modulator (151), thus possibly allowing modulation to out-perform subtraction.

To perform infrared rheo-optical measurements of polymer films undergoing small amplitude oscillatory strains, Noda, Dowrey, and Marcott have employed a triple modulation scheme using a dispersive instrument (163,164). The three modulations used were 1) chopping the IR beam, 2) sample strain, and 3) polarization modulation. In response to a 0.1%, 100 Hertz strain, they obtained a dichroic difference of 1.3×10^{-4} absorbance units in the 1465 cm^{-1} band of a high density polyethylene film.

Experimental

A Hinds International series II photoelastic modulator with a ZnSe crystal was used (165). The ZnSe optical element at 750 cm^{-1} has a low transmission value of 50%; and the lower limit for which half wave retardance can be produced is 1250 cm^{-1}. The ZnSe crystal is 5 cm in diameter and a mask 1.6 cm in diameter was used to ensure that the retardance was uniform over the infrared beam. The crystal is driven at 74 KHz (ω_d), alternating the polarization at 148 Khz ($2\omega_d$). The modulator control unit allows the wavelength of half wave retardance to be set and provides a reference signal at ω_d and $2\omega_d$.

A mount was constructed to hold the modulator in the beam with the modulator principal axes rotated 45° from sample parallel and perpendicular directions.

A Harrick quad diamond polarizer, mounted before the sample compartment, can be placed into the IR beam and set at any angle or can be removed out of the beam. When a polarizer was required after the modulator, a Perkin Elmer wire grid polarizer was mounted on the modulator.

A PAR model 124A lock-in amplifier was used as a phase sensitive amplifier (mixer). A model 116 preamplifier was used in the direct input mode and the input high pass filter was set to 40 KHz with a Q of 1. The lock-in amplifier has a specified frequency response up to 200 KHz, presumably adequate for the input channel, but in reality the

mixer was required to have a higher limit. The in-phase mixer output signal for a 150 KHz sine wave input is a $|\sin wt|$ or $\sin^2 wt$ waveform with a fundamental frequency of 300 KHz plus higher frequency harmonics. The 90° out of phase mixer output signal has even stronger high frequency harmonics. The limited frequency response causes a phase shift between the fundamental and harmonics, producing an uninterpretable mixer output signal. This prevents the reference phase from being adjusted while observing the mixer output with an oscilloscope. Nonetheless, the mixer provides a reasonable signal proportional to the amplitude of the $2\omega_d$ component of the input signal. The signal must be taken directly from the mixer output because the following output stages (with an approximately 1 msec time constant) would attenuate the $\omega_{\tilde{\nu}}$ components (100 Hz to 10 KHz) severely. Care must be taken not to overload the input preamplifier stage which has a 1.6 volt clipping level. The maximum IR detector signal is ±10 volts but this level is attenuated by all the optical elements used in the modulation experiment.

The detector signal from the Nicolet FT-IR was taken from the detector 1 input on the beam path control board (Figure 44) and routed to the lock-in input. The lock-in output is returned to the detector 2 input on the beam-path control board. This allows a selection of the AC or DC interferogram by selecting detector 2 or 1 through the FT-IR operating software. respectively. The signal is removed and reinserted before the band pass filters of the FT-IR as seen in the block diagram of Figure 34.

Figure 44. Fourier transform infrared signal path modifications for the polarization modulation experiment.

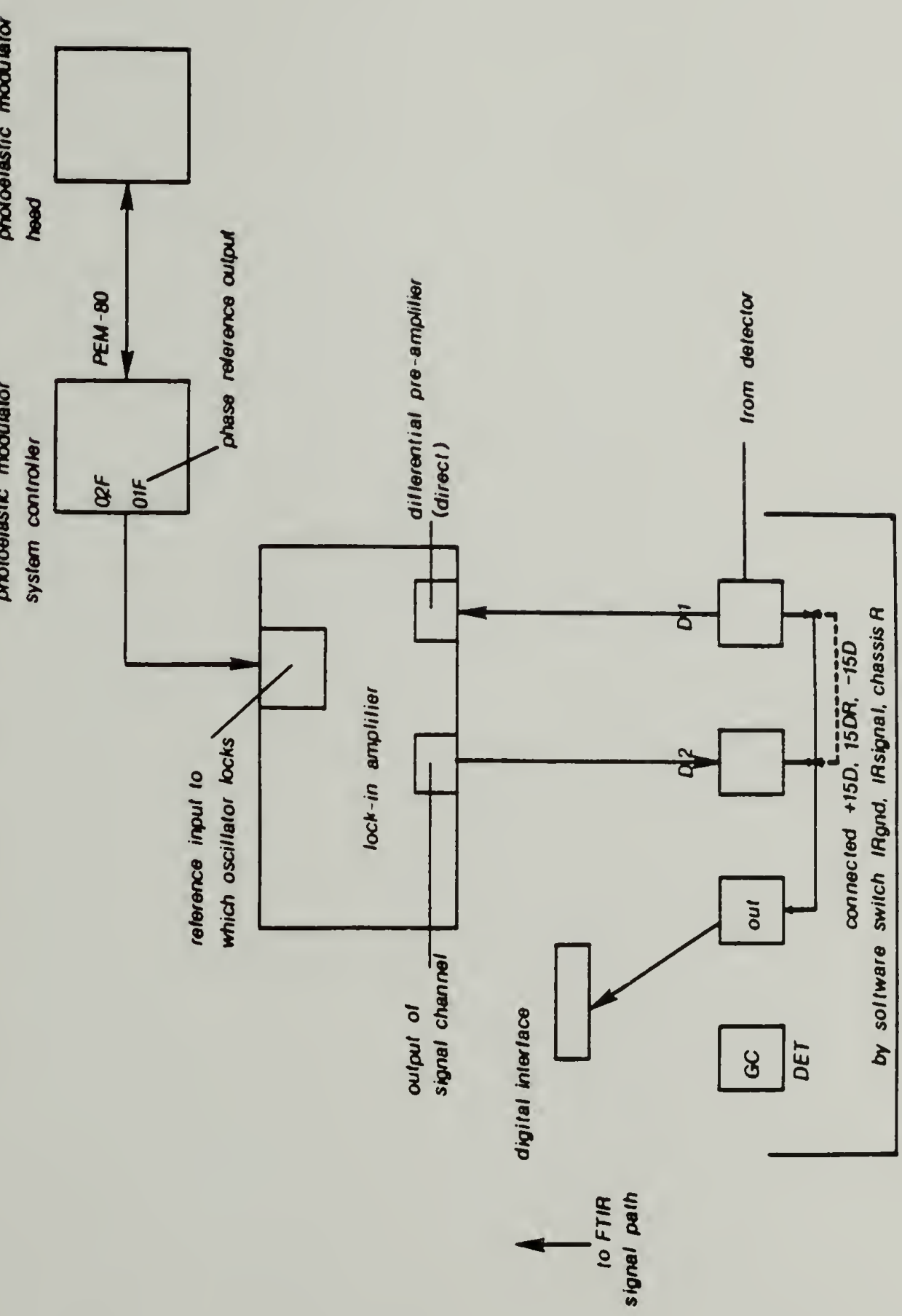
SCHEMATIC OF MODIFIED SIGNAL DETECTION AND PROCESSING
photoelastic modulator
system controller
PEM-80
photoelastic modulator head
Q2F
Q1F
phase reference output
differential pre-amplifier (direct)
from detector
reference input to which oscillator locks
lock-in amplifier
D1
Q2
output of signal channel
digital interface
out
GC
DET
connected +15D, 15DR, -15D
by software switch IRgnd, IRsignal, chassis R
detector switching on beam path control board
to FTIR signal path

Figure 44

Several authors have suggested that the parallel and perpendicularly polarized beam (incident on the sample) should be equalized when the modulator is placed after the sample (151,153). This minimizes the intensity of the AC interferogram and its dynamic range. This can have several side effects: 1) the strong central peak of the AC interferogram disappears. This prevents correlation of the peak location during the data collection. This also makes the signal difficult to distinguish on an oscilloscope when adjusting the lock-in amplifier. 2) When the intensities are equal, the difference spectrum baseline will be very close to zero and negative peaks can occur in the difference spectrum. These peaks are subject to phase correction errors when the AC interferogram is Fourier transformed (149,152). The normal phase correction techniques assume that there are no negative intensities in the signal and can incorrectly invert peaks in the difference spectrum. 3) Some optical element must be used to adjust the intensities and will result in a reduced signal level.

A polarizer set to 45 degrees before the sample can be used to ensure that equal parallel and perpendicular intensities reach the sample. Before the polarizer, the parallel intensity is about two times the vertical intensity in our spectrometer. Inserting the polarizer reduces the total intensity by at least 50 percent, but leaves the two components equal. If the intensities are not equalized, the effects on the signals is shown by modifying equations 5.4 and 5.5.

$$I_{dc} = 0.5[\chi \cdot I_o\, 10^{-A_\parallel} + I_o\, 10^{-A_\perp}]$$

$$I_{dc} = 0.5\, I_o\, [10^{-A_\parallel + \log \chi} + 10^{-A_\perp}] \qquad (5.39)$$

where χ is the ratio of $I_{o\parallel}$ to $I_{o\perp}$. Equation 5.6 becomes

$$I_{ac}/I_{dc} = \tanh \{0.5 \cdot \ln 10 \cdot (A_\parallel - A_\perp - \log \chi)\} \qquad (5.40)$$

which shows the effect to be a shift in the baseline of $\log \chi$ absorbance units. Care must be taken that the argument of tanh is not too large causing considerable error in the approximation of $\chi = \tanh\chi$. If the baseline shift is larger than $A_\parallel - A_\perp$, there will be no negative intensities in I_{ac} and phase errors will be unlikely.

The intensities may be equalized or not depending on the demands of the particular experiment. To maximize the signal reaching the detector, the intensities should be left unequalized. To minimize the dynamic range, the polarizer should be used at 45 degrees. The two disadvantages mentioned previously (difficulties correlating coadded interferograms and phase correction errors) can be reduced by rotating the polarizer slightly away from 45 degrees, thereby adding a central peak to the interferogram and a baseline shift to the difference spectrum.

Discussion

The advantages of polarization modulation may be divided into two types: intrinsic - relating to reduction in dynamic range and improvment in SNR due to differential as opposed to difference measurement, and practical - which result from not having to measure two separate

spectra and not having to rotate the sample or polarizer. The practical advantages include relaxing the requirement that the sample be identical when the parallel and perpendicular spectra are measured, which can be extremely difficult if the sample undergoes rapid irreversible changes. The polarization modulation technique also reduces the likelihood of having artifacts associated with non-uniform samples, IR beam profiles, and polarizer imperfections.

The practical advantages can be quite significant in IR rheo-optical experiments where time between spectra is an important parameter and where the sample is often changing continuously. The practical disadvantages should also be considered. These include a significant attentuation of the IR beam, a low frequency limit of about 800 cm^{-1}, as well as the cost, complexity, and an additional source of experimental complication.

Examination of the intrinsic advantages has shown that the dynamic range reduction of modulation is not that important. For subtraction, the measurement dynamic range is higher than the spectral dynamic range for measurement down to 2×10^{-4} absorbance units. This was proven by the continued decrease in noise with the square root of the number of scans. Therefore, measurement of spectral features down to the noise level should be possible. For different experimental conditions in which the measurement of the interferogram is dynamic range limited, modulation can significantly reduce the dynamic range to allow accurate measurements. The noise level should be essentially independent of the measurement technique; any advantage modulation

gains by using a higher measurement frequency (up to 100 x higher) can be easily lost during the modulation and demodulation processes.

The intended application of polarization modulation was rheo-optical studies. Noda et al. have shown that the dynamic dichroism is about 10^{-4} absorbance units or less in such experiments (163). However, the samples used often exhibit a static dichroism that is at least 10^{-2} absorbance units and often higher. The high SNR required to measure differences of this magnitude are difficult to obtain by any method. Noda et al. typically scanned about 2 cm^{-1}/min at a 16 cm^{-1} resolution. In their triple modulation experiment, they demodulated the strain dependence to eliminate the static dichroism and can directly measure the dynamic dichroism. With FT-IR, the strain frequencies fall at or below the Fourier frequencies and therefore cannot be demodulated.

The strain dependence in the small amplitude harmonic experiments using FT-IR can be determined using time-resolved FT-IR. However, before combining two such complex experiments, each must be well understood or the results will be totally unreliable. Because of the stringent repeatability requirements of TRS and the inefficiency in data collection of the present TRS implementation, the practical modulation advantages are quite significant even if the intrinsic advantages do not come into play.

Conclusion

Comparison of modulation and subtraction does not provide an

overwhelming advantage for modulation that would favor it over a much simpler and more straightforward subtraction technique. It was demonstrated that the measurement of noise reduction with increasing number of scans could be substituted for a direct calculation of interferogram dynamic ranges. These measurements showed a continued decrease in subtraction noise up to 1000 scans and this was taken as evidence that the interferogram was measured with adequate resolution.

The comparison of predicted and actual modulation efficiencies revealed a reduced actual efficiency at low retardation when the dichroism is very high. The decrease was attributed to light passing through the crossed polarizers due to imperfect polarization. The measured efficiency curve is required to correct the measured modulation spectra.

Direct comparison of the two technqiues for two polymer samples showed subtraction produced better results due to the optical losses of modulation. The PBT dichroic spectra for both techniques are identical except for the noise levels.

The modulation technique should be considered when the optical losses can be compensated by opening up the aperture (on a IBM-98 FT-IR for example), when a high dynamic range interferogram is encountered (a high interferometer throughput or a small area and/or high D* detector) or when the practical advantages warrant it (TRS dichroic experiments).

CHAPTER VI

SUMMARY AND FUTURE WORK

This chapter presents our conclusions regarding the utilization of vibrational spectroscopy to follow deformation induced microstructural response in polymers. Some suggestions and considerations for future efforts in this area of research are also given.

The low frequency Raman LAM technique was shown to be an excellent morphological tool to examine highly oriented, tensile drawn, or solid state extruded polyethylene because the LAM information is sensitive to the extensive conformational defects existing in these materials. A review of previous LAM studies emphasizing the effects of defects on the LAM vibrations was carried out. This understanding is necessary to interpret the Raman LAM spectra which were obtained. Our analysis of quenched and annealed 1000 molecular weight polyethylene samples confirmed that the defects disrupt the LAM considerably, effectively redistributing the intensities to higher frequencies. The exceptionally broad LAM obtained for a tensile drawn polyethylene sample indicates a morphology containing large amounts of structural defects. In contrast, the well ordered structure of the 1000 molecular weight fraction of polyethylene gives a relatively narrow LAM peak and length distribution. When this tensile drawn sample was annealed, the LAM peak narrowed, indicating structural reorganization which produced a more ordered structure and a peak in the length distribution.

The solid state extruded polyethylene samples of draw ratio 12, 24, and 36x were used to study the effect of varying draw ratio (DR) on the fibrillar microstructures. Our results from the spectroscopic study supplement the information previously obtained for these samples with a variety of other techniques. The LAM results showed that the distribution of straight chain lengths in the solid state extrudates shifted to considerably shorter chain lengths with increasing DR, suggesting a higher defect content. No single model in the literature could explain all the structural features observed with the various techniques. We have interpreted the LAM results as an increasing amount of conformational defects in the crystals at higher draw ratios.

A second area of our present study led to significant improvements in the sensitivity and time resolution of the infrared rheo-optical technique, which is used to follow microstructural changes that occur during polymer deformation. The introduction of Fourier transform infrared (FT-IR) spectrometers has made the infrared technique faster and more sensitive, yet measurement of fast (less than 1 second) structural response in polymers was still difficult or impossible until the development of time resolved spectroscopy (TRS). TRS enables improved S/N ratios through signal averaging and improved time resolution. We have developed a new TRS technique specifically designed for polymer deformation studies. The flexibility in the choice of strain waveforms and time resolutions (0.1 msec to 10 seconds) allows a direct comparison between the dynamic infrared data

and dynamic mechanical analysis. A number of studies have been carried out with the new technique including the analysis of the crystal-crystal phase transition of poly(tetramethylene terephthalate) presented in this dissertation.

Additional modifications to the new TRS technique have significantly improved the data collection efficiency. One modification allows valid data to be collected even when the interferogram peak location is not stable. In the past this was a major source of experimental difficulty. A second modification resulted in shorter times for collection of the entire set of interferograms by distributing the collected files more evenly among the various counter values (more even signal to noise ratio). By decreasing the overall experiment time, the requirement of repeatable sample response was eased, thus allowing a larger variety of samples to be studied.

Infrared rheo-optical investigations of poly(tetramethylene terephthalate) (4GT) and the random block copolymer of tetramethylene terephthalate and poly(tetramethylene oxide) were carried out. Previous studies of 4GT have shown that the mechanical properties are affected by a reversible, crystal-crsytal phase transformation (α to β) From a study of α to β transformation in 4GT, we have found the crystalline phase transition to be reversible with no observable delay between the macroscopic strain applied and the crystalline phase transition. In addition, we determined that the phase transformation takes place primarily for crystals with their c-axis parallel to the uniaxial deformation axis. We have demonstrated for the first time

that the α-β transition takes place within the crystalline tetramethylene terephthalate sequences of the copolymer. In the copolymer, the microstructural changes corresponding to the macroscopic stress-strain behavior have been characterized in terms of the extent of α-β transformation and the segmental orientation of the amorphous, α crystalline and β crystalline hard segments and the soft segments.

The polarization modulation technique was evaluated as a method to improve the measurement of extremely small spectroscopic differences such as the dichroic ratio changes as a function of strain. This technique has been shown in the literature to be useful when measuring small polarization differences for both circularly and linearly polarized infrared radiation. However, a detailed discussion of its advantages and limitations had not been presented previously. Our analysis of the reduction in the signal to noise ratio with increasing number of scans showed that the instrument dynamic range was adequate to accurately sample the subtraction interferogram. Therefore, effective signal averaging can be carried out. Since this was the case, modulation did not offer any improvement in S/N ratio or sensitivity compared to the much simpler subtraction technique. The modulation technique still offers the advantages that certain spectroscopic artifacts can be eliminated and that it is convenient to carry out.

Two potential areas of investigation by the LAM technique are presented. The interpretation of LAM spectra requires reliable determination of the low frequency baseline. The baseline can be characterized by a study of samples with well defined, narrow LAM

peaks. High pressure crystallization of polyethylene produces samples with highly extended chains. High pressure crystallization of narrow molecular weight distribution PE would give samples which can be used to measure and optimize the Rayleigh line rejection of the Raman spectrometer in the very low frequency region. This information would enable a much more accurate determination of the straight chain length distribution from the LAM spectrum.

The longitudinal acoustic mode was used in this dissertation to qualitatively determine the crystal defect content. Extension of this work to well defined samples would provide a basis for quantitative determination of defect content. Polyethylene samples prooduced by crystallization of thin films pulled from the melt exhibit a piled lamellar morphology (98). Their well defined crystal orientation allows precise measurement of the crystal dimensions and the angle of chain axis tilt with respect to the lamellar surface. In this case, the crystal thickness measurements by x-ray or electron microscopy and the stem length by Raman LAM should be comparable. After the LAM data has been corrected for the tilt of the chains away from the lamellar surface normal, the remaining difference is due to the presence of defects in the crystal stems. Therefore, the fraction of crystal stems containing defects can be estimated. The defect content can also be estimated from certain infrared or Raman bands which are sensitive to non-trans conformations. The amorphous contribution to these bands can be subtracted, leaving the crystal defect contributions. Additionally, the defect concentration may be esti-

mated from the increase in crystal density above its theoretical value.

In these melt crystallized thin films and in the high pressure crystallized samples, the defect content can be varied by annealing and partial melting. This allows the agreement between the three methods to be compared over a wide range of defect concentrations. After establishing the techniques in these simple systems, they could be used wth the ultra-oriented polyethylene samples or to study crystal melting and annealing mechanisms. Suggestions for further study of Hytrel® are given in the next section.

In the case of random block copoly(ether ester)s, selective deuteration could be used to facilitate studies of their microstructural deformation behavior. In the present study, the hard segment orientation and conformation changes were determined but the soft segment microstructural response was not well characterized. The extension of the rubbery, amorphous chains may produce both changes in their orientation and conformation. These conformation changes can easily be observed during crystallization of poly(tetramethylene oxide) but they are difficult to monitor in the copolymer because of band overlap with the more intense bands of the tetra methylene terephthalate segments. Preparation of copoly(ether ester)s using deuterated polyether or deuterated butane diol would eliminate much of the band overlap. Then, the microstructural response could be described by the strain and time dependence of the stress in the hard and soft segments as well as their orientation. From this data, the

number of statistical segments between the soft segment crosslinks and the load sharing between the crystalline and amorphous regions could be determined.

REFERENCES

1. T. Kanamoto, A. Tsuruta, K. Tanaka, M. Takeda, and R.S. Porter, Polymer J. 15, 327 (1983).
2. T. Ohta, Polym. Eng. and Sci. 23, 697 (1983).
3. A.E. Zachariades, W.T. Mead, and R.S. Porter, Chemical Rev. 80, 351 (1980).
4. A. Tsuruta, T. Kanamoto, K. Tanaka, and R.S. Porter, Polym. Eng. and Sci. 23, 521 (1983).
5. D.G. Peiffer, Polym. Eng. and Sci. 20, 167 (1980).
6. J. Clements and I.M. Ward, Polymer 24, 27 (1983).
7. W.W. Adams, R.M. Briber, E.S. Sherman, R.S. Porter, and E.L. Thomas, Polymer, in press.
8. A.G. Gibson, G.R. Davies, and I.M. Ward, Polymer 19, 684 (1978).
9. S. Nagou and K. Azuma, J. Macromol. Sci. Phys. B16, 435 (1979).
10. A. Peterlin, Polym. Eng. and Sci. 19, 118 (1979).
11. R.S. Porter, Polym. Prep., Am. Chem. Soc. 12(#2), 39 (1971).
12. W.N. Taylor and E.S. Clark, Polym. Eng. and Sci. 18, 518 (1978).
13. R.G. Snyder and J.R. Scherer, J. Polym. Sci., Polym. Phys. Ed. 18, 421 (1980).
14. R.G. Snyder, S.J. Krause, J.R. Scherer, J. Polym. Sci., Polym. Phys. Ed. 16, 1593 (1978).
15. D.H. Reneker and B. Fanconi, J. Appl. Phys. 46, 4144 (1975).
16. A. Peterlin, Colloid and Polym. Sci. 253, 809 (1975).
17. R.S. Stein, Accounts of Chemical Research 5, 121 (1971).

18. R.S. Stein, J. Polym. Sci. C15, 185 (1966).

19. D.P. Pope and A. Keller, J. Polym. Sci., Polym. Phys. Ed. 13, 533 (1975).

20. A. Peterlin, J. Mat. Sci. 6, 490 (1971).

21. K. Fujita, S. Suehiro, S. Nomura, and H. Kawai, Polym. J. 14, 545 (1982).

22. R. Yamada and R.S. Stein, J. Appl. Phys. 36, 3005 (1965).

23. Y. Kobayashi, S. Okajima, and A. Narita, J. Appl. Polym. Sci. 11, 2515 (1967).

24. Y. Uemura and R.S. Stein, J. Polym. Sci., A2 10, 1691 (1972).

25. T. Asada, J. Sasada, and S. Onogi, Polym. J. 3, 350 (1972).

26. K. Fujita, M. Daio, R. Okumrua, S. Suehiro, S. Nomura, and H. Kawai, Polym. J. 15, 449 (1983).

27. I.M. Ward and M.A. Wilding, Polymer 18, 327 (1977).

28. P.C. Painter, J. Havens, W.W. Hart, and J.L. Koenig, J. Polym. Sci., Polym. Phys. Ed. 15, 1237 (1977).

29. P.C. Painter, J. Runt, M.M. Coleman, and I.R. Harrison, J. Polym. Sci., Polym. Phys. Ed. 16, 1253 (1978).

30. Y. Kikuchi and S. Krimm, J. Macromol. Sci.- Phys. B4, 461 (1970).

31. H. Ishihara, I. Kimura, K. Saito, and H. Ono, J. Macromol. Sci. - Phys. B10, 591 (1974).

32. H.W. Siesler, Polym. Bull. 9, 557 (1983).

33. H.W. Siesler, Polym. Bull. 9, 382 (1983).

34. H.W. Siesler, Polym. Bull. 9, 471 (1983).

35. R. Zbinden, "Infrared Spectroscopy of High Polymers", Academic Press, New York, 1964.

36. R.J. Samuels, Die Makromol. Chemie, Suppl. 4, 241 (1981).

37. R.J. Samuels, "Structured Polymer Properties", Wiley, New York, 1974.

38. H.W. Siesler, J. Molec. Struct. 59, 15 (1980).

39. Peter R. Griffiths, "Chemical Infrared Fourier Transform Spectroscopy Chemical Analysis", Vol. 43, John Wiley & Sons, New York, 1975.

40. D.J. Burchell, J.E. Lasch, R.J. Farris, and S.L. Hsu, Polymer 23, 965 (1982).

41. J.E. Lasch, T. Masaoka, D.J. Burchell, and S.L. Hsu, Polym. Bull. 10, 51 (1983).

42. J.E. Lasch, D.J. Burchell, T. Masaoka, and S.L. Hsu, Appl. Spectrosc. 38, 351 (1984).

43. R.E. Murphy, F.H. Cook, and H. Sakai, J. Opt. Soc. Am. 65, 600 (1975).

44. H. Sakai and R.E. Murphy, Applied Optics 17, 1342 (1978).

45. A.W. Mantz, Appl. Optics 17, 1347 (1978).

46. A.W. Mantz, Appl. Spectrosc. 30, 459 (1976).

47. W.G. Fately and J.L. Koenig, J. Polym. Sci., Polym. Lett. Ed. 20, 445 (1982).

48. A.A. Garrison, R.A. Crocombe, G. Mamantov, and J.A. deHaseth, Appl. Spectrosc. 34, 399 (1980).

49. R. Jakeways, I.M. Ward, M.A. Wilding, I.H. Hall, I.J. Desborough, and M.G. Pass, J. Polym. Sci., Polym. Phys. Ed. 13, 799 (1975).

50. C.A. Boye, Jr. and J.R. Overton, Bull. Am. Phys. Soc., Ser. 2 19, 352 (1974).

51. M. Yokouchi, Y. Sakakibara, Y. Chantani, H. Tadakoro, T. Tanaka, and K. Yoda, Macromolecules 9, 266 (1976).

52. B. Stambaugh, J.L. Koenig, and J.B. Lando, J. Polym. Sci., Polym. Phys. Ed. 17, 1053 (1979).

53. Z. Mencik, J. Polym. Sci., Polym. Phys. Ed. 13, 2173 (1975).

54. M.G. Brereton, G.R. Davies, T. Smith, and I.M. Ward, Polymer 19, 17 (1978).

55. B.J. Cella, J. Polym. Sci., Polym. Symp. Ed. 42(2), 727 (1973).

56. R.W. Seymour, J.R. Overton, and S.L. Cooper, Macromolecules 8, 331 (1975).

57. B. Kalb and A.J. Pennings, Polymer, 21, 3 (1980).

58. P.D. Griswald, A.E. Zachariades, and R.S. Porter, Polym. Eng. Sci., 18, 861 (1978).

59. A.G. Gibson, I.M. Ward, B.N. Cole, and B.J. Parsons, J. Mater. Sci., 9, 1193 (1974).

60. K. Yamada and M. Takayanagi, J. Appl. Polym. Sci., 27, 2091 (1982).

61. A. Peterlin, Colloid and Polym. Sci., 253, 809 (1975).

62. A.G. Gibson, G.R. Davies, and I.M. Ward, Polymer, 19, 683 (1978).

63. E.S. Clark and L.S. Scott, Polym. Eng. Sci. 14, 682 (1974).

64. P.H. Shu, D.J. Burchell and S.L. Hsu, J. Polym. Sci., Polym. Phys. Ed., 18, 1421 (1980).

65. A. Peterlin and R.G. Snyder, J. Polym. Sci., Polym. Phys. Ed., 19, 1727 (1981).

66. E.S. Sherman, R.S. Porter, and E.L. Thomas, Polymer, 23, 1069 (1982).

67. T. Shimanouchi and M. Tasumi, Indian J. Pure and Appl. Phys., 9, 958 (1971).

68. G.R. Strobl and R. Eckel, Colloid and Polym. Sci., 258, 570 (1980).

69. W.L. Peticolas, G.W. Hibler, J.L. Lippert, A. Peterlin, and H. Olf, Appl. Phys. Lett., 18, 87 (1971).

70. S. Mizushima and T. Shimanouchi, J. Am. Chem. Soc., 71, 1320 (1949).

71. R.F. Schaufele and T. Shimanouchi, J. Chem. Phys., 47, 3605 (1967).

72. H. Takeuchi, T. Shimanouchi, M. Tasumi, G. Vergoten and G. Fleury, Chem. Phys. Lett., 28, 449 (1974).

73. H.G. Olf, A. Peterlin, and W.L. Peticolas, J. Polym. Sci., Polym. Phys. Ed., 12, 359 (1976).

74. S.L. Hsu, G.W. Ford, and S. Krimm, J. Polym. Sci., Polym. Phys. Ed., 15, 1769 (1977).

75. S.L. Hsu and S. Krimm, J. Appl. Phys., 48, 4013 (1977).

76. S.L. Hsu and S. Krimm, J. Appl. Phys., 47, 4265 (1976).

77. C. Chang, and S. Krimm, J. Polym. Sci., Polym. Phys. Ed., 17, 2163 (1979).

78. G.R. Strobl and R. Eckel, J. Polym. Sci., Polym. Phys. Ed., 14, 913 (1976).

79. G.R. Strobl, J. Polym. Sci., Polym. Phys. Ed., 21, 1357 (1983).

80. M. Glotin and L. Mandelkern, J. Polym. Sci., Polym. Phys. Ed. 21, 29 (1983).

81. G.V. Fraser, Polymer, 19, 857 (1978).

82. R.T. Harley, W. Hayes, and J.F. Twisleton, J. Phys. (C) Solid State, 6, L167 (1973).

83. A.T. Young, Physics Today, 35(1), 42 (1982).

84. Q.L. Liu and C.H. Wang, Macromolecules, 16, 1900 (1983).

85. J.F. Scott, The Spex Speaker, 17(2), 1972, Spex Industries, Metuchen, NJ, 1972.

86. J.F. Rabolt and C.H. Wang, Macromolecules, 16, 1698 (1983).

87. B. Fanconi and J. Crissman, J. Polym. Sci., Lett. Ed., 13, 421 (1975).

88. R.G. Snyder, J.R. Scherer, and A. Peterlin, Macromolecules 14, 77 (1981).

89. J.R. Sherer and R.G. Snyder, J. Chem. Phys., 72, 5798 (1980).

90. J. Mazur and D.H. Reneker, Bull. Am. Phys. Soc. 29(#3), 448 (1984).

91. J.L. Koenig and D.L. Tabb, J. Macromol. Sci.-Phys. B9, 141 (1974).

92. Y.K. Wang, D.A. Waldman, R.S. Stein, and S.L. Hsu, J. Appl. Phys. 53, 6591 (1982).

93. P.J. Hendra, H.P. Jobic, and K. Holland-Mortiz, J. Polym. Sci., Polym. Lett. Ed., 13, 365 (1975).

94. C.J. Farrel and A. Keller, J. Mat. Sci. 12, 966 (1977).

95. E.S. Sherman, Ph.D. Thesis, University of Massachusetts (Amherst), 1980.

96. C.M. Hartwig, E. Wiener, and S.P.S. Porto, Bull. Am. Phys. Soc. 15, 327 (1970).

97. L.E. Alexander, "X-Ray Methods in Polymer Science", R.E. Krieger Pub. Co., New York, 1979.

98. W.W. Adams, Ph.D. Thesis, University of Massachusetts (Amherst), 1984.

99. B. Crist and N. Morosoff, J. Polym. Sci., Polym. Phys. Ed. 11, 1023 (1973).

100. R.W. Hendricks, J. Appl. Cryst., 11, 15 (1978).

101. M. Tasumi and S. Krimm, J. Chem. Phys. 46, 755 (1967).

102. M. Glotin and L. Mandelkern, Colloid and Polym. Sci. 260, 182 (1982).

103. G.R. Strobl and W. Hagedorn, J. Polym. Sci., Polym. Phys. Ed. 16, 1181 (1978).

104. Nicolet Laser Raman System, Nicolet Instrument Corporation, 5225 Verona Road, Madison, WI.

105. Spex Datamate, Spex Industries, 3880 Park Ave., Metuchen, NJ 08840.

106. R.P. Young, in "Infrared and Raman Spectroscopy", Part B, E.G. Brame, Jr. and J.G. Grasselli, Eds., Marcel Dekker Inc., NY 1977.

107. D. Peiffer, S.D. Hong, and R.S. Stein, J. Polym. Sci., Polym. Phys. 13, 1945 (1975).

108. R. Yamada, C. Hayashi, and S. Onogi, International Union of Pure and Applied Chemists, Macromolecular Symposium, 1966.

109. R.S. Stein, S. Onogi, K. Sasaguri, and D.A. Keedy, J. Appl. Phys. 34, 80 (1963).

110. R.S. Stein, J. Appl. Polym. Sci. 5, 96 (1961).

111. G.B. Wang and S.L. Cooper, Macromolecules 16, 775 (1983).

112. G.M. Estes, R.W. Seymour, and S.L. Cooper, Macromolecules 4, 452 (1971).

113. D.S. Hubbel and S.L. Cooper, J. Polym. Sci., Polym. Phys. Ed. 15, 1143 (1977).

114. D. Lefebvre, B. Jasse, and L. Monnerie, Polymer 22, 1616 (1981).

115. F.J. Lu, E. Benedetti, and S.L. Hsu, ACS Advances in Chemistry Series, in press.

116. J.D. Ferry, "Viscoelastic Properties of Polymers", 3rd edition, John Wiley and Sons, New York, 1980.

117. MOOG Inc., Industrial Division, East Aurora, New York 14052.

118. D.J. Burchell and S.L. Hsu, ACS Symposium Series #203, "Instrumental and Physical Characterization of Macromolecules", C.D. Craver, Ed., p. 533, 1983.

119. J.A. deHaseth, 1981 International Conference on Fourier Transform Infrared Spectroscopy, Proc. SPIE, 289, 34 (1981).

120. S. Hoshino, J. Powers, D.G. Legrand, H. Kawai, and R.S. Stein, J. Polym. Sci. 58, 185 (1962).

121. S. Onogi and T. Asada, J. Polym. Sci. C16, 1445 (1967).

122. S.E. Molis, W.J. MacKnight, and S.L. Hsu, Appl. Spctrosc., in press.

123. W.K. Witsieppe, Advances in Chem. 129, 39 (1973).

124. L. Zhu, G. Wegner, Makromol. Chemie 182, 3625 (1981).

125. R.M. Briber and E.L. Thomas, Polymer, in press.

126. P.C. Mody, G.L. Wilkes, and K.B. Wagener, J. Appl. Polym. Sci. 26, 2853 (1981).

127. A. Lilaonitkul, J.C. West, and S.L. Cooper, J. Macromol. Sci.-Phys. B12, 563 (1976).

128. G. Wegner, T. Fujii, W. Meyer, and G. Lieser, Die Ange Makromol. Chemie 74, 295 (1978).

129. L. Zhu, G. Wegner, and U. Bandora, Makromol. Chemie, 182, 3639 (1981).

129. R.M. Briber and E.L. Thomas, Bull. Am. Phys. Soc. 29(3), 448 (1984).

130. R.M. Briber, Ph.D. Thesis, University of Massachusetts, 1983.

131. I.M. Ward, M.A. Wilding, and H. Brody, J. Polym. Sci., Polym. Phys. Ed. 14, 263 (1976).

132. I.H. Hall and M.G. Pass, Polymer 17, 807 (1976).

133. P.C Gillette, S.D. Dirlikov, J.L. Koenig, and J.B. Lando, Polymer 23, 1760 (1982).

134. H.W. Siesler, Makromol. Chem. 180, 2261 (1979).

135. H.W. Siesler, J. Polym. Sci., Polym. Lett. Ed. 17, 453 (1979).

136. K. Holland-Moritz and H.W. Siesler, Polym. Bull. 4, 165 (1981).

137. G.R. Davies, T. Smith, and I.M. Ward, Polymer 21, 221 (1980).

138. K. Tashiro, Y. Nakai, M. Kobayashi, and H. Tadakoro, Macromolecules 13, 137 (1980).

139. W. Strohmeir and W.F.X. Frank, Colloid and Polym. Sci. 260, 937 (1982).

140. P.L. Taylor and V.K. Dalye, Bull. Am. Phys. Soc. 29(3), 408 (1984).

141. L.W. Jelinski, J.J. Dumais, and A.K. Engel, Macromol. 16, 403 (1983).

142. L.W. Jelinski, J.J. Dumais, P.I. Watnick, A.K. Engel, and M.D. Sefcik, Macromol. 16, 409 (1983).

143. L.W. Jelinski, J.J. Dumais, and A.K. Engel, Macromol. 16, 492 (1983).

144. B. Stambaugh, J.B. Lando, and J.L. Koenig, J. Polym. Sci., Polym. Phys. Ed. 17, 1063 (1979).

145. P. Gillette, J. Lando, J. Koenig, H. Brown, E. Kramer, and P. Mills, Bull. Am. Phys. Soc. 28(3), 395 (1983).

146. D.H. Bilderback, Operations Manager, Cornell High Energy Synchrotron Source, Cornell University; private communications.

147. L.A. Nafie and D.W. Vidrine, in "Fourier Transform Infrared Spectroscopy", Vol. 3, J.R. Ferraro and L.J. Basile, Eds., Academic Press, New York, 1982.

148. L.A. Nafie and M. Diem, J. Appl. Spectrosc. 33, 130 (1979).

149. E.D. Lipp, C.G. Zimba, L.A. Nafie, and D.W. Vidrine, J. Appl. Spectrosc. 36, 496 (1982).

150. E.D. Lipp, C.G. Zimba, and L.A. Nafie, Chem. Phys. Lett. 90, 1 (1982).

151. A.E. Dowrey and C. Marcott, Appl. Spectrosc. 36, 414 (1982).

152. C. Marcott, Appl. Spectrosc. 38, 442 (1984).

153. W.G. Golden, D.S. Dunn, and J. Overend, J. Catalysis 71, 395 (1981).

154. M.F. Russel, M. Billardon, and J.P. Badoz, Appl. Optics 11, 2375 (1972).

155. M. Grosjean and M. Legrand, Compt. Rend. 251, 2150 (1960).

156. L. Velluz, M. Legrand, and M. Grosjean, "Optical Circular Dichroism", Academic Press, New York, 1973.

157. R.S. Stein, J. Appl. Polym. Sci. 5, 96 (1961).

158. A.E. Allegrezza, Jr., R.W. Seymour, H.N. Ng, and S.L. Cooper, Polymer 15, 433 (1974).

159. I. Chabay and G. Holzworth, Appl. Optics 14, 454 (1975).

160. J.C. Kemp, J. Opt. Soc. Am. 59, 950 (1969).

161. E. Hecht and A. Zajac, "Optics", Addison-Wesley, 1979.

162. C.H. Perry, R. Geick, and E.F. Young, Appl. Optics 5, 1171 (1966).

163. I. Noda, A.E. Dowrey, and C. Marcott, J. Polym. Sci., Polym. Lett. Ed. 21, 99 (1983).

164. I. Noda, A.E. Dowrey, and C. Marcott, International Union of Pure and Applied Chemists, 28th Macromolecular Symposium, 1982.

165. Hinds International, Inc. P.O. Box 4327, Portland, Oregon 97208.

A P P E N D I X

COMPUTER PROGRAMS USED TO CONTROL THE RAMAN SPECTROMETER

Explanation

The Pascal program is composed of a main program body and procedures for the collection of the data, storage of the data into files, and communication with another Nicolet computer. The main program body gets the user commands and calls the appropriate procedures to execute the commands. The global variables which store the spectrum and its parameters are declared in the main program. An examination of the collection routines (in File SCANX.SRC) along with Figure 15 provides a step by step explanation of the system operation during data collection. The data storage routines (in file DISKX.SRC) are the most difficult portion of the program to understand. Their structure could possibly be simplified by rewriting them in Pascal/MT+5.0, a more complete version of Pascal. The addition of character strings in this new version allows the replacement of the procedures readstr, nameparser, and access with one statement: read (filename). The calls to the procedure WNI and function GNI and their associated buffers and variables can also be replaced by single statements. WNI becomes write (file, i) and GNI becomes read (file,i). Nevertheless, the two main procedures diskread and diskwrite would remain essentially the same.

Communication with the Nicolet computer is hampered by the Nicolet's lack of handshaking and buffering on its serial communications port. The Nicolet does not indicate when characters are coming in too fast for it to process. The maximum input rate depends on the program that is receiving the characters. To overcome these problems in our programs, a portion of data is sent to the Nicolet and then the sending program waits until the Nicolet asks for more data. Using this scheme, two types of programs can be written, very specific or very general. A general program might be able to send any number of lines of characters with any line length. The Raman data would be put into character format, sent to the Nicolet, and then turned back into numbers. A scheme of this sort can also be used to send any other data that can be put into character format (ASCII). However, this type of program is more difficult to design and is not suited to tasks that must be synchronized between two quite different computers. Therefore, a more specific program was written allowing only three data types to be sent to the Nicolet: 1) a single character, 2) an integer, or 3) any one of three different single character acknowledgement messages. The Nicolet can only send back acknowledgement messages or single characters.

BASIC programs have been written on the Nicolet to directly manipulate the Raman files. The Raman files stored both on the Nicolet and microcomputer disks have the same format. The first 50 integers are set aside to store the collection parameters and the spectral data follows (one data point per integer). These programs allow all the

sophisicated computer programs available for analysis of the infrared data to be used for the Raman data as well. Therefore, subtraction of the basline or Rayleigh scattering corrections for temperaturae and frequency perturbations to give the LAM all-trans segment length distributions are possible. The Nicolet-supplied curve fitting progrm CAP and the Nicolet laser Raman software package can also be used to analyze our Raman data. A Fortran program was written which interpolates the Raman data to form FT-IR data files. These data files can then be plotted, displayed, smoothed, integrated, and otherwise manipulated with the extensive software of the Nicolet FT-IR program.

Program Listings

File RAMANX.PAS

```
Program Ramanx;

(* RAMANX EDITED FROM RAMAN3.SRC 11/12/81 JEL *)
(* TYPES VERSION DATE AND NAMES *)
const specsize = 4095 ;
var present , final : real ;
    numpts : integer ;
    ch,bell : char ;
    header : array[0..49] of integer ;
    spectrum : array[0..specsize] of integer ;

(*$I diskx *)   (* contains access, WNI, GNI, diskread, and diskwrite *)
(*$I scanx  *)   (* contains collect and position *)
(*$I nicx   *)   (* is nicolet *)

begin (*ramanX *)
  bell :=chr(7) ; (* rings terminal *)
  writeln(' ramanx 11/16/81 ');
  writeln(' nicx  scanx  diskx ');
repeat
  writeln ;
  writeln('this program can do the following ') ;
```

```
writeln(' (C)ollect a spectrum and store it into memeory ') ;
writeln(' (W)rite the spectra in memory onto disc ') ;
writeln(' (R)ead a spectrum from disc into memory ') ;
writeln(' (N) transfer a spectrum from memory to the nicolet ') ;
writeln(' (M)ove the spectrometer from  A  to   B  ') ;
writeln(' (Q)uit this program   ') ;
writeln ;
writeln(' please enter  C  W  R  N  M  or  Q      return ') ;

readln(ch) ;
if ch = 'C' then collect
else if ch = 'W' then diskio(false)
else if ch = 'R' then diskio(true)
else if ch = 'N' then nicolet2
else if ch = 'Q' then exit
else if ch = 'M' then begin
      writeln ;
      writeln('          M O V E') ;
      writeln ;
      writeln('enter present cm-1          return ') ;
      readln(present) ;
      writeln('enter final cm-1     return ') ;
      readln(final) ;
      position(final,present) ;
      end ;   (* remove ";" if another else if added *)

until false ; (* forever *)
end . (* RAMANX *)
```

File SCANX.PAS

```
(* SCANX WAS EDITED FROM SCAN.SRC 11/12/81 JEL *)

procedure position(final,present:real) ;
(*       definitions of bits of control port $84          *)
(*      bit #     function      explain                    *)
(*      OUT                                                *)
(*      4         stop/run      monochrm. cm-1             *)
(*      5         clock         pulses to momchr cm-1      *)
(*      6         down/up       monochr.  direction        *)

const lowdly = 100 ;
    highdly = 100 ;
    initdly = 300 ;
var   up : boolean ;
    numsteps, cnx, ii, loopcount : integer ;
    cch : char ;
```

```
begin

(* bring spec stop high, (leave high forever ) *)
    setbit(cnx,4) ;
    output[$84] := cnx ;

repeat
    (* set up *)
    if final > present then up := true else up := false ;
    numsteps := round(10 * abs(final - present) ) ;

    (* move *)
    if up = true then setbit(cnx,6) else clrbit(cnx,6) ;
    for loopcount := 1 to initdly do ;
    for ii := 1 to numsteps do
        begin
        clrbit(cnx,5) ;
        output[$84] := cnx ;
        for loopcount := 0 to lowdly do ;
        setbit(cnx,5) ;
        output[$84] := cnx ;
        for loopcount := 0 to highdly do ;
        end ;

    clrbit(cnx,5) ;
    output[$84] := cnx ;

    (* check position *)
    writeln(' ') ;
    writeln('final position is ',final) ;
    writeln ;
    writeln('if correct enter Y else enter N     return') ;
    readln(cch) ;
    writeln(' ') ;
    if (cch = 'Y') or (cch = 'y') then exit ;
    writeln ;
    writeln('enter current CM-1     return ') ;
    readln(present ) ;
until false (* loop forever leave via exit *)
end; (*position*)

procedure collect ;
(*              bit definitions of port $84              *)
(*      bit #           explaination                     *)
(*      OUT                                              *)
(*      0       digit readin clock to counter            *)
(*      1       resets counter to zero                   *)
```

```
(*      2       counter start                                   *)
(*      3       clears timer interrupt(bit 4 in)                *)
(*      7       timer start                                     *)

(*      IN                                                      *)
(*      0-3     BCD counter data, six digits                    *)
(*      4       timer finished, also wired                      *)
(*                      to counter hold                         *)


label 3 ;
const
    hgch        = $74 ;
    lwch        = $78 ;   (* not connected *)
    tua         = $84 ;
    lowdly      = 100 ;
    highdly     = 100 ;
    initdly     = 300 ;
    mask        = $10 ;

var   dlt, dlw,
    cwn ,enp,stp : real ;
    ttime : real ;
    numpts,
    timerval,temp1,temp2,
    i,ii,j,jj,y,
    cnx,
    counts,indigit : integer ;
    lowchar,highchar : char ;
    upscan : boolean ;
    cch : char ;
    (* header and spectrum aren't *)
    (* passed in proced. they *)
    (* are shown here for clarity *)
    (*header : array[0..49] of integer ; *)
    (* spectrum : array[0..specsize] of integer ; *)

function intensity : integer ;
begin  (*intensity  *)

    (* reset counter *)
    clrbit(cnx,1) ;
    output[$84] := cnx ;
    setbit(cnx,1) ;
    output[$84] := cnx ;
```

```
(* start timer and counter *)
clrbit(cnx,2) ;
clrbit(cnx,7) ;
output[$84] := cnx ;
setbit(cnx,2) ;
setbit(cnx,7) ;
output[$84] := cnx ;

(* wait for a timeout *)
wait(tua,mask,false) ;      (* mask = $10 for bit #4 *)

(* readin counts *)
counts := 0 ;
for i := 1 to 6 do
    begin
    clrbit(cnx,0) ;
    output[$84] := cnx ;
    setbit(cnx,0) ;
    output[$84] := cnx ;
    indigit := ord( input[$84]  ) ;
    indigit := indigit & $0F ;
    write(indigit);
    if counts > 3276 then write(' count overflow',ii) ;
    counts := 10 * counts + indigit ;
    end ;

    writeln ;
    if counts >= 0 then intensity := counts
    else intensity := -9999 ;

    (* new clear timer interupt *)
    (* also brings hold counter up *)
    clrbit(cnx,3) ;
    output[$84] := cnx ;
    setbit(cnx,3) ;
    output[$84] := cnx ;
end ; (* intensity *)


begin (* body of collect *)
    writeln ;
    writeln('         D A T A   C O L L E C T ') ;
    writeln ;

repeat
    (* get values fron terminal *)
    writeln(' enter starting  CM-1       return ') ;
```

```
readln(stp) ;
writeln(' enter ending    CM-1        return ') ;
readln(enp) ;
writeln ;
writeln(' enter delta cm-1 per point   return ') ;
readln(dlw) ;
writeln('enter delta time per point    return ') ;
readln(dlt) ;

(* calculate constants *)
(* calc dev const and initialize *)
if enp > stp then upscan := true else upscan := false ;
if dlw < 0.05 then dlw := 1 ;
numpts := round(  abs(stp - enp )  / dlw ) + 1 ;
if numpts > specsize then
    writeln(bell,'TOO MANY DATA PTS ',specsize,' MAX PTS.');
if (dlt > 0.01 ) and (dlt < 10.0) then
    timerval := round( 1000.0 * (10.0 - dlt) )
else
    begin writeln(bell,'bad value of dlt',bell);
    dlt := 0.0 ;
    timerval := 500 ;
    end ;

(* check *)
    writeln ;
    writeln ;
    writeln('  START       ',stp,'  CM-1');
    writeln('  END         ',enp,'  CM-1');
    writeln('  DELTA CM-1  ',dlw,'  CM-1 / POINT');
    writeln('  delta time  ',dlt,'  SEC. / POINT');
    writeln;
    writeln('  total # points  ',numpts,'  DATA POINTS');
    ttime := numpts * dlt / 60 ;
    writeln('  total time      ',ttime,'  MINUTES');

    writeln ;
    writeln(' DO YOU WISH TO CHANGE THESE VALUES ?  Y OR N  return ') ;
    readln(cch) ;
until  (cch<>'Y') ;

    (* calc count up for timer *)
    (* timer will count up from timerval *)
    (* to 9999,    each digit of timerval *)
    (* is output in its binary form   *)
    (* each digit goes to 4 bits and *)
    (* two 4 bit digits pack in highchar *)
    (* and two into lowchar  *)
    (* lowchar is wired  zeros on the timer *)
```

```
for i := 1 to 2 do
    begin
    temp1 := timerval mod 10 ;
    timerval := timerval div 10 ;
    temp2 := timerval mod 10 ;
    timerval := timerval div 10 ;
    highchar := chr(16*temp2 + temp1) ;
    if i = 1 then lowchar := highchar ;
    end ;

(* output to timer *)
output[hgch] := highchar ;
output[lwch] := lowchar ;
writeln(ord(highchar) div 16,' ',ord(highchar&$0F),'time value');

(* reset timer interrupt *)
clrbit(cnx,3) ;
output[$84] := cnx ;
setbit(cnx,3) ;
output[$84] := cnx ;

(* bring spec stop line up *)
setbit(cnx,4) ;
output[$84] := cnx ;

    (* set dir line *)
    if upscan = true then
        setbit(cnx,6)
    else clrbit(cnx,6) ;

(* end of intialize *)

    writeln('enter current CM-1       return ') ;
    readln(cwn) ;
    position(stp,cwn) ;
    ii := 0 ;
    (* take two intensities to allow timer circuit to settle*)
    y := intensity ;
    y := intensity ;
    writeln ;

    for ii := 0 to (numpts-1) do
        begin
        y := intensity ;
        spectrum[ii] := y ;
```

```
    (* move monochromater *)
    clrbit(cnx,5) ;
    for j := 1 to lowdly do output[$84] := cnx ;
    for jj := 1 to round(10 * dlw ) do
        begin
        clrbit(cnx,5) ;
        for j := 1 to lowdly do output[$84] := cnx ;
        setbit(cnx,5) ;
        for j:= 1 to highdly do output[$84] := cnx ;
        end ;
    clrbit(cnx,5) ;
    output[$84] := cnx ;
    (* end of move *)
    end ;
writeln('end of scan ') ;

(* HEADER SECTION *)
header[0] := 1 ; (*version # *)
header[1] := round(10 *stp ) ;
header[2] := round(10 *enp ) ;
header[3] := round(10 *dlw ) ;
header[4] := round(1000 *dlt ) ;
header[5] := numpts ;
for ii := 6 to 49 do header[ii] := $CC ;
end ; (* of collect body  *)
```

File DISKX.PAS

```
(* diskiox edited from diskio.src 11/13/81 jel *)
(* should now allow backspacing during filename entry *)
(* also checks to see if file exists before writing *)
(*a new one with the same name *)

procedure diskio(fread:boolean) ;

CONST  BUFSIZE = 63 ;

TYPE  BUFFER = ARRAY[0..BUFSIZE] OF INTEGER ;
    TITTLE = ARRAY[0..11] OF CHAR ;
var
    FILETITLE : TITTLE ;
    eof, werr : boolean ;
    outbuf : buffer ;
    oFCB  : text ;
    result,index : integer ;
    int, ii , nulldata : integer ;
```

```
procedure access(VAR title : tittle  ) ;
    const maxlen = 22;
    type string = array[1..maxlen] of char ;
    var  chindex : integer ;
        ch : char ;
        inlen,outlen : integer;
        instr,outstr :  string;

procedure readstr(var slen:integer;var sval:string) ;
    (*routine allowing deletes of an input string *)
var i: integer;
    ch:char;

begin
    sval[1] := ' ' ;
    move(sval[1],sval[2], maxlen-1 ); (*blank string*)
    slen := 0;
    repeat
     read(ch) ;
     case ord(ch) of
        $0D : exit ; (* carriage return *)
        $7f,8 : (*delete=$7f  backspace =08 *)
            begin
            if slen > 0 then
                begin
                (* blank char in string *)
                sval[slen] := ' ';
                slen := slen - 1;
                (*blank deleted char on terminal *)
                if ord(ch) = 127 then write(chr(08) );
                write ( ' ' ,chr(08)  );
                end
            end;
        else (* case of other char *)
             (* new char in string*)
            if (ch >= ' ') and (slen <maxlen) then
                begin
                slen :=succ(slen);
                sval[slen] := ch ;
                end
     end  (* case statement *)
  until false ;
end; (*readstr*)

procedure nameparser(var inlen,outlen:integer;var inval,outval:string);
(* changes string into cpm format *)
```

```
var i, j : integer ;
begin
    outlen := 0 ;  outval[1] := ' ' ;
    move(outval[1], outval[2], 11); (*blank output string*)
    outval[1] := chr(0) ; (*set disk # to zero for current disk *)
    i := 1; j := 2;
    if (inval[2] = ':') then (* disk drive letter was given *)
        begin
        outval[1] := chr( ord(inval[1]) - ord('A') +1);
        i := i + 2 ;  (*3*)
        end;
    while ( i <= inlen) and (ord(inval[i]) <> 46 ) do (* chr(46)="." *)
        begin
        outval[j] :=  inval[i]  ;
        j := j+1; i :=i+1 ;
        end;
    if i > inlen then  exit ;
    i :=i+1; (*skip period *)
    j := 10 ; (*point to ext part of filename *)

    while (i <= inlen) and (j <= 12) do
        begin
        outval[j] := inval[i];
        j:=j+1; i :=i+1;
        end;
end ; (*nameparser*)

begin (* access file *)
    writeln ;
    writeln('enter  #filename.EXT       return ') ;
    writeln ;
    readstr(inlen,instr);
    nameparser(inlen,outlen,instr,outstr);
    move(outstr[1],title[0],12);
    writeln;
    write( ord(title[0] ), ' ' ) ;
    for chindex := 1 to  11 do
        begin
        write(title[chindex]) ;
        if chindex = 8 then write ('.') ;
        end ;
    writeln ;
end ; (* of file access *)

(*-----------------------------------------*)
(* explanation in pascal manual (fileio.src )   *)
(*      ROUTINE:        WNI                     *)
(*      PURPOSE:        WRITE A integer TO A FILE *)
```

```
(*                                                  *)
(*      INPUTS:          F : TEXT FILE             *)
(*                       BUF : I/O BUFFER          *)
(*                       INDX : INDEX INTO BUF     *)
(*                       int : INPUT integer TO WRITE*)
(*      OUTPUT:                                     *)
(*                       ERR : BOOLEAN SET TO      *)
(*                             TRUE IF DISK FULL   *)
(*                                                 *)
(*-------------------------------------------------*)

PROCEDURE WNI(VAR F : TEXT;
              VAR BUF : BUFFER;
              VAR INDX : INTEGER;
              VAR ERR : BOOLEAN;
              VAR int : integer);

VAR
  RESULT : INTEGER;
  I : INTEGER;

BEGIN (* WNI *)
  WRITELN(INT);
  BUF[INDX] := int;
  INDX := INDX + 1;
  ERR := FALSE;
  IF INDX <= BUFSIZE THEN
    EXIT
  ELSE
    BEGIN
      FOR I := 1 TO (BUFSIZE + 1) DIV 64 DO
        BEGIN
          BLOCKWRITE(F,BUF[(I-1)*64],RESULT);
          IF RESULT <> 0 THEN
             BEGIN
               ERR := TRUE;
               EXIT
             END
        END;
      INDX := 0
    END

END; (* WNI *)


FUNCTION GNI(VAR F:TEXT;
             VAR BUF:BUFFER;
             VAR INDX : INTEGER;
             VAR EOF:BOOLEAN) : integer;
```

```
VAR
  RESULT : INTEGER;
  I : INTEGER;
 int: integer; (* FOR SPEED *)

BEGIN (* GNI *)

  IF INDX > BUFSIZE THEN
    BEGIN
      FOR I := 1 TO (BUFSIZE+1) DIV 64 DO
        BEGIN
          BLOCKREAD(F,BUF[(I-1)*64],RESULT);
          IF (RESULT <> 0) AND (I = 1) THEN
            BEGIN
              int := -9999;
              GNI := int;
              EOF := TRUE;
              EXIT
            END
        END;
      INDX := 0
    END;

  int := BUF[INDX];
  GNI := int;
  INDX := INDX + 1;
  EOF := false
(* valid eof is no longer determined *)
(* except for full records *)
(* ei. file is multiple of 128 bytes *)
END; (* GNI *)

procedure diskread ;

(* gets filename thru procedure access and           *)
(* puts data into header[0:49] and spectrum[0:numpts] *)
(* numpts is read from file, numpts = header[5]      *)
(* the following must be defined in the calling program *)
(* procedures access and GNI                         *)
(* constant specsize, the size of spectrum and       *)
(* bufsize, the size of buffer                       *)
(* variables header:array[0..49] of integer          *)
(* spectrum :array[0..specsize]                      *)
(* oldfile, EOF : boolean                            *)
(* index, result, int, ii, numpts :integer           *)
(* oFCB : text,  outbuf:buffer                       *)
(* filetitle :tittle (array[0..11] of char )         *)
(* most of the above are used with GNI               *)
```

```
var ch : char ;
begin (* diskread *)
    writeln ;
    writeln('                D I S K R E A D ') ;
    writeln ;
    access(filetitle) ;
    open(oFCB, filetitle, result ) ;
    if result = 255 then
        begin
        writeln('unable to open input file ') ;
        exit ;
        end ;

    index := bufsize + 1 ; (* forces GNI to fill outbuf from disk  *)

    for ii := 0 to 49 do
        begin
        int := GNI(oFCB, outbuf, index, EOF) ;
        header[ii] := int ;
        if EOF = true then
            begin
            writeln(' unexpected EOF while reading header ') ;
            exit ;
            end ;
        end ;

    numpts := header[5] ;
    if (numpts < 1) or (numpts > specsize) then
        begin
        writeln(' numpts from file header is out of range ') ;
        exit ;
        end ;

    for ii := 0 to numpts do
        begin
        int := GNI(oFCB, outbuf, index, EOF ) ;
        spectrum[ii] := int ;
        if EOF = true then
            begin
            writeln('unexpected EOF while reading in spectrum ') ;
            exit ;
            end ;
        end ;

    writeln('  file has been read  ') ;
    writeln ;

end ; (* of diskread *)
```

```
procedure diskwrite ;
(* write header and spectrum          *)
(* into filename obtained thru access *)
(* uses same variable as diskread     *)

begin (* diskwrite *)
    writeln ('              D I S K W R I T E ') ;
    access(filetitle) ;
    open(oFCB, filetitle, result ) ;
    if result <> 255 then
        begin
        writeln('file allready exists');
        writeln('do you wish to destroy the old data ? ');
        writeln(' enter  Y  or N         return');
        readln(ch);
        if (ch <> 'Y') then exit ;
        delete(oFCB) ;
        end ;
    create(oFCB,filetitle,result) ;
    if result = 255 then
        begin
        writeln('unable to open output file ') ;
        exit ;
        end ;

    index := 0 ;
    for ii := 0 to 49 do
        begin
        int := header[ii] ;
        WNI(oFCB, outbuf, index, werr, int) ;
        if werr = true then
            begin
            writeln('erorr in writeing header to disk ') ;
            exit ;
            end ;
        end ;

    numpts := header[5] ;
    for ii:= 0 to numpts do
        begin
        int := spectrum[ii] ;
        WNI(oFCB, outbuf, index, werr, int ) ;
        if werr = true then
            begin
            writeln('error in writing to file ') ;
            exit ;
            end ;
        end ;
```

```
    if index < bufsize then
        begin
        nulldata := -9999 ;
        for int := index to bufsize + 1 do
            WNI(oFCB, outbuf, index, werr, nulldata ) ;
        end ;
    close(oFCB,result) ; writeln('file close result' , result ) ;
    writeln ;
end ; (*of disk output *)

begin (* procedure body of diskio *)
    if fread = false then diskwrite
    else diskread ;
    exit ;
end ;
```

File NICX.PAS

```
(* NICX WAS EDITED FROM NIC2.SRC 11/12/81 JEL *)
(*  SHOULD EXIT PROCEDURE FOR MOST ERRORS     *)
(*  FILENAME TO NIC ALLOWS BACKSPACE AND ANY NUMMBER OF CHARS *)

PROCEDURE NICOLET2 ;
(* send header(0-5) and spectrum to nicolet *)

CONST Z1=$41;
    Z2=$42;
    Z3=$43 ;
    (* ASCII values of ack,eos,eom  *)
    (* Z1-> A , Z2 -> B , Z3 -> C   *)
    VERSION = 1 ;
    CRL = 141 ;
TYPE PROTOCOL = (ACK, EOS, EOM) ;
VAR CH, CR :
    CHAR; I,J:integer ;
    TEST:BOOLEAN;
    NAME : ARRAY[0..20] OF CHAR ;

PROCEDURE INITNIC ;
CONST BAUD300 = $84 ;
    BAUD9600 = $C0 ;
    BAUD19200 = $10 ;
    BAUD4800 = $20 ;
    HIGHBAUD = $11 ;   (* RESETS FOR BAUDS > 9600 *)
    RESET = $01 ;
    INTMASK = 00 ;
```

```
BEGIN  (*  INIT NIC *)
    OUTPUT[$80] := BAUD4800 ;
    OUTPUT[$83] := INTMASK ;
    OUTPUT[$82] := RESET ;
END ;

FUNCTION GETNIC : CHAR ;
BEGIN
    WAIT($80,$40,00) ;
    CH :=INPUT[$81] ;
    GETNIC := CHR(ORD(CH) & $7F)  ; (* CLEARS PARITY BIT *)
END ;

PROCEDURE PUTNIC(CH:CHAR) ;
BEGIN
    WAIT($80,$80,00);
    CH := CHR(ORD(CH) ! $80 ) ;
    (* SET HIGH BIT OF CH  (FOR MARK PARITY) *)
    OUTPUT[$81] := CH ;
END ;

PROCEDURE SEND(MESSAGE:INTEGER) ;
BEGIN
    IF (MESSAGE) = 0 THEN
        WRITE([addr(PUTNIC)], CHR(Z1) ,CR )
    ELSE IF (MESSAGE) = 1 THEN
        WRITE([addr(PUTNIC)], CHR(Z2) ,CR )
    ELSE IF (MESSAGE) = 2 THEN
        WRITE([addr(PUTNIC)], CHR(Z3), CR )
    ELSE
        WRITELN('ERROR IN NIC ') ;
END ;

FUNCTION RECEIVE(MESSAGE:INTEGER) : BOOLEAN ;
    VAR CH : CHAR;
        INMESS : PROTOCOL ;
BEGIN
    READ([addr(GETNIC)], CH) ;
    IF CH=CHR(Z1) THEN
        INMESS := ACK
    ELSE IF CH = CHR(Z2) THEN
        INMESS := EOS
    ELSE IF CH = CHR(Z3) THEN
        INMESS := EOM ;
    IF (MESSAGE) = ORD (INMESS) THEN
        RECEIVE := TRUE
    ELSE
        RECEIVE := FALSE ;
END ; (* RECEIVE *)
```

```
PROCEDURE TRANSMIT(INT:INTEGER) ;
    VAR TEST : BOOLEAN ;
BEGIN
    TEST := RECEIVE(ORD(ACK)) ;
    WRITE( [addr(PUTNIC)], INT, CR) ;
END ;

BEGIN (* PROCEDURE BODY NICOLET *)
    INITNIC ;
    CR := CHR(CRL) ; (*SET CARRAIGE RETURN *)
    WRITELN;
    WRITELN('      NICOLET FILE TRANSFER   ') ;
    WRITELN ;

(* BEGIN SET UP *)
        WRITE([addr(PUTNIC)],  'G' ) ;
        WRITELN('START NICOLET PROGRAM NOW  THEN ENTER 1  return ') ;
        READLN(CH) ;
        WRITE( [addr(PUTNIC)], CR ) ;
        READ([addr(GETNIC)], CH ) ;
        IF CH <> 'G' THEN
            BEGIN WRITELN('ERROR G EXPEXTED ');
            EXIT;
            END;

        SEND(ORD(ACK)) ;
        SEND(ORD(EOS)) ;
        SEND(ORD(EOM)) ;
        TEST := RECEIVE(ORD(ACK)) ;
        IF TEST = FALSE THEN
            BEGIN WRITELN('ERROR ACK EXP. 3SEND');
            EXIT;
            END;
(* END SETUP *)

(* BEGIN FILENAME *)
        READ([addr(GETNIC)], CH ) ;
        IF CH <> 'F' THEN
            BEGIN WRITELN('ERROR F EXPECTED ');
            EXIT;
            END;
        WRITELN ;
        WRITELN('  ENTER NICOLET FILENAME     RETURN ') ;
        I := 0 ;
        REPEAT
            READ(CH) ;
            IF ((ORD(CH) = $08) OR (ORD(CH) = 127 )) THEN
                IF I=0 THEN (* *)
```

```
        ELSE
            BEGIN  I:=I-1 ;
            NAME[I]:=' ';
            IF ORD(CH) = 127 THEN WRITE(CHR(08) );
            WRITE(' ',CHR(08) );
            END

    ELSE
        BEGIN  NAME[I] := CH ;
        I:=I + 1 ;
        END;
UNTIL (ORD(CH)=$0D)  ;
I:=I-1;
FOR J:=0 TO I DO
    BEGIN WRITE( [addr(PUTNIC)], NAME[J]);
    WRITE( NAME[J]);
    END;

WRITELN;
SEND(ORD(EOS)) ;
TEST := RECEIVE(ORD(ACK)) ;
IF TEST=FALSE THEN
    BEGIN WRITELN('ERROR ACK EXP AFTER FILENAME ');
    EXIT;
    END;
(* END FILENAME *)

(* BEGIN FILE HEADER *)
    FOR I := 0 TO 5 DO
        TRANSMIT(HEADER[I]) ;
    TEST := RECEIVE(ORD(ACK)) ;
    IF TEST=FALSE THEN
        BEGIN WRITELN('ERROR ACK EXP AFTER HEADER ');
        EXIT;
        END;
(* END FILE HEADER *)

    NUMPTS := HEADER[5] ;

(* BEGIN  DATA XFER *)
    READ([addr(GETNIC)], CH ) ;
    IF CH <> 'D' THEN
        BEGIN WRITELN('ERROR D EXP');
        EXIT;
        END;
```

```
    FOR I := 0 TO (NUMPTS-1) DO
        TRANSMIT(SPECTRUM[I]) ;
    SEND(ORD(EOS)) ;
    TEST := RECEIVE(ORD(ACK)) ;
    IF TEST = TRUE THEN
        WRITELN ('TRANSFER COMPLETED ') ;
    WRITELN ;
(* END OF DATA XFER *)
END ; (*NICOLET PROCEDURE*)
```

Signal List of the Raman Microcomputer System

Timer

Pin #	Function
L	1 Mhz clock in
M	start
N	done
P	reset
Y	ground
Z	+5 volts

timer period is set by 4 BCD digits

1-4 most significant digit - bits 1248 respectively

5-8 second most significant digit - bits 1248 respectively

9-12 third most significant digit - tied to ground

13-16 fourth most significant digit - tied to ground

Monochromator drive

Pin #	Function
1	stop
2	step clock

3	direction (down)
10	ground

Counter

Pin #	Function
1-4	data BCD 1,2,4,8 (note 1)
5	data print clock
6	*system hold
7	stop
8	start
9	reset
10-13	*display BCD 1,2,4,8
14	*display clock
15	ground

*not used

note 1: The six digits of the count value are sent out serially one digit at a time by the data print clock. Each digit has 4 BCD bits 1, 2, 4, and 8.

Computer Parallel Port A

Input

Bit #	Function
0	BCD1 data from counter
1	BCD2
2	BCD4
3	BCD8

4	timer done
5-7	not connected

Output

Bit #	Function
0	counter print clock
1	counter reset
2	timer start
3	timer reset
4	spectrometer stop
5	spectrometer step
6	spectrometer direction
7	counter start

Computer Parallel Port B

Input

Unused

Output

Bit #	Function
0-3	timer period, most significant digit BCD 1248 respectively
4-7	timer period, second most significant digit BCD 1248